The Mid-Pleistocene landscape history of the Lower Aare Valley with emphasis on subglacial overdeepening

Inaugural dissertation

of the Faculty of Science,

University of Bern

presented by

Lukas Gegg

from Eichstätt, Germany

Supervisors of the doctoral thesis:

Prof. Dr. Flavio S. Anselmetti

Dr. Marius W. Buechi

Institute of Geological Sciences,

University of Bern

The Mid-Pleistocene landscape history of the Lower Aare Valley with emphasis on subglacial overdeepening

Inaugural dissertation

of the Faculty of Science,

University of Bern

presented by

Lukas Gegg

from Eichstätt, Germany

Supervisors of the doctoral thesis:

Prof. Dr. Flavio S. Anselmetti

Dr. Marius W. Buechi

Institute of Geological Sciences,

University of Bern

Accepted by the Faculty of Science.

Bern, October 19th 2021

The Dean

Prof. Dr. Zoltan Balogh

Abstract

Throughout the most recent part of geological history, glaciers repeatedly built up in the Alps and advanced into the mountain foreland, episodically covering the majority of Switzerland and neighbouring regions with ice. This had severe geomorphic impacts that include the subglacial erosion of overdeepenings. These closed basins are not only a potential source of geohazards, but also contain valuable resources and archives of past environments, and therefore deserve our closer attention. However, our knowledge of i) the erosional mechanisms and the subglacial conditions that lead to the formation of overdeepenings, and ii) of the number, the timing, and the extent of Alpine glaciations, is still very limited.

The present thesis is centred around four scientific boreholes in the Lower Aare Valley in northern Switzerland and addresses the above-mentioned uncertainties. The study area hosts the overdeepened Gebenstorf-Stilli Trough, whose subsurface morphology is the first major focus. It is constrained by borehole and geophysical data that together reveal a complex trough shape controlled by the particular local bedrock architecture comprising rocks of varying subglacial erodibility. The results further highlight the important role of basal water in overdeepening erosion, which is further corroborated in a second case study. There, surficial brecciation of the walls of a paleokarst network in limestone underlying the overdeepening is presented. Following detailed macro- and microscopic analysis, it is interpreted as the result of subglacial hydrofracturing, and thus illustrates the extreme water pressures below the glacier ice.

Finally, the focus is shifted towards the sedimentary archives of the Gebenstorf-Stilli Trough and its surrounding. Based on a multi-method sedimentological approach, the diverse Quaternary deposits are characterised and their depositional history is reconstructed. Several phases of glacial and glaciofluvial reactivation of the major drainage pathways as well as contributions from confluent glaciers are identified. An integration of luminescence data indicates that overdeepening erosion in the Lower Aare Valley dates back to MIS 10 or earlier, and that the local sedimentary record spans large parts of the Middle and Late Pleistocene.

Friends made along the way

All the work that is presented in the following would not have been possible without the support and guidance by many outstanding people.

I would like to say thank you foremost to Flavio and Marius, who gave me the freedom and trust to make this project mine, to design the analyses and the publications in my own way, but who also were always available for advice and guided me into the right direction. But it was not all about work: the coffees and barbecues, the field trips and retreats – It was an absolute pleasure!

For their energetic help, but more importantly the fun in the field, in the lab, and in front of the PC, I want to cordially thank the QBO team (Andrea, Bennet, Daniel, Dominik and Dominik, Kim, Marius, Sebastian, and Simon). I further received precious inputs and support, and had great discussions with the entire Overdeepening Discussion Group (Dimitri, Fabio, Guilhem, Michi, and Patrick), as well as with Alfons, Catharina, Franziska, Fritz, Hendrik, Julia, Marina, Naki, Natacha, Stefano, Valentin, Yama, and many others. To you, and to the entire IfG, I also want to say a big thank you for the warm and supportive environment.

I would like to thank my dear colleagues at Nagra (Friedl, Gaudenz, Gela*, Luka, Michi, and Tom) and the University of Freiburg (Alex, Daniela, and Frank), as well as Andreas and Lukasz (GeoExplorers), Hansruedi (Dr. von Moos AG), Lori (roXplore), and Maria (Hohenheim), who provided me with beautiful material and data and/or valuable feedback and recommendations for my studies and my manuscripts. Further, I want to thank my former mentors in Munich for the excitement for geology, and for helping me get where I am today (Anke, Bettina, Bernhard, Guilhem and Ulli, Miriam, and many more). And, of course, thanks a lot to Bernhard (University of Salzburg) for his willingness to actually read and review this entire thesis.

Also, many thanks are due to Nagra for making this journey possible, and to the people behind AGAQ, CH-QUAT, and CUSO-ESPP for all the nice memories made outside of the project.

Contents

This page is intentionally left blank.

Panoramic view of Aletsch Glacier (Valais, Switzerland).

I. Introduction

1. Background and Motivation

> *Tiefe Wasser sind nicht still.*
>
> *'Deep waters don't run silent.'*
>
> *- Rammstein: Rosenrot (2005)*

1.1. What is an overdeepening?

Strongly fluctuating climate conditions and the repeated build-up and expansion of ice masses at the earth's poles and in mountain ranges characterised the most recent part of geological history (Ehlers and Gibbard, 2007; Lisiecki and Raymo, 2005). Like the glaciations themselves, their recognition is only relatively young: The first identifications of ice-rafted or ice-derived sediment far from present-day glaciers were made by 18th century scholars, and it took another ~100 years for such ideas to become broadly accepted (Krüger, 2013). With increasing prevalence of the 'ice age' concept in the scientific world however, the erosive potential of glacier systems – ice and melt water – was soon perceived as well (*e.g.* Davis, 1900; Johnson, 1909; Ramsay, 1878). The term 'overdeepening' is attributed to Albrecht Penck (Cook and Swift, 2012; Evans, 2008), and in the work that should become the fundament of Alpine Quaternary geology, Penck and Brückner (1909) already framed the 'rules of overdeepening'. However, the term was only roughly defined and used synonymously with deep subglacial erosion, focused in the major Alpine 'troughs'.

Today, overdeepenings are generally defined as subglacially eroded closed basins, *i.e.* they are characterised by an adverse slope at their distal end (Alley *et al.*, 2003b; Cook and Swift, 2012; Hooke, 1989). Occurring in all presently and formerly glaciated regions of the world (Cook and Swift, 2012, and references therein), overdeepened basins are common subglacial landforms. In Switzerland, for example, 5-10 % of the surface area of the Alpine foreland are underlain by Pleistocene overdeepenings (*e.g.* Fig. I-1; Dürst Stucki and Schlunegger, 2013).

Besides such young basins, the geological record further includes spectacular examples from the glaciations of the Permo-Carboniferous (Visser, 1987), the Ordovician (Clerc *et al.*, 2013), and potentially the Ediacaran (Li *et al.*, 2020). Recent studies finally suggested the existence of thousands of yet hidden subglacial basins below the ice masses of Antarctica and Greenland (Patton *et al.*, 2016), but also those of the Andes (Colonia *et al.*, 2017), the Himalayas (Furian *et al.*, 2021; Linsbauer *et al.*, 2016), and the European Alps (Haeberli *et al.*, 2016; Magnin *et al.*, 2020).

A distinction should be made between the sometimes synonymously applied terms overdeepening and tunnel valley. While 'overdeepening' is a morphologically descriptive term that refers to landforms of a broader environmental setting, tunnel valleys are landforms that are formed by a specific erosion process, namely through subglacial meltwater erosion at ice sheet margins (Cofaigh, 1996; Kehew *et al.*, 2012; Lonergan *et al.*, 2006; Van der Vegt *et al.*, 2012). As a result, not all overdeepenings are necessarily tunnel valleys, whereas most tunnel valleys are, or contain, overdeepened basins.
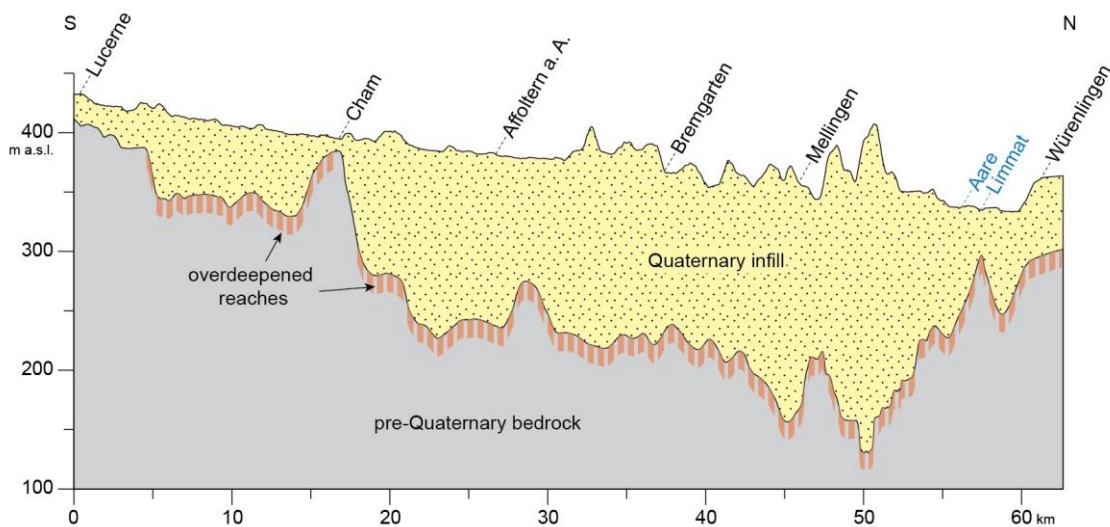
Fig. I-1: Longitudinal section depicting the pre-Quaternary bedrock topography along the Reuss/Lower Aare Valley between Lucerne and Würenlingen (Loepfe *et al.*, in prep.; Pietsch and Jordan, 2014). Large parts of the valley are underlain by overdeepenings (hatched red).

Major overdeepenings are over 100 km long and well over 1 km deep, so that the bases of some intra-mountain overdeepenings lie below sea level (Dürst Stucki and Schlunegger, 2013; Eyles *et al.*, 1990; Mullins and Hinchey, 1989). Consequently, several of the world's largest contemporaneous lakes are entirely or partially hosted by overdeepened basins, including the Great Lakes of North America (Larson and Schaetzl, 2001) and Lake Ladoga in Russia (Subetto *et al.*, 1998), as well as the 'Zungenbeckenseen' of the Alpine foreland (*e.g.* Lake Constance, Lake Geneva, Lake Garda; Penck and Brückner, 1909; Preusser *et al.*, 2010).

The scientific interest in overdeepenings is growing (Fig. I-2), and this chapter gives an overview over the socio-economic and academic motivations to study these basins as well as the processes of their formation. It further introduces the study area and the major issues addressed by the present thesis and the overarching research project.
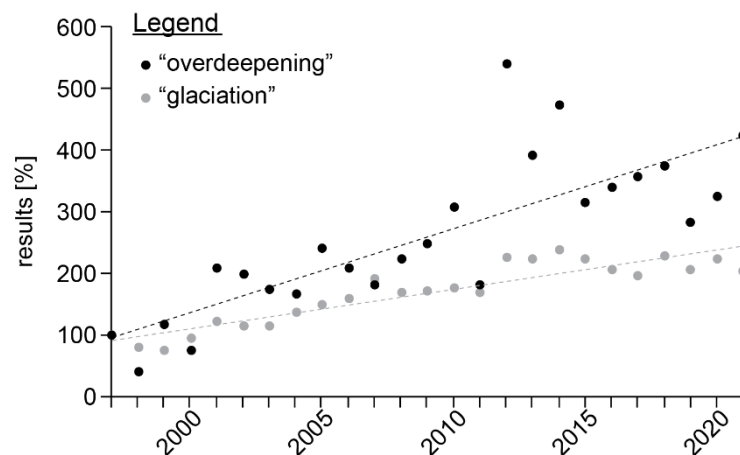
Fig. I-2: Numbers of search results (journal articles and book chapters) for the terms 'overdeepening' and, for reference, 'glaciation' at ScienceDirect.com for the past 25 years (number of results in 1998 = 100 %) illustrate the growing scientific interest in the topic.

1.2. Why should we care?

1.2.1. The present-day state of the cryosphere

We are living in a time of climate change, with ever new temperature records surpassing one another on a regular basis (Cheng *et al.*, 2021; Readfern, 2020; Voosen, 2021; Zhao *et al.*, 2020). Consequently, both the Earth's polar ice masses (Paolo *et al.*, 2015; Thomas *et al.*, 2006) as well as its mountain glaciers are decaying at increasing rates (Davies and Glasser, 2012; Maurer *et al.*, 2019). This affects also the European Alps: Recent studies estimate that Switzerland might be largely glacier-free by the end of the century (Huss, 2012; Sommer *et al.*, 2020), and Germany even by the end of the decade (Hagg *et al.*, 2008; Mayer *et al.*, 2021). Thus one might ask, why should we care about glacial geology in general, and subglacial overdeepenings in specific?

1.2.2. Past overdeepenings

After abandonment by the occupying glacier, overdeepened basins act as water and sediment sinks. Sediment input rates under continued glacial influence are often very large, and as a result, many overdeepenings are quickly infilled and their lakes silted up entirely (De Winter *et al.*, 2012; Owen *et al.*, 2003; see also chapter IV). In this stage, overdeepenings need to be considered, for example, in construction and tunnelling works, as the loose sediment infill may be very different in strength and consistency from the host rock (Henningsen, 2002). Quickly deposited sediment with a high water content is especially prone to destabilisation by internal deformation and fluidisation (Mills, 1983; Pisarska-Jamrozy and Weckwerth, 2013). This is exemplified by a tragic incident during the attempted construction of a first Lötschberg Tunnel in the Bernese Oberland in 1908, when blasting their way into an infilled overdeepening cost the lives of 24 workers, as the liquefied valley infill flooded the tunnel (Waltham, 2008). Loose sediment infills of overdeepened basins also react very differently from solid rock to ground motion during an earthquake. Johnson and Silva (1981), for example, have observed surface accelerations amplified by multiples in unconsolidated sediment as opposed to bedrock (*cf.* Bauer *et al.*, 2001; Faccioli *et al.*, 2002; Pratt *et al.*, 2017), which need to be accounted for in housing and infrastructure projects.

Overdeepenings and, generally, (peri-)glacial deposits are not only potential sources of hazard, but also of valuable resources. Overdeepened basin infills frequently contain decametres of sand and gravel that are in high demand as raw materials (Bisht, 2021; Gavriletea, 2017). In light of the ongoing construction boom and the depletion of suitable deposits, this demand will likely continue to increase, which offers economic opportunities to formerly glaciated countries and regions (Bendixen *et al.*, 2019; Sverdrup *et al.*, 2017). Furthermore, the permeable and porous sedimentary infills are well suited host rocks for other valuable resources. An example are hydrocarbon deposits – oil and gas – in Paleozoic tunnel valleys of northern Africa (Hirst *et al.*, 2002; Huuse *et al.*, 2012; Soua, 2013). Pleistocene overdeepenings in contrast frequently host relevant groundwater resources (Huuse *et al.*, 2003, and references therein; Seiler, 1990; Sharpe *et al.*, 2003). New sources of clean drinking water will become increasingly important in the future, as shallow groundwater is frequently impaired by overexploitation and pollution, while global demand steadily increases (Petersen *et al.*, 2016; UNESCO, 2021).

Their role as sediment traps makes overdeepened basins finally promising targets of scientific exploration. The Pleistocene terrestrial record, particularly in the vicinity of mountain ranges, is frequently characterised by discontinuous deposition both in space and time, alternating with phases of intensive erosion. As a consequence, the preservation potential of the glacial, proglacial, and periglacial sediments is generally low, and the geological record fragmentary (Hughes *et al.*, 2019; Merritt *et al.*, 2019). Thus, the Pleistocene environmental histories, especially predating the last glacial cycle, of many formerly glaciated regions of the world can only be very poorly constrained (*e.g.* Abramowski *et al.*, 2006; Astakhov, 2013; Calvet *et al.*, 2011; Clague and Ward, 2011; Gibbard and Clark, 2011; Harrison, 2004). Trapped below the fluvial base level, deposits in overdeepenings have a much higher preservation potential than coeval deposits in non-overdeepened settings (Cook and Swift, 2012; Livingstone *et al.*, 2012). It is not uncommon that the infills of overdeepened basins comprise sediments delivered in several glacial cycles, separated from each other by hiati representing phases of partial re-excavation (Astakhov, 2013; Buechi *et al.*, 2017b; Burschil *et al.*, 2018; Nitsche *et al.*, 2001; Preusser *et al.*, 2010; Schlüchter, 1989).

Overdeepenings are therefore unique geological archives, and the geophysical exploration, drilling and analysis of the basins and their infill can be immensely helpful to refine regional environmental histories. The connection of these histories to paleoclimate records is the fundament of understanding and predicting landscape responses to current and future climate change (*e.g.* Gardner *et al.*, 2006; Schildgen *et al.*, 2016).

1.2.3. Current overdeepenings

As closed basins, overdeepenings are capable of holding subglacial lakes, which have been known to drain in intense and potentially hazardous outburst floods referred to as jökulhlaups (Björnsson, 1992; Carrivick, 2011; Maizels, 1997). With ongoing ice retreat, overdeepened subglacial lakes eventually develop into proglacial lakes, which does not make them less problematic, as their environment is often a dynamic and unstable one. As glacier ice retreats and disintegrates, oversteepened rock walls and sediment bodies lose mechanical support (Kos *et al.*, 2016; Mancini and Lane, 2020), and may be further weakened by simultaneous permafrost thaw (Gruber and Haeberli, 2007; Krautblatter *et al.*, 2013). Resulting mass wasting events can be disastrous if they occur into large proglacial lakes and trigger glacio-lacustrine tsunamis (Carrivick and Tweed, 2013; Haeberli *et al.*, 2017). Currently, the number of proglacial lakes is growing worldwide (Mölg *et al.*, 2021; Shugar *et al.*, 2020), and with globally progressing glacier retreat, this trend is likely to continue and to increase the flood hazard for people in mountain regions (Colonia *et al.*, 2017; Furian *et al.*, 2021; Haeberli *et al.*, 2017; Veh *et al.*, 2020; Wilhelm *et al.*, 2012; Zheng *et al.*, 2021).

However, overdeepenings that are still in the lake phase can also provide valuable drinking water. This is especially relevant for human settlements that at present rely largely on glacial and/or snow-melt water which might become scarce as ice retreat continues (Barnett *et al.*, 2005; Cyranoski, 2005). Farinotti *et al.* (2019) estimated that newly formed glacial lakes should be sufficient to store several hundred km^3 of water by 2050, roughly equivalent to half of the annual runoff from glaciers worldwide.

Glacial lake reservoirs can further be used for energy production, with a potential annual yield on the order of 10^{15} Wh globally (Farinotti *et al.*, 2019), equalling to ~¼ of the current hydropower production, and ~4 % of the total electricity consumption (International Energy Agency, 2020). A sustainable use of this power resource can in some areas be a vital part of the transition to renewable energies.

1.2.4. Future overdeepenings

Finally, the topic of overdeepening erosion is especially relevant in the context of radioactive waste disposal. Due to the long half-lives of some relevant radionuclides, future disposal sites for (high-level) radioactive waste must be constructed in a way that guarantees stability for time scales of up to 1 Myr (Birkholzer *et al.*, 2012; Fyfe, 1999; Rao, 2001). For now, underground geological repositories are the best solution we can offer (Choppin and Wong, 1996; Nagra, 2014; Rempe, 2007). However, while the earth's glaciers are currently on the retreat, predictions of the climate in the more distant future are difficult to make, and new glaciations whose overdeepening activity could endanger such repositories are not unlikely to occur (Fischer *et al.*, 2015; Talbot, 1999). By forward modelling of both natural as well as anthropogenic factors, several studies suggest that extensive global glaciations will take place within the next 1 Myr (Archer and Ganopolski, 2005; Texier *et al.*, 2003), possibly initiating less than 100 kyr from now (Berger and Loutre, 2002; Crucifix and Rougier, 2009; Pimenoff *et al.*, 2011). For the planning and construction of permanently safe repositories, the understanding and consideration of the process of overdeepening erosion is thus vital.

Summing up, a profound knowledge about glacial geology in general, and subglacial overdeepenings in specific, are needed in order to mitigate potential risks and in order to use potential resources sustainably and efficiently (Fig. I-3). Besides their concrete socio-economic implications, overdeepenings can be archives of utmost scientific value, and help with solving some of the most pressing ecological issues of our time, provided that we read their records carefully. Herein lies the motivation of this thesis. It targets two major areas of uncertainty: i) the still highly disputed question, how and through which processes subglacial overdeepening erosion occurs, and ii) the unsatisfactory vagueness of the Pleistocene glaciation history of the Alps and their foreland.
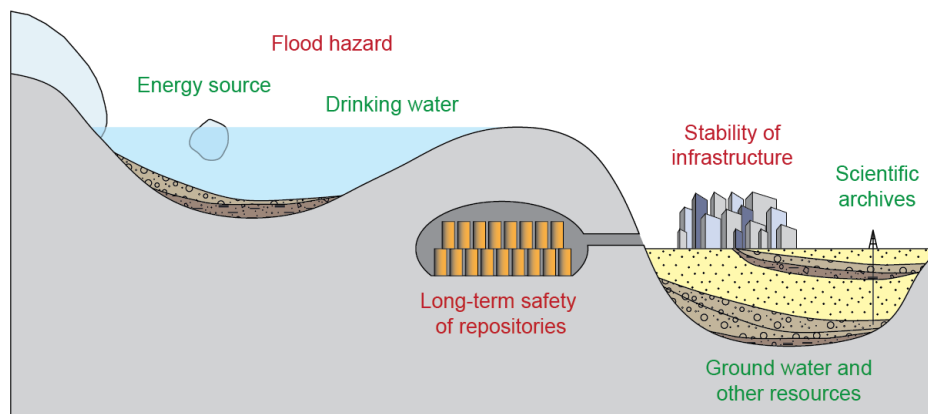
Fig. I-3: Why we should care: hazards and resources associated with overdeepened basins.

1.3. Process-mechanic uncertainties

Despite the abundance of overdeepenings, the responsible erosion processes as well as the key factors controlling and limiting their formation are still subject to debate. Unfortunately, direct observation of subglacial overdeepening erosion yet remains impossible, and we have to rely on indirect inferences from subglacial landforms and deposits, as well as on glaciological and hydrological considerations.

Two erosive agents come into play at the ice-sediment/bedrock interface: the glacier ice itself (*i.e.* glacial erosion) and basal water (*i.e.* subglaciofluvial erosion). Both are capable of rupturing and eroding the glacier bed, either through glaciotectonic shearing, fracturing, and plucking, or through hydraulic brecciation and flushing, respectively (Fig. I-4; *e.g.* Alley *et al.*, 1997; Alley *et al.*, 2019; Boulton, 1979; Van der Meer *et al.*, 2009; Van der Wateren, 2002). In addition, both can be debris-laden, which further increases their erosional efficiency through mechanic abrasion, scouring, and impacting (Fig. I-4; *e.g.* Alley *et al.*, 2019; Boulton, 1979; Chatanantavet and Parker, 2009; Glasser and Bennett, 2004; Lliboutry, 1994), and also chemical erosion may play a certain role (Hallet *et al.*, 1996). It is clear that these processes cannot be regarded separate from each other but are part of a continuum. In response to changing temperature and pressure conditions, for example seasonally, basal ice may melt and release debris, or basal water and sediment may freeze to the glacier base. In addition, water and ice flow are coupled and influence each other through positive and negative feedbacks (Alley *et al.*, 1997; Alley *et al.*, 2003a; Bell, 2008; Boulton *et al.*, 1995; Creyts and Clarke, 2010).

Two zones where large overdeepenings occur frequently have been identified in the vicinity of mountain ranges: the main intra-mountain valleys, and the distal foreland near past glacier termini (Cook and Swift, 2012; Magrani *et al.*, 2020; Preusser *et al.*, 2010). Large-scale analyses and models indicate that the dominant subglacial erosion processes differ between those two settings. Direct glacial erosion likely prevails under fast flowing ice streams in the mountain valleys, while vast amounts of subglacial water appear to play a central role in carving terminal overdeepenings (Dürst Stucki and Schlunegger, 2013; Egholm *et al.*, 2012; Herman *et al.*, 2011). However, it would probably be an oversimplification to attribute any given overdeepening to exclusively glacial or subglaciofluvial erosion. The general importance of fluid water flushing sediment from the glacier base and maintaining erosion, and facilitating plucking through pressure gradients was highlighted by Alley *et al.*, (1997, 2003a, 2019) and Hooke (1991), respectively. Also, clear sedimentological evidence for glaciotectonic thrusting and plucking in distal foreland settings exists, although such deposits have not yet been reported from the bases of foreland overdeepenings (*e.g.* LFA 4 in Buechi *et al.*, 2017a). The processes of subglacial overdeepening erosion as well as their external controlling factors, relative importances and mutual interactions thus remain elusive and enigmatic.
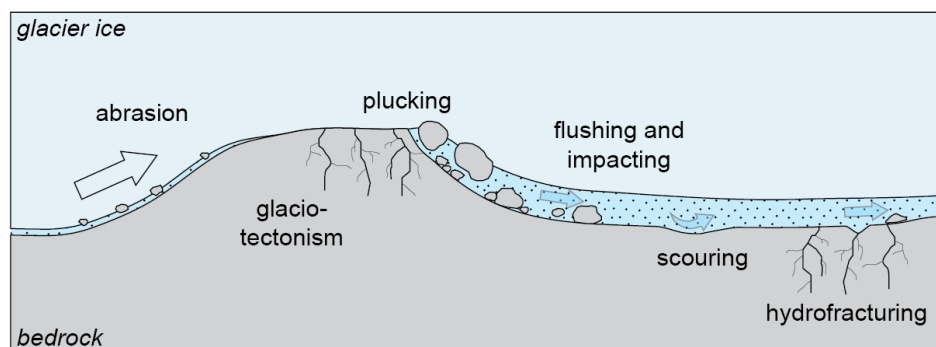
Fig. I-4: A variety of (mechanical) subglacial erosion processes contribute to the formation of overdeepenings in bedrock.

Further uncertainties lie in the spatial and, especially, the temporal pattern of subglacial overdeepening erosion, of which two concurring views exist. One of them considers the erosion a gradual, 'time-transgressive' process driven by continuous basal sliding and water discharge (Hooke, 1991; Kristensen *et al.*, 2008; Mooers, 1989). It has been shown that especially if supraglacial water is fed to the glacier base through moulins and flushes debris off the glacier bed, continued substantial erosion is feasible (Alley *et al.*, 2019; Boulton, 2006). In contrast, other studies suggest excavation of overdeepenings during catastrophic jökulhlaups (subglacial outburst floods; Alley *et al.*, 2006; Shaw, 2002). This has been inferred for overdeepenings and tunnel valleys *e.g.* in Antarctica (Denton and Sugden, 2005; Larter *et al.*, 2019), North America (Cutler *et al.*, 2002; Hooke and Jennings, 2006), and the North Sea (Piotrowski, 1997; Wingfield, 1990). While the continuous, steady-state erosion model has recently been favoured (Alley *et al.*, 2019), substantial subglacial erosion has been observed during an outburst flood in Iceland in 1996 (Russell *et al.*, 2007), suggesting that both models contribute to overdeepening formation.

The previous points highlight that overdeepening erosion is yet difficult to interpret and to predict, even in the case of an ideal, homogeneous bed. Such beds however exist only in model environments, whereas in reality, glaciers override and erode a variety of beds that differ lithologically and structurally. How such differences affect the overdeepening efficiency and extent has hardly been investigated. Connections between glacial erosion and lithological or structural properties of the respective bedrock have been made from outcrop (*e.g.* Dühnforth *et al.*, 2010; Glasser *et al.*, 1998; Krabbendam and Glasser, 2011) to valley scale (*e.g.* Augustinus, 1992; Brook *et al.*, 2004; Phillips *et al.*, 2010). However, they have mostly been made on presently exposed, non-overdeepened landforms, and their applicability to overdeepenings is questionable due to the specific hydrological and glaciological conditions in these enclosed basins. Studies focused on subglacial basin morphologies in mechanically varying bedrock are still lacking, but could significantly further our current understanding of the mechanisms of and controls on overdeepening erosion.

1.4. Regional stratigraphic uncertainties

The global-scale climate fluctuations can be traced throughout the Quaternary period based on continuous records. Well-studied archives include polar ice cores (*e.g.* Kindler *et al.*, 2014; Wolff *et al.*, 2010) and marine sediments (*e.g.* Lisiecki and Raymo, 2005; Mudelsee *et al.*, 2014). Several variables, *e.g.* $\delta^{18}O$ as a proxy of global ice volume, can be used to reconstruct the Earth's climatic evolution, and reveal that the Pleistocene is characterised by consistent cold/warm-oscillations. However, the period of these oscillations shifted from ∼40 kyr to ∼100 kyr in an event referred to as Mid-Pleistocene Transition at ∼1 Ma (Chalk *et al.*, 2017; Tziperman and Gildor, 2003). At the same time, the oscillation amplitude increased notably, illustrating that cold phases became less frequent, but more severe in the Middle Pleistocene. On a global scale, eight major 'ice ages' (MIS 6, 8, 10, …, 20) with extensive polar glaciations occurred between ca. 800 and 150 ka (Fig. I-5; Cohen and Gibbard, 2011; Lisiecki and Raymo, 2005). Attempts to correlate these global cold phases with terrestrial sedimentary records have however often remained unsuccessful: While such records, for example in mountain forelands, provide clear evidence of extensive regional glaciations, they are frequently fragmentary with entire glaciations apparently missing, and generally difficult to date (Hughes *et al.*, 2019).
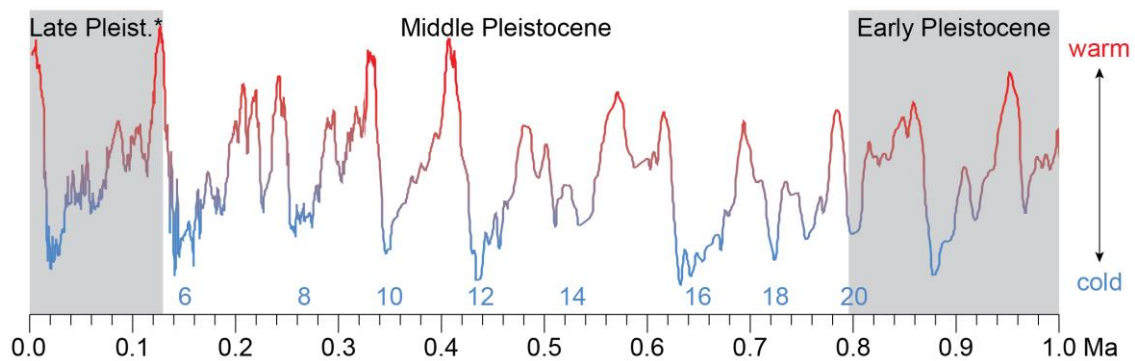
Fig. I-5: Global-scale climate fluctuations throughout the past 1 Ma illustrated by the marine isotope stack (from Cohen and Gibbard, 2011, altered). Even numbered marine isotope stages 6 to 20 correspond to major polar, and likely Alpine, glaciations of the Middle Pleistocene. * includes the Holocene.

This is illustrated by the example of the northern Alpine foreland. At present, several different regional stratigraphic schemes exist, with own naming conventions for glaciations identified in the geological record (Doppler *et al.*, 2011; Ellwanger *et al.*, 2011; Preusser *et al.*, 2011; Van Husen and Reitner, 2011). One commonality of these schemes is that they all comprise only three to four distinct Middle Pleistocene glaciations. It is not clear whether this is due to misinterpretation or fragmentarity of the respective archives, or whether not every global cold phase resulted in an Alpine glaciation (Hughes *et al.*, 2019). With the very limited availability of reliable absolute ages of the respective deposits, it is also questionable if the three to four regionally identified glaciations are generally correlative to each other, or if different (global) cold phases are represented in the present-day records. As an example, the "Riss" glaciation in Austria is correlated to MIS 6, whereas in Bavaria MIS 6 to 10 are binned to the "Riss" complex (Doppler *et al.*, 2011; Van Husen and Reitner, 2011). An investigation of the sedimentary records preserved in lakes in general, and in overdeepened basins in specific, combined with state-of-the-art dating techniques is a promising approach to resolve such regional uncertainties.

2. The Wasserschloss in the Lower Aare Valley

一石二鳥 *(yì shí ' èr niǎo)*

'One stone, two birds.'

- Chinese saying

2.1. Regional setting

The confluence area of the rivers Aare, Reuss, and Limmat in central northern Switzerland is commonly referred to as the 'Wasserschloss'. It is located ~25 km northwest of Zurich, and ~15 km south of the river Rhine and the Swiss-German border (Fig. I-6). Geologically, the Wasserschloss area is situated at the transition from the distal Molasse Basin into the northward-adjacent Jura Mountains. During Pleistocene ice advances, it was repeatedly reached and overridden by the tongues of Alpine glaciers, and its landscape shaped by diverse peri-, pro-, and subglacial processes.

2.2. Brief geological history

The basement below the Wasserschloss area consists of crystalline rocks that crop out in the Black Forest further north (Fig. I-6), and kilometre-thick Permo-Carboniferous sediments infilled in transverse fault-bound troughs that formed during the Variscan orogeny (Bachmann *et al.*, 1987; Bitterli-Dreher *et al.*, 2007; Diebold *et al.*, 1992). After cessation of the orogeny, the topography became eroded and flattened into an epicontinental platform that was covered by a several hundred-meter thick stack of Mesozoic sediments.

Over the Triassic, diverse terrestrial to shallow marine sediments – clastics, carbonates, and evaporites – that reflect repeated transgression and regression were deposited onto the basement peneplain (Jordan, 2016; Jordan *et al.*, 2016). Shallow marine conditions became permanent in Early through Middle Jurassic, under which mudstones, marls, and limestones formed (Bitterli-Dreher *et al.*, 2007; Jordan *et al.*, 2008). Water depth further increased towards the Late Jurassic, which is represented by thick carbonaceous marls overlain by micritic limestones (Bitterli-Dreher *et al.*, 2007; Gygi, 2000; Jordan *et al.*, 2008).
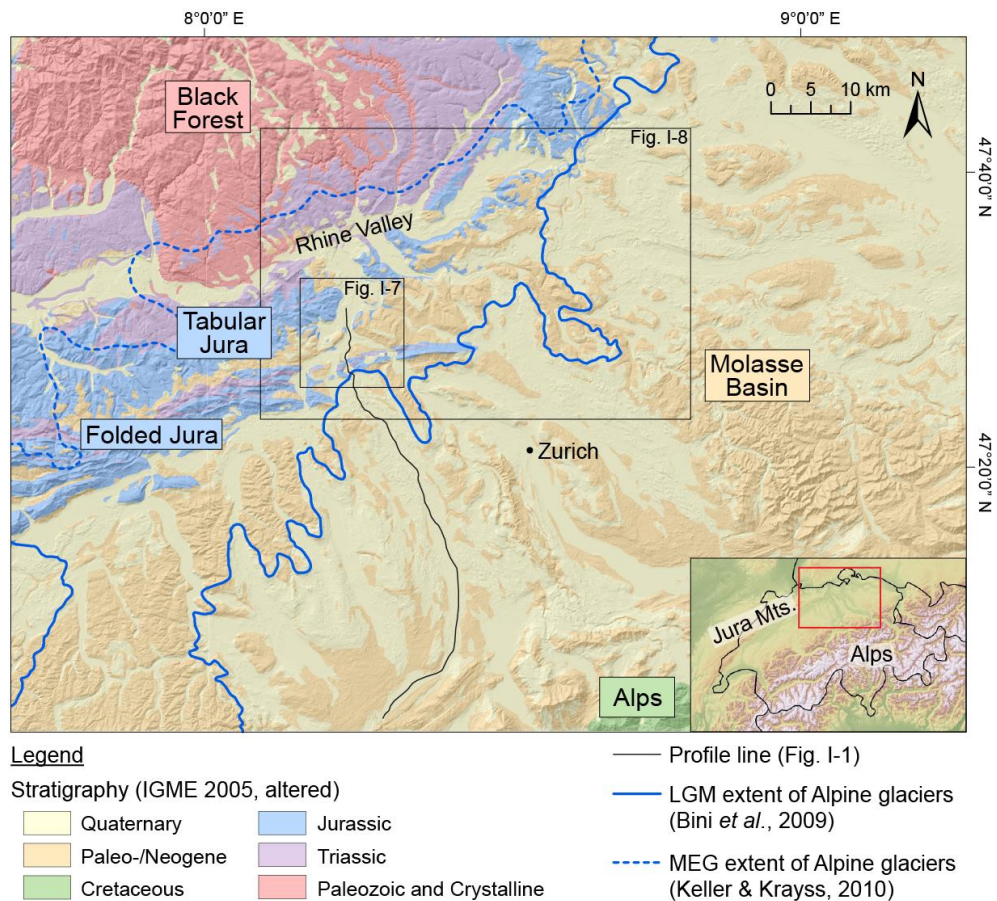
Fig. I-6: Regional-scale overview map of central northern Switzerland. The Wasserschloss area (inner rectangle; Fig. I-7) is situated at the southeastern margin of the Jura Mountains (Folded and Tabular Jura). IGME 2005: Commission for the Geological Map of the World *et al.* (2005).

The present-day Jura Mountains were uplifted on the forebulge of the emerging Alps in the Paleogene, and were subject to intensive erosion and karstification, resulting in a >100 Ma-hiatus (Berger *et al.*, 2005; Burkhard and Sommaruga, 1998; Pfiffner, 1986). Concurrently, the Molasse Basin began to subside and collect diverse clastic sediments derived from the young Alps (Fig. I-6). The Molasse sedimentation progressed northward, reached the study area in Late Oligocene, and accumulated predominantly heterogeneous sandstones through Early and Middle Miocene (Bitterli-Dreher *et al.*, 2007). The Late Miocene then saw the formation of the Folded Jura, which was upthrusted above a décollement horizon in Triassic evaporites (Burkhard, 1990; Laubscher, 1987; Looser *et al.*, 2021), and the cessation of Molasse sedimentation.

North of the Folded Jura, the Mesozoic strata of the Tabular Jura remained largely undeformed (Fig. I-6). At this time, the confluence of Aare, Reuss, and Limmat had presumably already been established at roughly its present-day position at the boundary of Folded and Tabular Jura (Fig. I-7; Ziegler and Fraefel, 2009).

Under the fluctuating climate conditions of the Quaternary with pronounced cold phases, glaciers formed in the high Alps and repeatedly advanced into the mountain foreland (Keller and Krayss, 2010; Preusser *et al.*, 2011). Decametre-thick glacial and proglacial deposits accumulated over the Pleistocene in paleovalleys that progressively lowered, resulting in a terrace stratigraphy with old sediments at higher, and young sediments at lower elevations (Graf, 1993, 2009), and below the glacier tongues, terminal overdeepenings were carved, especially where bedrock consisted of relatively soft Molasse deposits (Dürst Stucki and Schlunegger, 2013; Loepfe *et al.*, in prep.; Preusser *et al.*, 2010).

Throughout the Middle Pleistocene, the Wasserschloss area was overridden by glacier ice at least twice (Möhlin, or Most Extensive Glaciation MEG, and Beringen Glaciation), whereas the last-glacial ice advances (Birrfeld Glaciation with Last Glacial Maximum LGM) were less extensive and did not cross the Folded Jura (Fig. I-6; Bini *et al.*, 2009; Graf, 2009; Keller and Krayss, 2010; Preusser *et al.*, 2011). Several phases of overdeepening erosion carved the ~200 m deep and several kilometres wide Birrfeld Basin that is located just south of the Folded Jura chain, and its two narrow branch basins extending further to the north, the Hausen Trough and, focus of this thesis, the Gebenstorf-Stilli Trough (Fig. I-7; Graf, 2009; Loepfe *et al.*, in prep.; Nitsche *et al.*, 2001). Due to its geological history and architecture, the Wasserschloss area with the underlying Gebenstorf-Stilli Trough is an ideally suited study area to tackle the issues introduced in sections 1.3 and 1.4.

2.3. Key site for subglacial erosion

In the northern Alpine foreland, overdeepenings generally only occur where Molasse deposits form the underlying bedrock (Dürst Stucki and Schlunegger, 2013; Preusser *et al.*, 2010). Upon reaching the distal end of the Molasse Basin, overdeepenings abruptly shallow and terminate, for example the Birrfeld Basin and the Seetal Valley overdeepening further west (Loepfe *et al.*, in prep.; Nitsche *et al.*, 2001). The Hausen Trough and Gebenstorf-Stilli Trough are notable exceptions to this rule: Both cut through the upthrusted Mesozoic strata of the Folded Jura, and the latter additionally into the Tabular Jura (Fig. I-7).

The Gebenstorf-Stilli Trough is therefore not only incised into the heterogeneous but overall soft Molasse strata (Lat. *mollis* = weak) but also into very diverse and well consolidated Mesozoic sedimentary rocks (Bitterli-Dreher *et al.*, 2007; De Quervain and Frey, 1963). These are generally more resilient than the former (Dürst Stucki and Schlunegger, 2013; Kühni and Pfiffner, 2001), but have pronounced internal differences in erosional resistance (Yanites *et al.*, 2017). In addition, the Mesozoic strata of Folded and Tabular Jura are characterised by different degrees of tectonic preconditioning: In contrast to the largely undisturbed Tabular Jura, the Folded Jura has been upthrusted, more intensively faulted, and affected by additional fracture sets (Graf *et al.*, 2006; Madritsch, 2015).

The setting of the Gebenstorf-Stilli Trough with its complex bedrock architecture is regionally unique. The bedrock below but also the sediments within the trough as well as its shape and dimensions may allow conclusions about the bedrock control of subglacial overdeepening, the dominant erosion processes, and the subglacial environment in general. These are the central subjects of chapters II and III.

2.4. Promising archives of environmental history

With deposits representing, to our current knowledge, the entirety of the Pleistocene foreland glaciations (Graf, 1993, 2009; Keller and Krayss, 2010; Preusser *et al.*, 2011), the area around the Wasserschloss contains regionally important archives of the Quaternary of the Alps. Being located outside the LGM ice extent, the older (pro-)glacial deposits and landforms have been spared strong Late Pleistocene overprint (Bini *et al.*, 2009). Especially the Middle Pleistocene is well represented in the study area: The Habsburg-Rinikerfeld Paleochannel is interpreted as one of the earliest Mid-Pleistocene landforms, and is infilled with deposits of several different glaciations, including glaciofluvial gravels, tills, and lacustrine fines (Fig. I-7; Bitterli-Dreher *et al.*, 2007; Graf, 2009). Together with the previously underexplored archive of the Gebenstorf-Stilli Trough, these deposits should allow to reconstruct a glacial and environmental history spanning several 100 kyr.

However, the area of the Wasserschloss is a promising archive not only due to the shear amount of deposits preserved there. As indicated, the location of the Aare-Reuss-Limmat confluence is considered to have been spatially stable at roughly its present location (Fig. I-7; Ziegler and Fraefel, 2009). Therefore, sediments derived from at least these three, but possibly also of the Rhone and Rhine catchments, are expected to occur, and have been recognised, within the Pleistocene deposits of the study area (Graf, 2009).

The archives of the Wasserschloss area therefore track the interplay of at least three major Alpine catchments over multiple glacial-interglacial cycles, possibly including evidence for relative glacier proximity and direct ice contact. The plenty of different deposits, and the interpretation of their paleo-glaciological and paleo-environmental signals is the main focus of chapter IV.
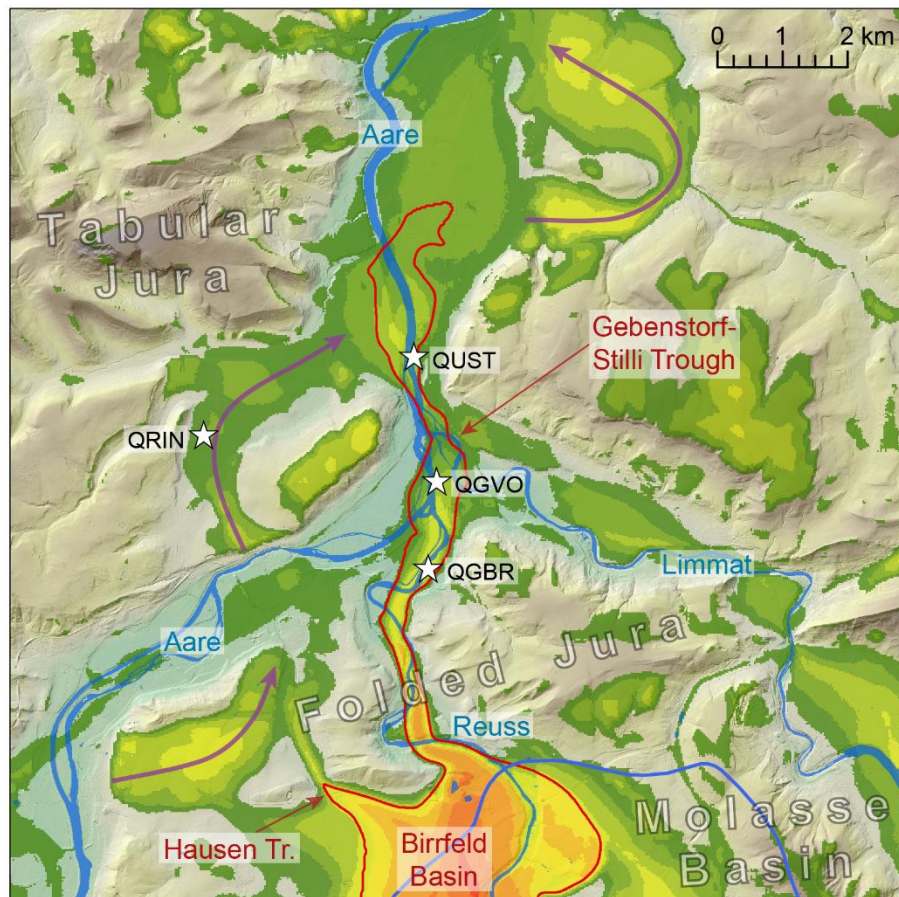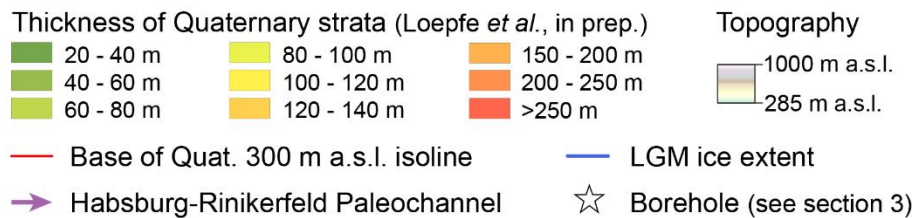
Fig. I-7: Overview map of the Wasserschloss area with major Pleistocene landforms (see Fig. I-6 for localisation).

3. The Quartärbohrungen project

Ihr wicht! Der Schauplatz wurde zu warm, und fern

wohnt ihr am Pol jetzt! Aber der Herrschende,

der dann zuletzt erschien, kennt euch!

Staunt der Geschichten, die ihr ihm kundet!

'Ye ceded! The stage became too warm, and far

away ye now live at the Pole! But the master

who then last appeared, knows ye!

Marvels at the tales ye tell him!'

- from K. F. Schimper: Die Eiszeit (1837)

translation from Krüger (2013)

3.1. Outline

This thesis was realised in the scope of the Quartärbohrungen (QBO; 'Quaternary drillings') project of the Quaternary Geology and Paleoclimatology Group of the University of Bern and the Swiss National Cooperative for the Disposal of Radioactive Waste (Nagra). The primary aims of the QBO project are i) to identify the mechanisms and controls of overdeepening erosion, and ii) to refine the glaciation history of northern Switzerland. The findings are not only of great scientific interest, but will help Nagra to propose the safest possible locations for Switzerland's future repositories of radioactive waste (Nagra, 2014).

Three study areas in central northern Switzerland have been specifically targeted with Quaternary drillings: the Wasserschloss / Lower Aare Valley, the Glatt-Rhine confluence, and the Lower Thur Valley (Fig. I-8). In 2018 through 2020, eleven boreholes were successfully completed, and yielded a total of ~1800 m of drill cores. The focus of the drilling campaign lay on excellent core quality that was guaranteed by combined application of different drilling methods, the usage of protective liners, and a sophisticated core handling workflow (as outlined in the respective data reports, see Table I-1).
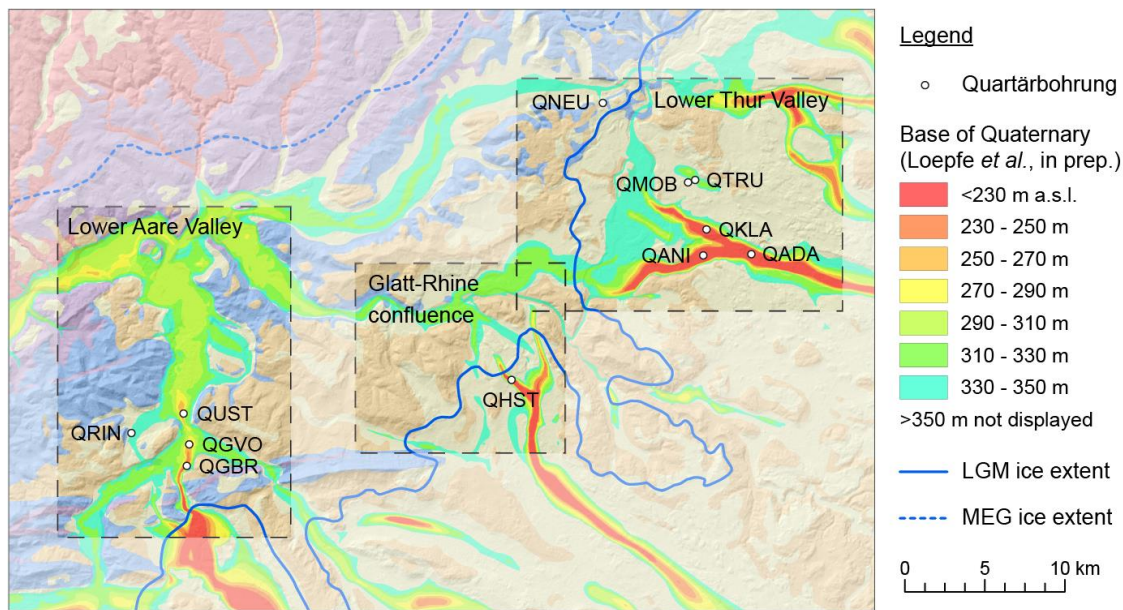
Fig. I-8: Target areas and boreholes of the Quartärbohrungen project (after Buechi, unpubl.; see Fig. I-6 for localisation and base map).

3.2. Quartärbohrungen in the Wasserschloss area

Four QBO were drilled in the Lower Aare Valley between March and October 2018 (Table I-1). Three of them were targeted at the Gebenstorf-Stilli Trough below the present-day Wasserschloss, and one at a paleolake in the Habsburg-Rinikerfeld channel (Fig. I-7, I-8).

These boreholes recovered ~350 m of high quality cores that record the entire Pleistocene sequence at the respective position, including several meters of the underlying bedrock, and build the backbone of the present thesis. And it turns out that deep waters, and mud, and sand, and rocks, in fact don't run that silent, if we choose to listen carefully...

Table I-1: Quartärbohrungen in the Wasserschloss area.

Borehole	Coordinates	Bedrock / final depth	Reference
Gebenstorf-Brüel (QGBR)	47°29'00" N, 8°14'11" E	111.5 m / 123.5 m	Gegg *et al.* (2019b)
Gebenstorf-Vogelsang (QGVO)	47°29'43" N, 8°14'18 E	64.9 m / 77.0 m	Gegg *et al.* (2019a)
Untersiggenthal (QUST)	47°30'46" N, 8°14'30" E	76.0 m / 86.4 m	Gegg *et al.* (2019c)
Riniken (QRIN)	47°30'09" N, 8°11'28" E	41.2 m / 52.7 m	Gegg *et al.* (2018)

4. References

Abramowski, U., Bergau, A., Seebach, D., Zech, R., Glaser, B., Sosin, P., Kubik, P. W., and Zech, W., 2006, Pleistocene glaciations of Central Asia: results from [10]Be surface exposure ages of erratic boulders from the Pamir (Tajikistan), and the Alay–Turkestan range (Kyrgyzstan): Quaternary Science Reviews, v. 25, no. 9-10, p. 1080-1096.

Alley, R., Cuffey, K., Evenson, E., Strasser, J., Lawson, D., and Larson, G., 1997, How glaciers entrain and transport basal sediment: physical constraints: Quaternary Science Reviews, v. 16, no. 9, p. 1017-1038.

Alley, R., Cuffey, K., and Zoet, L., 2019, Glacial erosion: status and outlook: Annals of Glaciology, v. 60, no. 80, p. 1-13.

Alley, R., Lawson, D., Larson, G., Evenson, E., and Baker, G., 2003a, Stabilizing feedbacks in glacier-bed erosion: Nature, v. 424, no. 6950, p. 758–760.

Alley, R. B., Dupont, T., Parizek, B., Anandakrishnan, S., Lawson, D. E., Larson, G., and Evenson, E., 2006, Outburst flooding and the initiation of ice-stream surges in response to climatic cooling: A hypothesis: Geomorphology, v. 75, no. 1-2, p. 76-89.

Alley, R. B., Lawson, D. E., Evenson, E. B., and Larson, G. J., 2003b, Sediment, glaciohydraulic supercooling, and fast glacier flow: Annals of Glaciology, v. 36, p. 135-141.

Archer, D., and Ganopolski, A., 2005, A movable trigger: Fossil fuel CO2 and the onset of the next glaciation: Geochemistry, Geophysics, Geosystems, v. 6, no. 5, DOI 10.1029/2004GC000891.

Astakhov, V. I., 2013, Pleistocene glaciations of northern Russia – a modern view: Boreas, v. 42, no. 1, p. 1-24.

Augustinus, P. C., 1992, The influence of rock mass strength on glacial valley cross-profile morphometry: A case study from the Southern Alps, New Zealand: Earth Surface Processes and Landforms, v. 17, no. 1, p. 39-51.

Bachmann, G., Müller, M., and Weggen, K., 1987, Evolution of the molasse basin (Germany, Switzerland): Tectonophysics, v. 137, no. 1-4, p. 77-92.

Barnett, T. P., Adam, J. C., and Lettenmaier, D. P., 2005, Potential impacts of a warming climate on water availability in snow-dominated regions: Nature, v. 438, no. 7066, p. 303-309.

Bauer, R. A., Kiefer, J., and Hester, N., 2001, Soil amplification maps for estimating earthquake ground motions in the Central US: Engineering Geology, v. 62, no. 1-3, p. 7-17.

Bell, R. E., 2008, The role of subglacial water in ice-sheet mass balance: Nature Geoscience, v. 1, no. 5, p. 297-304.

Bendixen, M., Overeem, I., Rosing, M. T., Bjørk, A. A., Kjær, K. H., Kroon, A., Zeitz, G., and Iversen, L. L., 2019, Promises and perils of sand exploitation in Greenland: Nature sustainability, v. 2, no. 2, p. 98-104.

Berger, A., and Loutre, M.-F., 2002, An exceptionally long interglacial ahead?: Science, v. 297, no. 5585, p. 1287-1288.

Berger, J.-P., Reichenbacher, B., Becker, D., Grimm, M., Grimm, K., Picot, L., Storni, A., Pirkenseer, C., Derer, C., and Schaefer, A., 2005, Paleogeography of the upper Rhine Graben (URG) and the Swiss Molasse basin (SMB) from Eocene to Pliocene: International Journal of Earth Sciences, v. 94, no. 4, p. 697-710.

Bini, A., Buoncristiani, J. F., Couterrand, S., Ellwanger, D., Felber, M., Florineth, D., Graf, H. R., Keller, O., Kelly, M., and Schlüchter, C., 2009, Die Schweiz während des letzteiszeitlichen Maximums (LGM) 1:500'000: Bundesamt für Landestopographie swisstopo.

Birkholzer, J., Houseworth, J., and Tsang, C.-F., 2012, Geologic disposal of high-level radioactive waste: Status, key issues, and trends: Annual Review of Environment and Resources, v. 37, p. 79-106.

Bisht, A., 2021, Conceptualizing sand extractivism: Deconstructing an emerging resource frontier: The Extractive Industries and Society.

Bitterli-Dreher, P., Graf, H. R., Naef, H., Diebold, P., Matousek, F., Burger, H., and Pauli-Gabi, T., 2007, Geologischer Atlas der Schweiz 1:25'000. Blatt 1070 Baden. Erläuterungen, Wabern, Bundesamt für Landestopogaphie swisstopo, 152 p.

Björnsson, H., 1992, Jökulhlaups in Iceland: prediction, characteristics and simulation: Annals of Glaciology, v. 16, p. 95-106.

Boulton, G., Caban, P., and Van Gijssel, K., 1995, Groundwater flow beneath ice sheets: Part I—Large scale patterns: Quaternary Science Reviews, v. 14, no. 6, p. 545-562.

Boulton, G. S., 1979, Processes of glacier erosion on different substrata: Journal of glaciology, v. 23, no. 89, p. 15-38.

Boulton, G. S., 2006, Glaciers and their coupling with hydraulic and sedimentary processes: Glacier science and environmental change, p. 2-22.

Brook, M. S., Kirkbride, M. P., and Brock, B. W., 2004, Rock strength and development of glacial valley morphology in the Scottish Highlands and northwest Iceland: Geografiska Annaler: Series A, Physical Geography, v. 86, no. 3, p. 225-234.

Buechi, M. W., Frank, S. M., Graf, H. R., Menzies, J., and Anselmetti, F. S., 2017a, Subglacial emplacement of tills and meltwater deposits at the base of overdeepened bedrock troughs: Sedimentology, v. 64, no. 3, p. 658-685.

Buechi, M. W., Graf, H. R., Haldimann, P., Lowick, S. E., and Anselmetti, F. S., 2017b, Multiple Quaternary erosion and infill cycles in overdeepened basins of the northern Alpine foreland: Swiss Journal of Geosciences, v. 111, p. 1-34.

Burkhard, M., 1990, Aspects of the large-scale Miocene deformation in the most external part of the Swiss Alps (sub-Alpine molasse to Jura fold belt): Eclogae Geologicae Helvetiae, v. 83, no. 3, p. 559-583.

Burkhard, M., and Sommaruga, A., 1998, Evolution of the western Swiss Molasse basin: structural relations with the Alps and the Jura belt: Geological Society, London, Special Publications, v. 134, no. 1, p. 279-298.

Burschil, T., Buness, H., Tanner, D. C., Wielandt-Schuster, U., Ellwanger, D., and Gabriel, G., 2018, High-resolution reflection seismics reveal the structure and the evolution of the Quaternary glacial Tannwald Basin: Near Surface Geophysics, v. 16, no. 6, p. 593-610.

Calvet, M., Delmas, M., Gunnell, Y., Braucher, R., and Bourlès, D., 2011, Recent advances in research on Quaternary glaciations in the Pyrenees: Developments in Quaternary Sciences, v. 15, p. 127-139.

Carrivick, J. L., 2011, Jökulhlaups: geological importance, deglacial association and hazard management: Geology Today, v. 27, no. 4, p. 133-140.

Carrivick, J. L., and Tweed, F. S., 2013, Proglacial lakes: character, behaviour and geological importance: Quaternary Science Reviews, v. 78, p. 34-52.

Chalk, T. B., Hain, M. P., Foster, G. L., Rohling, E. J., Sexton, P. F., Badger, M. P., Cherry, S. G., Hasenfratz, A. P., Haug, G. H., and Jaccard, S. L., 2017, Causes of ice age intensification across the Mid-Pleistocene Transition: Proceedings of the National Academy of Sciences, v. 114, no. 50, p. 13114-13119.

Chatanantavet, P., and Parker, G., 2009, Physically based modeling of bedrock incision by abrasion, plucking, and macroabrasion: Journal of Geophysical Research: Earth Surface, v. 114, no. F4, F04018.

Cheng, L., Abraham, J., Trenberth, K. E., Fasullo, J., Boyer, T., Locarnini, R., Zhang, B., Yu, F., Wan, L., and Chen, X., 2021, Upper Ocean Temperatures Hit Record High in 2020: Advances in Atmospheric Sciences, v. 38, p. 523-530.

Choppin, G., and Wong, P., 1996, Current status of radioactive waste disposal: Journal of radioanalytical and nuclear chemistry, v. 203, no. 2, p. 575-590.

Clague, J. J., and Ward, B., 2011, Pleistocene Glaciation of British Columbia, Developments in Quaternary Sciences, Volume 15, Elsevier, p. 563-573.

Clerc, S., Buoncristiani, J.-F., Guiraud, M., Vennin, E., Desaubliaux, G., and Portier, E., 2013, Subglacial to proglacial depositional environments in an Ordovician glacial tunnel valley, Alnif, Morocco: Palaeogeography, Palaeoclimatology, Palaeoecology, v. 370, p. 127-144.

Cofaigh, C. Ó., 1996, Tunnel valley genesis: Progress in physical geography, v. 20, no. 1, p. 1-19.

Cohen, K., and Gibbard, P., 2011, Global chronostratigraphical correlation table for the last 2.7 million years.

Colonia, D., Torres, J., Haeberli, W., Schauwecker, S., Braendle, E., Giraldez, C., and Cochachin, A., 2017, Compiling an inventory of glacier-bed overdeepenings and potential new lakes in de-glaciating areas of the Peruvian Andes: approach, first results, and perspectives for adaptation to climate change: Water, v. 9, no. 5, p. 336.

Commission for the Geological Map of the World, Asch, K., and Bellenberg, S., 2005, The 1:5 million international geological map of Europe and adjacent areas (IGME 5000), Hannover, Bundesanstalt für Geowissenschaften und Rohstoffe.

Cook, S. J., and Swift, D. A., 2012, Subglacial basins: Their origin and importance in glacial systems and landscapes: Earth-Science Reviews, v. 115, no. 4, p. 332-372.

Creyts, T. T., and Clarke, G. K., 2010, Hydraulics of subglacial supercooling: theory and simulations for clear water flows: Journal of Geophysical Research: Earth Surface, v. 115, no. F3, F03021.

Crucifix, M., and Rougier, J., 2009, On the use of simple dynamical systems for climate predictions: The European Physical Journal Special Topics, v. 174, no. 1, p. 11-31.

Cutler, P. M., Colgan, P. M., and Mickelson, D. M., 2002, Sedimentologic evidence for outburst floods from the Laurentide Ice Sheet margin in Wisconsin, USA: implications for tunnel-channel formation: Quaternary International, v. 90, no. 1, p. 23-40.

Cyranoski, D., 2005, Climate change: the long-range forecast: Nature, v. 438, no. 7066, p. 275-277.

Davies, B., and Glasser, N., 2012, Accelerating shrinkage of Patagonian glaciers from the Little Ice Age (~ AD 1870) to 2011: Journal of Glaciology, v. 58, no. 212, p. 1063-1084.

Davis, W. M., 1900, Glacial Erosion in the Valley of the Ticino: Appalachia, v. IX, p. 136-156.

De Quervain, F., and Frey, D., 1963, Geotechnische Karte der Schweiz 1:200.000: Blatt Nr. 2 Luzern–Zürich–St. Gallen–Chur: Erläuterungen: Kümmerly & Frey Geographischer Verlag.

De Winter, I. L., Storms, J. E., and Overeem, I., 2012, Numerical modeling of glacial sediment production and transport during deglaciation: Geomorphology, v. 167, p. 102-114.

Denton, G. H., and Sugden, D. E., 2005, Meltwater features that suggest Miocene ice-sheet overriding of the Transantarctic Mountains in Victoria Land, Antarctica: Geografiska Annaler: Series A, Physical Geography, v. 87, no. 1, p. 67-85.

Diebold, P., Naef, H., and Ammann, M., 1992, Zur Tektonik der zentralen Nordschweiz: Interpretation aufgrund regionaler Seismik, Oberflächengeologie und Tiefbohrungen: Nagra Technischer Bericht NTB 90-04, 277 p.

Doppler, G., Kroemer, E., Rögner, K., Wallner, J., Jerz, H., and Grottenthaler, W., 2011, Quaternary stratigraphy of southern Bavaria: E&G Quaternary Science Journal, v. 60, no. 2/3, p. 329-365.

Dühnforth, M., Anderson, R. S., Ward, D., and Stock, G. M., 2010, Bedrock fracture control of glacial erosion processes and rates: Geology, v. 38, no. 5, p. 423-426.

Dürst Stucki, M., and Schlunegger, F., 2013, Identification of erosional mechanisms during past glaciations based on a bedrock surface model of the central European Alps: Earth and Planetary Science Letters, v. 384, p. 57-70.

Egholm, D., Pedersen, V., Knudsen, M., and Larsen, N., 2012, Coupling the flow of ice, water, and sediment in a glacial landscape evolution model: Geomorphology, v. 141, p. 47-66.

Ehlers, J., and Gibbard, P. L., 2007, The extent and chronology of Cenozoic global glaciation: Quaternary International, v. 164, p. 6-20.

Ellwanger, D., Wielandt-Schuster, U., Franz, M., and Simon, T., 2011, The Quaternary of the southwest German Alpine Foreland (Bodensee-Oberschwaben, Baden-Württemberg, southwest Germany): E&G Quaternary Science Journal, v. 60, no. 2/3, p. 306-328.

Evans, I., 2008, Glacial erosional processes and forms: mountain glaciation and glacier geography. The History of the Study of Landforms or the Development of Geomorphology: Quaternary and Recent Processes and Forms (1890–1965) and the Mid-century Revolutions.: London, Geological Society, 413 p.

Eyles, N., Mullins, H. T., and Hine, A. C., 1990, Thick and fast: sedimentation in a Pleistocene fiord lake of British Columbia, Canada: Geology, v. 18, no. 11, p. 1153-1157.

Faccioli, E., Vanini, M., and Frassine, L., 2002, Complex site effects in earthquake ground motion, including topography: Proc. of 12th European Conference on Earthquake Engineering.

Farinotti, D., Round, V., Huss, M., Compagno, L., and Zekollari, H., 2019, Large hydropower and water-storage potential in future glacier-free basins: Nature, v. 575, no. 7782, p. 341-344.

Fischer, U. H., Bebiolka, A., Brandefelt, J., Follin, S., Hirschorn, S., Jensen, M., Keller, S., Kennell, L., Näslund, J.-O., and Normani, S., 2015, Radioactive waste under conditions of future ice ages, Snow and Ice-related Hazards, Risks and Disasters, Elsevier, p. 345-393.

Furian, W., Loibl, D., and Schneider, C., 2021, Future glacial lakes in High Mountain Asia: an inventory and assessment of hazard potential from surrounding slopes: Journal of Glaciology, v. 67, no. 264, p. 653-670.

Fyfe, W., 1999, Nuclear waste isolation: an urgent international responsibility: Engineering geology, v. 52, no. 3-4, p. 159-161.

Gardner, T. W., Webb, J., Davis, A. G., Cassel, E. J., Pezzia, C., Merritts, D. J., and Smith, B., 2006, Late Pleistocene landscape response to climate change: eolian and alluvial fan deposition, Cape Liptrap, southeastern Australia: Quaternary Science Reviews, v. 25, no. 13-14, p. 1552-1569.

Gavriletea, M. D., 2017, Environmental impacts of sand exploitation. Analysis of sand market: Sustainability, v. 9, no. 7, 1118.

Gegg, L., Kuster, A. M., Amschwand, D., Huber, M., Deplazes, G., Madritsch, H., and Buechi, M. W., 2019a, Quaternary Borehole QBO Gebenstorf-Vogelsang (QGVO) Data Report: Nagra Arbeitsbericht NAB 19-03, 8 p.

Gegg, L., Kuster, A. M., Deplazes, G., Madritsch, H., and Buechi, M. W., 2019b, Quaternary Borehole QBO Gebenstorf-Brüel (QGBR) Data Report: Nagra Arbeitsbericht NAB 19-02, 8 p.

Gegg, L., Kuster, A. M., Schmid, D., and Buechi, M. W., 2018, Quaternary Boreholes QBO Riniken-1 & -2 (QRIN1 & QRIN2) Data Report: Nagra Arbeitsbericht NAB 18-40, 8 p.

Gegg, L., Kuster, A. M., Schmid, D., Lemke, K., Deplazes, G., Madritsch, H., and Buechi, M. W., 2019c, Quaternary Borehole QBO Untersiggenthal (QUST) Data Report: Nagra Arbeitsbericht NAB 19-01, 8 p.

Gibbard, P. L., and Clark, C. D., 2011, Pleistocene glaciation limits in Great Britain, Developments in Quaternary Sciences, Volume 15, Elsevier, p. 75-93.

Glasser, N. F., and Bennett, M. R., 2004, Glacial erosional landforms: origins and significance for palaeoglaciology: Progress in Physical Geography, v. 28, no. 1, p. 43-75.

Glasser, N. F., Crawford, K. R., Hambrey, M. J., Bennett, M. R., and Huddart, D., 1998, Lithological and structural controls on the surface wear characteristics of glaciated metamorphic bedrock surfaces: Ossian Sarsfjellet, Svalbard: The Journal of geology, v. 106, no. 3, p. 319-330.

Graf, H. R., 1993, Die Deckenschotter der zentralen Nordschweiz: PhD thesis, ETH Zurich, 151 p.

-, 2009, Stratigraphie von Mittel-und Spätpleistozän in der Nordschweiz, Beiträge zur Geologischen Karte der Schweiz, 198 p.

Graf, H. R., Bitterli-Dreher, P., Burger, H., Bitterli, T., Diebold, P., and Naef, H., 2006, Geologischer Atlas der Schweiz 1:25'000, Blatt 1070 Baden: Bundesamt für Landestopografie swisstopo, Wabern, Switzerland.

Gruber, S., and Haeberli, W., 2007, Permafrost in steep bedrock slopes and its temperature-related destabilization following climate change: Journal of Geophysical Research: Earth Surface, v. 112, no. F2, F02S18.

Gygi, R. A., 2000, Integrated stratigraphy of the Oxfordian and Kimmeridgian (Late Jurassic) in northern Switzerland and adjacent southern Germany, Basel, Birkhäuser, 151 p.

Haeberli, W., Linsbauer, A., Cochachin, A., Salazar, C., and Fischer, U. H., 2016, On the morphological characteristics of overdeepenings in high-mountain glacier beds: Earth Surface Processes and Landforms, v. 41, no. 13, p. 1980-1990.

Haeberli, W., Schaub, Y., and Huggel, C., 2017, Increasing risks related to landslides from degrading permafrost into new lakes in de-glaciating mountain ranges: Geomorphology, v. 293, p. 405-417.

Hagg, W., Mayer, C., and Steglich, C., 2008, Glacier changes in the Bavarian Alps from 1989/90 to 2006/07: Zeitschrift für Gletscherkunde und Glazialgeologie, no. 1, p. 37-46.

Hallet, B., Hunter, L., and Bogen, J., 1996, Rates of erosion and sediment evacuation by glaciers: A review of field data and their implications: Global and Planetary Change, v. 12, no. 1-4, p. 213-235.

Harrison, S., 2004, The Pleistocene glaciations of Chile: Developments in Quaternary Sciences, v. 2, p. 89-103.

Henningsen, D., 2002, Lockergesteine als Baugrund, Geologie für Bauingenieure: Berlin/Heidelberg, Springer, p. 27-56.

Herman, F., Beaud, F., Champagnac, J.-D., Lemieux, J.-M., and Sternai, P., 2011, Glacial hydrology and erosion patterns: a mechanism for carving glacial valleys: Earth and Planetary Science Letters, v. 310, no. 3, p. 498-508.

Hirst, J., Benbakir, A., Payne, D., and Westlake, I., 2002, Tunnel valleys and density flow processes in the upper Ordovician glacial succession, Illizi Basin, Algeria: influence on reservoir quality: Journal of Petroleum Geology, v. 25, no. 3, p. 297-324.

Hooke, R. L., 1989, Englacial and subglacial hydrology: a qualitative review: Arctic and Alpine Research, v. 21, no. 3, p. 221-233.

-, 1991, Positive feedbacks associated with erosion of glacial cirques and overdeepenings: Geological Society of America Bulletin, v. 103, no. 8, p. 1104-1108.

Hooke, R. L., and Jennings, C. E., 2006, On the formation of the tunnel valleys of the southern Laurentide ice sheet: Quaternary Science Reviews, v. 25, no. 11-12, p. 1364-1372.

Hughes, P. D., Gibbard, P. L., and Ehlers, J., 2019, The "missing glaciations" of the Middle Pleistocene: Quaternary Research, v. 96, p. 161–183.

Huss, M., 2012, Extrapolating glacier mass balance to the mountain-range scale: the European Alps 1900–2100: The Cryosphere, v. 6, no. 4, p. 713-727.

Huuse, M., Le Heron, D., Dixon, R., Redfern, J., Moscariello, A., and Craig, J., 2012, Glaciogenic reservoirs and hydrocarbon systems: an introduction: Geological Society, London, Special Publications, v. 368, no. 1, p. 1-28.

Huuse, M., Lykke-Andersen, H., and Piotrowski, J. A., 2003, Geophysical investigations of buried Quaternary valleys in the formerly glaciated NW European lowland: significance for groundwater exploration: Journal of Applied Geophysics, v. 53, no. 4, p. 153-157.

International Energy Agency, 2020, Key World Energy Statistics 2020, 81 p.

Johnson, D. W., 1909, Hanging Valleys: Bulletin of the American Geographical Society, v. 41, no. 11, p. 665-683.

Johnson, L. R., and Silva, W., 1981, The effects of unconsolidated sediments upon the ground motion during local earthquakes: Bulletin of the Seismological Society of America, v. 71, no. 1, p. 127-142.

Jordan, P., 2016, Reorganisation of the Triassic stratigraphic nomenclature of northern Switzerland: overview and the new Dinkelberg, Kaiseraugst and Zeglingen formations: Swiss Journal of Geosciences, v. 109, no. 2, p. 241-255.

Jordan, P., Pietsch, J. S., Bläsi, H., Furrer, H., Kündig, N., Looser, N., Wetzel, A., and Deplazes, G., 2016, The middle to late Triassic Bänkerjoch and Klettgau formations of northern Switzerland: Swiss Journal of Geosciences, v. 109, no. 2, p. 257-284.

Jordan, P., Wetzel, A., and Reisdorf, A., 2008, Swiss Jura Mountains, in McCann, T., ed., The Geology of Central Europe, Volume 2, Geological Society of London, p. 823-923.

Kehew, A. E., Piotrowski, J. A., and Jørgensen, F., 2012, Tunnel valleys: Concepts and controversies—A review: Earth-Science Reviews, v. 113, no. 1-2, p. 33-58.

Keller, O., and Krayss, E., 2010, Mittel-und spätpleistozäne Stratigraphie und Morphogenese in Schlüsselregionen der Nordschweiz: E&G: Quaternary Science Journal, v. 59, no. 1-2, p. 88-119.

Kindler, P., Guillevic, M., Baumgartner, M., Schwander, J., Landais, A., and Leuenberger, M., 2014, Temperature reconstruction from 10 to 120 kyr b2k from the NGRIP ice core: Climate of the Past, v. 10, no. 2, p. 887-902.

Kos, A., Amann, F., Strozzi, T., Delaloye, R., von Ruette, J., and Springman, S., 2016, Contemporary glacier retreat triggers a rapid landslide response, Great Aletsch Glacier, Switzerland: Geophysical Research Letters, v. 43, no. 24, p. 12,466-12,474.

Krabbendam, M., and Glasser, N. F., 2011, Glacial erosion and bedrock properties in NW Scotland: abrasion and plucking, hardness and joint spacing: Geomorphology, v. 130, no. 3-4, p. 374-383.

Krautblatter, M., Funk, D., and Günzel, F. K., 2013, Why permafrost rocks become unstable: a rock–ice-mechanical model in time and space: Earth Surface Processes and Landforms, v. 38, no. 8, p. 876-887.

Kristensen, T. B., Piotrowski, J. A., Huuse, M., Clausen, O. R., and Hamberg, L., 2008, Time-transgressive tunnel valley formation indicated by infill sediment structure, North Sea–the role of glaciohydraulic supercooling: Earth Surface Processes and Landforms: The Journal of the British Geomorphological Research Group, v. 33, no. 4, p. 546-559.

Krüger, T., 2013, Discovering the Ice Ages: international reception and consequences for a historical understanding of climate, Leiden, Brill, 534 p.

Kühni, A., and Pfiffner, O.-A., 2001, The relief of the Swiss Alps and adjacent areas and its relation to lithology and structure: topographic analysis from a 250-m DEM: Geomorphology, v. 41, no. 4, p. 285-307.

Larson, G., and Schaetzl, R., 2001, Origin and evolution of the Great Lakes: Journal of Great Lakes Research, v. 27, no. 4, p. 518-546.

Larter, R. D., Hogan, K. A., Hillenbrand, C.-D., Smith, J. A., Batchelor, C. L., Cartigny, M., Tate, A. J., Kirkham, J. D., Roseby, Z. A., and Kuhn, G., 2019, Subglacial hydrological control on flow of an Antarctic Peninsula palaeo-ice stream: The Cryosphere, v. 13, no. 6, p. 1583-1596.

Laubscher, H., 1987, Die tektonische Entwicklung der Nordschweiz: Eclogae Geologicae Helvetiae, v. 80, no. 2, p. 287-303.

Li, M., Vandyk, T. M., Wu, G., Liu, W., Le Heron, D. P., and Xiao, Y., 2020, A window into the Great Unconformity: Insights from geochemistry and geochronology of Ediacaran glaciogenic rocks in the North China Craton: Journal of Asian Earth Sciences, v. 194, 104327.

Linsbauer, A., Frey, H., Haeberli, W., Machguth, H., Azam, M., and Allen, S., 2016, Modelling glacier-bed overdeepenings and possible future lakes for the glaciers in the Himalaya—Karakoram region: Annals of Glaciology, v. 57, no. 71, p. 119-130.

Lisiecki, L. E., and Raymo, M. E., 2005, A Pliocene-Pleistocene stack of 57 globally distributed benthic $\delta^{18}O$ records: Paleoceanography, v. 20, no. 1, PA1003.

Livingstone, S. J., Clark, C. D., Piotrowski, J. A., Tranter, M., Bentley, M. J., Hodson, A., Swift, D. A., and Woodward, J., 2012, Theoretical framework and diagnostic criteria for the identification of palaeo-subglacial lakes: Quaternary Science Reviews, v. 53, p. 88-110.

Lliboutry, L. A., 1994, Monolithologic erosion of hard beds by temperate glaciers: Journal of Glaciology, v. 40, no. 136, p. 433-450.

Loepfe, R., et al., in prep., Digitales Höhenmodell Basis Quartär der Nordschweiz – Version 2021 und ausgewählte Auswertungen: Nagra Arbeitsbericht.

Lonergan, L., Maidment, S. C., and Collier, J. S., 2006, Pleistocene subglacial tunnel valleys in the central North Sea basin: 3-D morphology and evolution: Journal of Quaternary Science: Published for the Quaternary Research Association, v. 21, no. 8, p. 891-903.

Looser, N., Madritsch, H., Guillong, M., Laurent, O., Wohlwend, S., and Bernasconi, S., 2021, Absolute Age and Temperature Constraints on Deformation along the Basal Décollement of the Jura Fold-and-thrust Belt from Carbonate U-Pb Dating and Clumped Isotopes: Tectonics, e2020TC006439.

Madritsch, H., 2015, Outcrop-scale fracture systems in the Alpine foreland of central northern Switzerland: Kinematics and tectonic context: Swiss Journal of Geosciences, v. 108, no. 2-3, p. 155-181.

Magnin, F., Haeberli, W., Linsbauer, A., Deline, P., and Ravanel, L., 2020, Estimating glacier-bed overdeepenings as possible sites of future lakes in the de-glaciating Mont Blanc massif (Western European Alps): Geomorphology, v. 350.

Magrani, F., Valla, P., Gribenski, N., and Serra, E., 2020, Glacial overdeepenings in the Swiss Alps and foreland: Spatial distribution and morphometrics: Quaternary Science Reviews, v. 243.

Maizels, J., 1997, Jökulhlaup deposits in proglacial areas: Quaternary Science Reviews, v. 16, no. 7, p. 793-819.

Mancini, D., and Lane, S., 2020, Changes in sediment connectivity following glacial debuttressing in an Alpine valley system: Geomorphology, v. 352, 106987.

Maurer, J. M., Schaefer, J., Rupper, S., and Corley, A., 2019, Acceleration of ice loss across the Himalayas over the past 40 years: Science Advances, v. 5, no. 6, eaav7266.

Mayer, C., Hagg, W., Weber, M., and Lambrecht, A., 2021, Zukunft ohne Eis. Zweiter Bayerischer Gletscherbericht - Klimawandel in den Alpen, Munich, Bayerisches Staatsministerium für Umwelt und Verbraucherschutz, 52 p.

Merritt, J. W., Gordon, J. E., and Connell, E. R., 2019, Late Pleistocene sediments, landforms and events in Scotland: a review of the terrestrial stratigraphic record: Earth and Environmental Science Transactions of the Royal Society of Edinburgh, v. 110, no. 1-2, p. 39-91.

Mills, P. C., 1983, Genesis and diagnostic value of soft-sediment deformation structures—a review: Sedimentary Geology, v. 35, no. 2, p. 83-104.

Mölg, N., Huggel, C., Herold, T., Storck, F., Allen, S., Haeberli, W., Schaub, Y., and Odermatt, D., 2021, Inventory and evolution of glacial lakes since the Little Ice Age: lessons from the case of Switzerland: Earth Surface Processes and Landforms.

Mooers, H. D., 1989, On the formation of the tunnel valleys of the Superior lobe, central Minnesota: Quaternary Research, v. 32, no. 1, p. 24-35.

Mudelsee, M., Bickert, T., Lear, C. H., and Lohmann, G., 2014, Cenozoic climate changes: A review based on time series analysis of marine benthic $\delta^{18}O$ records: Reviews of Geophysics, v. 52, no. 3, p. 333-374.

Mullins, H. T., and Hinchey, E. J., 1989, Erosion and infill of New York Finger Lakes: Implications for Laurentide ice sheet deglaciation: Geology, v. 17, no. 7, p. 622-625.

Nagra, 2014, Konzepte der Standortuntersuchungen für SGT Etappe 3: Nagra Arbeitsbericht NAB 14-83, 101 p.

Nitsche, F., Monin, G., Marillier, F., Graf, H., and Ansorge, J., 2001, Reflection seismic study of Cenozoic sediments in an overdeepened valley of northern Switzerland: the Birrfeld area: Eclogae Geologicae Helvetiae, v. 94, no. 3, p. 363-371.

Owen, L. A., Derbyshire, E., and Scott, C. H., 2003, Contemporary sediment production and transfer in high-altitude glaciers: Sedimentary Geology, v. 155, no. 1-2, p. 13-36.

Paolo, F. S., Fricker, H. A., and Padman, L., 2015, Volume loss from Antarctic ice shelves is accelerating: Science, v. 348, no. 6232, p. 327-331.

Patton, H., Swift, D., Clark, C., Livingstone, S. J., and Cook, S. J., 2016, Distribution and characteristics of overdeepenings beneath the Greenland and Antarctic ice sheets: Implications for overdeepening origin and evolution: Quaternary Science Reviews, v. 148, p. 128-145.

Penck, A., and Brückner, E., 1909, Die Alpen im Eiszeitalter, Leipzig, Tauchnitz, 393 p.

Petersen, L., Heynen, M., and Pellicciotti, F., 2016, Freshwater resources: past, present, future: International Encyclopedia of Geography: People, the Earth, Environment and Technology, p. 1-12.

Pfiffner, O. A., 1986, Evolution of the north Alpine foreland basin in the Central Alps: Special Publications of the International Association of Sedimentologists, v. 8, p. 219-228.

Phillips, E., Everest, J., and Diaz-Doce, D., 2010, Bedrock controls on subglacial landform distribution and geomorphological processes: Evidence from the Late Devensian Irish Sea Ice Stream: Sedimentary Geology, v. 232, no. 3-4, p. 98-118.

Pietsch, J., and Jordan, P., 2014, Digitales Höhenmodell Basis Quartär der Nordschweiz - Version 2014 und ausgewählte Auswertungen: Nagra Arbeitsbericht NAB 14-02, 69 p.

Pimenoff, N., Venäläinen, A., and Järvinen, H., 2011, Climate scenarios for Olkiluoto on a time-scale of 120,000 years, Eurajoki, Posiva Oy, 102 p.

Piotrowski, J. A., 1997, Subglacial hydrology in north-western Germany during the last glaciation: groundwater flow, tunnel valleys and hydrological cycles: Quaternary Science Reviews, v. 16, no. 2, p. 169-185.

Pisarska-Jamrozy, M., and Weckwerth, P., 2013, Soft-sediment deformation structures in a Pleistocene glaciolacustrine delta and their implications for the recognition of subenvironments in delta deposits: Sedimentology, v. 60, no. 3, p. 637-665.

Pratt, T. L., Horton Jr, J. W., Muñoz, J., Hough, S. E., Chapman, M. C., and Olgun, C. G., 2017, Amplification of earthquake ground motions in Washington, DC, and implications for hazard assessments in central and eastern North America: Geophysical Research Letters, v. 44, no. 24, p. 12,150-12,160.

Preusser, F., Graf, H. R., Keller, O., Krayss, E., and Schlüchter, C., 2011, Quaternary glaciation history of northern Switzerland: E&G Quaternary Science Journal, v. 60, p. 282-305.

Preusser, F., Reitner, J. M., and Schlüchter, C., 2010, Distribution, geometry, age and origin of overdeepened valleys and basins in the Alps and their foreland: Swiss Journal of Geosciences, v. 103, no. 3, p. 407-426.

Ramsay, A. C., 1878, The physical geology and geography of Great Britain: a manual of British geology, E. Stanford, 639 p.

Rao, K., 2001, Radioactive waste: The problem and its management: current science, v. 81, no. 12, p. 1534-1546.

Readfern, G., 2020, Death Valley temperature rises to 129.9F – possibly the hottest ever reliably recorded, The Guardian: theguardian.com, Scott Trust

Rempe, N. T., 2007, Permanent underground repositories for radioactive waste: Progress in nuclear energy, v. 49, no. 5, p. 365-374.

Russell, A. J., Gregory, A. R., Large, A. R., Fleisher, P. J., and Harris, T. D., 2007, Tunnel channel formation during the November 1996 jökulhlaup, Skeiðarárjökull, Iceland: Annals of Glaciology, v. 45, p. 95-103.

Schildgen, T. F., Robinson, R. A., Savi, S., Phillips, W. M., Spencer, J. Q., Bookhagen, B., Scherler, D., Tofelde, S., Alonso, R. N., and Kubik, P. W., 2016, Landscape response to late Pleistocene climate change in NW Argentina: Sediment flux modulated by basin geometry and connectivity: Journal of Geophysical Research: Earth Surface, v. 121, no. 2, p. 392-414.

Schlüchter, C., 1989, The most complete Quaternary record of the Swiss Alpine Foreland: Palaeogeography, Palaeoclimatology, Palaeoecology, v. 72, p. 141-146.

Seiler, K., 1990, Groundwater balance and flow pattern in overdeepened sections of valleys in the Bavarian Alps: IAHS Publication, v. 190, p. 329-337.

Sharpe, D. R., Pugin, A., Pullan, S., and Gorrell, G., 2003, Application of seismic stratigraphy and sedimentology to regional hydrogeological investigations: an example from Oak Ridges Moraine, southern Ontario, Canada: Canadian Geotechnical Journal, v. 40, no. 4, p. 711-730.

Shaw, J., 2002, The meltwater hypothesis for subglacial bedforms: Quaternary International, v. 90, no. 1, p. 5-22.

Shugar, D. H., Burr, A., Haritashya, U. K., Kargel, J. S., Watson, C. S., Kennedy, M. C., Bevington, A. R., Betts, R. A., Harrison, S., and Strattman, K., 2020, Rapid worldwide growth of glacial lakes since 1990: Nature Climate Change, v. 10, no. 10, p. 939-945.

Sommer, C., Malz, P., Seehaus, T. C., Lippl, S., Zemp, M., and Braun, M. H., 2020, Rapid glacier retreat and downwasting throughout the European Alps in the early 21 st century: Nature communications, v. 11, no. 1, p. 1-10.

Soua, M., 2013, First evidence of tunnel valley-like formation during the late Ordovician" subgalacial" period in Southern Tunisia Influence on the Jeffara sandstone reservoir quality: Middle East Oil and Gas Show and Conference, Society of Petroleum Engineers.

Subetto, D. A., Davydova, N. N., and Rybalko, A. E., 1998, Contribution to the lithostratigraphy and history of Lake Ladoga: Palaeogeography, Palaeoclimatology, Palaeoecology, v. 140, no. 1-4, p. 113-119.

Sverdrup, H. U., Koca, D., and Schlyter, P., 2017, A simple system dynamics model for the global production rate of sand, gravel, crushed rock and stone, market prices and long-term supply embedded into the WORLD6 model: BioPhysical Economics and Resource Quality, v. 2, no. 2, 8.

Talbot, C., 1999, Ice ages and nuclear waste isolation: Engineering Geology, v. 52, no. 3-4, p. 177-192.

Texier, D., Degnan, P., Loutre, M., Lemaitre, G., Paillard, D., and Thorne, M., 2003, Modelling sequential BIOsphere systems under CLIMate change for radioactive waste disposal. Project BIOCLIM, Chatenay Malabry, National Radioactive Waste Management Agency of France, 11 p.

Thomas, R., Frederick, E., Krabill, W., Manizade, S., and Martin, C., 2006, Progressive increase in ice loss from Greenland: Geophysical Research Letters, v. 33, no. 10, L10503.

Tziperman, E., and Gildor, H., 2003, On the mid-Pleistocene transition to 100-kyr glacial cycles and the asymmetry between glaciation and deglaciation times: Paleoceanography, v. 18, no. 1, p. 1-1-1-8.

UNESCO, 2021, The United Nations world water development report 2021: valuing water, Paris, UNESCO, 187 p.

Van der Meer, J. J., Kjær, K. H., Krüger, J., Rabassa, J., and Kilfeather, A., 2009, Under pressure: clastic dykes in glacial settings: Quaternary Science Reviews, v. 28, no. 7-8, p. 708-720.

Van der Vegt, P., Janszen, A., and Moscariello, A., 2012, Tunnel valleys: current knowledge and future perspectives: Geological Society, London, Special Publications, v. 368, no. 1, p. 75-97.

Van der Wateren, D. M., 2002, Processes of glaciotectonism, Modern and Past Glacial Environments, Elsevier, p. 417-443.

Van Husen, D., and Reitner, J. M., 2011, An outline of the Quaternary stratigraphy of Austria: E&G Quaternary Science Journal, v. 60, no. 2/3, p. 366-387.

Veh, G., Korup, O., and Walz, A., 2020, Hazard from Himalayan glacier lake outburst floods: Proceedings of the National Academy of Sciences, v. 117, no. 2, p. 907-912.

Visser, J., 1987, The palaeogeography of part of southwestern Gondwana during the Permo-Carboniferous glaciation: Palaeogeography, Palaeoclimatology, Palaeoecology, v. 61, p. 205-219.

Voosen, P., 2021, Global temperatures in 2020 tied record highs: Science, v. 371, no. 6527, p. 334-335.

Waltham, T., 2008, Lötschberg tunnel disaster, 100 years ago: Quarterly journal of engineering geology and hydrogeology, v. 41, no. 2, p. 131-136.

Wilhelm, B., Arnaud, F., Enters, D., Allignol, F., Legaz, A., Magand, O., Révillon, S., Giguet-Covex, C., and Malet, E., 2012, Does global warming favour the occurrence of extreme floods in European Alps? First evidences from a NW Alps proglacial lake sediment record: Climatic Change, v. 113, no. 3, p. 563-581.

Wingfield, R., 1990, The origin of major incisions within the Pleistocene deposits of the North Sea: Marine Geology, v. 91, no. 1-2, p. 31-52.

Wolff, E., Barbante, C., Becagli, S., Bigler, M., Boutron, C., Castellano, E., De Angelis, M., Federer, U., Fischer, H., and Fundel, F., 2010, Changes in environment over the last 800,000 years from chemical analysis of the EPICA Dome C ice core: Quaternary Science Reviews, v. 29, no. 1-2, p. 285-295.

Yanites, B. J., Becker, J. K., Madritsch, H., Schnellmann, M., and Ehlers, T. A., 2017, Lithologic effects on landscape response to base level changes: A modeling study in the context of the Eastern Jura Mountains, Switzerland: Journal of Geophysical Research: Earth Surface, v. 122, no. 11, p. 2196-2222.

Zhao, W., Zhou, N., and Chen, S., 2020, The Record-Breaking High Temperature over Europe in June of 2019: Atmosphere, v. 11, no. 5, p. 524.

Zheng, G., Allen, S. K., Bao, A., Ballesteros-Cánovas, J. A., Huss, M., Zhang, G., Li, J., Yuan, Y., Jiang, L., and Yu, T., 2021, Increasing risk of glacial lake outburst floods from future Third Pole deglaciation: Nature Climate Change, v. 11, p. 411-417.

Ziegler, P. A., and Fraefel, M., 2009, Response of drainage systems to Neogene evolution of the Jura fold-thrust belt and Upper Rhine Graben: Swiss journal of geosciences, v. 102, no. 1, p. 57-75.

This page is intentionally left blank.

Subglacial erosion features in the Athabasca Glacier forefield (British Columbia, Canada).

II. How an overdeepening is eroded, and what its shape tells us

This chapter investigates the subsurface morphology of the Gebenstorf-Stilli Trough in the context of its complex bedrock architecture. Based on borehole and seismic data, geological controls on overdeepening erosion are identified, and evidence for basal water as the prevailing erosive agent is presented. The manuscript has been published in Geomorphology 394 under the [Creative Commons Attribution 4.0 International](#) license (open access) as

Gegg, L.[1], Deplazes, G.[2], Keller, L.[3], Madritsch, H.[2], Spillmann, T.[2], Anselmetti, F. S.[1], & Buechi, M. W.[1]: 3D morphology of a glacially overdeepened trough controlled by underlying bedrock geology (DOI 10.1016/j.geomorph.2021.107950).

[1] Institute of Geological Sciences and Oeschger Centre for Climate Change Research, University of Bern, Baltzerstrasse 1+3, 3012 Bern, Switzerland

[2] National Cooperative for the Disposal of Radioactive Waste (Nagra), Hardstrasse 73, 5430 Wettingen, Switzerland

[3] roXplore gmbh, Oberfeldstrasse 6, 8514 Amlikon-Bissegg, Switzerland

1. Abstract

Subglacial overdeepenings are common elements of mountain forelands and have considerable implications for human infrastructure. Yet, the processes of overdeepening by subglacial erosion and especially the role of bedrock geology are poorly understood. We present a case study of the Gebenstorf-Stilli Trough in northern Switzerland, a foreland overdeepening with a regionally unique, complex underlying bedrock geology: In contrast to other Swiss foreland overdeepenings, it is incised not only into Cenozoic Molasse deposits, but also into the underlying Mesozoic bedrock. In order to constrain the trough morphology in 3D, it was targeted with scientific boreholes as well as with seismic measurements acquired through analysis of surface waves. Our results reveal an unexpectedly complex trough morphology that appears to be closely related to the bedrock geology. Two sub-basins are incised into calcareous marls and Molasse deposits, and are separated by a distinct ridge of Jurassic limestones, indicating strong lithological control on erosional efficiency. We infer generally relatively low glacial erosion efficiency *sensu stricto* (*i.e.* quarrying and abrasion) and suggest that the glacier's basal drainage system may have been the main driver of subglacial erosion of the Gebenstorf-Stilli Trough.

2. Introduction

Subglacial overdeepenings, closed troughs eroded below the fluvial base level, are common elements of formerly glaciated mountain forelands (Cook and Swift, 2012). In the northern European Alpine example, they underlie ~10 % of the land surface (Dürst Stucki and Schlunegger, 2013). Despite their significance for, among others, construction projects, groundwater and radioactive waste disposal (Preusser *et al.*, 2010; Stumm, 2010), the understanding of overdeepenings in terms of formation processes and controlling factors is limited and subject to debate (Cook and Swift, 2012; Alley *et al.*, 2019). This applies especially to the influence of bedrock geology on the efficiency of subglacial erosion (Goudie, 2016).

Several authors (*e.g.* Augustinus, 1992, Brook *et al.*, 2004) have reported a correlation of rock mass strength and glacial trough cross section, with steep and narrow troughs developing in resistant bedrock, and wide and shallow troughs in weak lithologies. However, effects of more complex patterns of bedrock lithology have hardly been studied. As an exception, Pomper *et al.* (2017) reported deeper-reaching subglacial erosion where the Lower Salzach Valley (Austria) is underlain by soft Cretaceous marls as opposed to lime- and dolostones. Further, Harbor (1995) modelled glacial erosion into bedrock with a weak zone in the trough centre, and observed increased downcutting, narrowing and steepening initiating in but, not restricted to, the weak zone. On a smaller scale, Glasser *et al.* (1998) showed by detailed field mapping that discontinuities from bedrock foliation parallel to the ice flow enhance erosion through quarrying, whereas discontinuities orthogonal to ice flow rather increase abrasion. Similarly, the orientation of sedimentary bedding has a discernible influence on basal ice velocity and thus on subglacial landform morphology (Phillips *et al.*, 2010). Quarrying is frequently considered the more efficient glacial erosion process (*e.g.* Cohen *et al.*, 2006; Zoet *et al.*, 2013; Alley *et al.*, 2019), but in weak and poorly jointed rocks, abrasion might outweigh quarrying (Krabbendam and Glasser, 2011). The importance of jointing and joint spacing has been further highlighted by Dühnforth *et al.* (2010), who found a strong correlation of glacial erosion rates and fracture density (see also Hooyer *et al.*, 2012; Becker *et al.*, 2014). Most of these investigations specifically focused on glacial erosion in non-overdeepened settings.

In overdeepenings, characterised by an adverse slope at the distal end, the subglacial hydrological conditions are very different (Cook and Swift, 2012). In order to maintain erosion, sediment has to be evacuated from the glacier base against this adverse slope, whereby pressurised melt water plays an important role (Alley *et al.*, 1997, 2019; Cook and Swift, 2012; Buechi *et al.,* 2017). The abundance of subglacial water steadily increases towards the glacier snout, where it facilitates the erosion of large terminal overdeepenings even under diffluent ice (Herman *et al.*, 2011). There, subglacial water has been suggested to be the main driver of subglacial erosion, analogous to tunnel valleys (Cofaigh, 1996; Dürst Stucki *et al.*, 2010; Fiore *et al.*, 2011; Dürst Stucki and Schlunegger, 2013). It is therefore questionable to what extent the findings of subglacial erosion in non-overdeepened settings can be applied to the formation and evolution of overdeepened glacial troughs.

This study sheds light on the morphology of a subglacial overdeepening in the northern Alpine foreland of Switzerland, based on borehole and seismic data. The selected overdeepening is of special interest and relevance due to its unique, complex bedrock geology. The connection of the trough morphology with bedrock architecture and the area's tectonic setting allow inferences about the geological controls and the processes of overdeepening erosion.

3. Study area

The study area is located in northern Switzerland, close to the eastern termination of the WSW-ENE trending Jura Mountains (Fig. II-1). The local bedrock stratigraphy comprises Triassic and Jurassic sediments deposited on an epicontinental platform and unconformably overlain by Cenozoic clastics of the northern Alpine Molasse Basin (Bitterli-Dreher *et al.*, 2007; Jordan *et al.*, 2008).

The oldest rocks exposed at the surface of the study area are shallow marine limestones and dolomites of the Schinznach Formation (Fm.; late Middle Triassic; Figs. II-2A, -S1). They are overlain by the Middle to Late Triassic Bänkerjoch Fm., an alternation of gypsum/anhydrite with claystone and dolomite, and Klettgau Fm., a heterogeneous unit comprising mostly marl, silt- and sandstone. The following Early Jurassic Staffelegg Fm. as well as the Opalinus Clay of the early Middle Jurassic consist of marine claystones, siltstones and marls. During the later Middle Jurassic, marls and limestones (PKI: Passwang Fm., Klingnau Fm., Ifenthal Fm.; Fig. II-S1) were deposited in a shallow sea that deepened towards the early Late Jurassic, when the predominantly calcareous marls of the Wildegg Fm. formed (Gygi, 2000; Deplazes *et al.*, 2013). These marls transition gradually over few meters to decameters into bedded and massive marine limestones of the Villigen and Burghorn Fms. (in the following referred to as «Malmkalk»; Fig. II-S1; Gygi, 2000; Bitterli-Dreher *et al.*, 2007; Jordan *et al.*, 2008).

In the Paleogene, the Mesozoic strata of the Jura Mountains were uplifted on the forebulge of the Alpine orogeny and began being eroded and karstified, while further south/southeast the Molasse Basin subsided (Fig. II-1; Pfiffner, 1986; Berger *et al.*, 2005). In Oligocene-Miocene times heterogeneous sandstones, siltstones, and marls of the Lower Freshwater, Upper Marine, and Upper Freshwater Molasse were deposited in the study area, and generally remained rather poorly lithified (Fig. II-S1; Bitterli-Dreher *et al.*, 2007). The Molasse deposition ended in the Late Miocene, around the same time the Folded Jura (FJ) formed. It was upthrusted as a consequence of collisional tectonics in the Central Alps via thin-skinned deformation above an evaporitic décollement horizon within Middle to Upper Triassic evaporites (Laubscher, 1962; Burkhard, 1990).

This décollement horizon crops out along the Jura Main Thrust that formed between 9 and 4 Ma (Figs. II-1B, -2A; Looser *et al.*, 2021). The Mesozoic sequences south of it, *i.e.* within its hanging wall, are affected by a dense stack of thrusts and dip moderately towards the south (Fig. II-2A; Malz *et al.* 2015). By contrast, north of the Jura Main Thrust the Mesozoic strata dip only very gently southward (Tabular Jura: TJ; Fig. II-2A). While the Mesozoic is overlain by a wedge of Molasse deposits immediately north of the Jura Main Thrust, continuously older rocks are exposed further to the north, where they form plateaus (*e.g.* in the northwest of Fig. II-2).

During the Pleistocene, multiple advances of Alpine glaciers reached far into the foreland and considerably reshaped the landscape (Graf, 2009; Keller & Krayss, 2010; Preusser *et al.*, 2011). This includes the subglacial erosion of overdeepenings, most of which are carved exclusively into Molasse deposits (Fig. II-1; Graf, 2009; Preusser *et al.*, 2010). An exception is the Gebenstorf-Stilli Trough (GST), which cuts through the FJ and into the TJ (Fig. II-2; Jordan, 2010). It extends ~9 km northward from the Birrfeld Basin (Nitsche *et al.*, 2001) into the present-day confluence area of the rivers Aare, Reuss and Limmat and has a distinctly elongated shape with a maximum width of ~1 km (enclosed by the 300 m a.s.l. isoline; Bitterli-Dreher *et al.*, 2007; Pietsch and Jordan, 2014). The maximum trough depth exceeds 110 m below surface and 75 m below the lowest known Pleistocene base level (PBL, 300 m a.s.l.; Graf, 2009; Gegg *et al.*, 2020). Situated entirely outside the LGM (Bini *et al.*, 2009), the GST was presumably incised during the late Middle Pleistocene (Bitterli-Dreher *et al.*, 2007; Graf, 2009). The significant narrowing from the wide Birrfeld Basin towards the GST coincides with a change in trough morphology from U-shaped to V-shaped (Jordan, 2010; Dürst Stucki and Schlunegger, 2013). It has been hypothesised that the narrowing and change in shape are a result of the dominant bedrock lithology changing from rather soft, poorly lithified Molasse sandstones, siltstones and marls in the south towards the more resistant limestones and marls of the Jura Mountains in the north (Bitterli-Dreher *et al.*, 2007; Jordan, 2010).
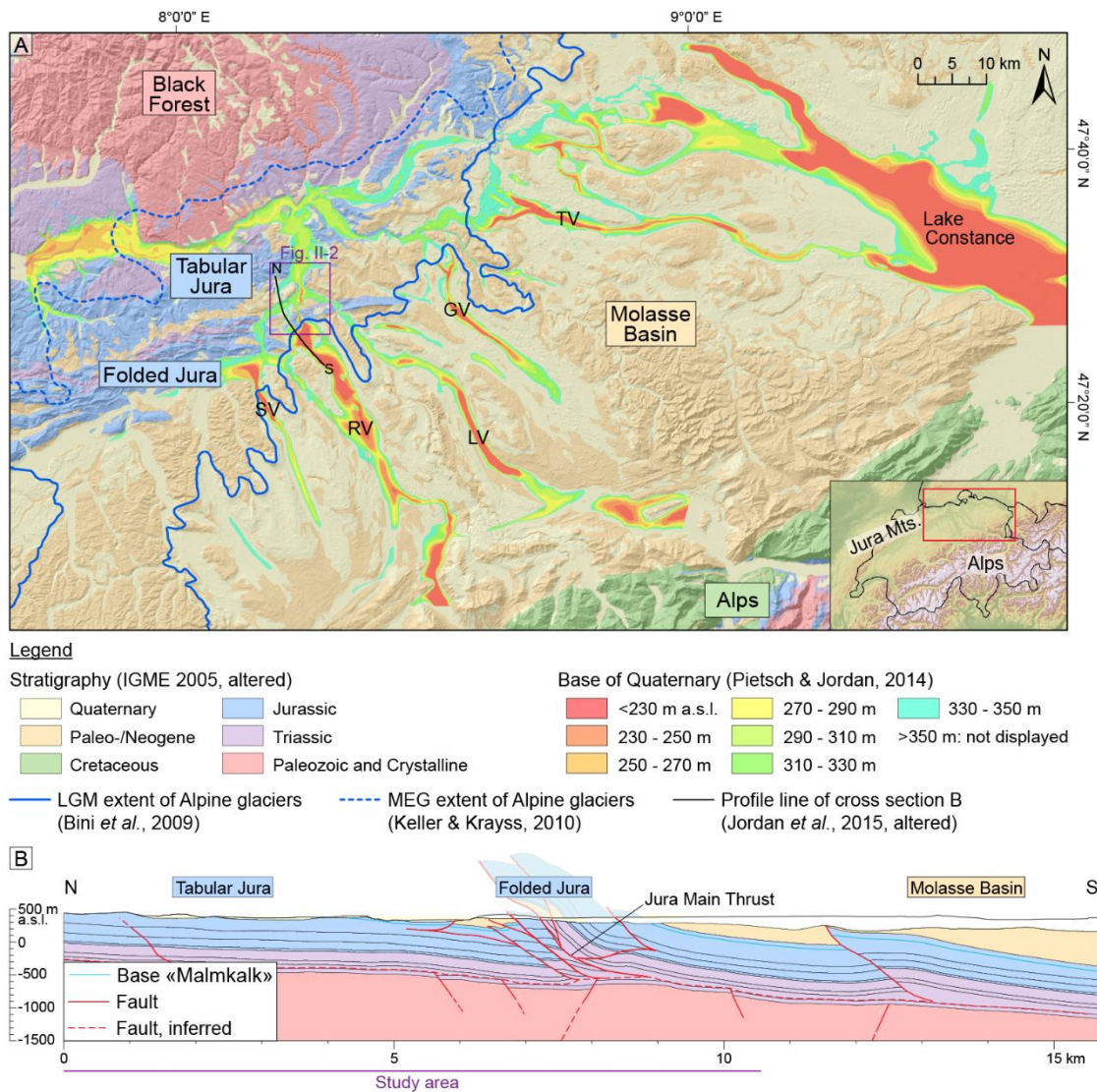
Fig. II-1: Overview map of central and eastern northern Switzerland with major tectonic units and surface geology (A; IGME 2005: Commission for the Geological Map of the World *et al.*, 2005; LGM: Last Glacial Maximum; MEG: Most Extensive Glaciation). The cross-section (B; from Jordan *et al.*, 2015, altered) illustrates the tectonic architecture of the study area (purple box in A). Note that foreland overdeepenings (SV: Seetal Valley, RV: Reuss Valley, LV: Limmat Valley, GV: Glatt Valley, TV: Thur Valley) generally only occur within the Molasse basin, with the exception of the Gebenstorf-Stilli Trough (Fig. II-2).
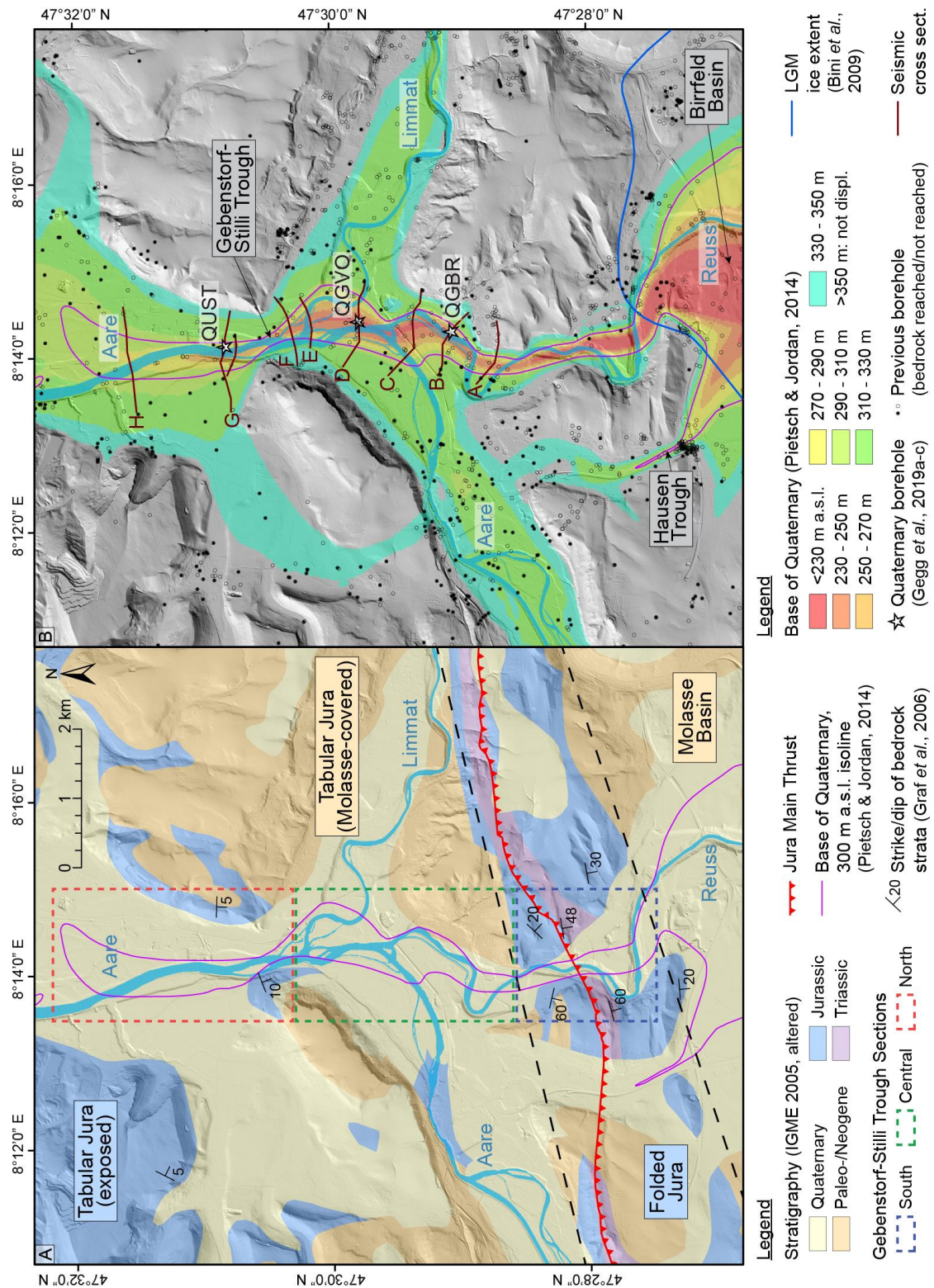
Fig. II 2: Overview map of the Gebenstorf-Stilli Trough. A: Simplified surface geology. B: Locations of boreholes and acquisition lines of seismic cross sections. For localisation, please refer to Fig. II-1.

4. Methodology

The Gebenstorf-Stilli Trough was investigated with three scientific boreholes along its trough axis (Fig. II-2B). These are, from south to north, QGBR (47°29'00" N, 8°14'11" E; Gegg *et al.*, 2019b), QGVO (47°29'43" N, 8°14'18 E; Gegg *et al.*, 2019c), and QUST (47°30'46" N, 8°14'3" E; Gegg *et al.*, 2019a). All three boreholes terminated at least 10 m into the bedrock to allow for a confident bedrock identification. Recovery and core quality were maximised by combined application of pneumatic hammering ('Düsterloh Hammer') and wire-line drilling with a triple-tube core barrel. After detailed stratigraphic logging of the drill cores, selected 1-m-intervals were sampled for petrographic analysis of coarse-grained sediments (>100 clasts >15 mm in diameter, if not indicated otherwise).

To further constrain the morphology of the Gebenstorf-Stilli Trough, we recorded ambient noise on ~230 seismic 3-component stations that were distributed along eight acquisition lines (Fig. II-2B; Nagra, 2021). The data processing workflow is sketched on Fig. II-3 and involved computation of the horizontal-to-vertical spectral ratio (HVSR) for each of the 10-30 min long recordings and picking of the respective fundamental frequency f_0 (Fig. II-3A; SESAME European research project, 2004). The frequency of the pulse maximum f_0 depends on the depth of the shear wave (S-wave) velocity contrast indicative for the bedrock below unconsolidated sediments. In case of ambiguity in the spectral information, f_0 was selected conservatively, with regard to the bedrock model of Pietsch and Jordan (2014).

Conversion of f_0 to bedrock depth z is possible if the average S-wave velocity of the Quaternary strata $v_{s,E}$ is known (eq. (i); see Nakamura, 1989, for details). It was determined by joint inversion of ~50 active measurements after Dziewonski *et al.* (1969; multiple frequency analysis MFA) in combination with deeper reaching ESAC measurements (extended spatial auto correlation; Ohori *et al.*, 2002; typically one measurement per acquisition line) following Dal Moro *et al.* (2018). This process provided one S-wave velocity function per line, which was windowed for the intra-Quaternary part (S-wave velocity < 1100 m/s; Wiemer *et al.*, 2015) and averaged to obtain location-specific $v_{s,E}$ values (Fig. II-3B). These were applied to eq. (i) for conversion of f_0 into depth profiles of the base of Quaternary (Fig. II-3C).

(i) $\quad z = v_{s,E} / 4 * f_0$

We base our study on a geological and morphological interpretation of the resulting cross sections (Fig. II-3D) integrating surface (1 : 25'000 geological map: Graf *et al.*, 2006; 2 m LiDAR DEM: Swisstopo, 2013) and subsurface information (drill logs from the borehole database of the Swiss Cooperative for the Disposal of Radioactive Waste (Nagra); previous 25 m base of Quaternary DEM: Pietsch and Jordan, 2014). For cross section construction, boreholes with a distance of max. 200 m from the respective acquisition line were projected parallel to the isolines of the Gebenstorf-Stilli Trough by Pietsch & Jordan (2014). The base of Quaternary was fitted to the boreholes while maintaining the seismically determined trough shape. Interpretations are focused on the overdeepened part of the trough, *i.e.* that lying below PBL at $\sim$300 m a.s.l. (Graf, 2009). The same applies to the V-index (VI; Zimmer & Gabet, 2018) as a quantifier of trough shape. A perfectly V-shaped trough with even flanks would be characterised by a VI of 0, whereas increasing values correspond to more concave flanks, *i.e.* an increasingly U-shaped cross section.
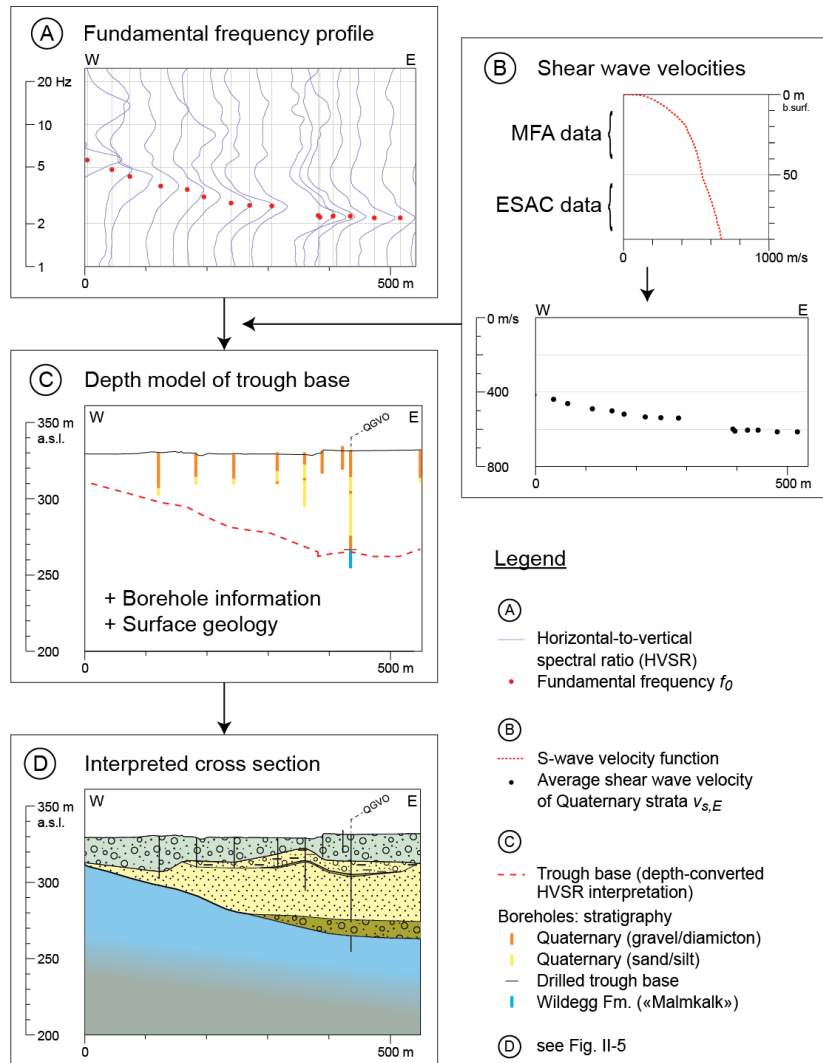
Fig. II-3: Workflow applied for the construction of the cross sections from the geophysical data exemplified by a clip of acquisition line D. The fundamental frequency profile (A) is, with help of the shear wave velocity profile (B), converted into a depth model of the trough base (C), and complemented with borehole and surface data to a finalised geological cross section (D).

5. Results

5.1. Planform morphology

In terms of bedrock geology, the GST can be subdivided into three sections of approximately equal length. The southern section is embedded in the Folded Jura (FJ), whereas the middle section is mostly incised into Molasse deposits, and the northern section into the Mesozoic of the Tabular Jura (TJ, Fig. II-2A). These three sections show striking differences in planform morphology (Pietsch and Jordan, 2014): both the TJ and FJ sections are narrow (300-400 m at 300 m a.s.l) and either straight in their entirety or composed of straight segments, respectively. In contrast, in the Molasse section the trough takes a sinuous course towards north while widening gradually (up to ~800 m at 300 m a.s.l.) until a sudden constriction at the transition to the TJ. The sinuosity index S of the Molasse section, defined as the ratio between total length of the trough axis between two selected points and the shortest connection of said points, is 1.06 (Fig. II-S3). Our boreholes and seismic acquisition lines cover the central (QGBR, QGVO, lines A-E) and northern (QUST, lines F-H) sections of the GST (Fig. II-2B).

5.2. Boreholes

QGBR and QGVO recovered Late Pleistocene Niederterrasse gravels overlying a thick unit of lacustrine/deltaic sand and several meters of basal coarse-grained sediment, while the trough infill in QUST almost exclusively comprises gravels (Fig. II-4; see Fig. II-2B for locations). The coarse-grained deposits consist largely of far-travelled, *i.e.* Alpine or Molasse-derived, clast lithologies dominated by grey limestones, diverse sandstones, and quartzites (Fig. II-4). Lithologies of the local Jura Mountains play a subordinate role: Light beige limestone clasts that can be attributed to the Villigen Fm. («Malmkalk») make up no more than 18 % (usually below 10 %), and calcareous marl clasts attributed to the Wildegg Fm. were not encountered in the chosen intervals. Only the lowermost ~0.3 m of the Quaternary infill at QGBR consists predominantly of light limestone fragments, and the lowermost ~0.4 m of QUST contains individual soft marly clumps identified as Wildegg Fm. (Gegg *et al.*, 2019a,b).

The boreholes reached the base of the overdeepening in depths of 111.5 m (225.8 m a.s.l.), 64.9 m (266.1 m a.s.l.), and 76.0 m (255.2 m a.s.l.), respectively (Fig. II-4). Light beige limestones of the «Malmkalk» were encountered below the overdeepening in QGBR and QGVO, and grey calcareous marls of the Effingen Member, Wildegg Fm., in QUST. We combined these findings with the logs of >450 existing boreholes in the perimeter as well as a 1 : 25'000 scale geological map (Graf *et al.*, 2006) to a base Quaternary subcrop map (see section 6.2). The generally massive «Malmkalk» is characterised by frequent stylolites in varying orientations including horizontal and vertical, as well as shallow (<40 °), southeast-dipping fractures with an average spacing of ~0.6 m in QGBR, and ~1.4 m in QGVO (corrected after Terzaghi, 1965). Deep-reaching, sediment-filled paleokarst predating the Quaternary and exhibiting presumed subglacial hydrofractures was encountered in QGBR (Gegg *et al.*, 2020). The calcareous marls of the Wildegg Fm. have a similar fracture spacing of ~1.1 m in QUST, and contain intervals where the rock is softened or granular-disintegrating. The bedrock surface is truncated by a karst cavity in QGBR, but developed as a sharp, horizontal boundary in QGVO and QUST with minor drilling-induced disturbance by fresh fracturing and/or grinding.

5.3. Surface-seismic sections

The interpreted cross sections are plotted on Fig. II-5, and Fig. II-S2A-H show the individual cross sections together with the respective raw data. The uncertainty of the applied method is difficult to quantify as it depends on multiple factors, such as the heterogeneity of the trough infill, the local inclination of the base of Quaternary, the impedance contrast to the bedrock, the presence of other geological boundaries (*e.g.* Molasse-Mesozoic) in close proximity, and the amplitude and frequency of industrial noise. Empirically, the seismic measurements are in good accordance with boreholes in the vicinity (max. distance 170 m). Average differences amount to -7/+10 m, with maximum values of -21/+22 m (over- and underestimation, respectively; see Table II-S2). An exception is the site of borehole QGBR, where the trough depth is underestimated by ~30 m, however this borehole is located close to the trough wall that has likely affected the respective measurements (Table II-S2, Fig. II-5).

The intra-Quaternary shear wave velocities show an increasing trend towards the north (~500 m/s at 50 m depth for lines A and B, ~550 m/s for lines C and D; ~600 m/s for line G). Although these differences are smaller than the variations along a given line, they correlate with a trough infill that becomes increasingly more coarse-grained and higher in density towards the north (Fig. II-4; Gegg *et al.*, 2019a-c).
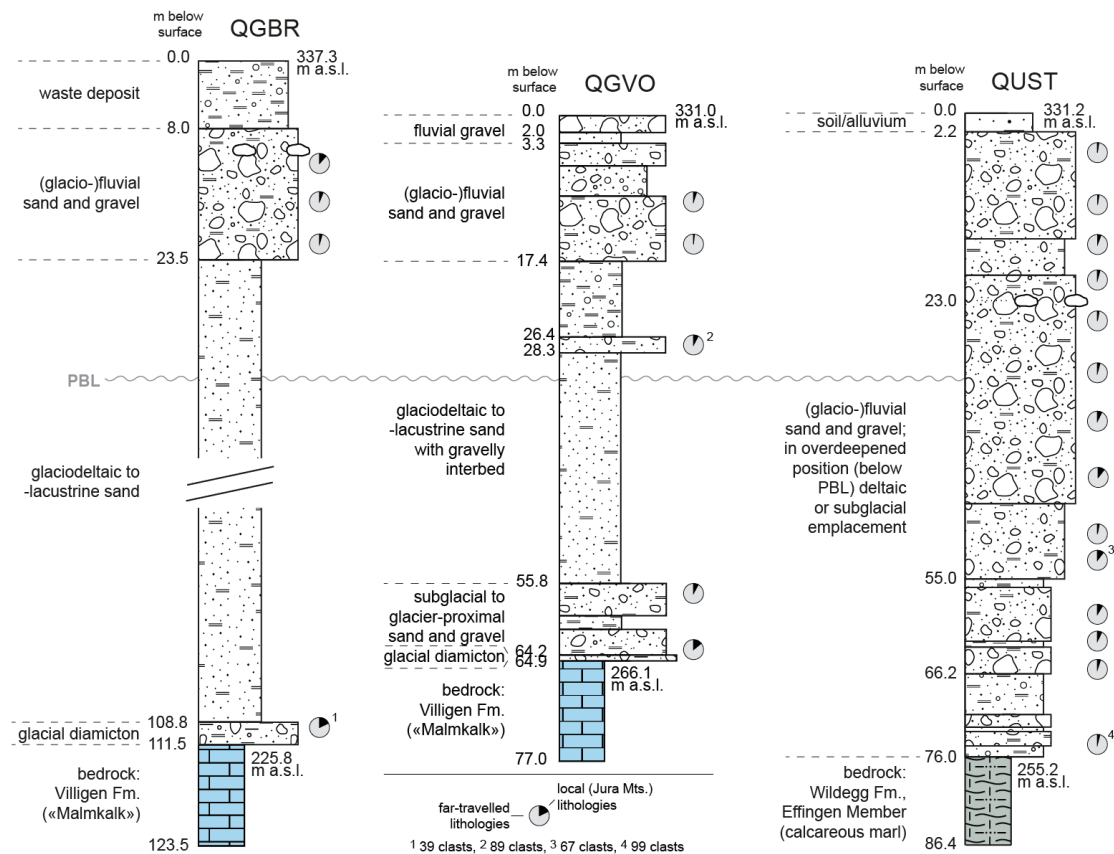
Fig. II-4: Lithological logs of Quaternary boreholes QGBR, QGVO, and QUST (from Gegg *et al.*, 2019a-c, altered). PBL marks the lowest known Pleistocene base level at ~300 m a.s.l. (Graf, 2009). Pie charts show the ratio of local limestones vs. far-travelled clasts in coarse-grained sediments (>100 clasts >15 mm, if not indicated otherwise).

The cross sections show a trough composed of two sub-basins (Gebenstorf Basin in the central and Stilli Basin in the northern trough section; 'nested basins' after Patton *et al.*, 2016) separated by a distinct bedrock ridge (Lauffohr Ridge, Figs. II-5, -6). The GST gradually widens from ~350 to ~800 m at 300 m a.s.l. (*i.e.* at PBL; Graf, 2009) between lines A and D while transitioning from a V- to a more U-shaped cross section (VI increases from 0.2 to 0.4).

This widening coincides with a shallowing of the overdeepened centre from its maximum depth at ~225 to ~265 m a.s.l., following the trend of the «Malmkalk» surface that rises towards the TJ (Fig. II-6), and as a result, the overdeepened cross sectional area remains approximately constant (Fig. II-5). North of line D, the trough narrows abruptly and further shallows to ~295 m a.s.l. at line E, where the bedrock geology changes gradually from «Malmkalk» to the underlying marl (Wildegg Fm.; Fig. II-5). Further north (lines F-H), seismic data are afflicted by greater uncertainties than in the south. The trough deepens to at least 255 m a.s.l. at QUST, and the distinct trough shoulder east of QUST (constrained by a second borehole on line G, Figs. II-5, -S2G) suggests a rather U-shaped cross section (VI = 0.6). The overdeepening terminates close to line H, with an average adverse slope of ~1.6 ° between lines G and H (Fig. II-6).

Fig. II-5 (next page): Interpreted surface-seismic cross sections A-H (see also Fig. II-S2A-H). For location of the cross sections, see inset map or Fig. II-2B. Profile traces X and Y refer to Fig. II-6. VI = V-index (Zimmer & Gabet, 2018), CA = overdeepened cross sectional area (below 300 m a.s.l.).
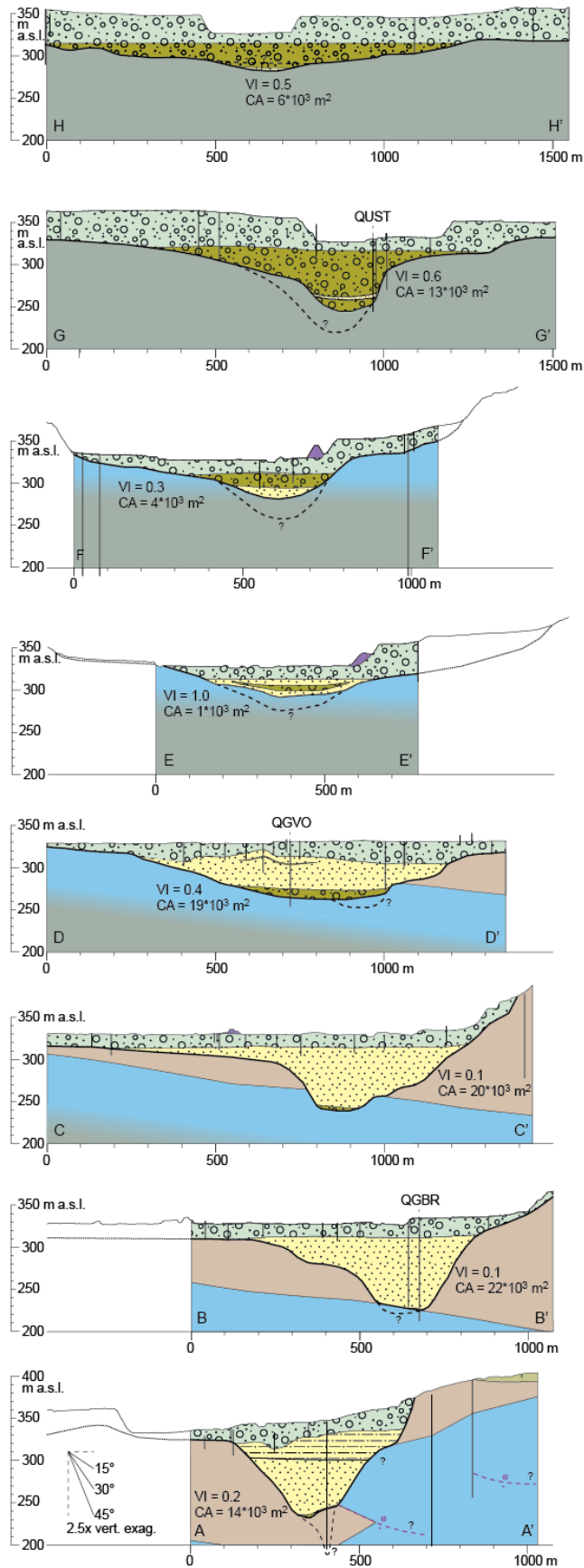
Legend (Fig. II-5 / Fig. II-6)

- Railway embankment
- Niederterrasse
- Lacustrine silt
- Lacustrine sand
- Coarse-grained trough infill
- Hochterrasse
- Tiefere Deckenschotter
— Base of Quaternary (BQ)
.?. BQ, alternative interpretation
⋯ BQ (Graf et al., 2006; Pietsch & Jordan, 2014)
- Upper Freshwater Molasse
- Upper Marine Molasse
- Lower Freshwater Molasse
- «Malmkalk» } with gradual
- Wildegg Fm.   } transition
- Supposed thrust fault
| Borehole

Map
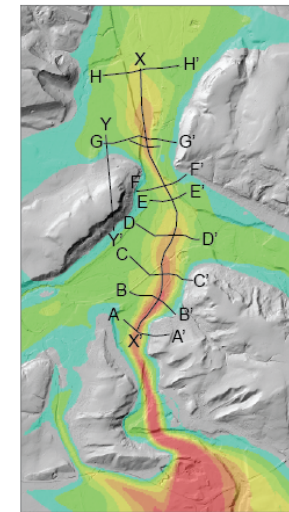
Base of Quaternary (this study)

- <230 m a.s.l.
- 230 - 250 m
- 250 - 270 m
- 270 - 290 m
- 290 - 310 m
- 310 - 330 m
- 330 - 350 m
- >350 m: not displayed

57

6. Discussion

6.1. Planform morphology

6.1.1. Paleo-ice flow and erosion

Dürst Stucki and Schlunegger (2013) distinguish two general types of overdeepenings in the vicinity of the Alps, i) proximal Alpine-type overdeepenings composed of straight segments, and ii) distal, anastomosing foreland-type overdeepenings (see also Magrani *et al.*, 2020). These morphologies are interpreted as a result of geological as well as paleo-glaciological differences: While Alpine-type overdeepenings are carved into zones of weakness (*i.e.* fault zones) by thick ice streams in the mountain valleys, foreland-type overdeepenings occur in the generally rather poorly lithified Molasse deposits independently from structural weak zones (Preusser *et al.*, 2010; Dürst Stucki and Schlunegger, 2013). Pressurised subglacial melt water plays an important role especially in the erosion of foreland overdeepenings near the glacier termini (Herman *et al.*, 2011; Alley *et al.*, 2019), and could possibly be its main driver (Dürst Stucki *et al.*, 2010; Dürst Stucki and Schlunegger, 2013).Morphologically, the central section of the GST resembles a typical foreland overdeepening, whereas the southern (FJ) and northern (TJ) sections have more similarities with inner-Alpine overdeepenings. This morphological variability occurs despite the common distal position, similar melt water availability (periodically high) and ice thickness (low), suggesting the same prevailing erosional mechanisms (see section 6.2.2; Herman *et al.*, 2011; Cook and Swift, 2012). We infer that in the case of the GST, the morphological differences are controlled predominantly by the bedrock geology and resulting pre-glacial topography.

The Mesozoic strata outcropping in the FJ and TJ have a higher bulk erosional resistance than the Molasse deposits (Kühni and Pfiffner, 2001) despite strong internal variations (Yanites *et al.*, 2017) and it has been shown before that glacial troughs tend to be narrower in more resilient rocks (Augustinus, 1992; Brook *et al.*, 2004). In addition, the erosional resistance of the Mesozoic has facilitated the Jura Mountains to persist as a low mountain range for several millions of years, whereas the Molasse Basin topography is comparatively levelled off. As a consequence, while Pleistocene ice flow over Molasse deposits could diverge to the sides, the FJ and TJ sections of the GST lie within distinct, likely pre-existing valleys (Ziegler and Fraefel, 2009). These valleys constrained the ice and basal water flow, which is often accompanied by an increase in velocity and erosional activity (Hallet, 1979; Herman *et al.*, 2015, Patton *et al.*, 2016). Given the similar trough widths in FJ and TJ, it appears that the different tectonic histories of both units are not expressed through significantly different erosional susceptibilities, which could be due to the structural strike of the FJ being orthogonal to paleo-ice flow (Glasser *et al.*, 1998).

Although comparatively poorly constrained, the width of the overdeepened (below 300 m a.s.l.) GST appears to remain largely constant across the FJ (Fig. II-1; Bitterli-Dreher *et al.*, 2007; Pietsch and Jordan, 2014) where bedrock properties change drastically over short distances (Yanites *et al.*, 2017). In contrast to the modern valley, the shape of the buried overdeepening is seemingly little affected by short-scale variations in erosional resistance, which applies also to the Hausen Trough further west (Fig. II-2B; Graf, 2009; Pietsch & Jordan, 2014). This suggests that there is a certain inertia in trough morphology, which can adjust only gradually to bedrock changes. This hypothesis is supported by the slow and gentle widening of the GST after the transition from the FJ into the northward adjacent Molasse. As a result, the GST remains comparatively narrow even in its central section, with a maximum width that is more typical of inner-Alpine than for foreland overdeepenings (Table II-1).

6.1.2. The role of structural preconditioning

The Gebenstorf-Stilli Trough is the only known overdeepening of the northern Alpine foreland that extends significantly (*i.e.* kilometers) beyond the Molasse Basin (Fig. II-1; Jordan, 2010), raising the question why such localised incision into the Mesozoic strata was possible at this specific position. Previously, structural geological control enabling the breach of the (fluvial) Aare Valley into the exposed TJ (approx. at line F) has been suggested (Haldimann *et al.*, 1984). The straight and/or kinked morphology of those GST sections incised into Mesozoic bedrock support the idea that the overdeepening, and the likely preceding fluvial valley system (Ziegler and Fraefel, 2009), could follow discrete fault zones in the bedrock (similar to *e.g.* the inner-Alpine valleys of the rivers Rhone and Adda). This hypothesis is in the following reviewed based on our investigations.

At the outcrop-scale, N-S fractures, mostly with strike-slip kinematics, are a typical characteristic of Upper Jurassic limestones across the study area and beyond (Figs. II-7, -S4; Madritsch, 2015). Minor N-S striking faults have been recognised in elongation of the GST (Matousek *et al.*, 2000) and along strike of the FJ to the east (Diebold *et al.* 2006; Jordan *et al.*, 2011). However, a densification of this kind of structures around the breach of the GST, especially in the TJ, is not discernable. In addition, individual strike-slip faults do not appear to have a strong structural imprint on the immediately surrounding Mesozoic bedrock (*e.g.* increase of fracture density, cataclasis development) according to field observations in the vicinity of the GST (Fig. II-S4). No evidence for a major fault zone underneath the overdeepened trough has been observed in two regional seismic campaigns (Sprecher and Müller, 1986; Madritsch *et al.*, 2013). However, the presence of a strike-slip fault zone with minor vertical throw hindering its seismic detection (Nagra, 2019) in the subsurface of the GST cannot be excluded. Despite the lack of evidence for a distinct fault zone, we can therefore not rule out structural control for the breach of FJ and TJ and/or glacial erosion thereafter.

In contrast to the southern and northern GST sections, the central section is characterised by a gently sinuous planform morphology. Its sinuosity (S = 1.06) is similar to other distal Molasse-hosted overdeepenings in the northern Alpine foreland (Pietsch and Jordan, 2014; Fig. II-S3), *e.g.* Seetal Valley (S = 1.07), middle Reuss Valley (S = 1.05), Limmat Valley (S = 1.07), Glatt Valley (S = 1.12) and Thur Valley (S = 1.05), and generally similar to tunnel valleys (Cofaigh, 1996; van der Vegt *et al.*, 2012). This morphology has previously been interpreted as indicative for erosion of the poorly lithified Molasse independent from structural control (*i.e.* not along straight fault segments; Preusser *et al.*, 2010; Dürst Stucki and Schlunegger, 2013).

6.2. Trough morphology in 3D

6.2.1. Lithological control on subglacial erosion

The maximum depth of the GST of ≥112 m below surface (~225 m a.s.l.) is typical for Swiss foreland overdeepenings (Table II-1; Magrani *et al.*, 2020). It is reached just beyond the FJ in the southern sub-basin (Gebenstorf Basin, GB) that shallows considerably further north. The shallowing of the GB occurs entirely within the narrow band of the «Malmkalk» that emerges at angle of ~4° towards the northwest, where it is exposed and referred to as TJ (Figs. II-5, -6). This suggests strong lithological control for the depth of the basin: It appears that the subglacial erosional efficiency decreased significantly upon reaching the Jurassic limestones. A similar erosion pattern was observed in a seismic study of Lake Neuchâtel (NW Switzerland; Ndiaye *et al.*, 2014), whose overdeepened floor reaches down to, but is not significantly incised into, the Mesozoic strata under ~200 m of Molasse cover. In QGBR, deep-reaching sediment-filled paleokarst was encountered in the limestone (Gegg *et al.*, 2020). The fact that even karstified and presumably weakened «Malmkalk» was preserved and not completely eroded by the overdeepening glacier emphasises its erosional resistance (see also Ndiaye *et al.*, 2014). Moreover, the paleokarst walls throughout the bedrock interval of QGBR show abundant, randomly oriented surficial fractures, some of which are filled with intruded sediment (Gegg *et al.*, 2020).
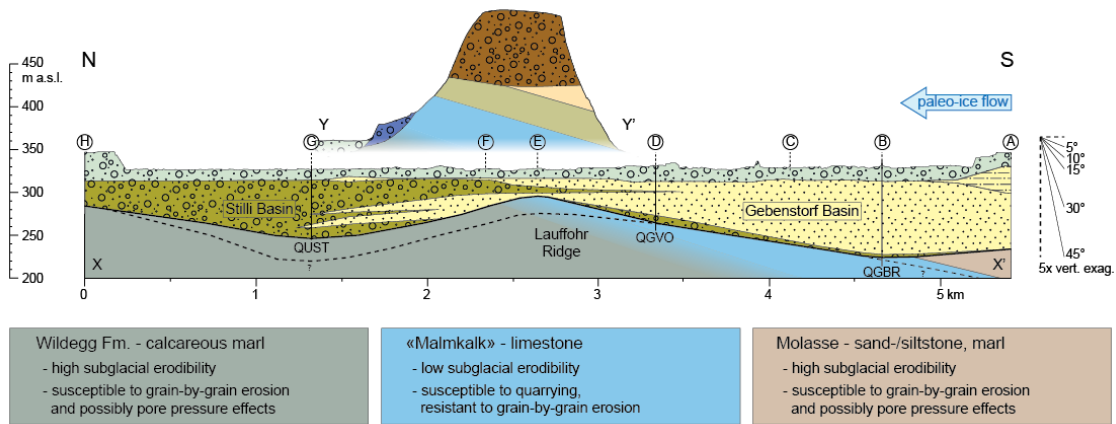
Fig. II-6: Longitudinal section X of the Gebenstorf-Stilli Trough compiling cross sections A to H. Section Y through the Tabular Jura escarpment illustrates the dip of the bedrock strata. For localisation and legend, please refer to Fig. II-5. Relative erodibilities and presumed erosion processes of the relevant bedrock lithologies are summarised at the bottom (see section 6.2.2).

Table II-1: Quantitative comparison of the Gebenstorf-Stilli Trough (GST) with other overdeepenings in Switzerland (based on Magrani *et al.*, 2020). * The approach by Magrani *et al.* (2020) uses a minimum sediment thickness or water column of 20 m to define overdeepening extent, thus maximum width is given 20 m below present-day ground surface.

		Max. depth [m] below surface	Max width [m] 20 m below surf.*	Terminal adverse slope [°]
Alpine overdeepenings	Average	337	1453	2.7
	Median	288	962	1.7
Foreland overdeepenings	Average	180	2024	1.0
	Median	115	1298	0.6
Gebenstorf-Stilli Trough		≥112	920	1.6

The authors conclude that subglacial hydrofracturing is the most plausible explanation for the origin of these fractures, and that their abundance could point towards a multitude of subglacial water pressure events. Such a record would require erosion rates low enough to allow for prolonged direct contact of the karstified limestone with the glacier's basal drainage system. However, we consider possible that the limited downcutting over the «Malmkalk» may have led to increased lateral erosion within the overlying Molasse, as the shallowing of the GB coincides with a doubling in trough width, so that the overdeepened cross sectional area remains nearly constant (see Fig. II-5, sections A-D).

The shallowest depth of the GST is reached at the crest of the Lauffohr Ridge, where the base of the southward-dipping Jurassic limestone is breached (Figs. II-6, -7). There, the GST is barely overdeepened as its base is close to PBL at 300 m a.s.l. (Graf, 2009). In the underlying calcareous marls of the Wildegg Fm. erosional efficiency was again increased and culminated in the Stilli Basin (SB). We hypothesise that the enhanced erosion rates are the result of an interplay of several paleoglaciological as well as geological factors. Firstly, an abrupt increase in ice and melt water flux have likely increased subglacial erosion at the confluence of the catchments of Aare, Reuss, and Limmat (*cf.* MacGregor *et al.*, 2000; Pomper *et al.*, 2017). According to Ziegler and Fraefel (2009), this confluence had been established before, and remained largely fixed throughout, the Pleistocene. The deepening of the GST into the SB initiates where the three present-day valleys merge (Fig. II-7), and it is not unlikely that a major ice confluence occurred at the same position during excavation of the GST. This position lies along the escarpment of the TJ (Figs. II-6, -7), an area of increased topography, where ice flow was again focused into a morphologically defined valley, which may have further accelerated flow velocity (see section 6.1.1; Hallet, 1979; Herman *et al.*, 2015; Patton *et al.*, 2016). An increase in erosion rate towards the SB could thus be achieved through increased ice flux and velocity alone. In addition to that, Yanites *et al.* (2017) attributed generally lower erosional resistance (to fluvial downcutting) to the Wildegg Fm. when compared to the «Malmkalk» (see also Pomper *et al.*, 2017).

This is supported not only by their slope-forming and cliff-forming nature (see Fig. II-7), respectively, but also by our drill cores: In contrast to the «Malmkalk» , the Wildegg Fm. is occasionally soft or disintegrating (see also Laws & Deplazes, 2007), and in the GST infill its clasts are not preserved, except for individual soft fragments in the lowermost ~0.4 m of QUST. Finally, additional structural weakening of the bedrock below the SB can again not be excluded (see *e.g.* Haldimann *et al.*, 1984, and faults mapped by Matousek *et al.*, 2000).

It should be noted that a potential narrow and steep-walled inner gorge (Dürst Stucki *et al.*, 2012; Jansen *et al.*, 2014; Montgomery & Korup, 2011) inside the GST could possibly not be imaged by our chosen methodology. This is due to the spacing of acquisition points, and due to the HVSR peak widening related to steeply inclined reflectors (Dietiker *et al.*, 2018). The existence of such a gorge can thus not be excluded. Below the trough centre at line A (Figs. II-5, -S2A), the inconclusive log of a (destructively drilled) geothermal probe records unconsolidated sand to a depth slightly below 200 m a.s.l. With regard to our seismic measurements (which are in good accordance with Pietsch & Jordan, 2014), we interpret a singular gravel layer at 245 m a.s.l. as coarse-grained sediment at the base of the Gebenstorf-Stilli Trough, but a significantly deeper trough base is possible at this position.

The morphology of the GST is in strong contrast to the Birrfeld Basin, from which it originates, and which is significantly wider (>3.5 km at 300 m a.s.l.; Figs. II-1, -2) and deeper (<150 m a.s.l.; Pietsch & Jordan, 2014). Aside from the differing dominant bedrock lithologies (Molasse vs. Mesozoic, respectively; Bitterli-Dreher *et al.*, 2007; Jordan, 2010), this is likely a consequence of the position and multiphase origin of the Birrfeld. We suspect that the FJ had a damming effect on the Pleistocene ice advances into the foreland, with ice repeatedly accumulating, basal melt water flow concentrating, and subglacial erosion focusing just south of it (approx. at the local LGM; Bini *et al.,* 2009). As a result, the Birrfeld Basin is composed of several inlaid basin generations (Graf, 2009; Jordan, 2010; Nitsche *et al.,* 2001). The same effect could explain the widening of the terminal Seetal Valley overdeepening below the town of Rupperswil (Fig. II-1; Pietsch & Jordan, 2014).
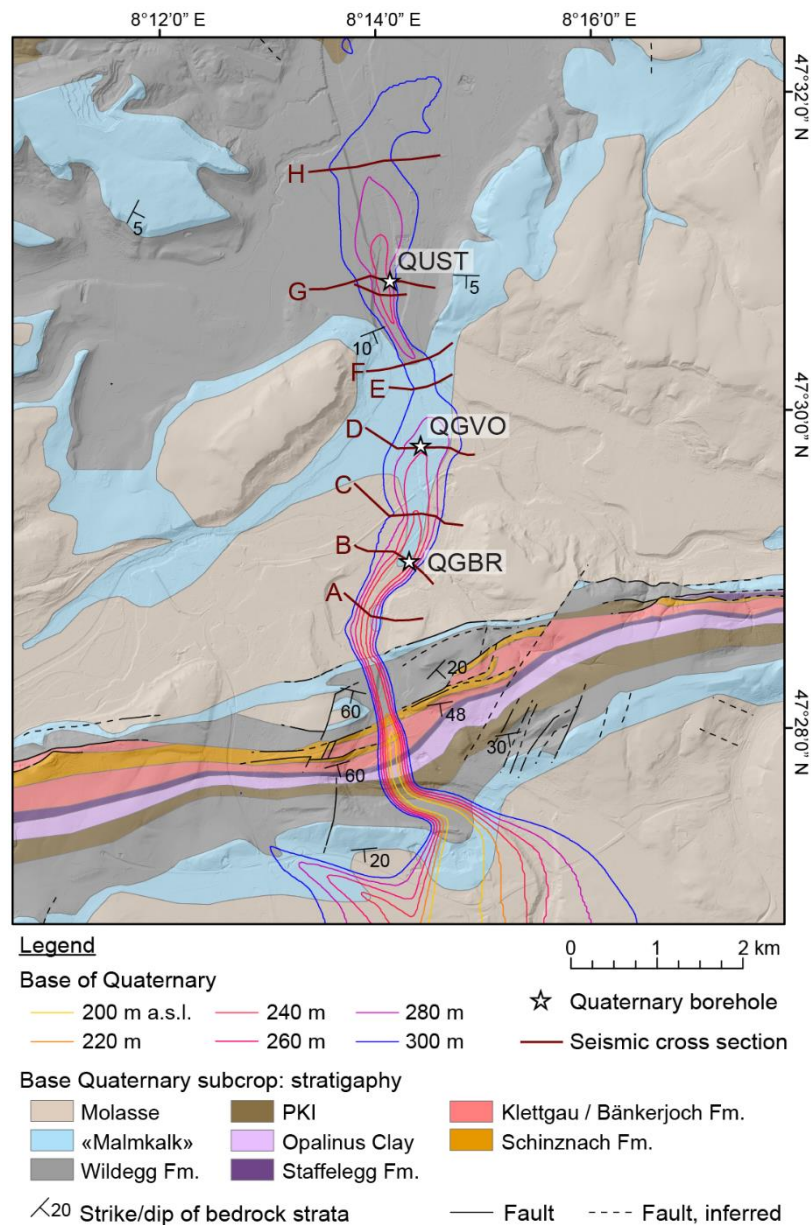
Fig. II-7: Revised elevation model of the Gebenstorf-Stilli Trough (Loepfe *et al.*, in prep.) with underlying bedrock geology, combining surface geological information (Graf *et al.*, 2006) with borehole data.

6.2.2. Mechanisms of overdeepening erosion

Our study reveals that the «Malmkalk» was relatively resistant to the subglacial erosion that excavated the trough (Fig. II-6). We infer this predominantly from the morphology of the GST that shallows abruptly upon reaching the limestone, and deepens again immediately after the limestone is breached.

Although the abundant stylolites and fault planes as well as karst features of the «Malmkalk» should have facilitated glacial erosion *sensu stricto* by quarrying (Dühnforth *et al.*, 2010; Krabbendam and Glasser, 2011), this erosion process was apparently rather inefficient. Relatively low glacial erosion efficiency is further supported by the low percentage of locally derived limestone clasts in the basal coarse-grained trough infill: with exception of the lowermost few decimeters of QGBR and QUST, it is not significantly higher than in the Niederterrasse gravels at the top of the GST infill (Fig. II-4). In addition, the bedrock directly below the base of the GST, even where it is pervaded by paleokarst (Gegg *et al.,* 2020), is generally intact without evidence for glaciotectonic crushing or shearing at the former ice-bed interface (Van der Wateren, 2002). Although the representativity of three boreholes is low, the absence of glaciotectonic structures indicates that ice-bed coupling, and therefore glacial erosivity, was limited at least during the final stage of the GST incision (Hart and Boulton, 1991; Lee and Phillips, 2013). This is a consequence of high basal water pressure at the glacier base (Piotrowski and Tulaczyk, 1999; Fischer and Clarke, 2001; Buechi *et al.*, 2017), of which presumed hydrofractures within the paleokarst in QGBR provide additional record (Gegg *et al.*, 2020).

These observations support the idea that subglacial water played a crucial role during the excavation of the GST. Periodically, basal water flow must have been sufficiently high to strip debris off the glacier bed and evacuate it out of the overdeepening, in order to enable ongoing erosion (Alley *et al.*, 1997, 2019; Cook and Swift, 2012; Buechi *et al.,* 2017). This flushing appears to have been rather efficient, because little basal coarse-grained sediment is preserved in the GST (<10 m in QGBR and QGVO; Fig. II-4), and because large parts of this sediment are gravelly instead of diamictic, *i.e.* have been washed out or reworked. While the terminal (between lines G and H; ~1.6 °) as well as the internal adverse slope of the GST (between lines B and E; ~1.9 °) are comparatively steep (Table II-1), they obviously did not significantly impede the evacuation of water and sediment from the basin (*cf.* Hooke, 1991; Alley *et al.*, 1997; Cook and Swift, 2012). Consequently, much steeper adverse slope sections exist within Swiss foreland overdeepenings (*e.g.* in the Lower Glatt Valley; Buechi *et al.*, 2017; see also Pietsch & Jordan, 2014).

Our findings can be interpreted in order to support the idea that subglacial water was in fact the main driver of erosion of the GST (Dürst Stucki *et al.*, 2010; Fiore *et al.*, 2011; Dürst Stucki and Schlunegger, 2013). This would explain the resilience of the «Malmkalk», as its decimeter- to meter-scale fracture spacing could be too large to allow for plucking by fluid water (Whipple *et al.*, 2000; Sklar and Dietrich, 2001). In contrast, subglacial erosion of sand- and siltstone (Molasse) and marl (Wildegg Fm., Molasse) was far more efficient in the GST (Fig. II-6; Ndiaye *et al.*, 2014). Compared to the Villigen Fm. limestone, the rather poorly lithified Molasse, and likely also the locally soft or disintegrating Wildegg Fm., are more readily eroded grain-by-grain by flowing water. The build-up of elevated pore pressures above impermeable interbeds or above the lower-permeability «Malmkalk», and associated liquefaction (Janszen *et al.*, 2012; Ravier *et al.*, 2015; Wenau and Alves, 2020), may have further enhanced erosion in these softer lithologies.

Whether this presumed subglacial erosion by water occurs predominantly through the long-term steady flow of seasonal melt water (*e.g.* Mooers, 1989) or through catastrophic outburst of subglacial reservoirs ('jökulhlaups'; *e.g.* Shaw, 2002) is subject to debate (Alley *et al.*, 2019). Both models are conceivable in the case of the GST: In the study area, three major regional drainage routeways (Aare, Reuss, Limmat) with a combined present-day catchment area of over 17'500 km^2 collide, capable of delivering vast amounts of meteoric and melt water. Additionally, it is conceivable that outburst events *e.g.* from the Birrfeld Basin could have released short-lived pulses of subglacial water (Fig. II-2B; Gegg *et al.,* 2020).

7. Summary and conclusions

With the aim of better constraining the morphology of the overdeepened Gebenstorf-Stilli Trough (GST), a seismic campaign employing surface wave analysis was conducted. The combined approach of active and passive measurements succeeded at imaging the trough base and, calibrated and complemented with borehole data, allowed us to develop a well-constrained model of the GST (Fig. II-7) that is currently being incorporated into an updated version of the Base of Quaternary model of northern Switzerland by Nagra (Loepfe *et al.*, in prep.). The chosen methodology is therefore a well-suited and cost-effective approach for mapping overdeepened basins.

Our results suggest that the trough morphology is considerably controlled by the underlying bedrock geology. Due to relatively high erosional resistance, resulting high relief and constrained ice flow conditions, the overdeepening is inner-Alpine-like and narrow across the Folded Jura. In contrast, where it transitions into the weaker Molasse deposits further north, the GST becomes wider and more sinuous, similar to other foreland overdeepenings. The trough widening in the Molasse is interpreted as a consequence of less constrained ice flow but likely also of the underlying, more resistant «Malmkalk» (Jurassic limestone) rising towards the north. The trough shallowing culminates in a bedrock ridge whose top lies close to the lowest known Pleistocene base level (*i.e.* in non-overdeepened position). Further north, erosion depth increased again resulting in a second sub-basin. This is due to weaker marls underlying the trough, aided by ice flow being again topographically constrained and possibly increased due to glacier confluence. Thus, we propose that bedrock geology and ensuing topography exert substantial control on subglacial overdeepening erosion. In addition, we suspect that based on borehole data, the morphological complexity of overdeepenings may generally be underestimated.

The different resiliences to subglacial erosion together with a lack of evidence of glaciotectonism as well as the composition of the basal coarse-grained trough infill, which is poor in locally derived material, suggest that both glacial coupling and therefore glacial erosion *sensu stricto*, especially through plucking, was relatively inefficient in the GST. In contrast, the scarcity of well-preserved basal diamict, signs of subglacial hydrofracturing, as well as the paleoglaciological setting in general indicate that availability and pressure of basal water must have been periodically very high. This basal water played a significant role in overdeepening erosion, and we consider possible that it may have been its main driver. This would render the GST and other Alpine foreland overdeepenings analogs of tunnel valleys, as has previously been suggested.

However, it would probably be an oversimplification to attribute any given overdeepening to exclusively glacial or melt water erosion. The subglacial incision process is likely more complex, and the dominant mechanisms time-dependant (*e.g.* glacial erosion during peak glacial conditions, and enlargement by melt water during deglaciation). It should be noted that studies investigating erosion by melt water and its geological controls are restricted to the subaerial environment. The erosive impact of subglacial water on the overdeepened glacier bed is poorly understood, and should be targeted by future work.

8. References

Alley, R., Cuffey, K., Evenson, E., Strasser, J., Lawson, D., Larson, G., 1997. How glaciers entrain and transport basal sediment: physical constraints. Quaternary Science Reviews, 16(9), 1017-1038.

Alley, R., Cuffey, K., Zoet, L., 2019. Glacial erosion: status and outlook. Annals of Glaciology, 1-13.

Augustinus, P.C., 1992. The influence of rock mass strength on glacial valley cross-profile morphometry: A case study from the Southern Alps, New Zealand. Earth Surface Processes and Landforms, 17(1), 39-51.

Becker, R.A., Tikoff, B., Riley, P.R., Iverson, N.R., 2014. Preexisting fractures and the formation of an iconic American landscape: Tuolumne Meadows, Yosemite National Park, USA. GSA Today, 24(11), 4-10.

Berger, J.-P., Reichenbacher, B., Becker, D., Grimm, M., Grimm, K., Picot, L., Storni, A., Pirkenseer, C., Derer, C., Schaefer, A., 2005. Paleogeography of the upper Rhine Graben (URG) and the Swiss Molasse basin (SMB) from Eocene to Pliocene. International Journal of Earth Sciences, 94(4), 697-710.

Bini, A., Buoncristiani, J.F., Couterrand, S., Ellwanger, D., Felber, M., Florineth, D., Graf, H.R., Keller, O., Kelly, M., Schlüchter, C., 2009. Die Schweiz während des letzteiszeitlichen Maximums (LGM) 1:500'000. Bundesamt für Landestopographie swisstopo.

Bitterli-Dreher, P., Graf, H.R., Naef, H., Diebold, P., Matousek, F., Burger, H., Pauli-Gabi, T., 2007. Geologischer Atlas der Schweiz 1:25'000. Blatt 1070 Baden. Erläuterungen. Bundesamt für Landestopografie swisstopo, Wabern, Switzerland.

Brook, M.S., Kirkbride, M.P., Brock, B.W., 2004. Rock strength and development of glacial valley morphology in the Scottish Highlands and northwest Iceland. Geografiska Annaler: Series A, Physical Geography, 86(3), 225-234.

Buechi, M.W., Frank, S.M., Graf, H.R., Menzies, J., Anselmetti, F.S., 2017. Subglacial emplacement of tills and meltwater deposits at the base of overdeepened bedrock troughs. Sedimentology, 64(3), 658-685.

Burkhard, M., 1990. Aspects of the large-scale Miocene deformation in the most external part of the Swiss Alps (sub-Alpine molasse to Jura fold belt). Eclogae Geologicae Helvetiae, 83(3), 559-583.

Cofaigh, C.Ó., 1996. Tunnel valley genesis. Progress in physical geography, 20(1), 1-19.

Cohen, D., Hooyer, T.S., Iverson, N.R., Thomason, J., Jackson, M., 2006. Role of transient water pressure in quarrying: A subglacial experiment using acoustic emissions. Journal of Geophysical Research: Earth Surface, 111, F03006.

Commission for the Geological Map of the World, Asch, K., Bellenberg, S., 2005. The 1:5 million international geological map of Europe and adjacent areas (IGME 5000). Bundesanstalt für Geowissenschaften und Rohstoffe.

Cook, S.J., Swift, D.A., 2012. Subglacial basins: Their origin and importance in glacial systems and landscapes. Earth-Science Reviews, 115(4), 332-372.

Dal Moro, G., Moustafa, S.S., Al-Arifi, N.S., 2018. Improved holistic analysis of Rayleigh waves for single-and multi-offset data: joint inversion of Rayleigh-wave particle motion and vertical-and radial-component velocity spectra. Pure and Applied Geophysics, 175(1), 67-88.

Deplazes, G., Bläsi, H., Schnellmann, M., Traber, D., 2013. Sedimentologie und Stratigraphie der Effinger Schichten. Nagra Arbeitsbericht NAB 13-16.

Diebold, P., Bitterli-Brunner, P., Naef, H., 2006. Geologischer Atlas der Schweis 1:25'000, Blatt 1069/1049 Frick-Laufenburg. Bundesamt für Landestopographie swisstopo, Wabern.

Dietiker, B., Pugin, A.J.-M., Crow, H.L., Mallozzi, S., Brewer, K.D., Cartwright, T.J., Hunter, J.A., 2018. HVSR measurements in complex sedimentary environment and highly structured resonator topography–comparisons with seismic reflection profiles and geophysical borehole logs, Symposium on the Application of Geophysics to Engineering and Environmental Problems 2018, 324-330.

Dühnforth, M., Anderson, R.S., Ward, D., Stock, G.M., 2010. Bedrock fracture control of glacial erosion processes and rates. Geology, 38(5), 423-426.

Dürst Stucki, M., Reber, R., Schlunegger, F., 2010. Subglacial tunnel valleys in the Alpine foreland: an example from Bern, Switzerland. Swiss journal of geosciences, 103(3), 363-374.

Dürst Stucki, M., Schlunegger, F., 2013. Identification of erosional mechanisms during past glaciations based on a bedrock surface model of the central European Alps. Earth and Planetary Science Letters, 384, 57-70.

Dziewonski, A., Bloch, S., Landisman, M., 1969. A technique for the analysis of transient seismic signals. Bulletin of the seismological Society of America, 59(1), 427-444.

Fiore, J., Girardclos, S., Pugin, A., Gorin, G., Wildi, W., 2011. Würmian deglaciation of western Lake Geneva (Switzerland) based on seismic stratigraphy. Quaternary Science Reviews, 30(3-4), 377-393.

Fischer, U.H., Clarke, G.K., 2001. Review of subglacial hydro-mechanical coupling: Trapridge glacier, Yukon Territory, Canada. Quaternary International, 86(1), 29-43.

Gegg, L., Buechi, M.W., Ebert, A., Deplazes, G., Madritsch, H., Anselmetti, F.S., 2020. Brecciation of glacially overridden palaeokarst (Lower Aare Valley, northern Switzerland): result of subglacial water-pressure peaks? Boreas, 49(4), 813–827.

Gegg, L., Kuster, A.M., Amschwand, D., Huber, M., Deplazes, G., Madritsch, H., Buechi, M.W., 2019a. Quaternary Borehole QBO Gebenstorf-Vogelsang (QGVO) Data Report. Nagra Arbeitsbericht NAB 19-03.

Gegg, L., Kuster, A.M., Deplazes, G., Madritsch, H., Buechi, M.W., 2019b. Quaternary Borehole QBO Gebenstorf-Brüel (QGBR) Data Report. Nagra Arbeitsbericht NAB 19-02.

Gegg, L., Kuster, A.M., Schmid, D., Lemke, K., Deplazes, G., Madritsch, H., Buechi, M.W., 2019c. Quaternary Borehole QBO Untersiggenthal (QUST) Data Report. Nagra Arbeitsbericht NAB 19-01.

Glasser, N.F., Crawford, K.R., Hambrey, M.J., Bennett, M.R., Huddart, D., 1998. Lithological and structural controls on the surface wear characteristics of glaciated metamorphic bedrock surfaces: Ossian Sarsfjellet, Svalbard. The Journal of geology, 106(3), 319-330.

Goudie, A.S., 2016. Quantification of rock control in geomorphology. Earth-Science Reviews, 159, 374-387.

Graf, H.R., 2009. Stratigraphie von Mittel-und Spätpleistozän in der Nordschweiz. Beiträge zur Geologischen Karte der Schweiz. Bundesamt für Landestopografie swisstopo, Wabern, Switzerland

Graf, H.R., Bitterli-Dreher, P., Burger, H., Bitterli, T., Diebold, P., Naef, H., 2006. Geologischer Atlas der Schweiz 1:25'000, Blatt 1070 Baden. Bundesamt für Landestopografie swisstopo, Wabern, Switzerland.

Gygi, R.A., 2000. Integrated stratigraphy of the Oxfordian and Kimmeridgian (Late Jurassic) in northern Switzerland and adjacent southern Germany. Birkhäuser, Basel.

Haldimann, P., Naef, H., Schmassmann, H., 1984. Fluviatile Erosions-und Akkumulationsformen als Indizien jungpleistozäner und holozäner Bewegungen in der Nordschweiz und angrenzenden Gebieten. Nagra Technischer Bericht NTB, 84(16).

Hallet, B., 1979. A theoretical model of glacial abrasion. Journal of Glaciology, 23(89), 39-50.

Harbor, J.M., 1995. Development of glacial-valley cross sections under conditions of spatially variable resistance to erosion. Geomorphology, 14(2), 99-107.

Hart, J.K., Boulton, G.S., 1991. The interrelation of glaciotectonic and glaciodepositional processes within the glacial environment. Quaternary Science Reviews, 10(4), 335-350.

Herman, F., Beaud, F., Champagnac, J.-D., Lemieux, J.-M., Sternai, P., 2011. Glacial hydrology and erosion patterns: a mechanism for carving glacial valleys. Earth and Planetary Science Letters, 310(3), 498-508.

Herman, F., Beyssac, O., Brughelli, M., Lane, S.N., Leprince, S., Adatte, T., Lin, J.Y., Avouac, J.-P., Cox, S.C., 2015. Erosion by an Alpine glacier. Science, 350(6257), 193-195.

Hooke, R.L., 1991. Positive feedbacks associated with erosion of glacial cirques and overdeepenings. Geological Society of America Bulletin, 103(8), 1104-1108.

Hooyer, T.S., Cohen, D., Iverson, N.R., 2012. Control of glacial quarrying by bedrock joints. Geomorphology, 153, 91-101.

Jansen, J.D., Codilean, A.T., Stroeven, A.P., Fabel, D., Hättestrand, C., Kleman, J., Harbor, J.M., Heyman, J., Kubik, P.W., Xu, S., 2014. Inner gorges cut by subglacial meltwater during Fennoscandian ice sheet decay. Nature communications, 5(1), 1-7.

Janszen, A., Spaak, M., Moscariello, A., 2012. Effects of the substratum on the formation of glacial tunnel valleys: an example from the Middle Pleistocene of the southern North Sea Basin. Boreas, 41(4), 629-643.

Jordan, P., 2010. Analysis of overdeepened valleys using the digital elevation model of the bedrock surface of Northern Switzerland. Swiss Journal of Geosciences, 103(3), 375-384.

Jordan, P., Eberhard, M., Graf, H.R., Diebold, P., Jost, J., Schurch, R., 2011. Geologischer Atlas der Schweiz 1:25'000, Blatt 1089 Aarau. Bundesamt für Landestopografie swisstopo, Wabern.

Jordan, P., Malz, A., Heuberger, S., Pietsch, J., Kley, J., Madritsch, H., 2015. Regionale geologische Profilschnitte durch die Nordschweiz und 2D-Bilanzierung der Fernschubdeformation im östlichen Faltenjura: Arbeitsbericht zu SGT Etappe 2. Nagra Arbeitsbericht NAB 14-105.

Jordan, P., Wetzel, A., Reisdorf, A., 2008. Swiss Jura Mountains. Pienkowski, G., & Schudack, M.(coordinators). Jurassic. In: McCann, T.(Ed.). The Geology of Central Europe, second ed., 823-923.

Keller, O., Krayss, E., 2010. Mittel-und spätpleistozäne Stratigraphie und Morphogenese in Schlüsselregionen der Nordschweiz. E&G: Quaternary Science Journal, 59(1-2), 88-119.

Krabbendam, M., Glasser, N.F., 2011. Glacial erosion and bedrock properties in NW Scotland: abrasion and plucking, hardness and joint spacing. Geomorphology, 130(3-4), 374-383.

Kühni, A., Pfiffner, O.-A., 2001. The relief of the Swiss Alps and adjacent areas and its relation to lithology and structure: topographic analysis from a 250-m DEM. Geomorphology, 41(4), 285-307.

Laubscher, H.P., 1962. Die Zweiphasenhypothese der Jurafaltung. Eclogae Geologicae Helvetiae, 55, 1-22.

Laws, S., Deplazes, G., Dr. Heinrich Jäckli AG, 2007. Geologie und Hydrogeologie der Effinger Schichten im Tafeljura und am Jurasüdfuss. Nagra Arbeitsbericht NAB 07-28.

Lee, J.R., Phillips, E., 2013. Glacitectonics–a key approach to examining ice dynamics, substrate rheology and ice-bed coupling. Proceedings of the Geologists' Association, 124(5), 731-737.

Loepfe, R., *et al.*, in prep. Digitales Höhenmodell Basis Quartär der Nordschweiz – Version 2021 und ausgewählte Auswertungen. Nagra Arbeitsbericht.

Looser, N., Madritsch, H., Guillong, M., Laurent, O., Wohlwend, S., Bernasconi, S., 2021. Absolute Age and Temperature Constraints on Deformation along the Basal Décollement of the Jura Fold-and-thrust Belt from Carbonate U-Pb Dating and Clumped Isotopes. Tectonics, 40(3), e2020TC006439.

MacGregor, K., Anderson, R., Anderson, S., Waddington, E., 2000. Numerical simulations of glacial-valley longitudinal profile evolution. Geology, 28(11), 1031-1034.

Madritsch, H., 2015. Outcrop-scale fracture systems in the Alpine foreland of central northern Switzerland: Kinematics and tectonic context. Swiss Journal of Geosciences, 108(2-3), 155-181.

Madritsch, H., Meier, B., Kuhn, P., Roth, P., Zingg, O., Heuberger, S., Naef, H., Birkhäuser, P., 2013. Regionale strukturgeologische Zeitinterpretation der Nagra 2D-Seismik 2011/12. Nagra Arbeitsbericht NAB 13-10.

Magrani, F., Valla, P., Gribenski, N., Serra, E., 2020. Glacial overdeepenings in the Swiss Alps and foreland: Spatial distribution and morphometrics. Quaternary Science Reviews, 243, 106483.

Malz, A., Madritsch, H., Kley, J., 2015. Improving 2D seismic interpretation in challenging settings by integration of restoration techniques: A case study from the Jura fold-and-thrust belt (Switzerland). Interpretation, 3(4), SAA37-SAA58.

Matousek, F., Wanner, M., Baumann, A., Graf, H., Nüesch, R., Bitterli, T., 2000. Geologischer Atlas der Schweiz 1:25'000. Blatt 102 Zurzach. Bundesamt für Landestopografie swisstopo, Wabern, Switzerland.

Montgomery, D.R., Korup, O., 2011. Preservation of inner gorges through repeated Alpine glaciations. Nature Geoscience, 4(1), 62-67.

Mooers, H.D., 1989. On the formation of the tunnel valleys of the Superior lobe, central Minnesota. Quaternary Research, 32(1), 24-35.

Nagra, 2019. Preliminary horizon and structure mapping of the Nagra 3D seismics JO-15 (Jura Ost) in time domain. Nagra Arbeitsbericht NAB 18-34.

Nagra, 2021. Morphology of the Overdeepened Gebenstorf-Stilli Trough (Lower Aare Valley) from Seismic Surface Wave Investigations. Nagra Arbeitsbericht NAB 21-18.

Nakamura, Y., 1989. A method for dynamic characteristics estimation of subsurface using microtremor on the ground surface. Railway Technical Research Institute, Quarterly Reports, 30(1), 25-33.

Ndiaye, M., Clerc, N., Gorin, G., Girardclos, S., Fiore, J., 2014. Lake Neuchâtel (Switzerland) seismic stratigraphic record points to the simultaneous Würmian deglaciation of the Rhône Glacier and Jura Ice Cap. Quaternary Science Reviews, 85, 1-19.

Nitsche, F., Monin, G., Marillier, F., Graf, H., Ansorge, J., 2001. Reflection seismic study of Cenozoic sediments in an overdeepened valley of northern Switzerland: the Birrfeld area. Eclogae Geologicae Helvetiae, 94(3), 363-371.

Ohori, M., Nobata, A., Wakamatsu, K., 2002. A comparison of ESAC and FK methods of estimating phase velocity using arbitrarily shaped microtremor arrays. Bulletin of the Seismological Society of America, 92(6), 2323-2332.

Patton, H., Swift, D., Clark, C., Livingstone, S.J., Cook, S.J., 2016. Distribution and characteristics of overdeepenings beneath the Greenland and Antarctic ice sheets: Implications for overdeepening origin and evolution. Quaternary Science Reviews, 148, 128-145.

Pfiffner, O.A., 1986. Evolution of the north Alpine foreland basin in the Central Alps. Special Publications of the International Association of Sedimentologists, 8, 219-228.

Phillips, E., Everest, J., Diaz-Doce, D., 2010. Bedrock controls on subglacial landform distribution and geomorphological processes: Evidence from the Late Devensian Irish Sea Ice Stream. Sedimentary Geology, 232(3-4), 98-118.

Pietsch, J., Jordan, P., 2014. Digitales Höhenmodell Basis Quartär der Nordschweiz - Version 2014 und ausgewählte Auswertungen. Nagra Arbeitsbericht NAB 14-02.

Piotrowski, J.A., Tulaczyk, S., 1999. Subglacial conditions under the last ice sheet in northwest Germany: ice-bed separation and enhanced basal sliding? Quaternary Science Reviews, 18(6), 737-751.

Pomper, J., Salcher, B.C., Eichkitz, C., Prasicek, G., Lang, A., Lindner, M., Götz, J., 2017. The glacially overdeepened trough of the Salzach Valley, Austria: Bedrock geometry and sedimentary fill of a major Alpine subglacial basin. Geomorphology, 295, 147-158.

Preusser, F., Graf, H.R., Keller, O., Krayss, E., Schlüchter, C., 2011. Quaternary glaciation history of northern Switzerland. E&G Quaternary Science Journal, 60, 282-305.

Preusser, F., Reitner, J.M., Schlüchter, C., 2010. Distribution, geometry, age and origin of overdeepened valleys and basins in the Alps and their foreland. Swiss Journal of Geosciences, 103(3), 407-426.

Ravier, E., Buoncristiani, J.-F., Menzies, J., Guiraud, M., Clerc, S., Portier, E., 2015. Does porewater or meltwater control tunnel valley genesis? Case studies from the Hirnantian of Morocco. Palaeogeography, Palaeoclimatology, Palaeoecology, 418, 359-376.

SESAME European research project, 2004. Guidelines for the implementation of the H/V spectral ratio technique on ambient vibrations measurements, processing and interpretation, European Commission.

Shaw, J., 2002. The meltwater hypothesis for subglacial bedforms. Quaternary International, 90(1), 5-22.

Sklar, L.S., Dietrich, W.E., 2001. Sediment and rock strength controls on river incision into bedrock. Geology, 29(12), 1087-1090.

Sprecher, C., Müller, W., 1986. Geophysikalisches Untersuchungsprogramm Nordschweiz: Reflexionsseismik 82. Nagra Technischer Bericht NTB 84-15.

Stumm, D., 2010. Deep glacial erosion. Review with focus on tunnel valleys in northern Europe. Nagra Arbeitsbericht NAB 10-33.

Swisstopo, 2013. swissALTI3D. Federal Office of Topography swisstopo Wabern, Switzerland.

Terzaghi, R.D., 1965. Sources of error in joint surveys. Geotechnique, 15(3), 287-304.

Van der Vegt, P., Janszen, A., Moscariello, A., 2012. Tunnel valleys: current knowledge and future perspectives. Geological Society, London, Special Publications, 368(1), 75-97.

Van der Wateren, D.M., 2002. Processes of glaciotectonism, Modern and Past Glacial Environments. Elsevier, 417-443.

Wenau, S., Alves, T.M., 2020. Salt-induced crestal faults control the formation of Quaternary tunnel valleys in the southern North Sea. Boreas 49(4), 799-812.

Whipple, K.X., Hancock, G.S., Anderson, R.S., 2000. River incision into bedrock: Mechanics and relative efficacy of plucking, abrasion, and cavitation. Geological Society of America Bulletin, 112(3), 490-503.

Wiemer, S., Danciu, L., Edwards, B., Marti, M., Fäh, D., Hiemer, S., Wössner, J., Cauzzi, C., Kästli, P., Kremer, K., 2016. Seismic hazard model 2015 for Switzerland (SUIhaz2015). Swiss Seismological Service, ETH, Zurich, Switzerland.

Yanites, B.J., Becker, J.K., Madritsch, H., Schnellmann, M., Ehlers, T.A., 2017. Lithologic effects on landscape response to base level changes: A modeling study in the context of the Eastern Jura Mountains, Switzerland. Journal of Geophysical Research: Earth Surface, 122(11), 2196-2222.

Ziegler, P.A., Fraefel, M., 2009. Response of drainage systems to Neogene evolution of the Jura fold-thrust belt and Upper Rhine Graben. Swiss journal of geosciences, 102(1), 57-75.

Zimmer, P.D., Gabet, E.J., 2018. Assessing glacial modification of bedrock valleys using a novel approach. Geomorphology, 318, 336-347.

Zoet, L., Alley, R.B., Anandakrishnan, S., Christianson, K., 2013. Accelerated subglacial erosion in response to stick-slip motion. Geology, 41(2), 159-162.

9. Supplementary material

Supplement 1: Summary scheme of the pre-Quaternary stratigraphy of the study area (Fig. II-S1).

Supplement 2: Cross sections A to H, input data and interpretations (Fig. II-S2, A-H). Differences between seismic and drilled trough depth (Table II-S2).

Supplement 3: Sinuosities of distal foreland overdeepenings of Switzerland (Fig. II-S3).

Supplement 4: Structural survey of a major strike-slip fault in a «Malmkalk» outcrop (Fig. II-S4).
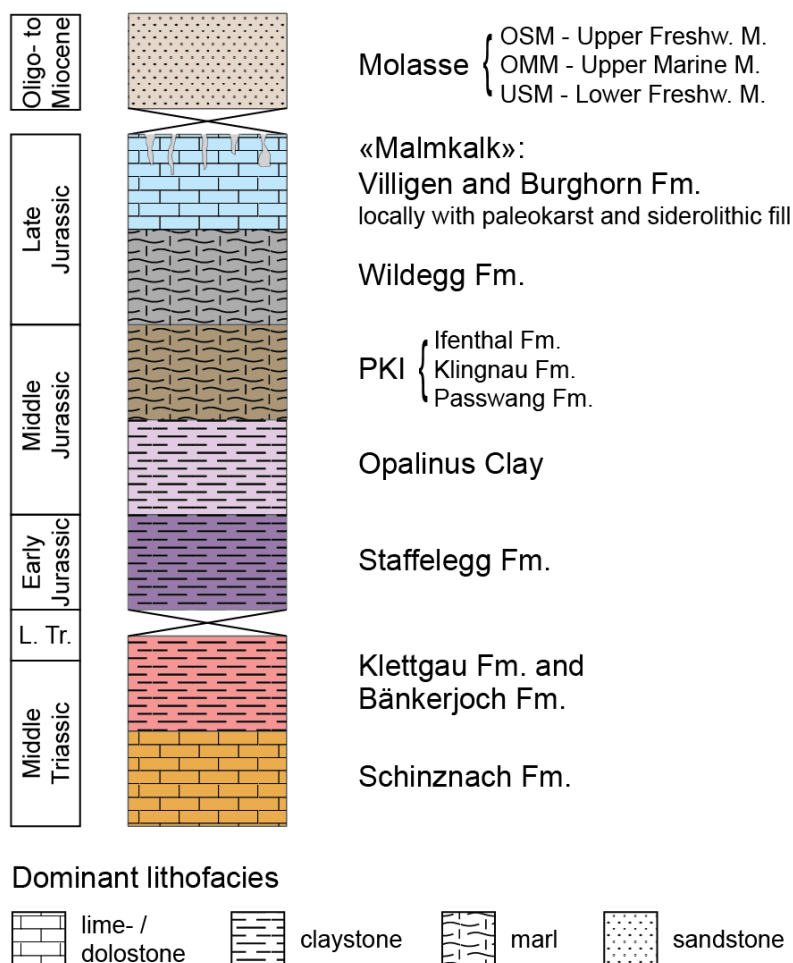
Fig. II-S1: Summary scheme of the pre-Quaternary stratigraphy of the study area.
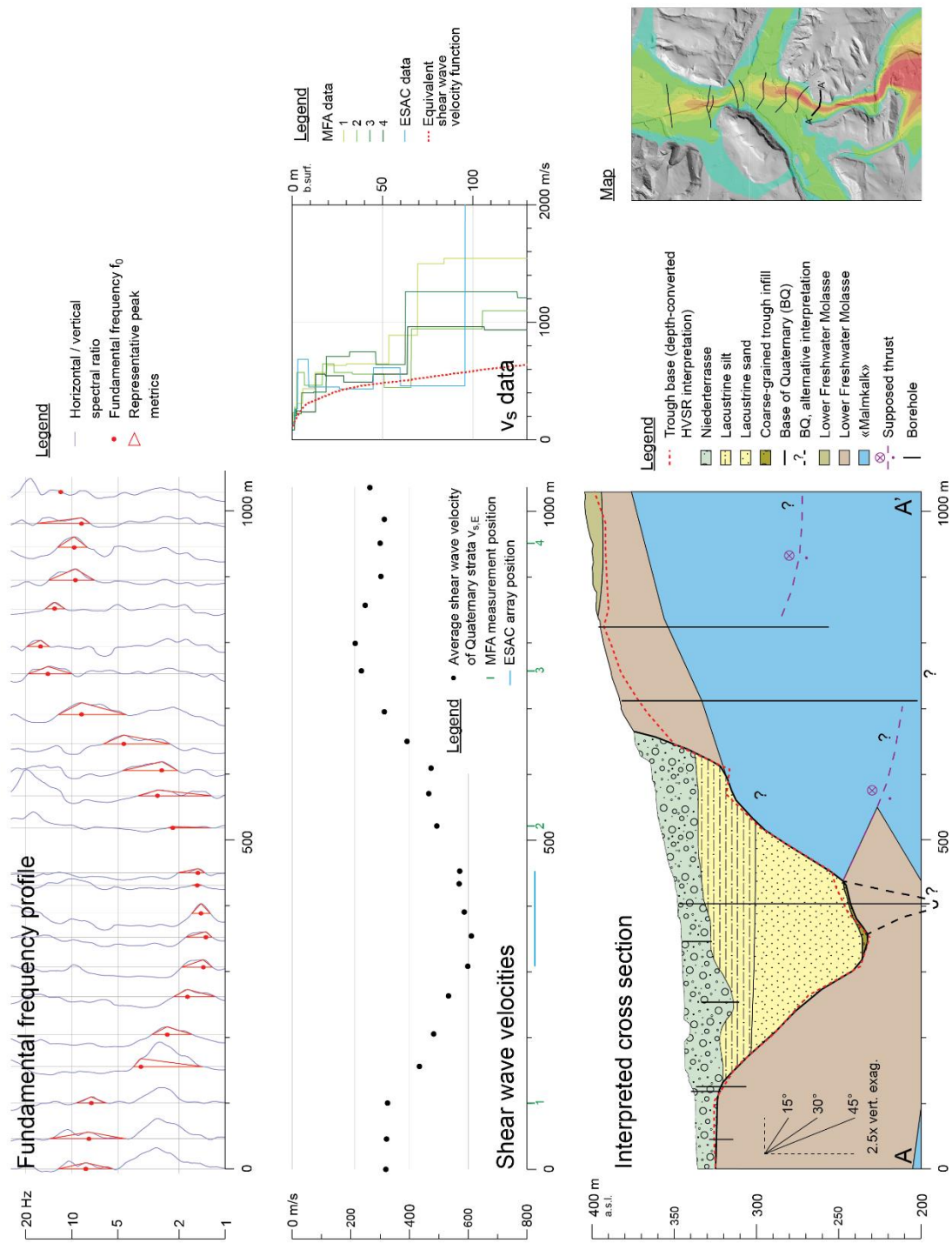
Fig. II-S2A: Cross section A, input data and interpretation.
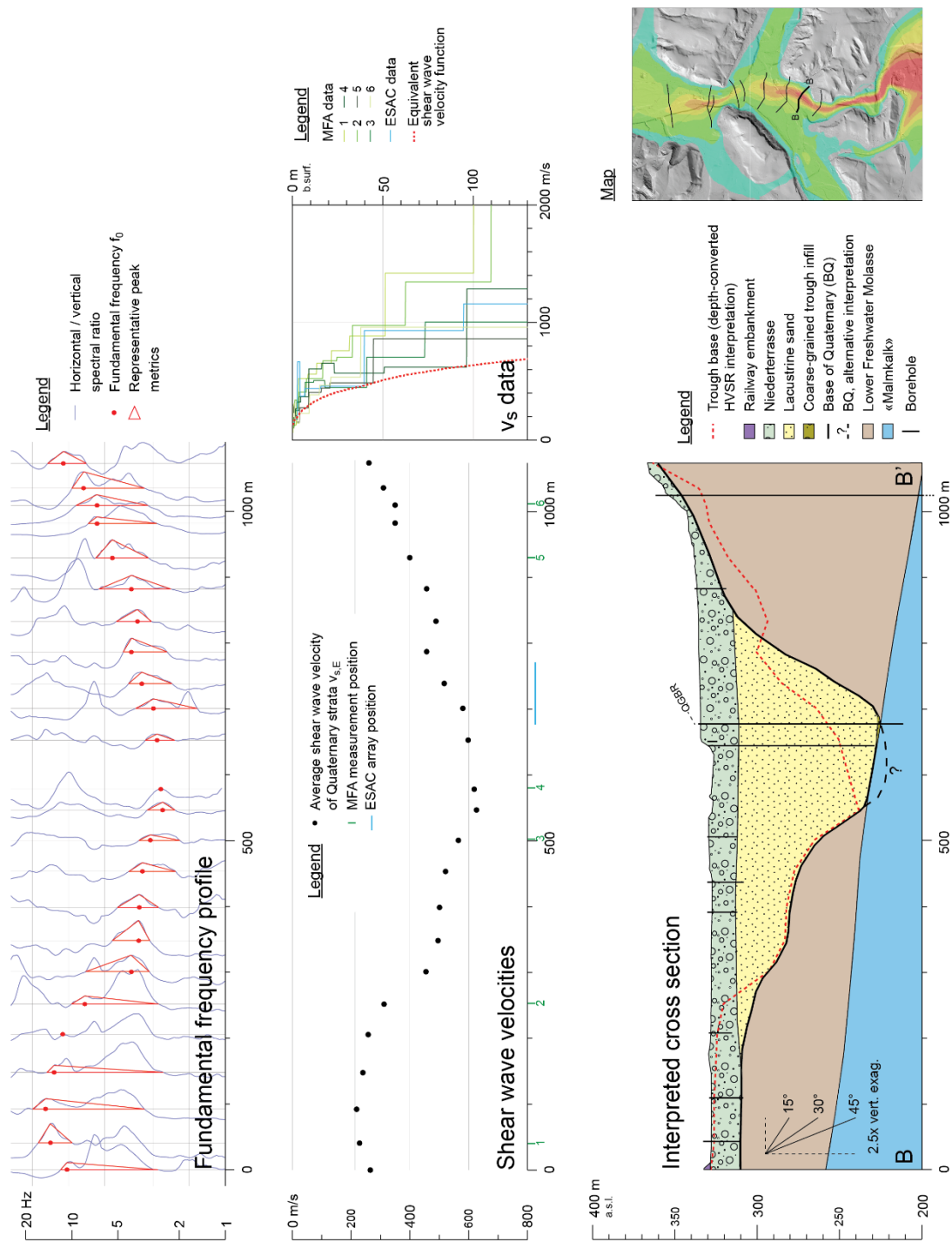
Fig. II-S2B: Cross section B, input data and interpretation.
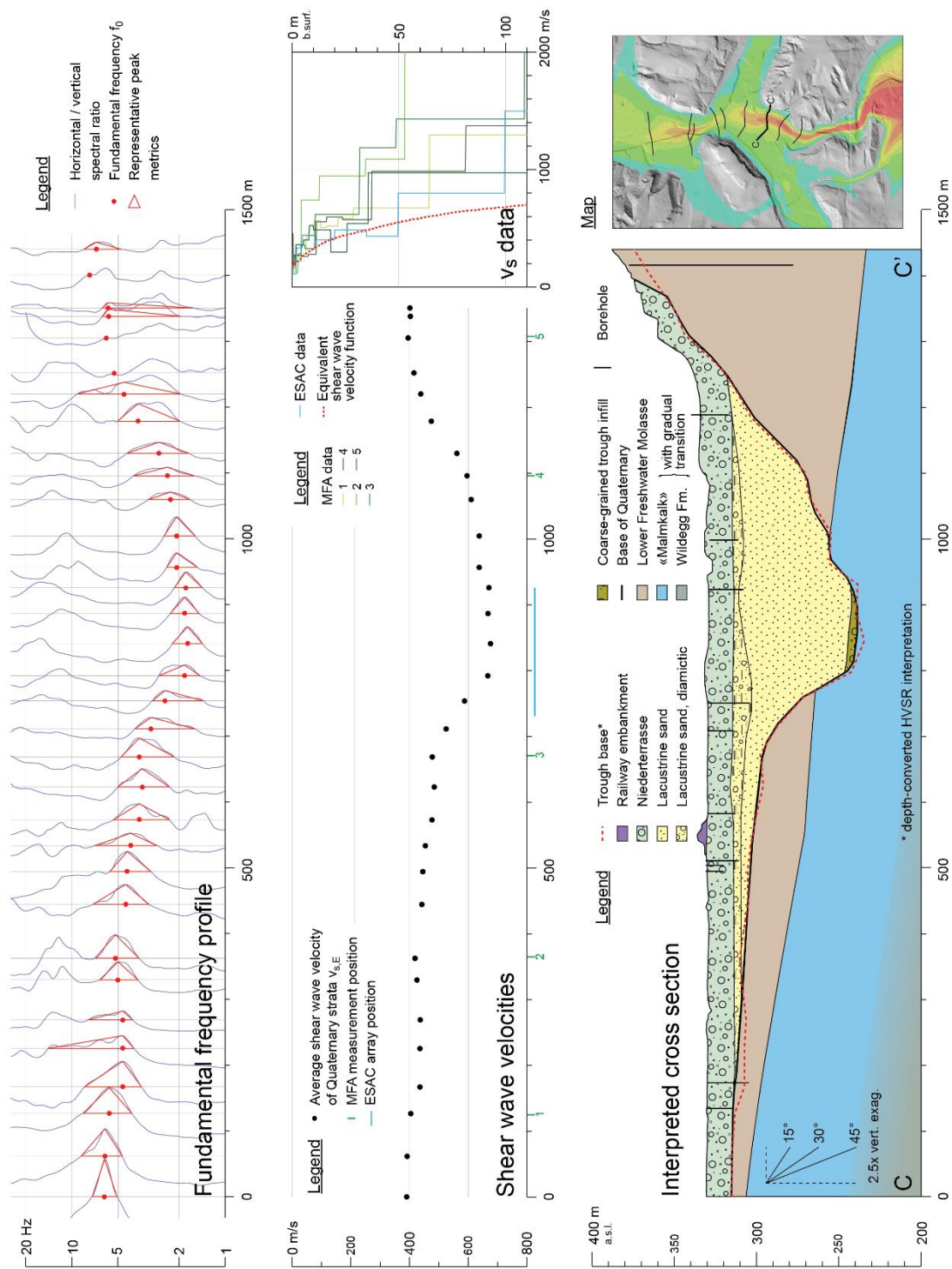
Fig. II-S2C: Cross section C, input data and interpretation.
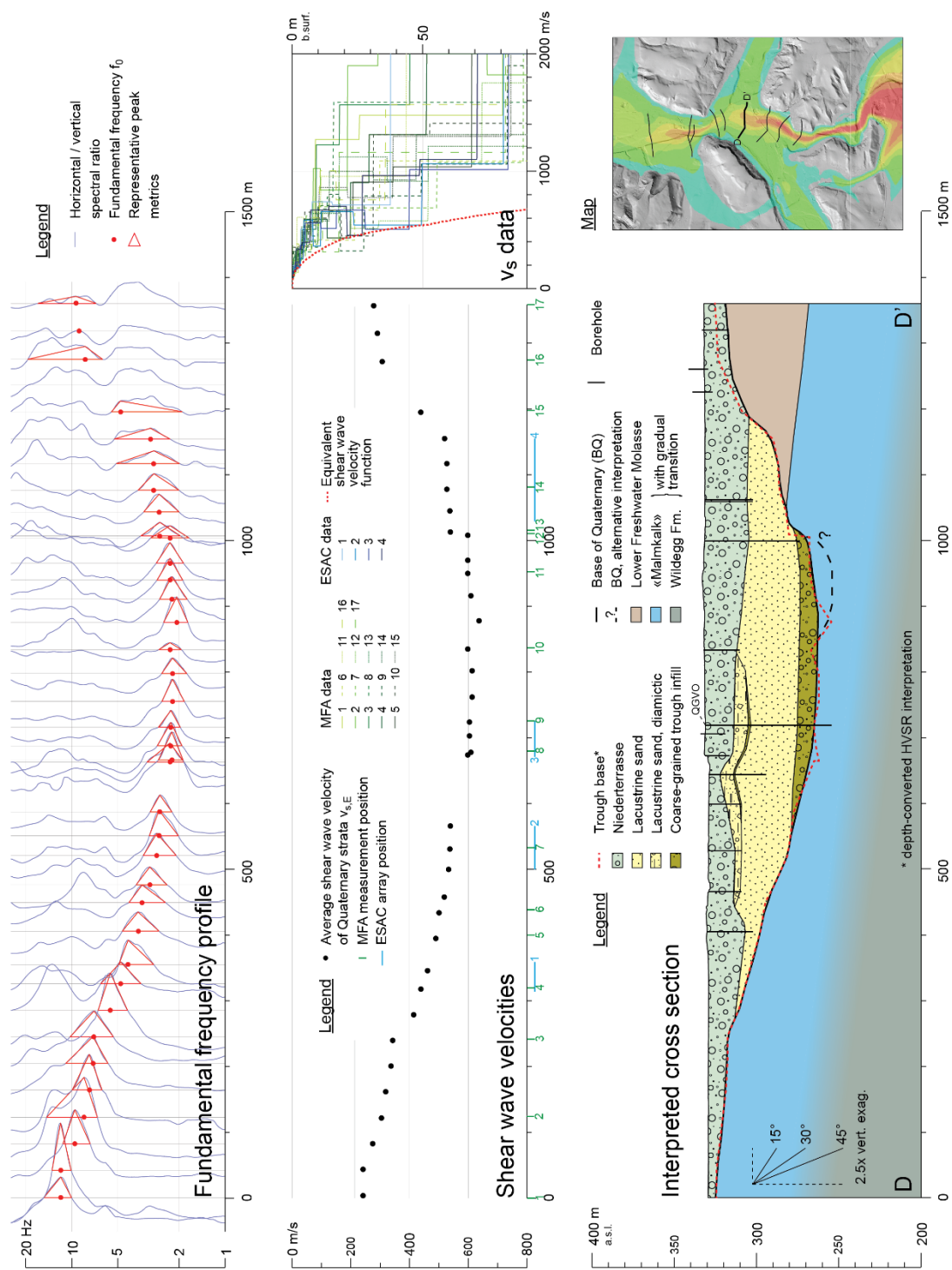
Fig. II-S2D: Cross section D, input data and interpretation.
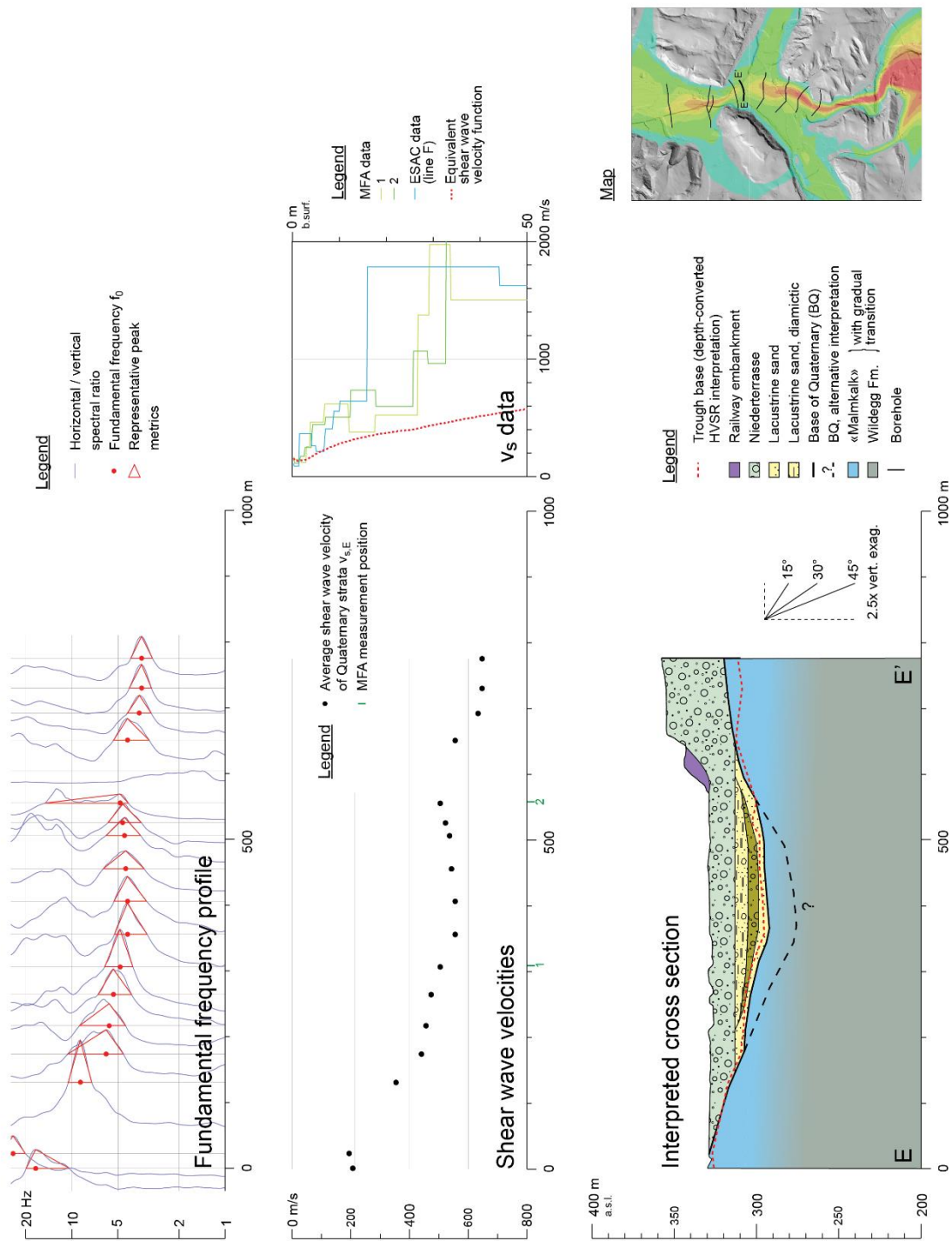
Fig. II-S2E: Cross section E, input data and interpretation.
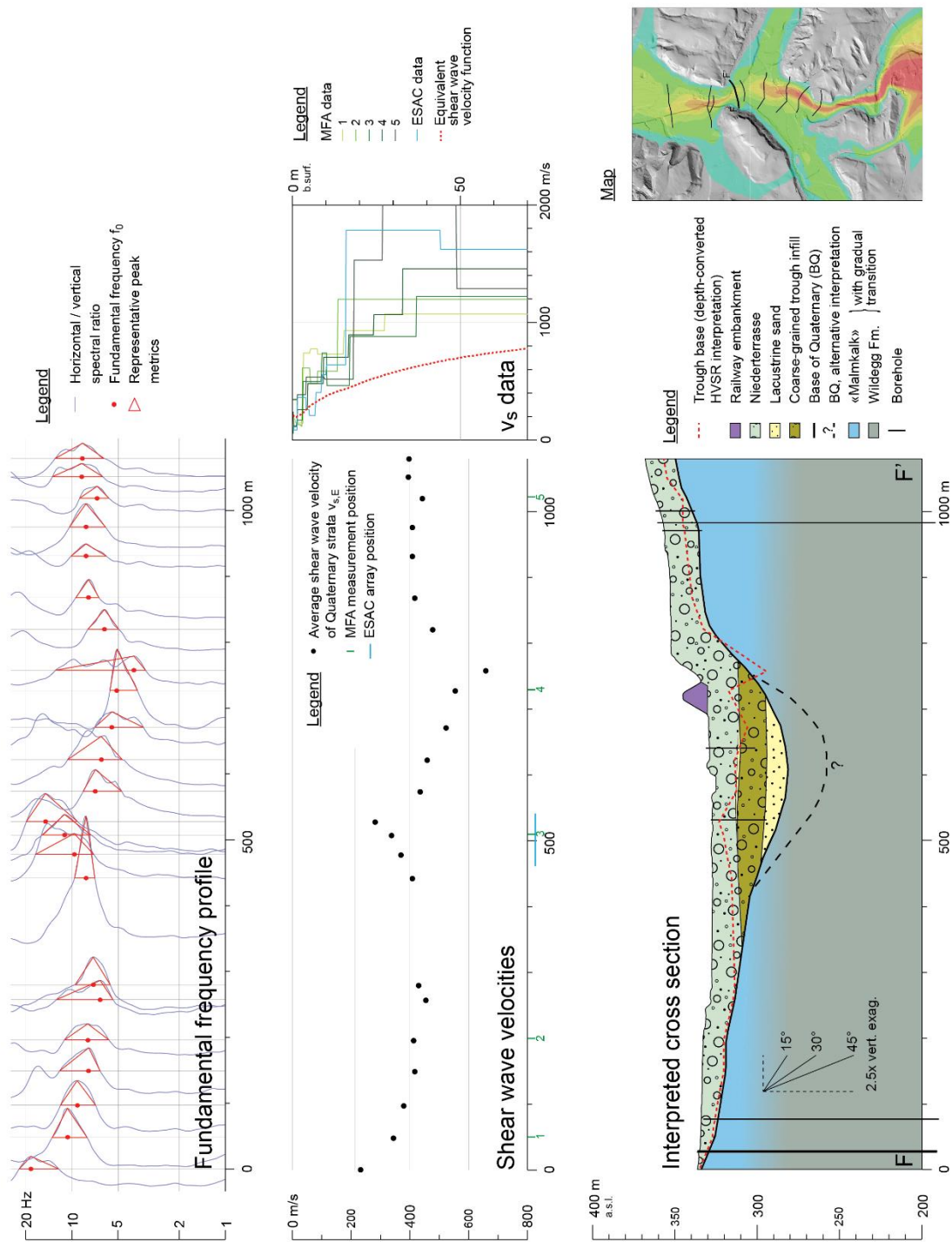
Fig. II-S2F: Cross section F, input data and interpretation.
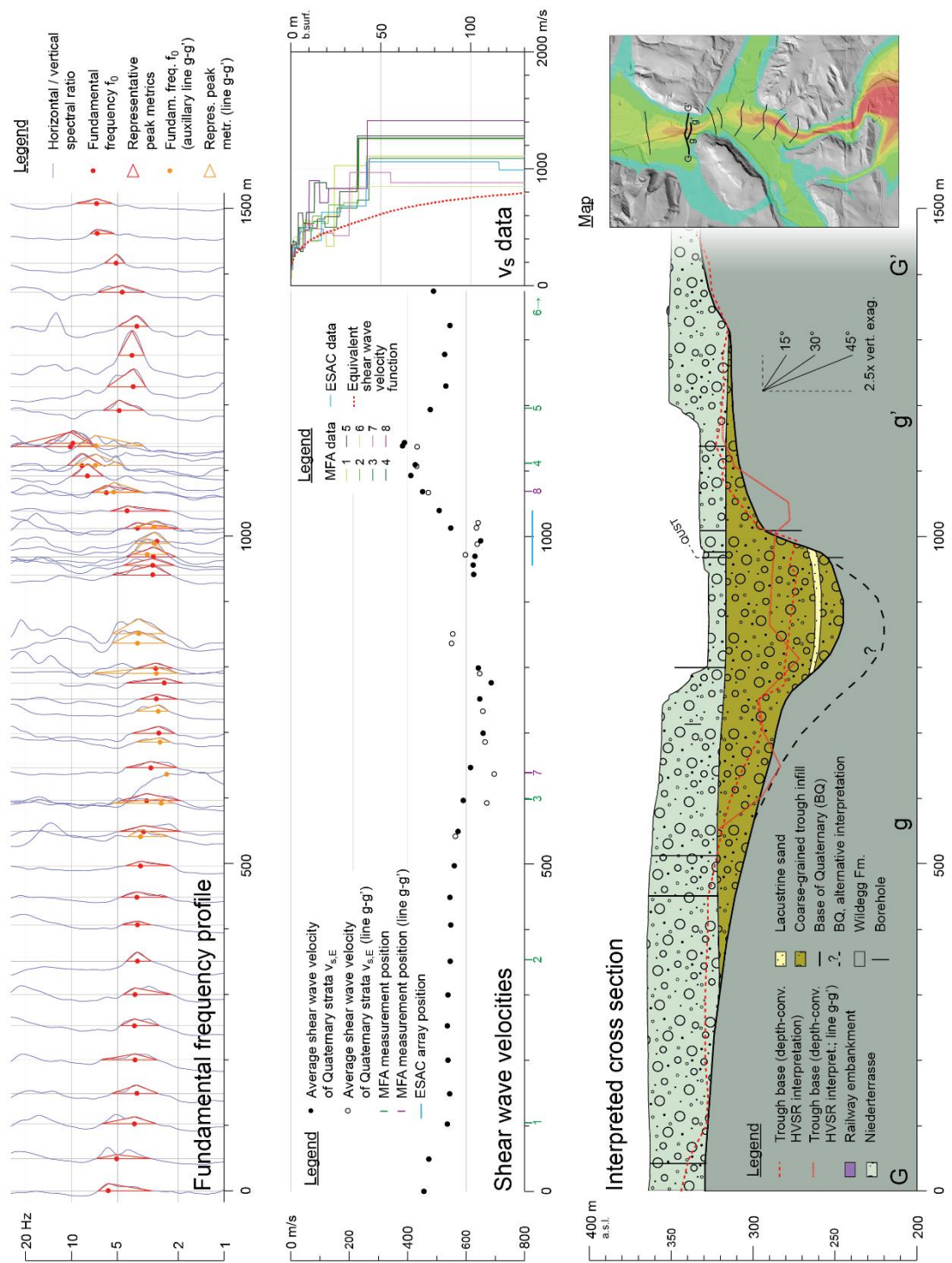
Fig. II-S2G: Cross section G, input data and interpretation.

83
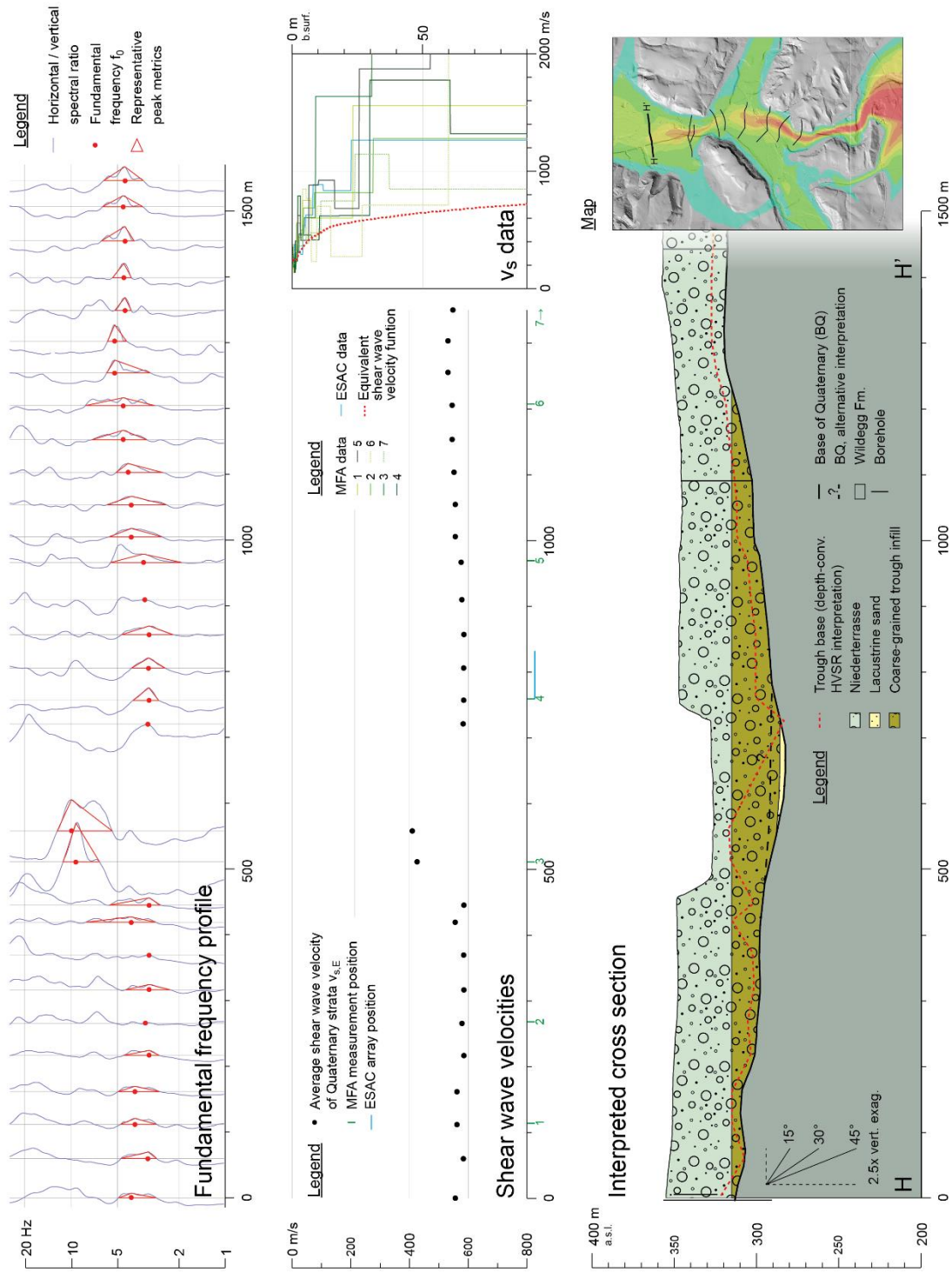
Fig. II-S2H: Cross section H, input data and interpretation.

Table II-S2: Differences between seismic and drilled base of Quaternary (BQu) along the Gebenstorf-Stilli Trough based on drill logs from the borehole database of Nagra. Drilled values are marked with (?) if they are taken from logs that do not specifically identify the underlying bedrock, but the described lithology suggests its interpretation.

| Sect. | Borehole type | Distance [m] | BQu [m a.s.l.] | | Diff. [m] |
			seismic	borehole	
A	Exploration borehole	170	325.9	316.0	9.9
A	Geothermal probe	0	322.3	322.8	-0.5
A	Geothermal probe	65	246.0	244.0 (?)	2.0
A	Geothermal probe	0	373.3	377.0	-3.7
A	Geothermal probe	0	393.3	377.0	16.3
B	Exploration borehole	20	392.5	398.0	-5.5
B	Geothermal probe	35	326.3	313.2	13.1
B	Exploration borehole	0	326.5	311.8	14.7
B	Exploration borehole	55	324.7	316.4	8.3
B	Scientific borehole QGBR	0	257.4	225.8	31.6
B	Exploration borehole	90	301.9	323.5	-21.6
B	Geothermal probe	55	335.1	349.0	-13.9
C	Exploration borehole	40	311.3	315.2	-3.9
C	Exploration borehole	85	307.1	312.7 (?)	-5.6
C	Geothermal probe	20	369.1	362.0	7.1
D	Scientific borehole QGVO	30	264.1	266.1	-2.0
D	Exploration borehole	0	324.0	317.7	6.3
E	Exploration borehole	50	311.9	319.9	-8.0
F	Geothermal probe	30	332.1	331.0	1.1
F	Geothermal probe	70	331.2	326.0	5.2
F	Geothermal probe	90	327.0	314.0	13.0
F	Exploration borehole	30	345.4	338.6	6.8
F	Geothermal probe	70	344.7	336.0	8.7
F	Exploration borehole	25	345.4	342.5	2.9
G	Exploration borehole	35	341.0	330.1	10.9
G	Exploration borehole	160	326.6	310.7 (?)	15.9
G	Exploration borehole	25	323.2	305.1 (?)	18.1
G	Scientific borehole QUST	0	276.0	255.2	20.8
G	Scientific boreh. (seism. survey)	155	296.4	291.0	3.4
G	Exploration borehole	140	321.6	312.2	9.4
H	Scientific boreh. (seism. survey)	25	321.0	315.3	5.7
H	Exploration borehole	175	320.4	324.0 (?)	3.6
H	Exploration borehole	0	326.6	318.2 (?)	8.4
average					-7.2/+9.8
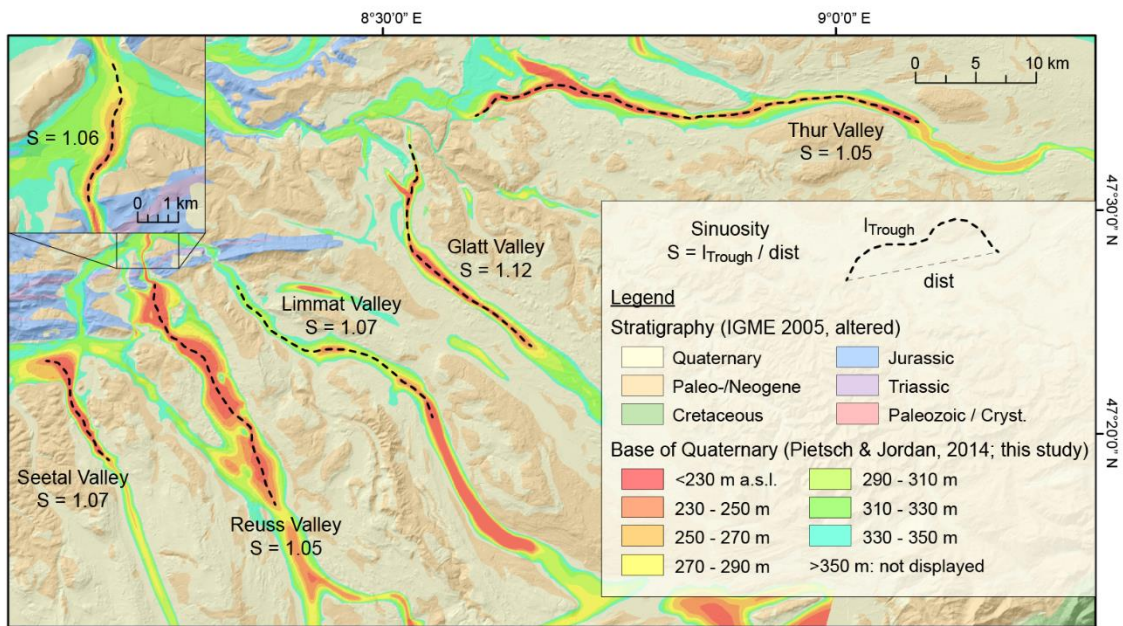
Fig. II-S3: Sinuosities of major distal foreland overdeepenings of Switzerland. Note that the sinuosity of the central GST segment (zoom-in; S = 1.06) is similar to other Molasse-hosted overdeepenings.
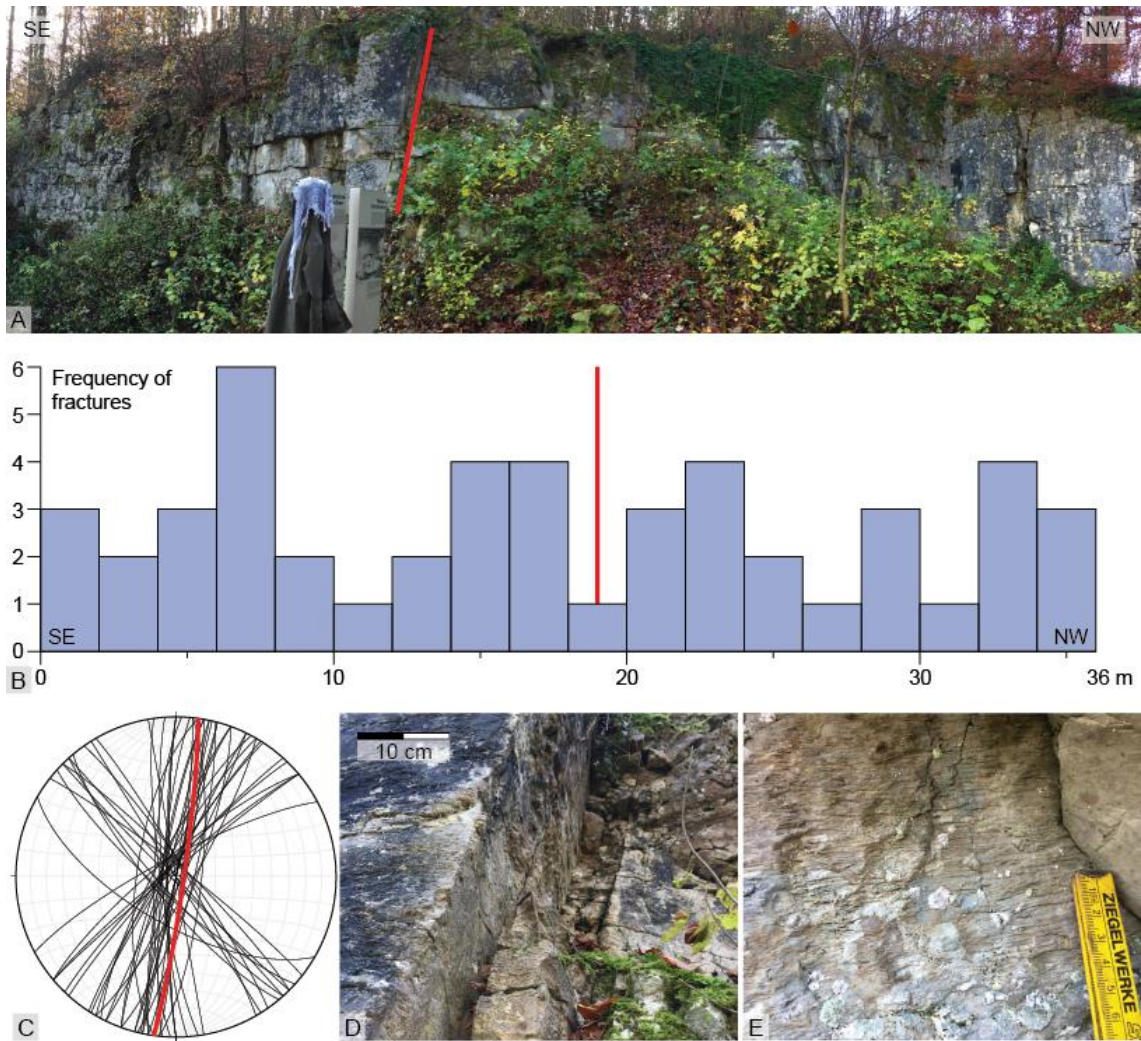
Fig. II-S4: Structural survey of a «Malmkalk» outcrop (notheastern slope of Scherzberg; 47°26′43″ N, 8°10′40″ E) exposing a major strike-slip fault (red line on A; panoramic photograph not to scale with B). We observe no increased frequency of (striated) fractures in vicinity of the fault at 19 m along the outcrop wall (B). Two groups of fractures occur, one with orientations similar to the major fault (100/85, red line), one with orientations of ~230/80 (C). D: Zoom-in on the core of the fault. E: Zoom-in on striated fracture plane (ruler is in centimetres).

This page is intentionally left blank.

Glacially overridden karstified limestone at The Burren (County Clare, Ireland).

III. A closer look into the subglacial environment

This chapter presents brecciation features in karstified limestone underlying the overdeepened Gebenstorf-Stilli Trough. These brecciation features and their sedimentary infill are examined in detail, and interpreted as products of subglacial hydrofracturing, thus providing an insight into the hydrological conditions at the glacier bed. The manuscript has been published in Boreas 49/4 as

Gegg, L.[1], Buechi, M. W.[1], Ebert, A.[2], Deplazes, G.[3], Madritsch, H.[3], and Anselmetti, F. S.[1], 2020, Brecciation of glacially overridden palaeokarst (Lower Aare Valley, northern Switzerland): result of subglacial water-pressure peaks? (DOI 10.1111/bor.12457).

[1] Institute of Geological Sciences and Oeschger Centre for Climate Change Research, University of Bern, Baltzerstrasse 1+3, 3012 Bern, Switzerland

[2] Geo Explorers AG, Wasserturmplatz 1, 4410 Liestal, Switzerland

[3] National Cooperative for the Disposal of Radioactive Waste (Nagra), Hardstrasse 73, 5430 Wettingen, Switzerland

1. Abstract

Water pressures at the base of active glacial overdeepenings are known to fluctuate strongly on various timescales. Rapid peaks in basal water pressure can lead to fracturing of the glacier bed, a process that has been described at numerous sites around the world, mostly based on large hydrofracture systems. This article presents drill cores from the base of a >100 m deep glacial overdeepening in the Lower Aare Valley in northern Switzerland that were investigated with high-resolution imaging (including X-ray computed tomography) as well as compositional and microstructural analysis. The drill cores recovered Jurassic limestones hosting palaeokarst voids infilled with blue clay. We identify this clay, based on its kaolinitic composition, as siderolithic Bolus Clay but in a rather atypical variety formed under reducing conditions. The surfaces of the palaeokarst walls show smoothly undulating as well as brecciated sections with form-fit interlocking clasts, which are the result of an *in situ* brecciation process. We discuss the origin of these particular fractures and argue that they are not related to (glacio-)tectonics or frost action. Instead, we favour an explanation by water pressure peaks that were transmitted to the void walls by the clayey karst filling, resulting in hydrofracturing. In addition to pervasive karstification and tectonic overprinting, this water pressure-driven fracturing may have assisted the deep incision of the overdeepening into the rheologically competent bedrock.

2. Introduction

A common feature of regions currently or previously covered by ice masses are glacial overdeepenings (Linton, 1963; Preusser *et al.* 2010; Patton *et al.* 2016). These are troughs eroded deeply into the substratum by debris-laden ice and water, often several hundred metres below the surface and the local base level. They are confined at all sides, with an adverse distal slope as a distinct characteristic and therefore have strong implications for the drainage system of an overlying glacier, allowing for diverse water pathways, subglacial ponding of large water volumes and possibly partial floatation of the glacier (Cook & Swift 2012). Consequently, basal water pressures can fluctuate strongly and rapidly with peak values reaching multiples of the local ice overburden pressure (Kavanaugh & Clarke 2000; Cook *et al.* 2006; Cook & Swift 2012). Ultimately, abrupt pressure peaks can result in rupturing of the glacier bed by subglacial hydrofracturing. Such processes have been identified and described in presently and previously glaciated areas around the world (Larsen & Mangerud 1992; van der Meer *et al.* 2009), including examples dating back to the Paleozoic (Ravier *et al.* 2014). Subglacial hydrofracturing is most frequently recognised in glacial sediments; examples in solid bedrock exist but have only rarely been described (Meehan *et al.* 1997; Lloyd Davies 2004; Phillips *et al.* 2013). Due to its higher tensile strength, fracturing of bedrock requires water pressures significantly higher than those needed for fracturing of unconsolidated sediment (Phillips 1972; Cosgrove 1995; Broughton 2018), and thus its record provides an insight into extreme conditions at the glacier base.

This study presents surficial brecciation features encountered in the void walls of a sediment-filled palaeokarst from the Lower Aare Valley in the Swiss Alpine foreland. Based on high-resolution imaging together with compositional and microstructural data, we discuss the origin of the observed structures and argue that they are possibly the result of peaks in subglacial water pressure.

3. Study area

Our study area is located in northern Switzerland, at the eastern margin of the WSW-ENE trending Jura mountains subdivided into the Jura fold-and-thrust belt and the northward adjacent Tabular Jura (Fig. III-1). Situated about 50 km northwest of the Alpine front, the Jura mountains are built up by Mesozoic sediments deposited on an epicontinental platform. In the study area, a diverse succession of carbonates, marls and siliciclastics dating from Triassic to Jurassic is exposed, with Upper Jurassic rocks (Malm) prevailing at the surface (Bitterli *et al.* 2000; Bitterli-Dreher *et al.* 2007): These are grey calcareous marl and limestone sequences of the Wildegg Fm. and overlying light-coloured micritic limestones of the Villigen Fm. In the Early Paleogene, the study area was uplifted on the forebulge of the approaching Alpine orogeny, which led to erosion and karstification of the Mesozoic carbonate plateau, while further south the Molasse Basin formed (Pfiffner 1986; Burkhard & Sommaruga 1998; Bitterli-Dreher *et al.* 2007). Karstification occurred mostly during Eocene times, when subtropical climate conditions prevailed and siderolithic deposits (formerly Bohnerz Fm.) developed from soil and limestone dissolution residues – a process that locally continued until the Miocene (Baumberger 1923; Hofmann 1991; Hofmann *et al.* 2017). These deposits consist of kaolinitic clay frequently referred to as "Bolus Clay" and may contain iron pisoliths and quartz sand (Baumberger 1923; Hofmann 1967). In Oligocene-Miocene times, Molasse sediments started to accumulate in the study area, with fine- to coarse grained clastics of the Lower Freshwater, Upper Marine, and Upper Freshwater Molasse (Berger *et al.* 2005; Bitterli-Dreher *et al.* 2007). The deposition ended in Late Miocene when the Jura fold-and-thrust belt was formed by thin-skinned deformation above an evaporitic decollement horizon (Laubscher 1962; Burkhard 1990).

Fig. III-1. Map of the study area displaying the position of the drillsite QGBR (47.4832° N, 8.2364° E), LGM ice extent, surface geology (simplified), and the position of the Gebenstorf-Stilli Trough as marked by thick Quaternary sediments. The inset on the left shows the regional geological context and the red rectangle indicates the study area at the eastern end of the Jura mountains.

During the Pleistocene, the study area was affected by a number of advances of Alpine glaciers (Graf 2009; Preusser *et al.* 2011). At the confluence area of the rivers Aare, Reuss and Limmat, the elongated Gebenstorf-Stilli Trough formed, a finger-like glacial overdeepening extending northward from the bowl-shaped Birrfeld Basin (Bitterli-Dreher *et al.* 2007; Fig. III-1). This 10 km-long trough has been incised into the Jura mountains by subglacial erosion, and reaches a depth of ~100 m below surface or 80 m below the lowest Pleistocene base level (300 m a.s.l.; Graf 2009). The overdeepened part of the trough below this base level does not exceed 800 m in width (Pietsch & Jordan 2014). The contrast in cross-section from the wide Birrfeld Basin in the south (Nitsche *et al.* 2001) towards the steeper and narrower Gebenstorf-Stilli Trough in the north is interpreted as a result of changing bedrock lithology from rather soft, poorly lithified Molasse sandstones towards the more resistant limestones and marls of the Jura mountains (Bitterli-Dreher *et al.* 2007). The Gebenstorf-Stilli Trough lies outside the local LGM glacier extent and was presumably eroded during the late Middle Pleistocene (Bitterli-Dreher *et al.* 2007; Graf, 2009). Today, the trough is infilled with sediment.

Erosive glacial overdeepening below the local base level requires that the adverse slope of the overdeepened basin does not exceed 1.2-1.7 the ice surface slope, as otherwise the ascending water will freeze and prevent flushing of the eroded material from the overdeepening (Hooke, 1991; Alley *et al.* 1997; Cook & Swift 2012). Hence the glacier ice must have towered considerably above the ground surface during the Gebenstorf-Stilli Trough formation, with more than 150 m of ice overlying the bedrock at the study site. The most elevated glacial deposits in the study area lie ~600 m a.s.l. (Graf *et al.* 2006; Bitterli-Dreher *et al.* 2007), corresponding to a maximum ice thickness of more than 350 m above the base of the Gebenstorf-Stilli Trough. The position of the study site, 18 km inward from the ice margin during the most extensive Möhlin Glaciation (Keller & Krayss 2010; Preusser *et al.* 2011), allows for an alternative estimation. LGM ice surface reconstructions give an average glacier thickness of ~350 m at the corresponding position (Jäckli 1970; Keller & Krayss 1993; Bini *et al.* 2009), suggesting a maximum possible ice thickness of ~450 m above the bottom of the Gebenstorf-Stilli Trough during the Pleistocene.

4. Methods

4.1. Core recovery and initial description

The borehole QGBR (Gegg *et al.* 2019) is located in the southern part of the Gebenstorf-Stilli Trough on the eastern bank of the river Reuss (47.4832° N, 8.2364° E; Fig. III-1). It was drilled in summer 2018 in context of the Quaternary investigation program of the Swiss National Cooperative for the Disposal of Radioactive Waste (Nagra). Target of this borehole was the infill of the glacially overdeepened Gebenstorf-Stilli Trough as well as the uppermost ~10 m of the bedrock. The 10 cm diameter bedrock cores, focus of this study, were drilled by wireline using a triple-tube core barrel where the core is protected by a plastic liner. A borehole geophysical survey recorded natural gamma ray measurements and an acoustic borehole image.

The cores were analysed at the Institute of Geological Sciences, University of Bern (IfG, UniBe) with a Geotek multi-sensor core logger (MSCL), which recorded bulk density by gamma attenuation, p-wave velocity and magnetic susceptibility in a 5 mm depth-resolution. X-ray computed tomography (CT) scans were acquired at the Institute of Forensic Medicine of UniBe and visualised using the freeware programs 3D Slicer (www.slicer.org; Kikinis *et al.* 2014) and ImageVIS 3D (www.sci.utah.edu/software/imagevis3d; Fogal & Krüger 2010). Detailed lithological and structural descriptions were carried out, including high-resolution core photography recorded with a line-scan camera.

4.2. Geochemical and mineralogical analysis

Bulk samples comprising typically ~40 g of material were collected for geochemical and mineralogical analysis. Total organic and inorganic carbon (TOC/TIC) were determined by combustion of small (few mg) sample amounts and analysis of the combustion gas in a thermal conductivity detector, and TIC was converted to $CaCO_3$ content by multiplying with a stoichiometric factor of 8.33.

Mineralogical compositions were determined by x-ray diffraction, with bulk and clay mineralogy being measured in two separate approaches. For bulk mineralogy, two dried and powderised samples were spiked with Al_2O_3 powder as an internal standard and pressed into sample holders. The measurements of bulk mineralogy were taken with an X'Pert PRO diffractometer (Cu tube, 45 kV, 40 mA, 5°–75° 2θ). The mineralogical composition was determined by a semi-automatic Rietveld refinement in HighScore Plus.

Clay mineralogy was determined from a set of seven oriented samples which were prepared by pipetting a few drops of a clay suspension obtained by Atterberg separation onto glass plates. The glass plates were left to dry and then placed in an ethylene glycol atmosphere at 50 °C for at least 24 h in order to saturate swellable clay minerals within the sample. Additional oriented samples were heated to 550 °C for at least 1.5 h in order to remove kaolinite and check for the presence of chlorite. Measurements were taken with a Philips PW1830 (Cu tube, 40 kV, 30 mA, 2°–40° 2θ), and clay mineral abundances were calculated from relative peak intensities (smectite at ~5.2° 2θ, illite at ~8.8° 2θ, kaolinite at ~12.5° 2θ). We employed the 100%-approach with in-house mineral intensity factors, thus the absolute results should be treated with caution (Kahle *et al.* 2002). Trace minerals were identified with the scanning electron microscope (SEM) at IfG.

4.3. Thin section and microscopic analysis

Despite the fragility of the limestone breccia we succeeded in producing a thin section ~2.5 cm in diameter. The sample was collected from the wall of a karst void at the edge of the core at 112.59 m depth. The breccia consists of limestone fragments between 2 and 10 mm embedded in blue clay. The sample was evacuated and impregnated with epoxy before being horizontally cut and ground. Finally, the section was polished with 6 and 3 μm diamond paste. Thin-section analysis was done with an Olympus BX41 microscope with attached SC30 camera. Additionally, one bulk sample (114.98 m depth) was used for palynological screening.

5. Results

5.1. Stratigraphy and macroscopic description

The borehole Gebenstorf-Brüel (QGBR) terminated at a depth of 123.5 m. The Pleistocene infill of the overdeepening below an anthropogenic refill (0.0-8.0 m depth) comprises glaciofluvial gravels (8.0-23.6 m) underlain by glaciodeltaic or -lacustrine sands (23.6-108.8 m) and glacial till (108.8-111.5 m) (Fig. III-2; Gegg *et al.* 2019). The bedrock was reached at 111.5 m depth and it consists of massive, light olive- to yellowish-grey micritic limestones of the Villigen Fm. of early Late Jurassic age (Oxfordian - Kimmeridgian; Bitterli *et al.* 2000). The transition from the till to the underlying bedrock is marked by a sharp decrease in the natural gamma log and magnetic susceptibility, and an increase in bulk density (Fig. III-2; Gegg *et al.* 2019). Several macrofossils, possibly sponges, and dark nodules with diameters of up to 2 cm were observed, as well as frequent stylolites in varying orientations ranging from horizontal to vertical. 19 faults were logged along the 12 m bedrock core section, 15 of which could be correlated to faults detected on the acoustic image of the borehole wall allowing for orientation measurements. 14 of these faults dip towards southeast with dip angles between 5° and 31°, and one dips westwards at an angle of 17° (Fig. III-2). The five non-correlated faults have dip angles between 5° and 45°.

The intervals 111.5-119.8 m and 121.0-121.5 m are penetrated by a 3D network of few millimetre- to several centimetre-wide interconnected voids identified as palaeokarst features. In the description of these features, we do not differentiate between incipient dissolution features, conduits or cavities, but simply refer to them as karst voids. The voids are filled with clayey sediment and angular limestone clasts up to fine gravel-size range. When fresh, the clayey matrix has a distinct turquoise blue colour – with some olive patches – that fades upon oxidation to blueish green and later to greenish or blueish grey (Fig. III-3). The filling displays a scaly fabric (Maltman 1994) that appears strongly consolidated and breaks in shards with shiny, slickenside-like surfaces. Palynological screening did not reveal any pollen within the clay.
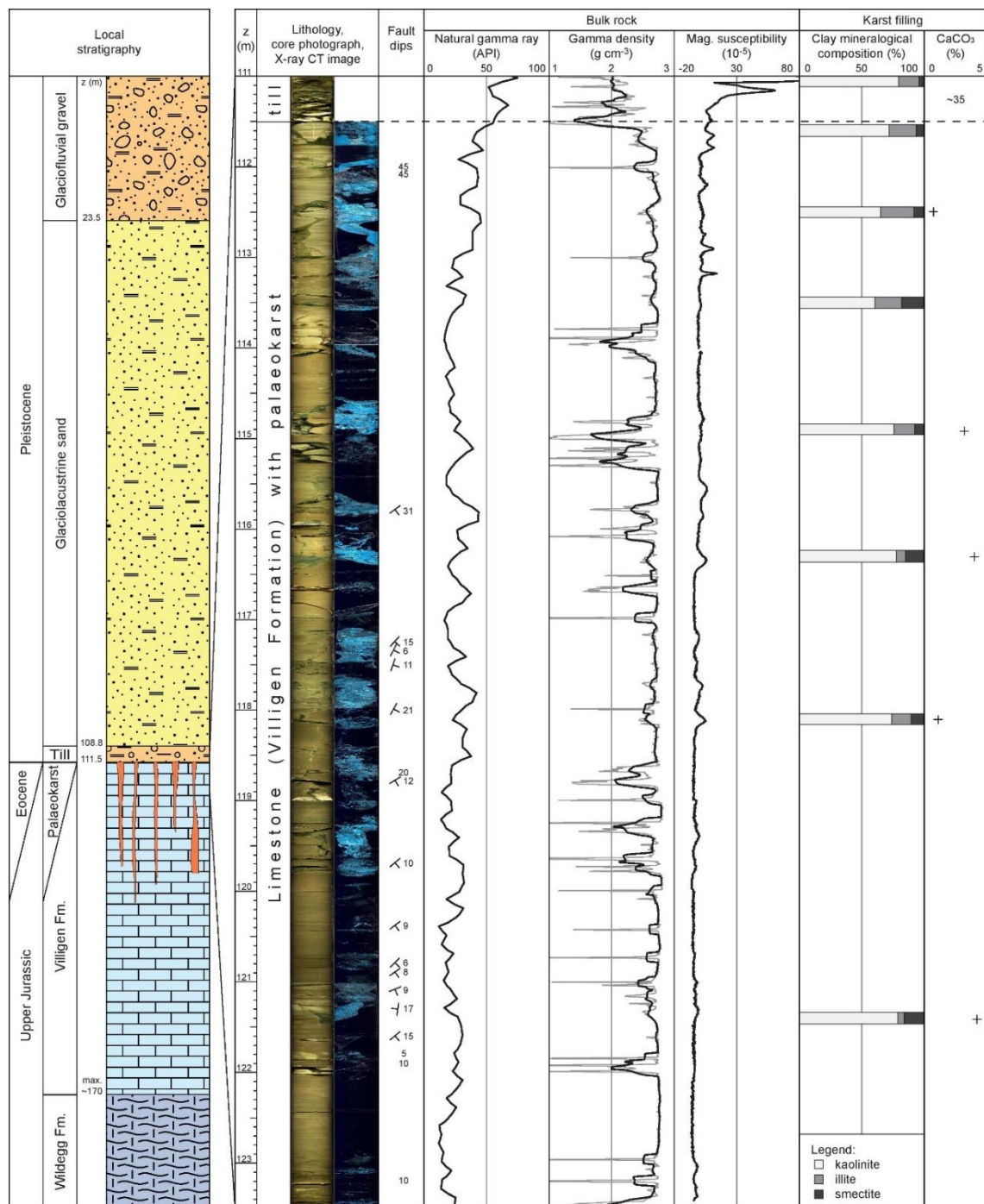
Fig. III-2. Overview plot of the 12.5 m bedrock section at bottom of the borehole QGBR (total depth 123.5 m) in the local stratigraphic context. Core photograph and X-ray CT image column (low-density material (palaeokarst filling) is light blue, high-density material (limestone) is black) are horizontally stretched by a factor of ~5. Dip direction of faults is given where correlation with ABI is possible. Gamma density is displayed as 20 cm moving average (black) and raw data (grey).

Two different void wall morphologies can be observed: i) smoothly undulating void walls with rough dissolution surfaces coated by a fine layer of dark brown clay (*e.g.* 112.5-112.9 m; Fig. III-3B); and ii) surficially brecciated void walls, with clayey filling material intruding into the fractures (*e.g.* 111.6-111.8 m; Fig. III-3C). In several places (*e.g.* 111.6-111.7 m), the fragments of the resulting limestone breccia are form-fit and interlocking, with only a narrow clay layer in between. Limestone fragments are usually limited to a few cm-wide zone around angular, fractured sections of the rock wall, no 'free-floating' clasts are observed in the larger cavities. In addition, we observe narrow (below 1 cm), sometimes branching fractures filled with angular host rock fragments and no or little clay extending from wider voids into the limestone (*e.g.* 116.1-116.3 and 118.4-118.8 m; Fig. III-3D).

5.2. Mineralogy and geochemistry of the palaeokarst filling

Bulk X-ray diffraction data of two samples (112.48 and 116.35 m depth) show that the void filling in borehole QGBR consists of ~85% clay minerals with some quartz (~10%) and calcite (up to 5%). The latter is in agreement with geochemical (TIC) data. The clay mineralogical composition is dominated by kaolinite (~60-80%) with some illite and smectite (Fig. III-2, Table III-S1). Minor amounts of chlorite could be detected in all samples. Furthermore, few autigenic baryte crystals were identified in the SEM. TOC contents range between 0.1-0.2%.
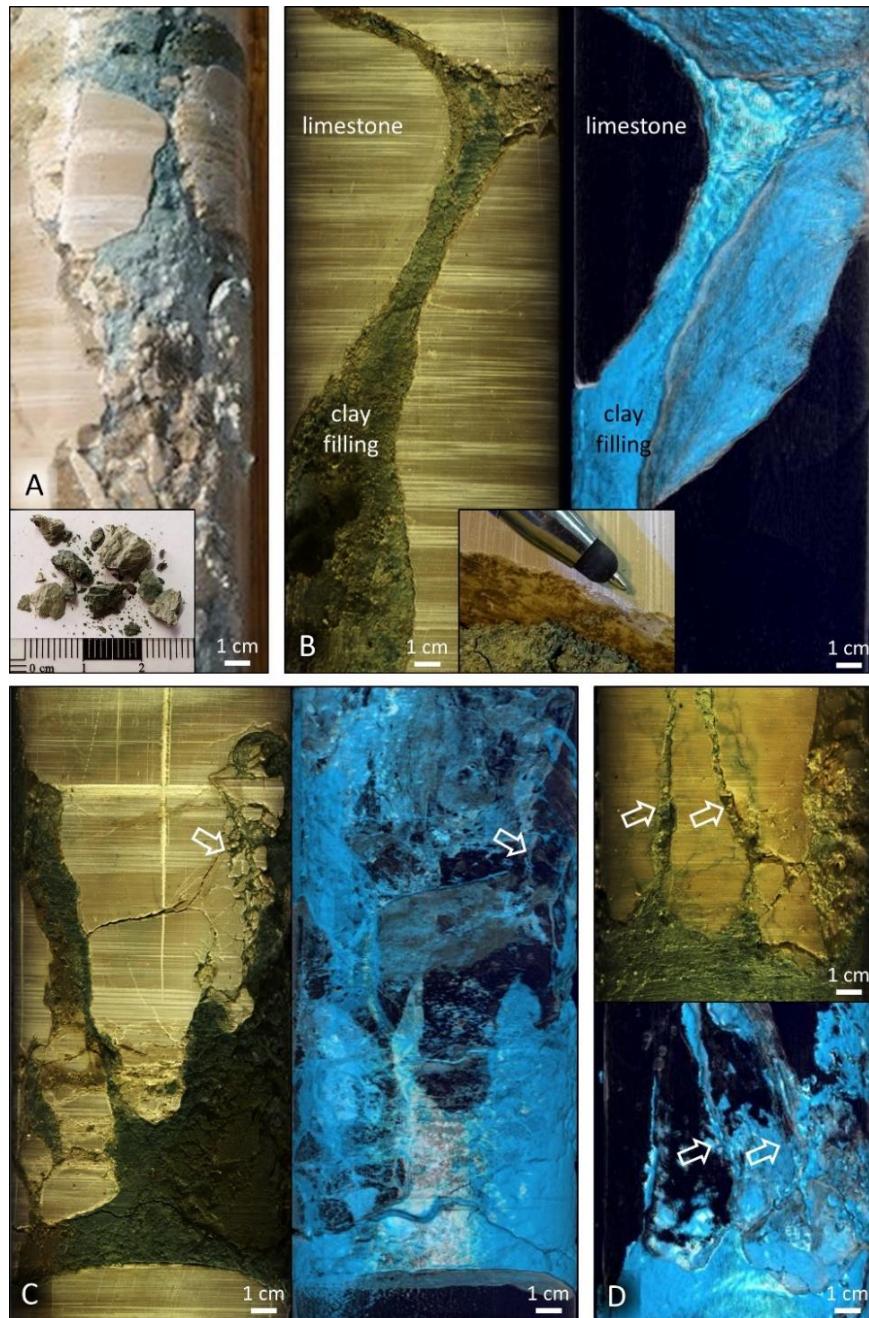
Fig. III-3. Palaeokarst voids: infill and wall morphologies. Note drilling-related surface grooves on the limestone surfaces. A. Photograph of the fresh core. Note the prominent blue colour of the clayey palaeokarst filling. Inset: dried filling broken into shards. B. Smoothly undulating void walls (112.5-112.8 m depth; left: core photograph, right: CT image, low-density material (clay filling) is light blue, high-density material (limestone) is transparent/black). Note the dark clay coating on the wall surfaces (inset). C. Brecciated void wall surfaces (111.6-111.8 m depth; left: core photograph, right: CT image). D. Narrow fractures filled with angular host rock fragments but only little clay (116.2-116.4 m depth; top: core photograph, bottom: CT image).

5.3. Microstructures

Microscopic analysis of the horizontally oriented thin section at 112.59 m depth confirmed that the breccia-like material at the palaeokarst wall consists of limestone with vein-like fractures, which not always can be distinguished from narrow karst voids, filled with clayey sediment. These randomly oriented features can be as narrow as few 10s of micrometres. Their infill consists of a light, clayey matrix, few sand grains and occasionally larger clasts, which are frequently form-fit interlocking. The clasts consist of limestone not distinguishable from the host rock (Fig. III-4A). The limestone bedrock contains stylolites, one of which was observed to gradually widen and transition into a lighter clay-filled fracture/void as described above (Fig. III-4B). The sediment within the fractures/voids is vaguely undulatory laminated parallel to their margins, and diffuse lobate structures are observed in a ~1 mm wide fracture/void (Fig. III-4C, D). Under crossed polarisers, optical anisotropy within the clay filling is evident (Fig. III-4E).
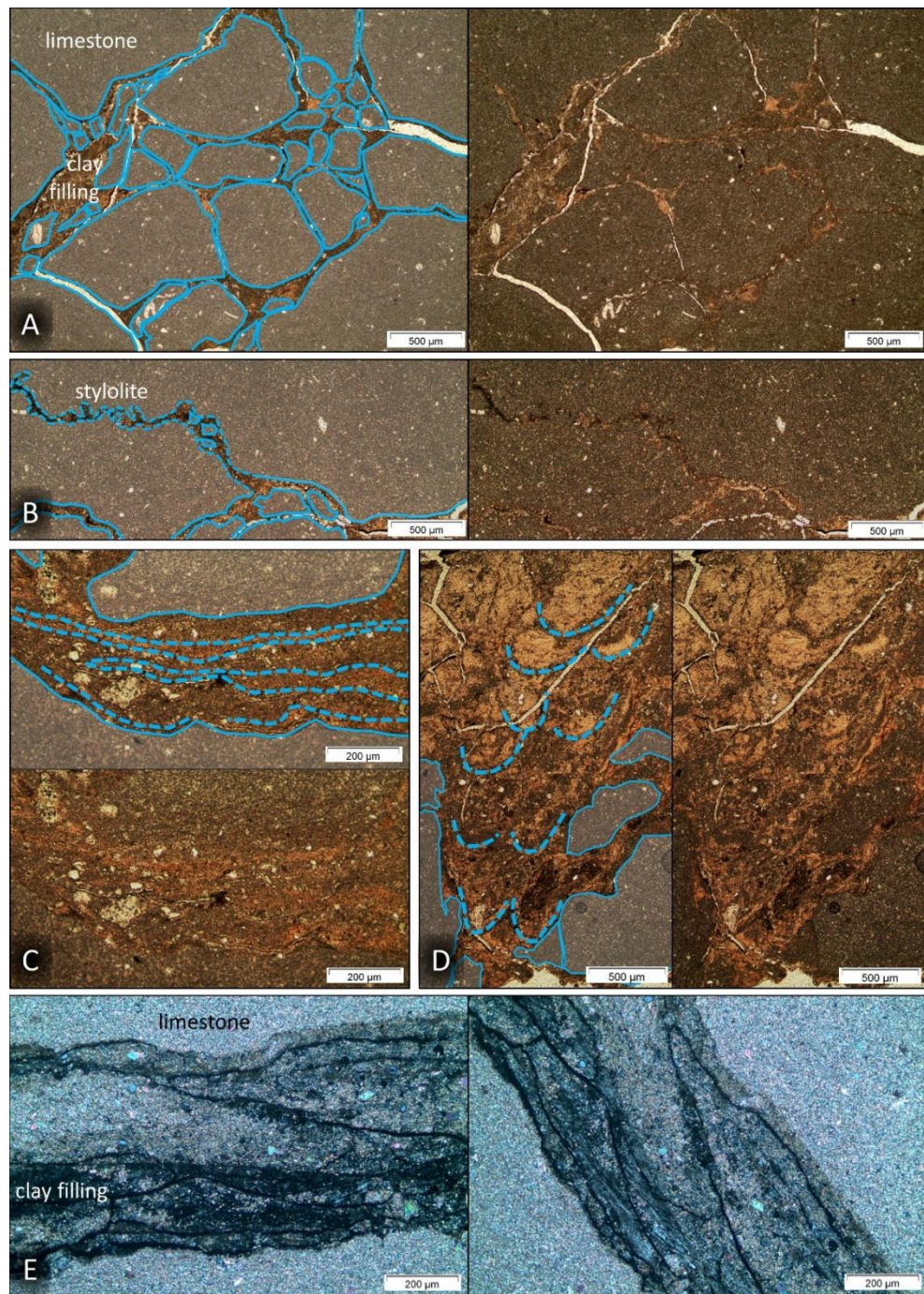
Fig. III-4. Microstructures in karstified limestone of QGBR (horizontally oriented thin section at 112.59 m depth). A. Palaeokarst void/fracture infilled with interlocking limestone fragments embedded in Bolus Clay. B. Transition of stylolite (dashed) into clay-filled void/fracture. C. Diffusely laminated Bolus Clay filling of void/fracture. D. Lobate microstructures ('ball-and-pillow structures', Maltman 1994; 'drip structures', van der Meer *et al.* 2009) in the filling of a larger void/fracture. E. Optical anisotropy of the clayey infill under crossed polarisers (black lines are cracks related to the preparation process).

6. Discussion

6.1. Origin of the karst void infill

A number of possible origins for the clayey material infilled into palaeokarst voids in the drill cores are tested by comparing the clay-mineral compositions to reference samples (Table III-S1). These include i) reworked Molasse deposits, which may show a variety of bright colours including greenish and blueish tones (Bitterli-Dreher *et al.* 2007), ii) infiltrated or injected subglacial till, and iii) pure insoluble residue from limestone dissolution. These reference materials have clay-mineral compositions dominated by illite, which agree with various analyses reported in literature (*e.g.* Peters 1969; Schmidt-Kaler & Salger 1986; Hofmann 1991; Schegg & Leu 1996), but are very different from the kaolinite-rich karst fillings observed in QGBR. Therefore, we rule out a Molasse as well as subglacial or pure residual origin of the karst fillings.

Illite-dominated clay mineral compositions are typical for sediments originated by prevailing physical erosion, as would be expected *e.g.* under a cold (Pleistocene) climate, while high abundances of kaolinite and smectite point to intense chemical weathering under warm conditions (Weaver, 1989; Chen *et al.* 2019). Palaeokarst voids in the Alpine foreland are frequently infilled with siderolithic sediments. These are of Eocene, possibly up to Miocene, age and developed from Terra Rossa-type soil formations under a subtropic climate as well as limestone dissolution residues (Baumberger 1923; Hofmann 1967; Hofmann *et al.* 2017). They consist of mostly kaolinitic Bolus Clay ("Boluston") with concentric iron oxide pisoliths ("Bohnerze") and some detrital quartz sand (Hofmann 1967; Hofmann 1991; Bitterli-Dreher *et al.* 2007). Two reference samples of Bolus Clay from borehole Bülach-1-1 (47.5427° N, 8.5204° E, 22 km E of QGBR) show clay mineral compositions of ~60% kaolinite and 40% of illite, and 5% of smectite in one of the samples (Table III-S1) – values that are similar to those of the karst filling in QGBR.

While typical Bolus Clay is Fe- and Al-rich and has a prominent ochre or red colour (Hofmann 1991; Bitterli-Dreher *et al.* 2007; Hofmann *et al.* 2017; see also Fig. III-6), in boreholes and especially in contact with limestone, blueish or green varieties of the Bolus Clay have been encountered (Hofmann 1967; Lemcke *et al.* 1968; Matter *et al.* 1988a; Matter *et al.* 1988b).

In the case of Nagra borehole WEI-1 near Weiach (18 km NE of QGBR), a downcore colour change of the Bolus Clay from 'typical' ochre towards blue-green is evident (Matter *et al.* 1988a). This evolution coincides with a change in clay mineralogy from almost pure kaolinite towards 65-70% kaolinite and 30-35% smectite (Matter *et al.* 1988a). Sediment petrography as well as clay mineral composition of the blueish Bolus Clay thus agree well with our palaeokarst fillings. We interpret the latter to consist of Bolus Clay in a blue-green variety.

The blue-green variety of the Bolus Clay is characterised by the absence of iron pisoliths in QGBR as well as in other boreholes (*e.g.* Lemcke 1955; Matter *et al.* 1988a). Instead, minor amounts of pyrite may be present (Lemcke 1955; Matter *et al.* 1988a). Further mineralogical data of the borehole Weiach show that goethite constitutes ~10% of the typical Bolus Clay but is not detectable within the blue-green clays (Nagra, unpubl.). The downcore development from typical ochre towards blue-green Bolus Clay therefore appears to involve the removal of iron oxides as well as the formation of smectite, likely under reducing conditions (*cf.* similar reduced clays in modern cave sediments of Papua New Guinea; Gillieson 1986). The smectite may act as an iron sink and could be the source of the distinct colour of the clays (Kohyama *et al.* 1973). The absence of iron minerals in the blue Bolus Clay also explains the generally low signal levels in magnetic susceptibility of the QGBR bedrock cores with only slightly increased values at larger karst voids (Fig. III-2).

The lowermost two Quaternary till samples of QGBR (110.94 and 111.04 m depth) show a very similar, kaolinite-dominated clay mineral composition. This, together with the olive-blue colour of the till matrix in the lowermost 50 cm, is interpreted as a result of incorporation of Bolus Clay into the till, probably due to subglacial erosion of karstified and Bolus Clay-filled limestone, and not as a result of the mobilisation and injection of till into the karst fillings.

This is supported by the uniformly low carbonate content of the Bolus Clay throughout the core, which is significantly lower than in the till (up to 5% and ~35%, respectively; see Fig. III-2). An insertion of till into the void filling would be visible by increased carbonate contents in the upper samples. Also, clasts of lithologies different from the karstified limestone are frequent in the till, but do not occur within the Bolus Clay.

6.2. Process of limestone brecciation

6.2.1. Non-sedimentary origin of the breccia

In the palaeokarst in QGBR we observe a combination of smoothly undulating wall rock morphologies and zones of brecciated host rock as well as limestone fragments embedded in the Bolus Clay filling. While sedimentary breccias with locally derived clasts are commonly deposited in karst voids or caves (Ford & Williams 2013), the breccia in QBR cannot be explained by a simple depositional process. Here, limestone clasts are in most cases restricted to a few centimetre-wide zone around angular, fractured sections of the palaeokarst wall but neither concentrated at the bottom, nor in horizontal layers within voids, as would be expected in a sedimentary karst breccia (*e.g.* Guendon 1984: photo 1). 'Free-floating' isolated clasts are absent within larger voids, which indicates that the palaeokarst filling originally consisted of well-sorted pure Bolus Clay without larger fragments. The observations point towards rock-wall fracturing after infilling of the karst voids resulting in the formation of an *in situ*-breccia. We frequently observe form-fit interlocking clasts which at several places can be pieced together via 2D slices of the CT scans and fit into breakouts of the void wall (Fig. III-5), which supports the idea that they are commonly derived from the rock wall that has been brecciated *in situ*. Additionally, the smoothly undulating, unbrecciated void walls are coated by a thin layer of dark brownish clay, which we interpret as a primary feature developed during karstification. This layer neither occurs on the brecciated surfaces nor on the limestone fragments embedded in the Bolus Clay, suggesting that these surfaces are younger than the unbrecciated palaeokarst walls.

6.2.2. Tectonic deformation

In the 12 m long bedrock core section of QGBR a total of 19 faults were logged with remarkably uniform shallow dips towards southeast (Fig. III-2). This speaks for their interpretation in the context of the Jura fold-and-thrust belt formation and is consistent with observations of outcropping corresponding limestones in the area (Madritsch 2015). This tectonic preconditioning likely facilitated the incision of the Gebenstorf-Stilli Trough and potentially played a role in the limestone brecciation observed in the drill cores. Despite the frequent occurrence of faults, the bedrock does however not appear strongly tectonised. While the karst wall surfaces are locally intensively brecciated, the larger-scale structure of the palaeokarst is intact. Evidence for major deformation of the karst walls and infill is lacking, *e.g.* clasts aligned in bands indicative of localised shearing (Lloyd Davies 2004). The distribution of limestone fragments in close vicinity to the palaeokarst walls, as well as the possibility to piece adjacent clasts together, further suggests that only limited clast dislocation and Bolus Clay deformation occurred during or after the brecciation of the karst wall surfaces. Also, in contrast to the observed bedrock faults, the surficial fractures in the karst void walls show no preferred orientation (*e.g.* Fig. III-3C).

More heavily tectonised Bolus Clay was recently recorded in Nagra borehole Bülach-1-1 (47.5427° N, 8.5204° E). It was drilled 22 km E of QGBR in a comparable position north of the Jura fold-and-thrust belt and dissected a gently dipping thrust fault branching off a complex E-W striking triangle zone (Malz *et al.* 2016; Nagra 2019). At a depth of over 500 m, Bülach-1-1 recovered Bolus-Clay-filled palaeokarst with large-scale shear planes, mirror-like faults and planar (fault-bound) contacts between rock wall and karst filling as well as large angular, but hardly form-fit limestone fragments dispersed in the Bolus Clay and partly aligned in bands (Fig. III-6). In contrast, brecciated karst wall surfaces that are abundant in QGBR were rarely encountered in Bülach-1-1.
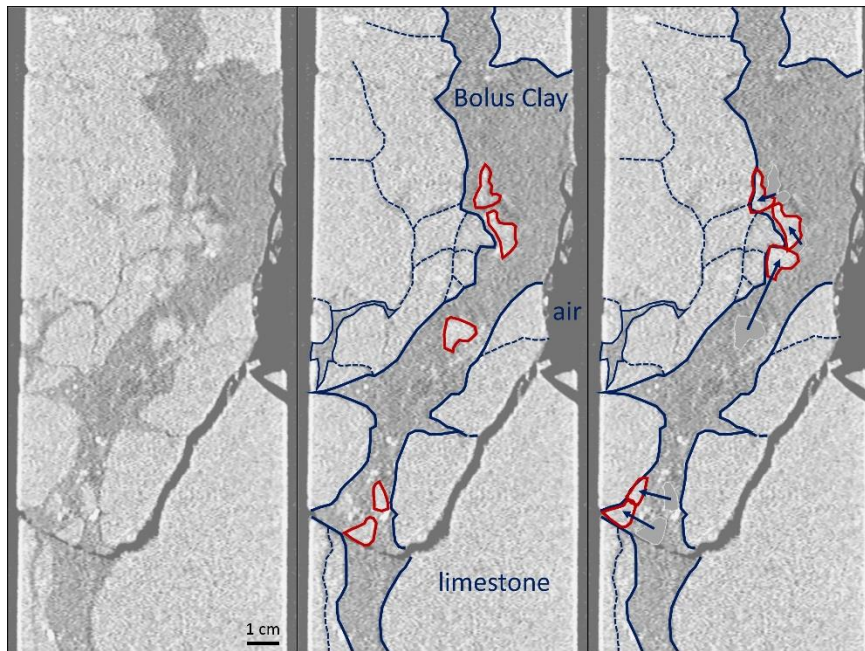
Fig. III-5. Limestone with palaeokarst, vertical 2D slice of a CT scan at ~112.5 m depth (left). The limestone can be distinguished well from the palaeokarst infill (middle). Note fragments of limestone embedded within the Bolus Clay (red outline). These fragments can be pieced back together and fit into breakouts of the wall rock (right), giving an impression of the void wall prior to brecciation.
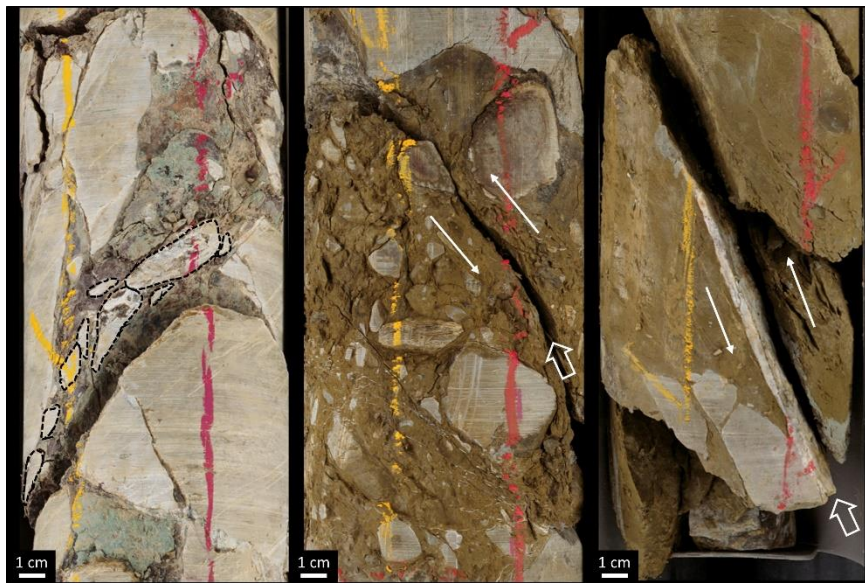
Fig. III-6. Indicators of strong tectonic overprinting of karstified, Bolus Clay-filled limestone in Nagra borehole Bülach-1-1. Left: fragments aligned in discrete band indicative of shearing (541.3-541.5 m depth). Middle: Larger palaeokarst void with dispersed, non-form-fit fragments and dissected by a fault (arrow; 549.8-550.0 m). Right: Fault plane with calcite mineralisation (arrow, 550.8-551.0 m). Photograph courtesy of Nagra.

Considering the deformation features in Bülach-1-1 we argue that the small-scale brecciation encountered in QGBR is not due to the comparatively mild tectonic deformations observed here. Instead, the brecciation of the karst void walls is regarded as the result of a secondary deformation process that occurred independently from tectonic structures, but not independently from the karst voids.

6.2.3. Glaciotectonism

Planar shearing under overriding glacier ice can produce abundant brecciation features, as presented by Passchier *et al.* (1998) in glacial sediments from borehole CRP-1 at Roberts Ridge, Antarctica. CRP-1 recovered several brecciated intervals that contain a variety of breccia types commonly separated by sharp horizontal boundaries (Passchier *et al.* 1998). In contrast, in QGBR the style of brecciation is uniform but without a preferred orientation suggesting an undirected underlying process. The breccias in CRP-1 also span the entire core width and thus appear to be more laterally extensive than in QGBR, where the brecciation originates from the sediment-filled palaeokarst voids and does not reach further into the limestone than a few centimetres. We thus infer that the brecciation features in QGBR are not the result of glaciotectonism caused by subglacial shearing of the karstified limestone. Also, a glaciotectonic origin of the faults observed in QGBR is unlikely, as such faults would be expected to dip steeply into the flow direction, *i.e.* towards north (Van der Wateren, 2002; Lloyd Davies, 2004).

6.2.4. Frost action

Freezing of water results in a volume increase by almost 10%, which can lead to pressure build-up and fracturing in porous rocks. Subglacial overdeepening erosion, in contrast, occurs where the glacier is warm-based, either by debris-laden ice sliding over its bed, or by subglacial meltwater (Dürst Stucki & Schlunegger 2013). Below warm-based glaciers, a water film is generated by pressure melting at the stoss side of irregularities in the bed (Weertman 1957, 1964). At the lee side of these irregularities, it can regelate. However, the regelation of water from this sub-millimetre thick film (Hallet 1979) may induce some traction and shearing of the bed, but likely not brecciation several metres below the bed surface.

With permafrost reaching as deep as 150 m into the bedrock during Pleniglacial conditions (Delisle 2003; Haeberli 2010), a temporary entire freezing of the karstified limestone in QGBR, while improbable, cannot completely be excluded. However, it is unlikely that this freezing could have resulted in frost bursting of the rock by volume expansion. To be extensive, this process demands rapid freezing so that pore pressures cannot be relieved by the migration of pore water (Matsuoka & Murton 2008) and a large number of freeze-thaw cycles (Potts 1970). Both is implausible under more than 150 m of glacier ice, where the rock is well insulated and thermally buffered. The same is true for rock fracturing by ice segregation and ice lens growth (Hallet *et al.* 1991; Murton *et al.* 2006; Matsuoka & Murton 2008) which is possible only if a threshold overburden pressure is not exceeded. This threshold overburden pressure is ~80 kPa in the idealised model case (Rempel, 2007), which corresponds to an ice thickness of less than 10 m.

6.2.5. Water pressure-driven brecciation

In order to explain the surficial brecciation features in the palaeokarst walls of Gebenstorf-Brüel, we favour fracturing driven by subglacial water pressure, which may be regarded as hydrofracturing in the widest sense and at a small (centimetre-decimetre) scale. Subglacial water pressures below warm-based glaciers are known to fluctuate on a number of timescales reaching values that exceed ice overburden pressure by a factor of up to 15, even in non-overdeepened settings (Kavanaugh & Clarke 2000). The build-up of high pressures is facilitated especially if water cannot escape from the subglacial drainage system. This is possible either if the subglacial drainage system is very inefficient or if the glacier front is frozen to the ground at the margin of the proglacial permafrost (Boulton & Caban 1995; Cook & Swift 2012). A rapid increase in subglacial water volume and pressure is possible *e.g.* during a jökulhlaup further up in the drainage area (Roberts *et al.* 2000; Stumm 2010). A potential source for a large meltwater outbreak could be the Birrfeld Basin just few kilometres south of the drill site (Fig. III-1). However, even without catastrophic events, basal water pressures have been shown to fluctuate considerably with distinct daily peaks during the melting season (Harper *et al.* 2002; Fudge *et al.* 2008).

If such water pressure peaks exceed the sum of overburden and tensile strength of the bedrock – or overburden only, if pre-existing bedrock fractures can be reactivated – brittle deformation can occur, typically as (subglacial) hydrofracturing (Cosgrove 1995; Boulton & Caban 1995; Rijsdijk *et al.* 1999; Jolly & Lonergan, 2002). Subglacial hydrofracturing has been described in numerous places around the world, most frequently in glacial sediments, but it also occurs in solid bedrock, where highest water pressures are required (Meehan *et al.* 1997; Lloyd Davies 2004; Phillips *et al.* 2013; Broughton 2018). Hydrofracture systems can extend over several tens of metres (Kumpulainen 1994; Phillips *et al.* 2013; Phillips & Hughes 2014). The fractures can be several decimetres to few metres wide and are in most cases filled by sediment that is laminated parallel to the fracture walls (Larsen & Mangerud 1992; Rijsdijk *et al.* 1999; van der Meer *et al.* 2009). Complex internal structures with laminae of different grain sizes that may be graded or cross-bedded suggest that hydrofracture systems are regularly open for a prolonged time with sustained, but fluctuating water through-flow (Phillips *et al.* 2013; Phillips & Hughes 2014).

During erosion of the Gebenstorf-Stilli Trough glacier ice must have had a considerable thickness of more than 150 m of ice overlying the bedrock at the site of QGBR. This is equivalent to an overburden of ~1.4 MPa, which is already at the same magnitude as the tensile strength of limestone (Nazir *et al.* 2013; Schön 2015). However, in an interconnected drainage system up to the accumulation area of the glacier occupying the Gebenstorf-Stilli Trough located high up in the Alps, peak hydraulic heads exceeding 1000 m are possible (Kavanaugh & Clarke 2000; Beaney & Hicks 2000), *e.g.* during a jökulhlaup. Such a drainage system discharges a large area, which may deliver pulses of large amounts of meltwater (Boulton & Caban 1995). The similarly thick Laurentide Ice Sheet in Canada has been shown to produce hydraulic heads and water pressures sufficient for fracturing and explosive pressure release through 100s of metres of bedrock (Christiansen *et al.* 1982; Broughton 2018). Fracturing driven by subglacial water pressure at the site of QGBR is therefore well conceivable.

The observed surficial brecciation features in the drill cores of QGBR fit some previous descriptions of glacially induced hydrofractures, *e.g.* by Broughton (2018), and are similar in appearance to experimental hydrofractures (Guo *et al.* 2014; Chen *et al.* 2015). Bolus Clay within the fractures (Fig. III-3C) shows some microstructures indicative for viscous deformation, fluidisation, and dewatering (Maltman 1994). These are wall-parallel lamination (Fig. III-4C), diffuse ball-and-pillow or drip structures (Fig. III-4D; Maltman 1994; van der Meer *et al.* 2009), as well as an optical anisotropy of the clay (Fig. III-4E), all of which are encountered in subglacial hydrofractures (van der Meer *et al.* 2009). However, open hydrofractures with sustained water through-flow do not seem to have existed in QGBR. Macroscopic sedimentary structures indicative for flow are lacking in the palaeokarst voids. There is further no evidence for the insertion of till or sediment-laden water into the karst filling. For example, carbonate contents in the Bolus Clay throughout the whole cored section are uniformly low with one magnitude less than in the overlying till (Fig. III-2). The distribution of limestone fragments in close vicinity to the palaeokarst walls they are derived from, as well as the mosaic-like fit of adjacent clasts (Fig. III-5), indicates that only limited deformation and material transport over not more than a few centimetres occurred within the karst voids during or after brecciation. Thus, classical subglacial hydrofracturing releasing pressure via fractures that allow for sustained water through-flow cannot be postulated for QGBR. Instead, a different model of pressure-driven brecciation at the site of QGBR is proposed, which may be regarded as hydrofracturing in the widest sense, *i.e.* a process that is driven by water pressure but does not culminate in the opening of highly permeable fractures with sustained water through-flow (Fig. III-7).

During erosion of the Gebenstorf-Stilli Trough, the palaeokarst filling was in direct contact with water at the temperate glacier base, and its pressure was transferred to the porewater within the clay. In addition, pressurised water from the glacier base may have been supplied to deeper voids via joints or faults, although we do not see evidence for this mechanism. Also, no evidence for water entering the karst system along the boundary between karst wall and clay infill occurs, neither in the shape of sedimentary structures nor as input of macroscopically or chemically identifiable till-derived material.
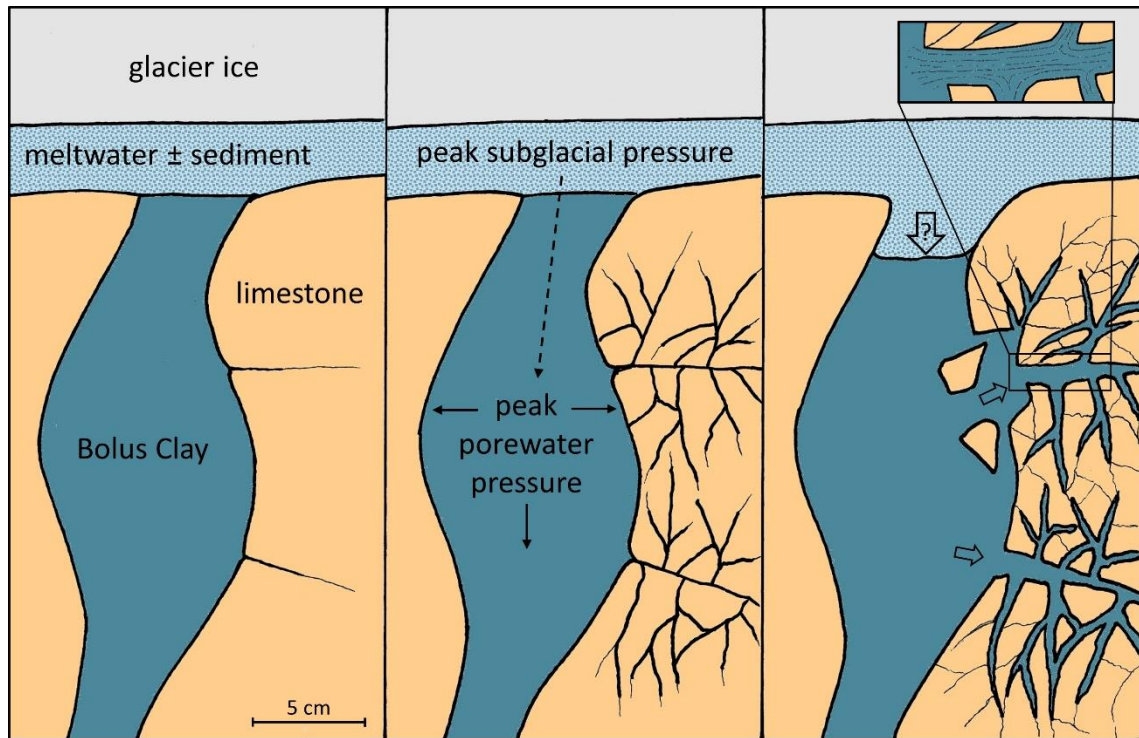
Fig. III-7. Conceptual model of water pressure-driven brecciation in QGBR. The Bolus Clay filling in the palaeokarst voids was in direct contact with the subglacial drainage system of the overriding, overdeepening glacier (left). Peak subglacial water pressures were transmitted via the porewater pressure of the clay filling, to the rock wall, initiating fracturing at points of weakness (middle). Opening of short (centimetre- to decimetre-scale) fractures within the rock wall allowed for the intrusion of Bolus Clay and pressing of the karst filling into the voids (right). Strong deformation of the Bolus Clay intruding into the newly formed fractures led to a diffusely laminated microstructure (inset) as well as ball-and-pillow/drip structures and optical anisotropy.

We infer that the Bolus Clay was water-saturated and has acted as a transmitter of pressure peaks from the subglacial system – be it pure water or a wet till bed – to the karst walls. These porewater pressure peaks may have been further amplified by ground shaking due to a small earth- or ice quake as a potential side effect of the increase in basal water availability (Ozaydin & Erguvanli 1980; Mortezale & Vucetic 2013). In response to the rapid pressure increase fracturing occurred at points of weakness. These points of weakness could be stylolites (see Fig. III-4B), but also pre-existing fractures that are abundant due to the local tectonic preconditioning. The observed limestone brecciation may have occurred at once or be the result of multiple brecciation events.

It appears to be restricted to a small scale with centimetre- to decimetre-long fractures. Similar brittle features have been encountered at the margins of larger-scale subglacial hydrofractures in western Canada by Broughton (2018).

It is inferred that the brecciation of the limestone resulted in steep pressure gradients, *i.e.* considerable stress acting on the palaeokarst infill in vicinity of the newly formed fractures, and that this allowed for the semi-plastic intrusion or viscous flow of small volumes of Bolus Clay into them. Natural clays are known to display a pronounced shear-thinning or thixotropic behaviour (Coussot 1995; Fossum 2012). Laboratory experiments have shown that under stress, the viscosity of sufficiently wet clay can decrease by six orders of magnitude (Khaldoun *et al.* 2009). The remobilised clay was strongly deformed, resulting in a diffusely laminated microstructure (Fig. III-4C), including ball-and-pillow/drip structures (Fig. III-4D; Maltman 1994; van der Meer *et al.* 2009). Internal shearing during the intrusion led to the alignment of clay minerals within the Bolus Clay, visible as anisotropy of the material (Fig. III-4E). When the deformation ceases, thixotropic materials recover and their viscosity increases again (Barnes 1997). The deformation and re-solidification under high pressures is assumed to be the reason for the consolidated appearance of the karst filling that approaches a scaly fabric (Maltman 1994). Some fractures (Fig. III-3D) apparently were not infilled with clay and remained partly open, containing only some limestone fragments; these could however be washed out by the drilling fluid.

6.3. Palaeokarst substratum and subglacial hydrology

Karstified bedrock can have a strong influence on the drainage network of an overriding glacier. It is usually highly permeable, thus subglacial water can enter the subsurface karst network and be efficiently drained from the glacier base (Smart 1983, 2004). The result can be a warm-based but largely unlubricated glacier whose sliding velocity and therefore erosional activity is greatly reduced (Smart 1983; Steinemann *et al.* 2020). The observations on our drill cores, however, show that this was not the case at the site of QGBR. The clayey pre-Pleistocene filling was obviously not flushed out of the palaeokarst system by subglacial water draining into it. There is also no evidence for any input of subglacial sediment into the Bolus Clay.

This shows that the palaeokarst at our study site was effectively sealed and deactivated by cohesive clay-sized sediment. Moreover, the inferred brecciation of the wall rock under water pressure peaks indicates that the karst void filling withstood even highest water pressures. Thus, a karstified and sediment-infilled substratum does not necessarily have a distinct effect on the hydrology of an overriding glacier when compared with an unkarstified one.

7. Conclusions

We encountered extensive palaeokarst voids within Upper Jurassic limestone underlying a glacial overdeepening in the borehole QGBR. The palaeokarst is infilled and sealed by clayey sediment with a prominent blue colour. Based on its kaolinitic composition, we identified it as a variety of siderolithic Bolus Clay of presumably Eocene age. This variety is characterised by a significant smectite content and the absence of iron oxides, and likely developed under reducing conditions.

We infer that the karstified and brecciated limestones recovered in QGBR depict an interaction between a glacier and its subglacial drainage system. The brecciation occurred *in situ* at the boundary between limestone and karst filling. We interpret that it is unlikely the result of (glacio-)tectonic deformation or frost action but was caused by peaks in subglacial water pressure. We further suggest that the karst void filling acted as a pressure transducer from the subglacial drainage system to the void wall, where small-scale rock failures occurred at points of weakness.

In summary, the bedrock in QGBR was weakened by pervasive palaeokarst and abundant tectonic faults, which likely favoured the deep erosion of the Gebenstorf-Stilli Trough into otherwise competent bedrock. The inferred water-pressure driven fracturing of the karstified limestone below the overriding glacier may have been an additional factor facilitating erosion of the subglacial overdeepening.

8. References

Alley, R., Cuffey, K., Evenson, E., Strasser, J., Lawson, D. & Larson, G. 1997: How glaciers entrain and transport basal sediment: physical constraints. Quaternary Science Reviews 16, 1017-1038.

Barnes, H. A. 1997: Thixotropy – a review. Journal of Non-Newtonian Fluid Mechanics 70, 1-33.

Baumberger, E. 1923: Bohnerz I. Die Vorkommen im Juragebirge. Beiträge zur Geologie der Schweiz, Geotechnische Serie 13, 5-154.

Beaney, C. L. & Hicks, F. E. 2000: Hydraulic modelling of subglacial tunnel channels, south-east Alberta, Canada. Hydrological Processes 14, 2545-2557.

Berger, J.-P., Reichenbacher, B., Becker, D., Grimm, M., Grimm, K., Picot, L., Storni, A., Pirkenseer, C., Derer, C. & Schaefer, A. 2005: Palaeogeography of the upper Rhine Graben (URG) and the Swiss Molasse basin (SMB) from Eocene to Pliocene. International Journal of Earth Sciences 94, 697-710.

Bini, A., Buoncristiani, J., Couterrand, S., Ellwanger, D., Felber, M., Florineth, D., Graf, H., Keller, O., Kelly, M. & Schlüchter, C. 2009: Die Schweiz während des letzteiszeitlichen Maximums (LGM) 1:500'000. Bundesamt für Landestopographie swisstopo, Wabern.

Bitterli-Dreher, P., Graf, H., Naef, H., Diebold, P., Matousek, F., Burger, H. & Pauli-Gabi, T. 2007: Geologischer Atlas der Schweiz 1:25'000. Blatt 1070 Baden. Erläuterungen. 152 p. Bundesamt für Landestopographie swisstopo, Wabern.

Bitterli, T., Graf, H., Matousek, F. & Wanner, M. 2000: Geologischer Atlas der Schweiz 1:25'000. Blatt 1050 Zurzach. Erläuterungen. 89 p. Bundesamt für Landestopographie swisstopo, Wabern.

Boulton, G. & Caban, P. 1995: Groundwater flow beneath ice sheets: Part II—Its impact on glacier tectonic structures and moraine formation. Quaternary Science Reviews 14, 563-587.

Broughton, P. L. 2018: Subglacial blowouts in western Canada: insights into extreme meltwater pressures and hydrofracturing. Boreas 47, 326-346.

Buechi, M. W., Frank, S. M., Graf, H. R., Menzies, J. & Anselmetti, F. S. 2017: Subglacial emplacement of tills and meltwater deposits at the base of overdeepened bedrock troughs. Sedimentology 64, 658-685.

Burkhard, M. 1990: Aspects of the large-scale Miocene deformation in the most external part of the Swiss Alps (sub-Alpine molasse to Jura fold belt). Eclogae Geologicae Helvetiae 83, 559-583.

Burkhard, M. & Sommaruga, A. 1998: Evolution of the western Swiss Molasse basin: structural relations with the Alps and the Jura belt. Geological Society, London, Special Publications 134, 279-298.

Chen, D., Pan, B., Ma, J., Hu, X., Geng, H. & Pang, H. 2019: Paleoclimatic record from the clay mineralogy of Quaternary sediments of drill core DWJ from Jiudong subbasin (western Hexi Corridor), NW China. Quaternary Research 93, 124-138.

Chen, Y., Nagaya, Y. & Ishida, T. 2015: Observations of fractures induced by hydraulic fracturing in anisotropic granite. Rock Mechanics and Rock Engineering 48, 1455-1461.

Christiansen, E., Gendzwill, D. & Meneley, W. 1982: Howe Lake: a hydrodynamic blowout structure. Canadian Journal of Earth Sciences 19, 1122-1139.

Commission for the Geological Map of the World, Asch, K. & Bellenberg, S. 2005: The 1:5 million international geological map of Europe and adjacent areas (IGME 5000). Bundesanstalt für Geowissenschaften und Rohstoffe, Hannover.

Cook, S. J. & Swift, D. A. 2012: Subglacial basins: Their origin and importance in glacial systems and landscapes. Earth-Science Reviews 115, 332-372.

Cook, S. J., Waller, R. I. & Knight, P. G. 2006: Glaciohydraulic supercooling: the process and its significance. Progress in Physical Geography 30, 577-588.

Cosgrove, J. 1995: The expression of hydraulic fracturing in rocks and sediments. Geological Society, London, Special Publications 92, 187-196.

Coussot, P. 1995: Structural similarity and transition from Newtonian to non-Newtonian behavior for clay-water suspensions. Physical Review Letters 74, 3971.

Delisle, G., Caspers, G. & Freund, H. 2003: Permafrost in north-central Europe during the Weichselian: how deep? Proceedings of the Eighth International Conference on Permafrost 2003, 187-191.

Dürst Stucki, M. & Schlunegger, F. 2013: Identification of erosional mechanisms during past glaciations based on a bedrock surface model of the central European Alps. Earth and Planetary Science Letters 384, 57-70.

Fogal, T. & Krüger, J. H. 2010: Tuvok, an Architecture for Large Scale Volume Rendering. Vision, Modeling and Visualization 10, 139-146.

Ford, D. & Williams, P. D. 2007: Cave interior deposits. In Ford, D. & Williams, P. D. (eds.): Karst hydrogeology and geomorphology, 271-321. John Wiley & Sons, Chichester.

Fossum, J. 2012: Flow of clays. The European Physical Journal Special Topics 204, 41-56.

Fudge, T., Humphrey, N. F., Harper, J. T. & Pfeffer, W. T. 2008: Diurnal fluctuations in borehole water levels: configuration of the drainage system beneath Bench Glacier, Alaska, USA. Journal of Glaciology 54, 297-306.

Gegg, L., Kuster, A. M., Deplazes, G., Madritsch, H. & Buechi, M. W. 2019: Quaternary Borehole QBO Gebenstorf-Brüel (QGBR) Data Report. Nagra Arbeitsbericht NAB 19-02, 8 p.

Gillieson, D. 1986: Cave sedimentation in the New Guinea highlands. Earth Surface Processes and Landforms 11, 533-543.

Graf, H. R. 2009: Stratigraphie von Mittel-und Spätpleistozän in der Nordschweiz. 198 p. Bundesamt für Landestopographie, Wabern.

Graf, H., Bitterli-Dreher, P., Burger, H., Bitterli, T., Diebold, P. & Naef, H. 2006: Geologischer Atlas der Schweiz 1:25'000, Blatt 1070 Baden. Bundesamt für Landestopografie swisstopo, Wabern.

Guendon, J.-L. 1984: Les paléokarsts des Alpes occidentales du Trias à l'Éocène. Karstologia 4, 2-10.

Guo, T., Zhang, S., Qu, Z., Zhou, T., Xiao, Y. & Gao, J. 2014: Experimental study of hydraulic fracturing for shale by stimulated reservoir volume. Fuel 128, 373-380.

Haeberli, W. 2010: Glaciological conditions in northern Switzerland during recent Ice Ages. Nagra Arbeitsbericht NAB 10-18, 28 p.

Hallet, B. 1979: Subglacial regelation water film. Journal of Glaciology 23, 321-334.

Hallet, B., Walder, J. & Stubbs, C. 1991: Weathering by segregation ice growth in microcracks at sustained subzero temperatures: Verification from an experimental study using acoustic emissions. Permafrost and Periglacial Processes 2, 283-300.

Harper, J. T., Humphrey, N. F. & Greenwood, M. C. 2002: Basal conditions and glacier motion during the winter/spring transition, Worthington Glacier, Alaska, USA. Journal of Glaciology 48, 42-50.

Hofmann, F. 1967: Über die Tertiärbildungen im Kanton Schaffhausen. Mitteilungen der Naturforschenden Gesellschaft Schaffhausen 28, 171-211.

Hofmann, F. 1991: Neue Befunde zur Geologie, zur Lagerstättenkunde und zum historischen Abbau der Bohnerze und Bolustone der Region Schaffhausen. Mitteilungen der Naturforschenden Gesellschaft Schaffhausen 36, 45-81.

Hofmann, F., Reichenbacher, B. & Farley, K. A. 2017: Evidence for> 5 Ma paleo-exposure of an Eocene–Miocene paleosol of the Bohnerz Formation, Switzerland. Earth and Planetary Science Letters 465, 168-175.

Hooke, R. L. 1991: Positive feedbacks associated with erosion of glacial cirques and overdeepenings. Geological Society of America Bulletin 103, 1104-1108.

Jäckli, H. 1970: Die Schweiz zur letzten Eiszeit 1:550.000. Eidgenössische Landestopographie, Wabern.

Jolly, R. J. & Lonergan, L., 2002: Mechanisms and controls on the formation of sand intrusions. Journal of the Geological Society 159, 605-617.

Kahle, M., Kleber, M. & Jahn, R. 2002: Review of XRD-based quantitative analyses of clay minerals in soils: the suitability of mineral intensity factors. Geoderma 109, 191-205.

Kavanaugh, J. L. & Clarke, G. K. 2000: Evidence for extreme pressure pulses in the subglacial water system. Journal of Glaciology 46, 206-212.

Keller, O. & Krayss, E. 1993: The Rhine-Linth Glacier in the upper Wurm: a model of the last Alpine glaciation. Quaternary International 18, 15-27.

Keller, O. & Krayss, E. 2010: Mittel-und spätpleistozäne Stratigraphie und Morphogenese in Schlüsselregionen der Nordschweiz. E&G Quaternary Science Journal 59, 88-119.

Khaldoun, A., Moller, P., Fall, A., Wegdam, G., De Leeuw, B., Méheust, Y., Fossum, J. O.& Bonn, D. 2009: Quick clay and landslides of clayey soils. Physical Review Letters 103, 188301, DOI: 10.1103/PhysRevLett.103.188301.

Kikinis, R., Pieper, S. D. & Vosburgh, K. G. 2014: 3D Slicer: a platform for subject-specific image analysis, visualization, and clinical support. In Jolesz, F. A. (ed.): Intraoperative imaging and image-guided therapy, 277-289. Springer, New York.

Kohyama, N., Shimoda, S. & Sudo, T. 1973: Iron-rich saponite (ferrous and ferric forms). Clays and Clay Minerals 21, 229-237.

Kumpulainen, R. A. 1994: Fissure-fill and tunnel-fill sediments: expressions of permafrost and increased hydrostatic pressure. Journal of Quaternary Science 9, 59-72.

Larsen, E. & Mangerud, J. 1992: Subglacially formed clastic dikes. Sveriges Geologiska Undersökning 81, 163-170.

Laubscher, H. P. 1962: Die Zweiphasenhypothese der Jurafaltung. Eclogae Geologicae Helvetiae 55, 1-22.

Lemcke, K. 1955: Die Fazies des Jura der Bohrung Scherstetten 1. Geologica Bavarica 24, 52-65.

Lemcke, K., Büchi, U. & Wiener, G. 1968: Einige Ergebnisse der Erdölexploration auf die mittelländische Molasse der Zentralschweiz. Bulletin der schweizerischen Vereinigung Petroleum-Geologen und -Ingenieure 35, 15-34.

Linton, D. L. 1963: The forms of glacial erosion. Institute of British Geographers Transactions and Papers 33, 1-28.

Lloyd Davies, M. 2004: A polar paradise: The glaciation of South Victoria Land, Antarctica. Academisch Proefschrift UvA Amsterdam, 304 p.

Madritsch, H. 2015: Outcrop-scale fracture systems in the Alpine foreland of central northern Switzerland: Kinematics and tectonic context. Swiss Journal of Geosciences 108, 155-181.

Maltman, A. 1994: Deformation structures preserved in rocks. In Maltman, A. (ed.): The geological deformation of sediments, 261-307. Springer Science+Business Media, Dordrecht.

Malz, A., Madritsch, H., Meier, B. & Kley, J. 2016: An unusual triangle zone in the external northern Alpine foreland (Switzerland): Structural inheritance, kinematics and implications for the development of the adjacent Jura fold-and-thrust belt. Tectonophysics 670, 127–143.

Matsuoka, N. & Murton, J. 2008: Frost weathering: recent advances and future directions. Permafrost and Periglacial Processes 19, 195-210.

Matter, A., Peters, T., Bläsi, H., Meier, J., Ischi, H. & Meyer, C. 1988a: Sondierbohrung Weiach. Geologie. Geologischer Bericht der Landeshydrologie und -geologie 6, 438 p.

Matter, A., Peters, T., Bläsi, H., Schenker, F. & Weiss, H. 1988b: Sondierbohrung Schafisheim. Geologie. Geologischer Bericht der Landeshydrologie und -geologie 8, 321 p.

Meehan, R. T., Warren, W. P. & Gallagher, C. J. 1997: The sedimentology of a Late Pleistocene drumlin near Kingscourt, Ireland. Sedimentary Geology 111, 91-105.

van der Meer, J. J., Kjær, K. H., Krüger, J., Rabassa, J. & Kilfeather, A. 2009: Under pressure: clastic dykes in glacial settings. Quaternary Science Reviews 28, 708-720.

Mortezale, A. R. & Vucetic, M. 2013: Effect of frequency and vertical stress on cyclic degradation and pore water pressure in clay in the NGI simple shear device. Journal of Geotechnical and Geoenvironmental Engineering 139, 1727-1737.

Murton, J. B., Peterson, R. & Ozouf, J.-C. 2006: Bedrock fracture by ice segregation in cold regions. Science 314, 1127-1129.

Nagra 2019: Preliminary horizon and structure mapping of the Nagra 3D seismics NL-16 (Nördlich Lägern) in time domain. Nagra Arbeitsbericht NAB 18-35, 63 p.

Nazir, R., Momeni, E., Armaghani, D. J. & Amin, M. M. 2013: Correlation between unconfined compressive strength and indirect tensile strength of limestone rock samples. Electronic Journal of Geotechnical Engineering 18, 1737-1746.

Nitsche, F., Monin, G., Marillier, F., Graf, H. & Ansorge, J. 2001: Reflection seismic study of Cenozoic sediments in an overdeepened valley of northern Switzerland: the Birrfeld area. Eclogae Geologicae Helvetiae 94, 363-371.

Ozaydin, K. & Erguvanli, A. 1980: The generation of pore pressures in clayey soils during earthquakes. Proceedings of the 7th World Conference on Earthquake Engineering, 326-330.

Passchier, S., Wilson, T. & Paulsen, T. 1998: Origin of Breccias in the CRP-1 Core. Terra Antartica 5, 401-409.

Patton, H., Swift, D., Clark, C., Livingstone, S. J. & Cook, S. J. 2016: Distribution and characteristics of overdeepenings beneath the Greenland and Antarctic ice sheets: Implications for overdeepening origin and evolution. Quaternary Science Reviews 148, 128-145.

Peters, T. 1969: Tonmineralogie einiger Glazialablagerungen im schweizerischen Mittelland. Ecologae Geologicae Helvetiae 62, 517-525.

Pfiffner, O. A. 1986: Evolution of the north Alpine foreland basin in the Central Alps. Special Publications of the International Association of Sedimentologists 8, 219-228.

Phillips, W. J. 1972: Hydraulic fracturing and mineralization. Journal of the Geological Society 128, 337-359.

Phillips, E., Everest, J. & Reeves, H. 2013: Micromorphological evidence for subglacial multiphase sedimentation and deformation during overpressurised fluid flow associated with hydrofracturing. Boreas 42, 395-427.

Phillips, E. & Hughes, L. 2014: Hydrofracturing in response to the development of an overpressurised subglacial meltwater system during drumlin formation: an example from Anglesey, NW Wales. Proceedings of the Geologists' Association 125, 296-311.

Pietsch, J. & Jordan, P. 2014: Digitales Höhenmodell Basis Quartär der Nordschweiz - Version 2014 und ausgewählte Auswertungen. Nagra Arbeitsbericht NAB 14-02, 69 p.

Potts, A. S. 1970: Frost action in rocks: some experimental data. Transactions of the Institute of British Geographers 49, 109-124.

Preusser, F., Graf, H. R., Keller, O., Krayss, E. & Schlüchter, C. 2011: Quaternary glaciation history of northern Switzerland. E&G Quaternary Science Journal 60, 282-305.

Preusser, F., Reitner, J. M. & Schlüchter, C. 2010: Distribution, geometry, age and origin of overdeepened valleys and basins in the Alps and their foreland. Swiss Journal of Geosciences 103, 407-426.

Ravier, E., Buoncristiani, J.-F., Guiraud, M., Menzies, J., Clerc, S., Goupy, B. & Portier, E. 2014: Porewater pressure control on subglacial soft sediment remobilization and tunnel valley formation: A case study from the Alnif tunnel valley (Morocco). Sedimentary Geology 304, 71-95.

Rempel, A. 2007: Formation of ice lenses and frost heave. Journal of Geophysical Research 112, DOI: 10.1029/2006JF000525.

Rijsdijk, K. F., Owen, G., Warren, W. P., McCarroll, D. & van der Meer, J. J. 1999: Clastic dykes in over-consolidated tills: evidence for subglacial hydrofracturing at Killiney Bay, eastern Ireland. Sedimentary Geology 129, 111-126.

Roberts, M. J., Russell, A. J., Tweed, F. S. & Knudsen, Ó. 2000: Ice fracturing during jökulhlaups: implications for englacial floodwater routing and outlet development. Earth Surface Processes and Landforms 25, 1429-1446.

Schegg, R. & Leu, W. 1996: Clay mineral diagenesis and thermal history of the Thonex Well, Western Swiss Molasse Basin. Clays and Clay Minerals 44, 693-705.

Schmidt-Kaler, H. & Salger, M. 1986: Obere Süßwassermolasse (OSM) und Bunte Breccie bei Bieswang (Südliche Frankenalb): neue Kernbohrungen und sedimentpetrographische Untersuchungen. Geologica Bavarica 89, 219–228.

Schön, J. H. 2015: Geomechanical Properties. In Schön, J. H. (ed.): Physical properties of rocks: Fundamentals and principles of petrophysics, 269-300. Elsevier, Amsterdam.

Smart, C. 1983: The hydrology of the castleguard karst, columbia icefields, Alberta, Canada. Arctic and Alpine Research 15, 471-486.

Smart, C. 2004: Glacierised and glaciated karst. In Gunn, J. (ed.): Encyclopedia of caves and karst science, 804-809. Fitzroy Dearborn, New York.

Steinemann, O., Ivy-Ochs, S., Grazioli, S., Luetscher, M., Fischer, U. H., Vockenhuber, C. & Synal, H. A. 2020: Quantifying glacial erosion on a limestone bed and the relevance for landscape development in the alps. Earth Surface Processes and Landforms, DOI: 10.1002/esp.4812.

Stumm, D. 2010: Deep glacial erosion. Review with focus on tunnel valleys in northern Europe. Nagra Arbeitsbericht NAB 10-33, 74 p.

Swisstopo 2013: swissALTI3D. Bundesamt für Landestopographie swisstopo, Wabern.

Van der Wateren, D. M. 2002: Processes of glaciotectonism. In Menzies, J. (ed.): Modern and Past Glacial Environments, 417-443. Butterworth-Heinemann, Oxford.

Weaver, C. E. 1989: Soils and Weathering. In Weaver, C. E. (ed.): Clays, muds, and shales, 103-189. Elsevier, Amsterdam.

Weertman, J. 1957: On the sliding of glaciers. Journal of Glaciology 3, 33-38.

Weertman, J. 1964: The theory of glacier sliding. Journal of Glaciology 5, 287-303.

9. Supplementary material

Table III-S1: Clay-mineral compositions determined for karst fillings in borehole QGBR as well as reference samples from QGBR, other Quaternary boreholes of the drilling campaign (QGVO = Gebenstorf-Vogelsang, 47.5952° N, 8.2382° E; QRIN = Riniken, 47.5021° N, 8.1913° E; QTRU = Trüllikon, 47.6405° N, 8.6624° E) and Nagra borehole Bülach-1-1 (Bul-1-1, 47.5427° N, 8.5204° E).

Borehole, sample depth	Kaolinite	Illite	Smectite
Karst filling			
QGBR, 111.60 m	72%	22%	6%
QGBR, 112.48 m	65%	27%	8%
QGBR, 113.53 m	61%	21%	18%
QGBR, 114.90 m	76%	17%	7%
QGBR, 116.35 m	78%	7%	15%
QGBR, 118.13 m	74%	15%	10%
QGBR, 121.42 m	79%	5%	16%
Reference samples: subglacial till			
QGBR, 108.86 m	23%	60%	17%
QGBR, 109.54 m	24%	53%	22%
QGBR, 110.94 m	76%	14%	10%
QGBR, 111.04 m	80%	16%	4%
QGVO, 64.63 m	25%	63%	11%
QRIN, 38.89 m	19%	81%	-
QRIN, 40.99 m	21%	79%	-
Reference samples: Lower Freshwater Molasse			
QTRU, 91.00 m	20%	49%	31%
QTRU, 95.00 m	24%	49%	27%
Reference sample: limestone dissolution residue (clayey coating of a fault plane)			
QGBR, 123.40 m	34%	66%	-
Reference samples: siderolithic "Bolus Clay"			
Bul-1-1, 539.00 m	56%	5%	39%
Bul-1-1, 550.30 m	60%	-	40%

128

This page is intentionally left blank.

Selected drill cores from the Quartärbohrungen of the Lower Aare Valley.

IV. Reconstruction of an environmental history

This chapter focuses on the various sedimentary archives of the Wasserschloss area. Based on drill core and outcrop analysis, the development of the Gebenstorf-Stilli Trough and the Habsburg-Rinikerfeld Paleochannel are reconstructed. The findings are integrated into the regional context and allow conclusions on several pre-LGM glaciations of the Alpine foreland. The manuscript is in preparation for submission under the working title

Gegg, L.[1], Anselmetti, F. S.[1], Deplazes, G.[2], Fuelling, A.[3], Madritsch, H.[2], Mueller, D.[3], Preusser, F.[3], and Buechi, M. W.[1], Multiple Alpine foreland glaciations recorded in the Pleistocene archives of the Lower Aare Valley.

[1] Institute of Geological Sciences and Oeschger Centre for Climate Change Research, University of Bern, Baltzerstrasse 1+3, 3012 Bern, Switzerland

[2] National Cooperative for the Disposal of Radioactive Waste (Nagra), Hardstrasse 73, 5430 Wettingen, Switzerland

[3] Institute of Earth and Environmental Sciences, University of Freiburg, Albertstraße 23b, 79104 Freiburg, Germany

1. Abstract

Throughout the Pleistocene, Alpine glaciers repeatedly advanced into the mountain foreland and temporarily covered large parts of northern Switzerland and its neighbouring areas in ice. However, the respective geological record is highly fragmentary and the regional glaciation history, especially before the last glacial maximum, is poorly understood. We explore the archives of the Lower Aare Valley in the confluence area with the rivers Reuss and Limmat, with focus on the overdeepened Gebenstorf-Stilli Trough. In four scientific boreholes, ~350 m of drill cores were recovered and complemented by samples from outcrops in the nearby glaciofluvial Habsburg-Rinikerfeld Paleochannel. A multi-method sedimentological approach including compositional and geotechnical analyses provides new insights into the local landscape evolution: We identify two glacial basin generations in the infill of the Gebenstorf-Stilli Trough that are overlain by Late Pleistocene Niederterrasse gravels. In addition, two distinct glaciofluvial gravel bodies are recognized in the neighbouring paleochannel, which also hosts paleo-lake deposits providing a high-resolution record of the environmental conditions during ice retreat. In the specific local setting, gravel petrographic compositions prove to be a powerful tool to identify inputs from the confluent catchments of Aare, Reuss, and Limmat, and to infer the respective ice-margin positions. An integration of luminescence ages as old as MIS 10 reveals that the Pleistocene archives of the Lower Aare Valley reach back well into the Middle Pleistocene. Multiple local phases of glacial, glaciolacustrine, and glaciofluvial re-occupation are recognized that add to, and significantly expand, the regional glaciation history.

2. Introduction

During the Pleistocene, the Alpine glaciers repeatedly advanced into the foreland, temporarily covering the majority of northern Switzerland in ice (Graf, 2009b; Preusser *et al.*, 2011; Seguinot *et al.*, 2018). These glaciations had a significant geomorphic impact through glaciofluvial dissection, erosion of subglacial overdeepenings, and accumulation of decametre-thick deposits. In alternating phases of deposition and erosion (Buechi *et al.*, 2017; Preusser and Graf, 2002) lies a major difficulty hindering Pleistocene research in the Alpine environment: the fragmentarity of the geological record. The remnants of entire glaciations may have been eroded and entirely obliterated by later ice advances (Hughes *et al.*, 2019; Merritt *et al.*, 2019), and as a result, the pre-last glacial stratigraphy and landscape history remains intricate and poorly constrained.

Previous studies have identified at least four major phases of ice advance into the Swiss foreland throughout the Middle Pleistocene, termed, from youngest to oldest, Beringen, Hagenholz, Habsburg, and Möhlin (Graf, 2009b; Preusser *et al.*, 2011; Schlüchter *et al.*, 2021). The Beringen Glaciation has been correlated with MIS 6 (~150 ka) with reasonable confidence (Buechi *et al.*, 2017; Lowick *et al.*, 2015; Preusser *et al.*, 2011), but the chronostratigraphic positions of older glaciations are largely unknown. Preusser *et al.* (2021) suggest a correlation of Habsburg with MIS 8 or 10 (~270 or ~340 ka), and of Möhlin (Most Extensive Glaciation MEG; Graf, 2009b; Preusser *et al.*, 2011) with MIS 12 (~420 ka). It is, however, not clear whether all of these phases represent full glaciations or separate advances within a particular glaciation (Graf, 2009b), as the Mid-Pleistocene glaciations may have been as complex as the last glacial cycle (*i.e.* the Late Pleistocene) that comprises several distinct advances (Gaar *et al.*, 2019; Ivy-Ochs *et al.*, 2008; Preusser, 2004; Seguinot *et al.*, 2018).

In the present study, we aim to reconstruct a local glaciation history, specifically throughout the Mid-Pleistocene, and integrate it into the regional context. Drill cores and outcrops in the Lower Aare Valley are investigated with a multi-method approach combining sedimentology, geochemistry, and geotechnics, and integrating luminescence ages. We lay special focus on lacustrine records as lakes, developed *e.g.* in subglacial overdeepenings, can be valuable archives of past glaciations (Buechi *et al.*, 2017; Preusser *et al.*, 2005; Preusser *et al.*, 2010; Schlüchter, 1989a, b).

3. Study area

The present-day confluence area of the rivers Aare, Reuss, and Limmat ("Wasserschloss") in Northern Switzerland is a key site for regional Quaternary geology (Dick *et al.*, 1996). It is located about 50 km northwest of the Alpine front, at the eastern margin of the Jura Mountains (Gegg *et al.*, 2021). The Jura Mountains, comprising the Folded Jura and the northward-adjacent Tabular Jura, consist of Mesozoic sediments – carbonates, marls and siliciclastics – deposited on an epicontinental platform (Bitterli-Dreher *et al.*, 2007; Bitterli *et al.*, 2000; Jordan *et al.*, 2008). In the early Paleogene, today's Tabular Jura was uplifted on the forebulge of the approaching Alpine orogeny, while to the south of it, the Molasse Basin subsided (Burkhard and Sommaruga, 1998; Pfiffner, 1986). The deposition of heterogeneous Molasse sands, silts, and marls progressed northward, reached the southern part of the study area in the Oligocene, but stopped in the Late Miocene with the upthrusting and emersion of the Folded Jura (Burkhard, 1990; Laubscher, 1962). The lithologically and structurally complex bedrock architecture gave rise to the study area's diverse topography that is different from many other Quaternary sites of the Alpine foreland (Gegg *et al.*, 2021).

The Pleistocene was not only characterized by a cooling climate, but also by repeated lowering of the regional base level (Bitterli-Dreher *et al.*, 2007; Bitterli *et al.*, 2000). Two units of glaciofluvial Deckenschotter (Höhere/Tiefere D.) are correlated to the Early Pleistocene, and intercalated tills attest that the corresponding ice advances reached already far into the foreland (Bitterli-Dreher *et al.*, 2007; Graf, 1993, 2009a). After abandonment of the Deckenschotter valleys, the Habsburg-Rinikerfeld paleochannel (HRPC; Fig. IV-1) and its northward continuation into the Hochrhein Valley were established, through which glaciofluvial drainage and glacial advance occurred throughout most of the Middle Pleistocene (Graf, 2009b). The respective deposits are referred to as Hochterrasse, and are subdivided into Habsburg Gravel, Ruckfeld Gravel, and Remigen Gravel. These units are presumed to represent three out of the four regionally identified glaciations (Habsburg, Hagenholz, Beringen; Bitterli-Dreher *et al.*, 2007; Graf, 2009b), and are correlated to the Upper, Middle, and Lower Hochterrasse of the Lower Aare Valley mapped by Matousek *et al.* (2000).

The Deckenschotter and Hochterrasse are morphostratigraphic units, but the subdivision of the Hochterrasse is mainly achieved by lithostratigraphy, as the individual gravels occur on similar elevations (roughly 350-450 m a.s.l. in the HRPC and Lower Aare Valley; Graf *et al.*, 2006; Matousek *et al.*, 2000). Occasional intercalated tills and glaciotectonic deformations in the Remigen Gravel as well as basal diamicts in the HRPC suggest that at least two Mid-Pleistocene ice advances reached into the study area (Bitterli-Dreher *et al.*, 2007; Graf, 2009b).

The Middle Pleistocene presumably also marked the onset of overdeepening in the Wasserschloss area, *i.e.* the subglacial carving of basins into the bedrock below the Pleistocene base level (today at ~300 m a.s.l.; Graf, 2009b; see also Cook and Swift, 2012; Dürst Stucki and Schlunegger, 2013). These basins are the Birrfeld and its two branch basins, the Hausen Trough and the Gebenstorf-Stilli Trough (GST, Fig. IV-1; Gegg *et al.*, 2021; Graf, 2009b; Pietsch and Jordan, 2014). The overdeepenings were eroded into the bedrock under high subglacial water pressure (Dürst Stucki and Schlunegger, 2013; Gegg *et al.*, 2021) and, following ice retreat, became infilled with subglacial gravels and diamicts as well as with lake deposits (Bitterli-Dreher *et al.*, 2007). Forming a connection between the Birrfeld and the HRPC, the Hausen Trough is presumably older than the GST, which lies below the present-day Reuss/Aare Valley. The erosion of the GST may have enabled the abandonment of the HRPC and establishment of the modern drainage configuration (Graf, 2009b). The Late Pleistocene Niederterrasse gravels are generally restricted to the present-day river valleys (Gaar *et al.*, 2019; Graf *et al.*, 2006).
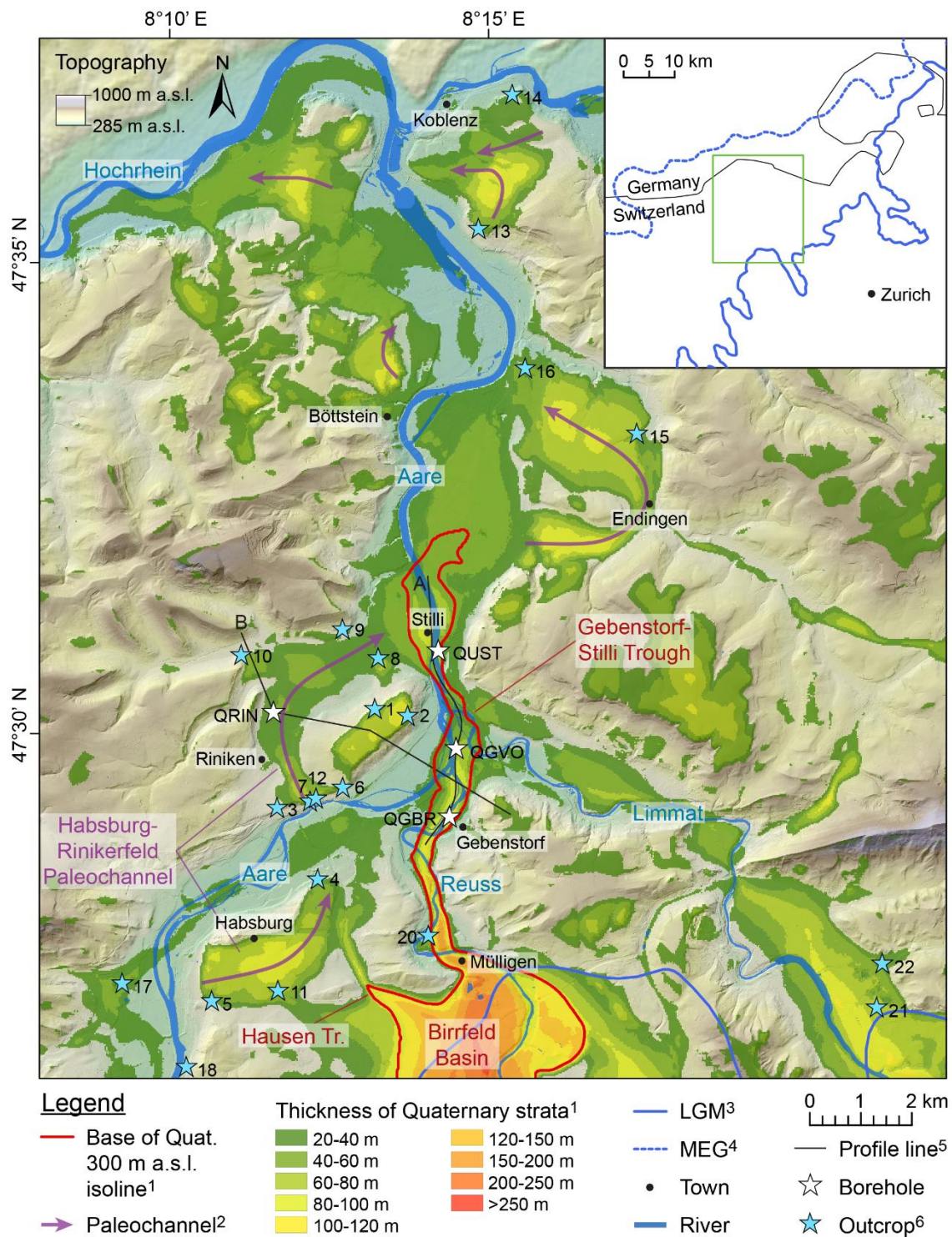
Fig. IV-1: Overview map of our study area in northern Switzerland (green rectangle in the inset). [1]: from Loepfe *et al.* (in prep.). [2]: after Graf (2009b). [3]: Alpine ice extent of the Last Glacial Maximum (Bini *et al.*, 2009). [4]: Ice extent of the Most Extensive Glaciation (Keller and Krayss, 2010). [5]: Profile lines for sections in Fig. IV-9 (A) and Fig. IV-10 (B). [6]: Outcrop numbers refer to Table IV-S1; outcrops mentioned in the text: 5 (Götschtel), 10 (Alpberg), 13 (Hönger).

4. Methodology

4.1. Drilling and field campaign

Our project comprises four scientific boreholes drilled in 2018 in context of the Quaternary investigation program of the Swiss National Cooperative for the Disposal of Radioactive Waste (Nagra). Three boreholes are located along the axis of the Gebenstorf-Stilli Trough, namely QGBR (latitude 47°29'00" N, longitude 8°14'11" E; Gegg *et al.*, 2019b), QGVO (47°29'43" N, 8°14'18 E; Gegg *et al.*, 2019a), and QUST (47°30'46" N, 8°14'3" E; Gegg *et al.*, 2019c). QRIN (47°30'09" N, 8°11'28" E; Gegg *et al.*, 2018) was targeted at the HRPC, and is a composite profile of two neighbouring boreholes. The 10 cm diameter drill cores, ~350 m in total, were recovered by pneumatic hammering and wireline coring using a triple tube core barrel where the core is protected by a plastic liner, allowing for excellent core quality. All boreholes recovered the entire Quaternary valley infill and terminated at least 10 m into the bedrock to guarantee a confident bedrock identification. After core recovery, a natural gamma log was acquired. Drilling was further complemented by an extensive field campaign studying and sampling over twenty outcrops in the study area (see Table IV-S1).

4.2. Initial core logging and sampling

After splitting of the individual drill cores, one half was shielded from light to allow later luminescence sampling and archived at the core repository of Nagra, while the other was processed at the Institute of Geological Sciences, University of Bern (IfG, UniBe). Bulk density, p-wave velocity and magnetic susceptibility were measured in 5 mm depth-resolution using a Geotek multi-sensor core logger (MSCL; Schultheiss and Weaver, 1992). Following line-scan imaging, detailed sedimentological and structural descriptions were carried out. Where the sediment was sufficiently fine-grained, we prepared smear slides and collected bulk sediment samples, each ~40 g of material, in sub-meter intervals for geochemical analysis. In selected core sections, we collected all clasts >15 mm diameter from entire core halves to assess gravel petrographical composition, and took undisturbed whole-core samples for geotechnical analysis prior to core splitting, both in 5-10 m intervals.

4.3. Compositional analysis

Water content was determined by weighing and freeze-drying of bulk sediment samples. Geochemical composition (total inorganic carbon TIC, total organic carbon TOC, total Sulphur TS, total nitrogen TN) by combustion of small (few mg) sample amounts and combustion gas analysis in a thermal conductivity detector. TIC was converted to $CaCO_3$ content by multiplication with a stoichiometric factor of 8.33. For gravel petrography we identified all clasts >15 mm in diameter from selected core halves, and all clasts >20 mm from volumetric samples collected in the field. The minimum clast diameters were chosen so that >100 clasts could be obtained per sample in most cases. For further evaluation, the data were simplified by classification into 13 lithology groups (Table IV-S2), due to some differentiations being gradual and thus poorly reproducible (*e.g.* light and dark grey limestones) or not regional-geologically meaningful (*e.g.* red sandstones and red conglomerates). The petrographic data were log-ratio transformed following Hammer (2018) and evaluated by principal component (PCA; variance-covariance matrix) and cluster analysis (Ward's method, Euclidean distance matrix) in Past 3 (Hammer *et al.*, 2001). In addition, we performed endmember analyses using the R packages EMMAgeo (Dietze and Dietze, 2019) and RECA (Seidel and Hlawitschka, 2015).

4.4. Geotechnical analysis

During initial core logging, we estimated undrained shear strength with a pocket vane tester in meter-intervals where the sediment was sufficiently cohesive, *i.e.* rich in fines. Undisturbed whole-core samples were later analysed at the geotechnical laboratory of the Bern University of Applied Sciences in Burgdorf (Switzerland). To prevent drying and alteration, they were stored refrigerated and sealed prior to analysis. We determined the preconsolidation pressure of sediment samples by oedometer testing (International Organization for Standardization, 2004). Horizontally oriented cylindrical samples (d = 50 mm, h = 20 mm) were cut out with a metal ring and placed in an oedometer chamber filled with deionized water. The samples were, under lateral confinement and enabled drainage, loaded with up to 3200 kN/m^2 in increments of 24 h.

After every loading step, the compaction was measured, and the results evaluated following the work per unit volume-approach by Becker *et al.* (1987). In addition, Atterberg Limits (liquid limit and plastic limit), *i.e.* the water contents at which the material behaves mechanically in norm-specified ways, were determined after Swiss Association of Road and Transportation Experts (2008).

5. Results

5.1. Lithostratigraphy and physical properties

Based on lithological variations, we distinguish five lithofacies associations (LFA 1-5) that overly bedrock. They are briefly characterized in the following.

5.1.1. Bedrock

The Quaternary strata (Fig. IV-2) overlie light micritic limestones of the Villigen Fm. in QGBR (contact in 111.5 m depth / at 225.8 m a.s.l.; Fig. IV-3) and QGVO (64.9 m depth / 266.1 m a.s.l.; Fig. IV-4), and olive grey calcareous marls of the Wildegg Fm., Effingen Member, in QUST (76.0 m depth / 255.2 m a.s.l.; Fig. IV-5; Gegg *et al.*, 2021) and QRIN (41.2 m depth / 337.6 m a.s.l.; Fig. IV-6). The limestone in QGBR is pervaded by paleokarst infilled with Paleogene sediment (Gegg *et al.*, 2020).

5.1.2. LFA 1 – Basal diamicts

Overlying the bedrock, all boreholes of our drilling campaign recovered basal diamicts (LFA 1) that can be subdivided into two subfacies associations LFA 1a and 1b. In the overdeepened Gebenstorf-Stilli Trough, these are soft to stiff and generally massive (LFA 1a; Figs. IV-2A, -3 to -5). The diamicts are 2.7 m thick in QGBR, 0.7 m in QGVO, and 1.3 m in QUST. They consist of mostly angular gravel clasts and cobbles embedded in a soft, yellowish grey to olive (partly blueish in QGBR) and clayey to sandy matrix, and can be clast- as well as matrix-supported. In QGBR and QGVO, LFA 1a contains occasional striated clasts, which were not encountered in QUST. The basal diamicts in QRIN are ~3.5 m thick and crudely bedded on a decimetre-scale (LFA 1b; Figs. IV-2B; -6). They comprise angular to well-rounded gravel clasts and cobbles in a stiff silty matrix of grey-beige to brown colour. In the top half, the diamicts are generally matrix-supported and contain frequent striated clasts, whereas the bottom half is clast-supported but lacks striated clasts.

Both basal diamicts are characterized by low water content (<15 %, <10 % in QRIN), intermediate to high bulk density (2.0-2.5 g/cm³), and intermediate gamma signals (30-50 API, 50-70 in QGBR). Magnetic susceptibility shows distinct peaks, with the exception of QUST, where the signal is generally low in the basal diamict. These peaks may relate to individual clasts, but we occasionally observe fragments of the drill bit, which create strong artificial peaks.

5.1.3. LFA 2 – Sandy gravels

5.1.3.1. Drill cores

Sandy gravels occur in all studied cores (LFA 2; Figs. IV-2C/D; -3 to -6) and generally consist of decimetre- to meter-scale beds that are frequently graded. They are yellowish to brownish grey; in QRIN we observe additionally rusty-orange grain coatings (36.8-35.8 m depth). Gravels overlying the basal diamicts in QGVO (64.2-55.8 m depth), QUST (bottom ~20 m), and QRIN (37.6-35.7 m) are poorly sorted with a significant silt and sand component, and contain massive or crudely bedded sand intercalations up to ~1 m in thickness. These basal gravels contain few striated clasts in QGVO and QRIN, and cemented nodules in QUST. The shallower gravels in QGBR (23.6-8.0 m depth), QGVO (17.4-0.0 m), and QUST (top ~20 m) consist of both poorly sorted intervals and well-sorted open framework-gravel as well as pure decimetre-scale sand layers. Individual clasts are predominantly rounded.

LFA 2 deposits have a high density (~2.5 g/cm^3), low gamma signals (frequently <25 API), and distinct, natural or artificial (see above), peaks in magnetic susceptibility. Water content ranges from ~10 % at the base of QRIN up to 30 % in near-surface samples.

5.1.3.2. Outcrops

Our study includes outcrops exposing sandy gravels attributed to the Tiefere Deckenschotter, Hochterrasse (with occasional interbedded diamicts), and Niederterrasse. Coordinates and brief descriptions of the studied outcrops are given in Table IV-S1, together with a list of all samples collected in the field.

5.1.4. LFA 3 – Massive and bedded sands and silts

Sand- and silt-dominated intervals (LFA 3) occur in QGBR, QGVO, and QRIN. Two subfacies associations LFA 3a and 3b can be distinguished. The successions of QGBR (108.8-23.6 m depth) and QGVO (55.8-17.4 m) largely consist of soft, yellowish to olive grey silty sands (LFA 3a; Figs. IV-3, -4) that are subdivided into massive (Fig. IV-2E) and well-bedded sections (Fig. IV-2F). The latter are characterized by 1-5 cm thick, olive-grey, coarse layers alternating with up to 2 cm thick, lighter yellowish grey, silt-dominated layers.

These bedded deposits are frequently deformed, including drilling-related drawdowns at the core edges but also convolution of the layering that may be unrelated to drilling-deformation. In QGVO, the LFA 3a section is interrupted by a coarse gravel (LFA 2) interbed from 28.3-26.5 m depth. Layers with infrequent dispersed gravel clasts occur throughout QGBR, and in the top half of QGVO (above 35 m depth). QGBR further recovered occasional decimetre- to meter-scale interbeds that are silt-dominated and, both below 80 m and above 45 m depth, frequently contain outsized clasts (Fig. IV-2G). Such a diamictic section also occurs at the top of LFA 3a in QGVO (22.3-17.4 m depth). There, individual *in situ*-cemented nodules have been encountered in the bottom 1 m.

The basal diamicts (LFA 1b) and gravels (LFA 2) in QRIN are overlain by ~2 m of very diverse, predominantly sandy deposits (LFA 3b, 35.7-33.5 m depth, Fig. IV-2H). They comprise crudely bedded sandy packages as well as finely laminated packages rich in silt and clay, and massive diamictic interbeds containing clasts up to medium gravel size. LFA 3b is brown-beige with orange-brown and greyish sections. These deposits contain several layers with cemented nodules and, close to their base, clay chips. The entire sections show abundant signs for deformation and convolution.

Densities of LFA 3 sediments are generally intermediate (2.0-2.2 g/cm^3), and magnetic susceptibility is low, with the exception of individual peaks especially in the top ~15 m of QGBR, which likely relate to outsized clasts. Gamma signals are low (<25 API) throughout QGVO, upward-declining (from >50 to <25 API) in QGBR, and elevated (~50 API) in QRIN. Water contents are between 15 and 30 % in QGVO and QRIN, and increase from 10-15 % to 15-20 % in QGBR.

5.1.5. LFA 4 – Bedded and laminated silts and clays

QRIN recovered ~26 m of fine-grained deposits comprising predominantly silt and clay with occasional, often graded, sandy layers (LFA 4). LFA 4 deposits do not occur in the other boreholes, but can be subdivided into four subunits LFA 4a-d in QRIN. The lowermost ~2.5 m (LFA 4a, 33.5-31.1 m depth, Fig. IV-2I) are crudely laminated/bedded on a millimetre- to centimetre scale with decimetre-thick massive packages and sandy interbeds. LFA 4a is brownish grey and locally intensively deformed resulting in a 'marbled' texture, which may be an original feature or drilling-induced.

It is overlain by ~8 m of thinly laminated, slightly sandy silts and clays with rhythmic bedding pattern of 2-3 cm thick olive grey packages of ~1-10 mm laminae alternating with ~5 mm thick, finer-grained and darker bands (LFA 4b, 31.1-23.4 m, Fig. IV-2J). The deposits are occasionally interrupted by up to 10 cm thick, sandy interbeds. Above a sharp colour change at ~26.1 m from dark brownish grey to lighter ochre-grey, a second rhythmic pattern of 3-4 cm thick orange-brown laminated packages every ~10 cm is superimposed onto LFA 4b. These packages (LFA 4c, 26.1-9.3 m, Fig. IV-2K/L) become progressively thinner but occur in increasing frequency and finally supersede LFA 4b entirely at ~23.4 m below ground.

LFA 4c fines are more homogeneous, with a relatively uniform fine lamination. While being orange-brown in alternating sequence with LFA 4b, they are medium beige-grey in colour where they are continuous (above ~23.4 m). In the upper half, above ~16.3 m, we observe four sub-meter intervals where the deposits are of a strikingly dark grey to black colour that fades to orange-brown upon oxidation. These intervals are more crudely bedded, softer and wetter than the remainder of LFA 4c. Near the top, ~10 m below ground, macroscopic plant fragments occur within a 30 cm thick, sandy intercalation. The uppermost ~2 m of fine-grained deposits in QRIN are again more diverse (LFA 4d, 9.3-7.4 m, Fig. IV-2M). They consist of interbedded laminated and massive packages of clay, silt, and sand with colours ranging from beige-grey to ochre-orange. At the very top, they contain again macroscopic plant fragments as well as cemented sand nodules.

Fine-grained deposits in QRIN are characterized by intermediate density (2.0-2.2 g/cm^3), elevated gamma signal (50-70 API in LFA 4a/b, ~50 API in LFA 4c/d), and low magnetic susceptibility with only minor distinct peaks that correlate with dark layers in the upper LFA 4c. Water contents are around 20-25 %, and more homogeneous in LFA 4c/d, where a slight upward increase is observed, than in LFA 4a/b.

5.1.6. LFA 5 – Cover diamicts

At the top of the respective successions, QGBR and QRIN recovered few meters of cover diamicts (LFA 5). In QGBR, these are 8.0 m thick and part of an anthropogenic waste deposit, with brick and metal fragments in an olive grey to black silt-dominated matrix. In QRIN we observe 7.4 m of predominantly beige to ochre-orange sandy diamicts (Fig. IV-2N). They are matrix-supported, thick-bedded (decimetres) with graded packages, and contain predominantly angular clasts that are locally covered by a fine rusty coat. Towards the surface, the matrix becomes progressively more fines-rich and brown. The cover diamicts in QRIN increase in gamma signal from ~25 to ~75 API from bottom to top, while density decreases from ~2.5 to ~2.0 g/cm3, and magnetic susceptibility remains generally low with only minor (low-intensity) peaks.

Fig. IV-2 (next page): Core photos representing lithofacies associations, width of all images is 10 cm. 2A: LFA 1a, massive sandy diamict at the base of QGVO (~64.4 m below ground). 2B: LFA 1b, matrix-supported, silt-dominated diamict (QRIN, 38.4 m). 2C: LFA 2, poorly sorted, fines-rich gravel (QUST, 65.6 m). 2D: LFA 2, sandy gravel fining upwards into sand (QGBR, 14.2 m). 2E: LFA 3a, massive sand with fine grained interbed (QGVO, 34.4 m). 2F: LFA 3a, silty sand with rhythmic bedding (QGBR, 55.6 m). 2G: LFA 3a, clayey sand with dispersed clasts, diamictic (QGBR, 101.9 m). 2H: LFA 3b, bedded clayey sand with cemented nodules (arrow; QRIN, 34.0 m). 2I: LFA 4a, crudely bedded, sandy silt and clay (QRIN, 31.2 m). 2J: LFA 4b, rhythmically banded silty clay (QRIN, 27.1 m). 2K: LFA 4b-4c transition: repeating orange-grey packages of LFA 4c (arrows) superimposed onto and, further upwards, gradually replacing LFA 4b sediments (see text; QRIN, 25.5 m). 2L: LFA 4c, laminated silty clay with occasional dark grey to black interbeds (QRIN, 15.8 m). 2M: LFA 4d, laminated, colourful sand, silt and clay (QRIN, 7.8 m). 2N: LFA 5, sandy diamict with rusty grain coatings (QRIN, 3.4 m). Note: anthropogenic waste deposits of QGBR are not displayed.

149
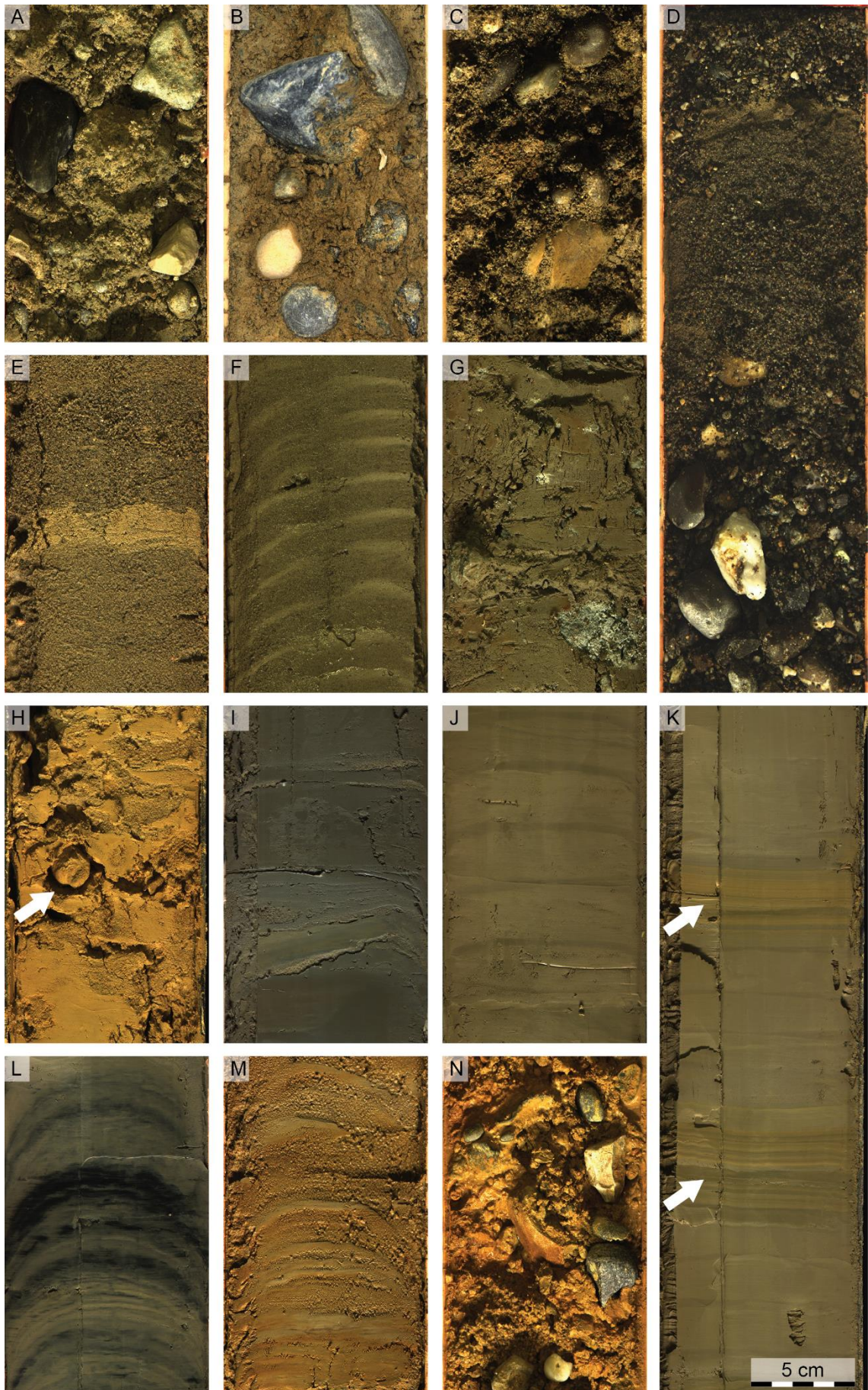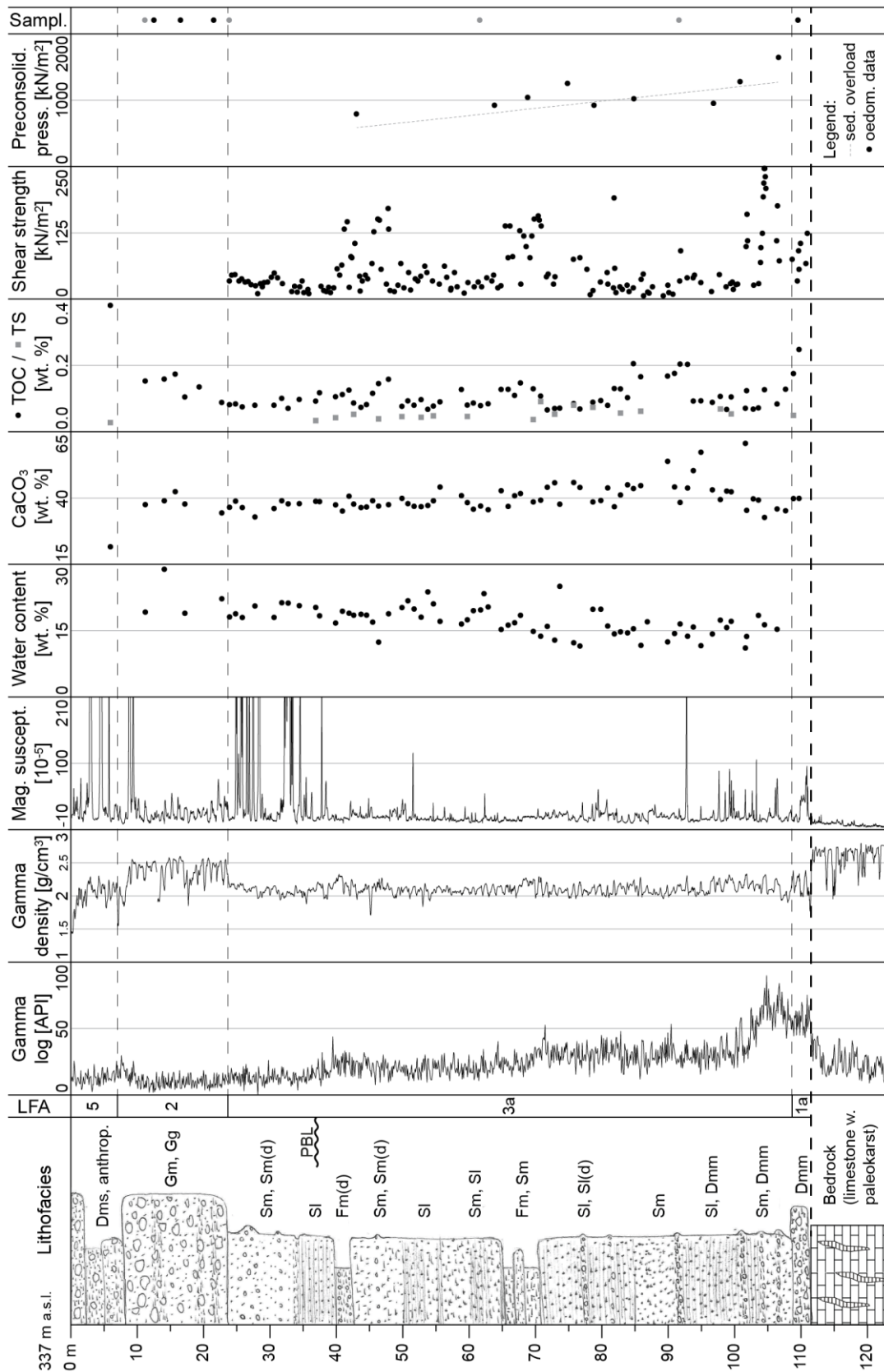
Fig. IV-3: Composite plot of borehole QGBR. Lithofacies codes refer to Eyles *et al.* (1983). PBL: lowest known Pleistocene base level (300 m a.s.l.; Graf, 2009). Samples: gravel petrography (black; see Table IV-S4) and luminescence (grey; Mueller *et al.,* in prep.).
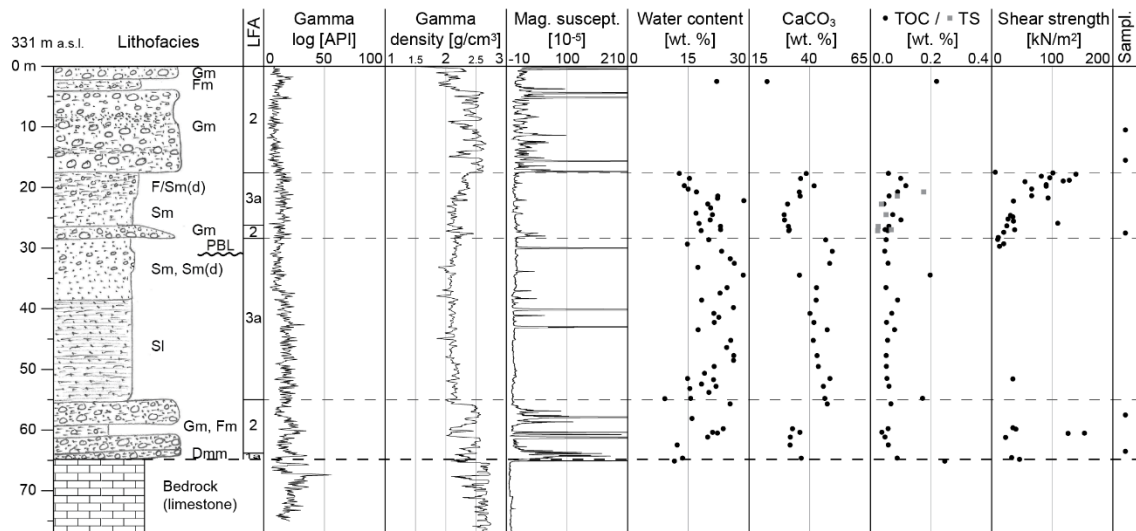
Fig. IV-4: Composite plot of borehole QGVO. Lithofacies codes refer to Eyles *et al.* (1983). PBL: lowest known Pleistocene base level (300 m a.s.l.; Graf, 2009). Samples: gravel petrography (see Table IV-S4).
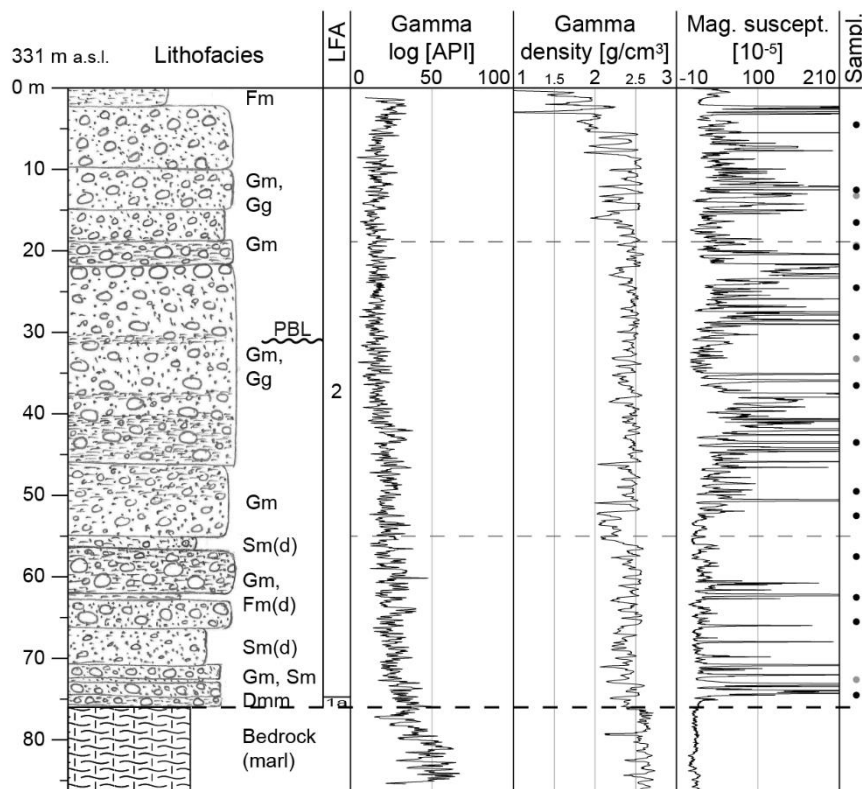
Fig. IV-5: Composite plot of borehole QUST. Lithofacies codes refer to Eyles *et al*. (1983). PBL: lowest known Pleistocene base level (300 m a.s.l.; Graf, 2009). Samples: gravel petrography (black; see Table IV-S4) and luminescence (grey; Mueller *et al.*, in prep.).
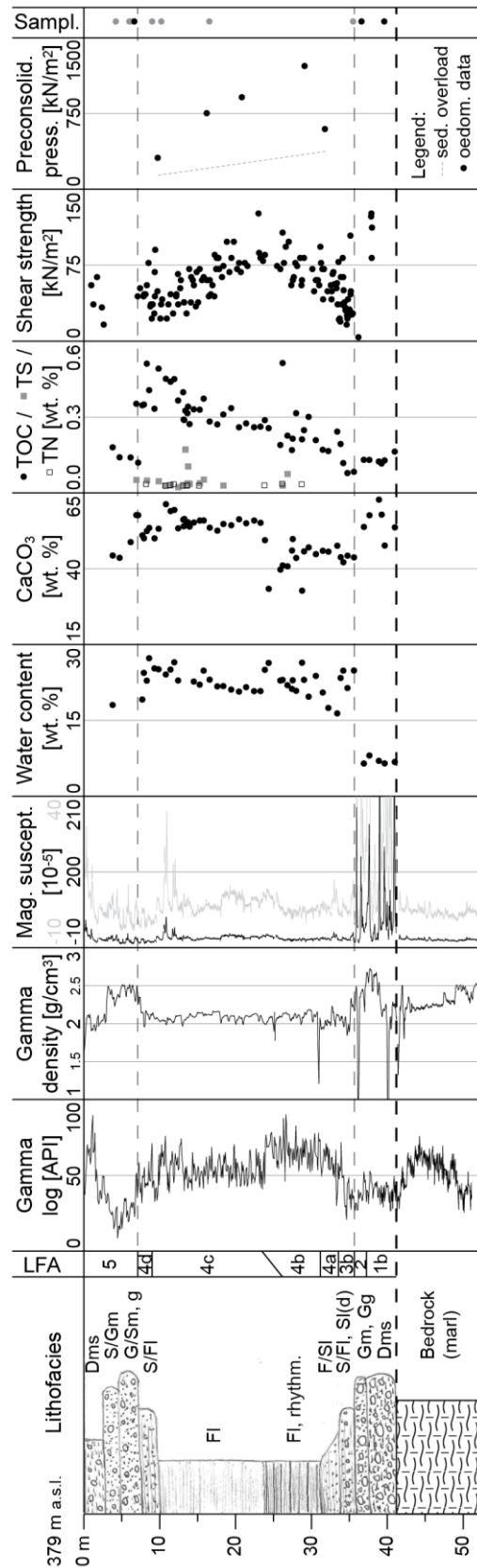
Fig. IV-6: Composite plot of borehole QRIN. Lithofacies codes refer to Eyles *et al.* (1983). Samples: gravel petrography (black; see Table IV-S4) and luminescence (grey; Mueller *et al.*, 2020).

5.2. Sediment composition

5.2.1. Geochemistry

Geochemical data are shown on Figs. IV-3, -4, and -6. LFA 3a sediments of QGBR and QGVO are characterized by TOC and TS values generally below 0.2 and 0.1 %, respectively. $CaCO_3$ content is generally ~40 %, but drops abruptly to ~30 % above the LFA 2 interbed of QGVO at 28.3-26.5 m depth (Fig. IV-4). In the fine-grained lacustrine sequence of QRIN, TOC increases gradually upcore from ~0.1 to ~0.5 % (Fig. IV-6). Both sulphur and nitrogen are detected in the upper parts of LFA 4b and LFA 4c/d, with maximum values below 0.2 %. A sharp upcore increase in $CaCO_3$ content from ~45 to ~55 % is observed at the LFA 4b-c transition (26.1-23.4 m depth; Fig. IV-6).

5.2.2. Gravel petrography

Gravel petrographic data are provided in Tables IV-S3 (drill cores) and -S4 (outcrops). Limestone clasts are generally most abundant, representing half to two thirds of most samples, followed by clastic sediments (sandstones and conglomerates; below one third), quartzites sensu lato (including vein quartz, cherts and radiolarites; below one third), and igneous clasts (below 10 %).

Principal component analysis (PCA) of the full dataset, *i.e.* integrating all lithology groups (Table IV-S2), clearly separates one sample from LFA 5 of QRIN (6.5-7.5 m depth; see section 6.2.2.3.) from the other samples based on its high content (>50 % as opposed to <20 %) in limestones of the Jura Mountains (Fig. IV-7, inset). In a second PCA excluding these limestones, which represent local erosion and reworking but are not indicative for an Alpine source, component 1 (PC1, x axis) distinguishes samples with high quartzite content (high PC1) from samples with a high content of siliceous Alpine limestones (Fig. IV-7; low PC1; both lithology groups have a correlation coefficient of -0.64). This distinction appears to be diagnostic for the sediment-delivering catchments, with high PC1 indicating a relatively increased Aare contribution, while lower PC1 indicate a relatively increased Reuss/Limmat contribution, as suggested by reference samples (green) from the Niederterrasse of the respective river valleys (see also Graf, 2009b). In contrast, component 2 (y axis) separates predominantly samples rich in Alpine limestones from samples rich in sandstones, and does not appear to be of catchment-diagnostic value.

A statistical distinction between the signals of Reuss and Limmat is difficult, but the latter is characterized by index lithologies (red sandstones: ~5 % in both Limmat reference samples, max. 1 % in Aare/Reuss reference samples; non-rhyolitic volcanics: ~1 % in both Limmat reference samples, none in Aare/Reuss reference samples; Table IV-S4; see also Graf, 2009b; Hantke, 1978).

An Aare-dominated petrography is thus inferred for all samples of QGBR and QRIN, while the samples of QGVO and QUST are interpreted to contain a considerable Reuss/Limmat component (Fig. IV-7). In QGVO, isolated red sandstones and/or non-rhyolitic volcanics were only sporadically encountered (except for the uppermost sample QGVO 10-11), whereas these lithologies occur more regularly in QUST, suggesting an increased Limmat influence in QUST compared to QGVO (Table IV-S4). In accordance with Graf (2009b), our data indicate further a rather variable mixed Aare/Reuss provenance for the Habsburg Gravel, and a well distinguishable Reuss/Limmat provenance for the Remigen Gravel in the HRPC (Fig. IV-7). The composition of the Hochterrasse further downstream the Aare Valley indicates a mixed provenance (Fig. IV-7). A Reuss-dominated petrography is further inferred for two samples of the Tiefere Deckenschotter of Bruggerberg, in agreement with the findings of Graf (1993). These results are generally confirmed by cluster analysis (Fig. IV-S1) as well as endmember analysis using the EMMAgeo package (Dietze and Dietze, 2019), which, in our case, appears to produce more reliable results than the RECA package (Seidel and Hlawitschka, 2015; Fig. IV-S2). Interestingly, both, cluster as well as endmember analysis, groups all samples of QGVO and QUST with Limmat reference samples, except for the gravel interbed of QGVO at ~28 m depth and the interval ~37-30 m depth of QUST, which are grouped with Reuss reference samples.

Fig. IV-7 (next page): Principal component analysis (PCA) of gravel petrographic data. The main plot includes all lithology groups except from locally derived (Jura Mountains) limestones, while the inset plot is based on PC analysis of the full dataset.
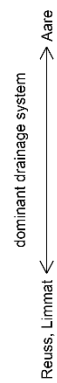
5.3. Geotechnical properties

5.3.1. Shear strength

In LFA 3a of QGBR, pocket vane testing revealed three distinct intervals (~40-50 m, ~65-70 m, and ~100-110 m) where shear strength is elevated from background values below 100 kPa up to 170 kPa, and in the deepest interval >250 kPa (Fig. IV-3). The upper LFA 3a section of QGVO shows upwards-increasing shear strength from ~20 to ~140 kPa (Fig. IV-4). Similarly, shear strength of QRIN deposits increases from ~20 kPa at the base of LFA 3b to ~130 kPa at the LFA 4b-4c boundary, but then decreases again to ~30 kPa at the top of LFA 4d (Fig. IV-6).

5.3.2. Preconsolidation pressure

Oedometer measurements from QGBR (9 samples) and QRIN (5 samples) were evaluated following the work per unit volume-approach by Becker *et al.* (1987) and the results compared to the calculated sediment overload in the present-day setting (Tables IV-1, -S5). Preconsolidation pressures determined for the QGBR samples are similar to the calculated overload (max. deviations -18 % / +35 %; Table IV-1; Fig. IV-3). In QRIN, preconsolidation pressures exceeding sediment overload by >250 % were determined for the intermediate three samples, and by 133 and 61 % for the uppermost and lowest sample, respectively (Table IV-1; Fig. IV-6). It should be noted that all samples of QGBR as well as the intermediate three samples of QRIN were recovered by rotary drilling, and both the uppermost and lowest QRIN sample by pneumatic hammering.

5.3.3. Atterberg Limits

10 QGBR samples, of which three proved to be sufficiently cohesive, and 6 QRIN samples were tested for Atterberg Limits (liquid limit LL and plastic limit PL; Table IV-S6). Results are plotted on Fig. IV-8. All samples plot above the A-line of Casagrande (1948), on or close to the T-line of glacial sediments (Boulton and Paul, 1976; Schlüchter, 1997; Trenter, 1999). The natural water contents (WC) of all samples lie between LL and PL, with the exception of QRIN 39.88, where WC is below the plastic limit (Table IV-S6). Liquidity indices LI ([WC-PL]/[LL-PL]; Schlüchter, 1984) range between 0.3-0.9 for all samples except QRIN 39.88, where LI is -0.8.

Table IV-1: Preconsolidation pressures determined from oedometer measurements of samples from QGBR and QRIN compared to the calculated present-day sediment overload (see also Figs. IV-3, -6).

QGBR			QRIN		
Depth [m]	**Sediment overload [kN/m²]**	**Prec. pressure [kN/m²]**	**Depth [m]**	**Sediment overload [kN/m²]**	**Prec. pressure [kN/m²]**
43.10	585	793 (+ 35 %)	9.65	134	312 (+ 133 %)
63.90	807	924 (+ 14 %)	16.26	203	751 (+ 270 %)
68.90	865	1042 (+ 20 %)	20.89	253	909 (+ 259 %)
74.90	927	1254 (+ 35 %)	29.15	342	1218 (+ 256 %)
78.90	973	924 (- 5 %)	31.88	369	594 (+ 61 %)
84.90	1033	1022 (- 1 %)			
96.90	1160	953 (- 18 %)			
100.90	1205	1281 (+ 6 %)			
106.90	1270	1646 (+ 30 %)			
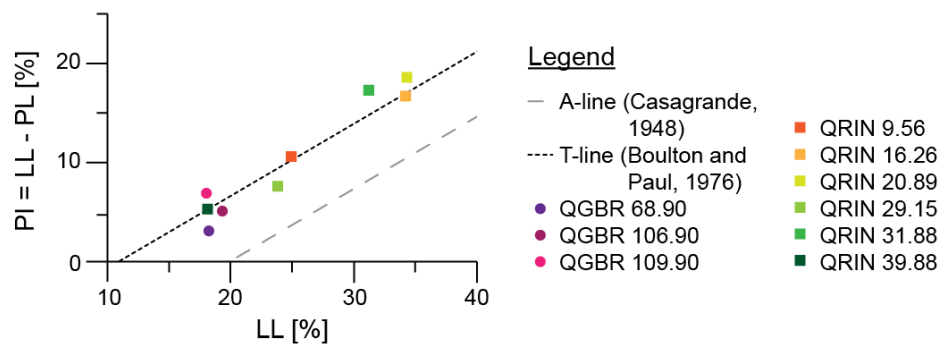
Fig. IV-8: Diagram plotting the Atterberg Limits of samples from QGBR and QRIN.

6. Discussion

6.1. Evolution of the overdeepened Gebenstorf-Stilli Trough

6.1.1. Subglacial erosion and onset of sedimentation

The Gebenstorf-Stilli Trough (GST) is one of two northward extensions of the Birrfeld Basin, and has been excavated in the context of an ice advance over the Birrfeld and the Jura fold-and-thrust belt along the present-day lower Reuss Valley (Gegg *et al.*, 2021). Following ice retreat, the Gebenstorf-Stilli Trough was infilled with diverse deposits reflecting its development after erosion. The sedimentary architecture is displayed on Fig. IV-9.
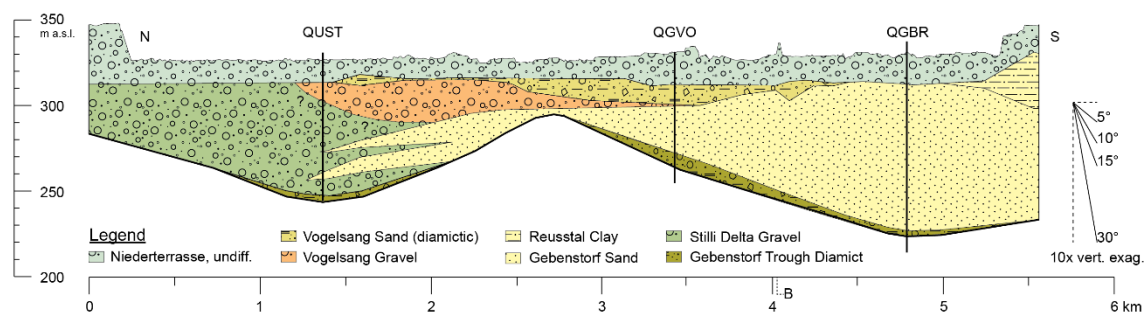
Fig. IV-9: Longitudinal section A (Gegg *et al.*, 2021, altered; see Fig. IV-1 for location) along the Gebenstorf-Stilli Trough. B: Intersection with profile B (Fig. IV-10).

Overlying the basal unconformity in the centre of the overdeepening, the Gebenstorf Trough Diamict comprises several metres of massive diamict and/or gravel (LFA 1a, 2). Striated clasts in QGBR and QGVO identify the diamict as an ice-derived deposit. In QGBR, the lowermost 0.5 m are stiff and compact, and may have been directly loaded by ice. In contrast, the remainder of the basal diamicts is more loose and soft, and has a water content >10 % (Fig. IV-4), which is larger than the sediment's plastic limit. This is consistent rather with waterlain glacigenic diamicts, *i.e.* deposits originating mainly from melt-out and subglacial mass movements, than overconsolidated subglacial tills dominated by processes such as lodgement (Evans *et al.*, 2006; Evans, 2007; Schlüchter, 1984, 1997). Although no (macroscopic) evidence for post-depositional deformation such as shear bands is observed, loading and homogenization by ice under high pore-water pressure, and thus low effective pressure can however not be excluded (Bell, 2002; Benn and Evans, 1996; Evans, 2007).

The basal infill of overdeepened basins typically contains metre- to decametre-thick basal glacigenic diamicts and till sequences (*e.g.* Lower Glatt Valley, Buechi *et al.* 2017; Birrfeld Basin, Dr. H. Jäckli AG and DMT GmbH & Co. KG, 2012; see also Nitsche *et al.*, 2001). In comparison, only little glacigenic diamicts were encountered in the GST, of which only a small percentage can be regarded as typical subglacial till. We explain this by efficient flushing of debris from the glacier base during erosion and ice occupation of the GST. The combined drainage area of Aare, Reuss, and Limmat delivered large amounts of melt water that passed through the narrow cross-section of the GST, while its sediments may have been largely retained by the Birrfeld Basin and the overdeepened reaches further up the Reuss Valley (Alley *et al.*, 1997; Alley *et al.*, 2019; Gegg *et al.*, 2021; Loepfe *et al.*, in prep.). The deposition of the Gebenstorf Trough Diamict reflects the cessation of this efficient flushing and thus the transition to subglacio-lacustrine conditions of the ice-decay rather than the pleniglacial phase.

6.1.3. Lacustrine phase

Above the basal diamicts, the several decametre-thick massive to bedded Gebenstorf Sand (LFA 3a) represents the glaciolacustrine infill of the overdeepening (Fig. IV-9). This interpretation is based on its uniform, entirely detrital sedimentology (Graf, 2009b), very low contents of organic material with TOC generally below 0.2 %, and no macro- and microfossils encountered (*cf.* Anselmetti *et al.*, 2010; Dehnert *et al.*, 2012). The dominant preservation of the sedimentary bedding further indicates a cold, inorganic environment without burrowing organisms (Zolitschka *et al.*, 2015). The lower part of the Gebenstorf Sand may have been partly emplaced under a floating, decaying glacier and thus incorporated some molten-out debris (Bitterli-Dreher *et al.*, 2007). A glacially-derived component in the basal Gebenstorf Sand is indicated by diamictic interbeds, their mechanical properties (Fig. IV-8; Boulton and Paul, 1976; Schlüchter, 1997; Trenter, 1999) as well as elevated gamma signals (>50 API) that are indicative for increased clay mineral content (Serra and Sulpice, 1975).

In contrast to several other records of overdeepened basin fills that also comprise thick units of basinal fines (Anselmetti *et al.*, 2010; Buechi *et al.*, 2017; Dehnert *et al.*, 2012), that of the GST is entirely sand-dominated. Only further south and stratigraphically higher up, a finer-grained Reusstal Clay occurs (Graf *et al.*, 2006; Graf and Burkhalter, 2016). This clay may have also been deposited and later eroded in the GST, which would correspond to an ancient lake level of at least ~330 m a.s.l. (Fig. IV-9). The preserved sandy infill of the trough indicates a comparatively glacier-proximal setting with high sediment input from three Alpine catchments. Massive LFA 3a sections point towards instabilities due to fast deposition and consequent soft-sediment deformation, but could also be drilling-related (Mills, 1983; Pisarska-Jamrozy and Weckwerth, 2013).

Especially in QGBR, the basin infill is horizontally well bedded, with darker, sand-dominated layers alternating with lighter and thinner, silt-dominated layers (Fig. IV-2F). These packages are encountered throughout the entire succession in relatively constant thickness of few centimetres. They are interpreted as clastic varves (Leonard, 1986; Peach and Perrie, 1975; Zolitschka *et al.*, 2015), and suggest an emplacement of the lacustrine sequence during a single, continuous phase over several thousand years. This is supported by the generally uniform sedimentology as well as by the only gradually changing geochemistry, *e.g.* $CaCO_3$ and TOC content (Fig. IV-3). However, repeatedly occurring intervals that are distinctly enriched in fines (and consequently of higher shear strength; Fig. IV-3) and/or contain dropstones may indicate centennial- to millennial-scale oscillations of a glacier front further south that influenced the sediment input into the basin (Chiverrell *et al.*, 2018; Smedley *et al.*, 2017). Consequently, Atterberg Limits of a sample from a diamictic bed at 68.9 m depth in QGBR suggest a glacially-derived component (Fig. IV-8; Boulton and Paul, 1976; Schlüchter, 1997; Trenter, 1999).

6.1.4. Origin of distal gravels

Overlying the Gebenstorf Trough Diamict, QUST recovered exclusively sandy gravel with occasional sand interbeds. Logs of more than a dozen previous boreholes in the study area confirm that the distal GST infill is generally gravelly (Stilli Delta Gravel; Fig. IV-9). Based on seismic and drilling data, we assume a total volume of these coarse-grained distal sediments of ~$5*10^7$ m³ (Fig. IV-9; Gegg *et al.*, 2021).

Two groundwater exploration boreholes (47°30'20" N, 8°14'11" E and 47°30'39" N, 8°14'04" E) further reveal an interdigitation of the Stilli Delta Gravel with the Gebenstorf Sand in the south, and thus a simultaneous deposition of both facies. The distal gravels of the GST must have been emplaced in a (glacio-)deltaic setting, which agrees well with the thick-bedded and frequently graded architecture (*e.g.* Gilbert *et al.*, 2017).

The petrographic composition of the gravels throughout QUST is dominated by far-travelled, Alpine lithologies (90 % and above; see Table IV-S3, Gegg *et al.*, 2021), precluding an origin from local erosion in the Jura Mountains. We also rule out reworking and redeposition of proglacial gravels from the Lower Aare Valley north of the GST, as there is no evidence for a temporary drainage reversal, such as index lithologies indicative for sediment input from the Hochrhein in the trough infill of QUST (*e.g.* rocks from the Black Forest, Hegau volcanics; Graf, 2009b). Counterintuitively, the Stilli Delta Gravel must have been deposited from upstream by glacial and/or glaciofluvial transport toward the distal trough end.

Near the trough base, a (sub-)glacial origin of the coarse-grained material, being transported towards the terminal slope of the overdeepening by water flow along the glacier base, cannot be excluded. However, further up the sequence, the gravels interfinger with well-sorted lacustrine sands that are likely not deposited in direct proximity to a glacier. The petrography of the Stilli Delta Gravel in QUST shows a strong Limmat signal (Table IV-S4; Figs. IV-S1, -S2), indicating that it has been delivered from the Limmat catchment laterally into the overdeepening, forming a gravel delta at the distal trough end, in front of the lacustrine sands. This hypothesis is plausible considering the bedrock morphology: Large parts of the Reuss Valley further south, *e.g.* the Birrfeld Basin (Fig. IV-1), are overdeepened and therefore prone to retain coarse-grained sediment, whereas in the Limmat Valley overdeepened sections occur only ~20 km upstream of the study area (Pietsch and Jordan, 2014), so that any coarse-grained material delivered into the valley in between would likely be transported into the GST.

6.1.5. Renewed ice advance

In contrast to the seemingly continuous sedimentology in QGBR and QUST, the Gebenstorf Sand is sharply overlain by a ~2 m-thick gravelly intercalation (Vogelsang Gravel) in QGVO at ~28 m depth (Fig. IV-9). This interbed coincides with an abrupt upsection decrease in $CaCO_3$ and a significant increase in fines as well as outsized gravel clasts (Fig. IV-4) that signals a drastic change in the basin sedimentation. A striated dark limestone clast at the top of the gravel bed together with the diamictic character of the overlying LFA 3a deposits (Vogelsang Sand; Fig. IV-9) indicates glacier proximity. This points towards a re-advance close to, and possibly over, the site of QGVO (although a reworking of older deposits, *e.g.* by a mass movement in the Tiefere Deckenschotter at Bruggerberg, cannot be excluded).

While this facies change occurs in several boreholes near QGVO, it is missing in the record of QGBR, where we observe no indication for a renewed ice contact. There, the upper Gebenstorf Sand is softer than in QGVO, and preconsolidation pressures determined by oedometer testing throughout the borehole are close to the present-day sediment overload indicating that the lacustrine succession has not been overconsolidated (Fig. IV-3; O'Regan *et al.*, 2016; Van Gelder *et al.*, 1990), and no indication for discrete water escape, such as subglacial hydrofractures, is observed (Van der Meer *et al.*, 2009). Therefore, it would seem plausible that the sedimentological break in QGVO is the result of a lateral advance into the GST, *e.g.* along the Limmat Valley. However, we need to stress that the dominantly sandy facies is not ideally suited for determination of preconsolidation pressures. In addition, its petrographic composition (Figs. IV-S1, -S2) indicates that the Vogelsang Gravel has a rather Reuss-dominated petrography, which speaks for an axial advance along the Reuss Valley and over the GST.

Whether this advance occurred during the same glacial cycle and only briefly after deposition of the underlying Gebenstorf Sand, or after a considerable hiatus, cannot be determined from the sedimentary facies. The same applies to the location of the boundary between Stilli Delta Gravel and Vogelsang Gravel (Fig. IV-9).

6.1.6. Post-lacustrine phase

The (glacio-)lacustrine infill of the GST is sharply truncated and overlain by ~15 m of Niederterrasse gravels (Graf *et al.*, 2006). Interglacial deposits, peat and/or soil have not been recovered in between. Borehole data indicate that the Niederterrasse gravels fill gentle channels incised into the lake deposits (Fig. IV-10; Gegg *et al.*, 2021). Several boreholes at the northern end of the GST further recovered limestone blocks at ~320 m a.s.l. (317.2 m a.s.l. or 13.9 m depth in QUST), which indicates an important event horizon near the base of the Niederterrasse (lying at ~313 m a.s.l.). Anthropogenic waste in the cover diamicts of QGBR identifies this material as a recent waste deposit (see also Graf *et al.*, 2006).

6.2. Evolution of the Habsburg-Rinikerfeld Paleochannel

6.2.1. Glacial and glaciofluvial activity

At the base of the HRPC, borehole QRIN recovered ~3.5 m of crudely bedded glacial diamicts overlain by ~2 m of poorly sorted gravels with a near-identical Aare-dominated petrographic composition. It is very similar to, and we thus suggest a correlation with, the Habsburg Gravel (Figs. IV-6, -7, -10). Gravel and underlying till could represent two different glacial cycles as has previously been assumed (Bitterli-Dreher *et al.*, 2007; Graf, 2009b), whose ice advances had equivalent provenances. However, it appears more likely that the two units have been deposited during the same glaciation, and that this glaciation advanced into and possibly beyond the Rinikerfeld. In their upper half (QRIN 37.6-39.1 m depth), the diamicts contain frequent faceted and striated clasts dispersed in a silty-sandy matrix, evidence for a direct ice contact (Evans *et al.*, 2006; Evans, 2007). In contrast, the lower half of the diamicts is clast-supported and lacks striated clasts, and may be interpreted as a mixture of glacigenic diamicts and proximal glaciofluvial gravels deposited in front of the advancing glacier. A negative liquidity index classifies the sediment as an overconsolidated till (Schlüchter, 1984).

The Remigen Gravel occurs on top of the Habsburg Gravel, occasionally in the shape of an incised channel infill (Fig. IV-11; Graf, 2009b; Graf *et al.*, 2006; Preusser *et al.*, 2011). It can be separated from the Habsburg Gravel based on its Reuss/Limmat-dominated petrography.

One sample attributed to the Habsburg Gravel north of Brugg (HS-Hfs; Table IV-S1; Graf *et al.*, 2006) is thus identified as Remigen Gravel based on petrographic composition (suggesting that the respective channel is slightly wider than previously assumed). The same applies to gravels outcropping in the Götschtel pit further south (Habsburg Gravel in Graf *et al.*, 2006) but attributed to the Remigen Gravel in Graf (2009b). The minimum ice extent during the according glaciation is documented from the northern margin of the Rinikerfeld by intercalated glacial deposits close to the former gravel pit at Alpberg (Fig. IV-10; Table IV-S2).
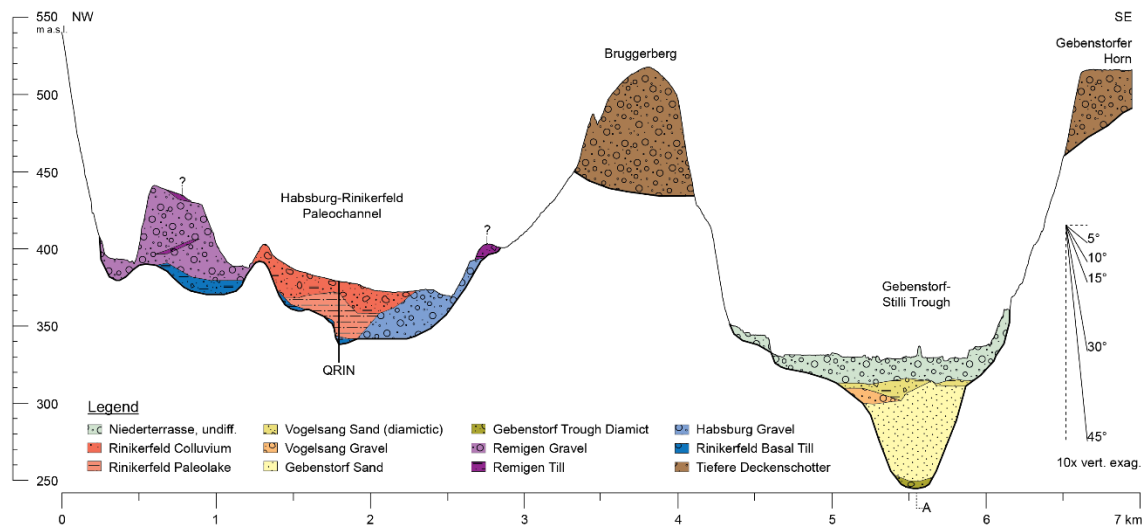
Fig. IV-10: Cross-section B (see Fig. IV-1 for location) through the study area illustrating the stratigraphy of the HRPC and the overdeepened GST. A: Intersection with profile A (Fig. IV-9).
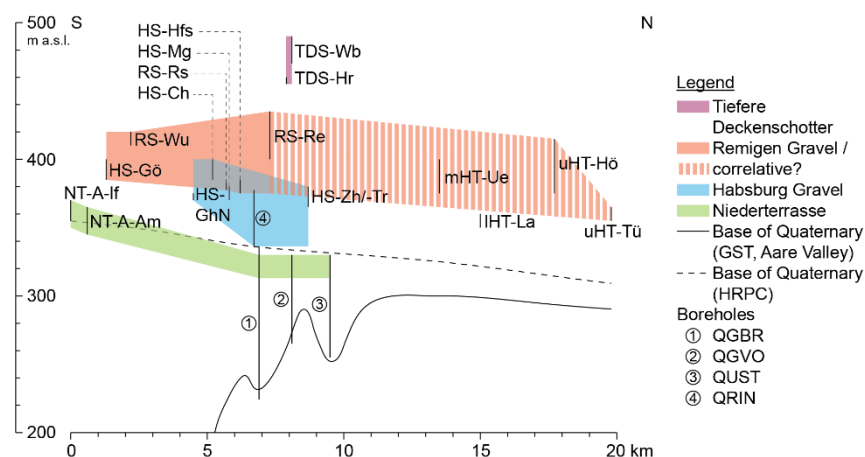
Fig. IV-11: Schematic longitudinal profile through the study area, from the Folded Jura in the south to the Hochrhein in the north (*cf.* Fig. IV-1). Polygons visualize the outcrop/drilled elevations of the different gravel units. Base of Quaternary from Loepfe *et al.* (in prep.).

164

The Remigen Gravel has been overridden by a later ice advance, as indicated by a till cap in the Alpberg pit as well as glaciotectonic deformations and crushed grains in the Götschtel pit. Evidence for an ice contact in the shape of striated clasts and conglomerate blocks is also encountered at the top of the Upper Hochterrasse in the Hönger gravel pit (Table IV-S1; Bugmann, 1961; Graf, 2009b). This unit is interpreted as a correlative to the Habsburg Gravel by Graf (2009b) but with a different, mixed Aare/Reuss/Limmat/Rhine petrography that is supported by our compositional data (Fig. IV-7; few schist clasts and an individual serpentinite are potential indicators for a Rhine component; Table IV-S4; Hantke, 1978). Based on the outcrop elevations and the ice contact at the top of both units, but predoimnantly dating results (section 6.3) we correlate the Upper Hochterrasse to the Remigen Gravel, while we suggest that the elevation of the Habsburg Gravel might correspond better to the Middle and Lower Hochterrasse (Fig. IV-11).

6.2.2. Lake formation in the Rinikerfeld

6.2.2.1. Lake establishment and initial sedimentation

Previous drillings have revealed the existence of a buried paleolake in the northern HRPC (local name Rinikerfeld). The Rinikerfeld Paleolake extends over ~1.5 x 0.5 km^2, its deposits are ~30 m thick and surrounded by glacial and glaciofluvial deposits (Fig. IV-10). The paleolake has been interpreted as part of an ice-decay landscape related to an early Mid-Pleistocene glaciation that predated the Habsburg Gravel (Bitterli-Dreher *et al.*, 2007; Graf, 2009b). Overlying till and glaciofluvial (presumably Habsburg-) gravel, the lacustrine sequence in QRIN starts with ~2 m of predominantly sandy deposits that are diverse in composition, with gravelly and silty, partly graded layers, and convoluted bedding (LFA 3b; Fig. IV-6). This speaks for lacustrine sedimentation dominated by small-scale mass wasting and traction currents, while clay chips indicate occasional high-energy events. Clear evidence for an ice contact is lacking (see also below), but the sedimentary facies is compatible with an ice-decay setting. The Rinikerfeld Paleolake may thus have originated as a kettle hole (Fleisher, 1986; Krüger *et al.*, 2010) or may have been dammed by a moraine ridge or landslide body (Carrivick and Tweed, 2013).

6.2.2.2. Lacustrine phase

At ~33.5 m below ground, the LFA 3b deposits of QRIN are sharply overlain by a ~26 m thick succession of relatively homogeneous lacustrine fines. The lowermost ~2.5 m (LFA 4a) have a rather crude and thick bedding and sand interbeds that, together with presumed soft-sediment deformation features (drilling-induced deformation cannot be excluded), suggests a high sedimentation rate (Mills, 1983; Pisarska-Jamrozy and Weckwerth, 2013). However, the well sorted nature of the deposits and the absence of dropstones indicates that the Rinikerfeld Paleolake was not an ice-contact lake. Above (31.0-23.4 m depth; LFA 4b), the lacustrine fines are clay-dominated and well bedded/laminated. The excellent preservation of the laminations, the lack of macrofossils (except from plant fragments towards the top of the lacustrine sequence) and autigenic calcite as well as the low TOC values (max. ~0.5 %; Fig. IV-6) support its interpretation as a continuously cold (glacial/stadial) lake (Anselmetti *et al.*, 2010; Dehnert *et al.*, 2012; Vogel *et al.*, 2010). A rhythmic pattern of ~5 mm thick, finer-grained dark bands every 2-3 cm indicates detrital varves (Leonard, 1986; Zolitschka *et al.*, 2015) whose summer layers have been deposited in several sediment-input events, *e.g.* phases of increased snowmelt. This interpretation suggests a sedimentation rate of few cm/yr, corresponding to deposition of this lacustrine section over few hundred years. The dark olive-grey colour and homogeneous facies of LFA 4b suggest deposition under reducing conditions in a stable, meromictic lake of considerable depth (*cf.* Anderson, 1985; Van Dijk *et al.*, 1978).

The LFA 4b-4c transition is characterised by an increasing $CaCO_3$ content coinciding with an abrupt drop in the gamma log (~45 to ~55 % and ~65 to ~50 API, respectively; Fig. 6). This indicates a change in sediment input that could represent a transition from an (indirectly) glacier-fed towards a more locally dominated lake, fed by runoff from the limestones and calcareous marls of the Jura Mountains (Karlén and Matthews, 1992). This transition could be explained by an abandonment of the Rinikerfeld by the previously occupying glacier, and drainage rerouting into a new channel, which would likely involve a sharp decrease in sedimentation rate (Regnéll *et al.*, 2019; Svendsen *et al.*, 2019). The modern Lower Aare Valley would be a plausible candidate for this new channel (Fig. 10).

LFA 4c first occurs in the shape of repeating, few cm thick orange-brown laminated packages starting at 26.1 m depth, which could represent more oxygenated conditions that became more frequent, and lastly continuous, at 23.4 m depth, and that may be explained *e.g.* by episodic lake-level fluctuations or increased mixing by wind (Moscariello *et al.*, 1998; Wennrich *et al.*, 2014). The sediments of LFA 4c are finely laminated with alternating lighter and darker layers that are significantly finer and less uniform than in LFA 4b, and that are interpreted as varves but with a lower and more variable sedimentation rate on the order of few mm/yr. Individual layers can be olive-grey or brownish, indicating fluctuating oxygenation (Van Dijk *et al.*, 1978). Occasional intercalated sand layers indicate higher-energy sedimentation events typical for a floodplain setting (Asselman and Middelkoop, 1995; He and Walling, 1998; Huybrechts, 2000). Assuming that the HRPC was abandoned in favour of the modern Lower Aare Valley during the lifetime of the paleolake, it is not unlikely that the Rinikerfeld was occasionally inundated by overbank floods from the new river valley that delivered fine-grained sediments from the catchment.

A distinct upward-increasing trend in TOC in the Rinikerfeld Paleolake illustrates ameliorating climate conditions (Fig. IV-6). Above ~16.3 m depth, dark grey to black intervals occur that, when exposed to air, quickly fade to a rusty brown, which indicates that the colour is due to finely dispersed sulphides (Rickard *et al.*, 2017). These intervals thus provide first macroscopic indications for organic matter, but possibly also for mild bioturbation as they are much more crudely bedded than the remainder of LFA 4c (Berner, 1985; Suits and Wilkin, 1998). They are overlain by macroscopic plant fragments occurring ~10 m below ground where the lacustrine fines become more diverse, with laminated and massive packages of clay, silt, and sand, and colours ranging from beige-grey to ochre-orange (LFA 4d). This marks the transition from a now silted-up lake basin to a shore setting, whose deposits, terminating 7.4 m below ground, contain again macroscopic plant fragments and may periodically have been subaerially exposed (Urban and Bigga, 2015). The inferred sedimentation rates of initially few cm/yr (LFA 4b), and later few mm/yr (LFA 4c) indicate a lifetime of the Rinikerfeld Paleolake of few thousand years.

6.2.2.3. Post-lacustrine phase

The sediments of the Rinikerfeld Paleolake is overlain by 7.4 m of thick-bedded matrix-supported diamicts whose petrographic spectrum consists of >50 % light limestones derived locally from the Mesozoic rocks of the Jura Mountains (Table IV-S3). The diamicts contain predominantly angular clasts without striations, and are very sandy but poor in silt and clay, which makes both a pure fluvial and a pure glacial origin implausible. Together, these characteristics are indicative for periglacial slope deposits (PSD), *i.e.* the products of frost cracking, cryoturbation, solifluction and/or debris flows (Raab *et al.*, 2007; Veit *et al.*, 2017), and we thus refer to these diamicts as Rinikerfeld Colluvium (Fig. IV-10). It is questionable whether active (glacio-)fluvial input into the Rinikerfeld Colluvium occurred. Reworking of older gravels appears to be the more likely explanation for the occurrence of well-sorted, far-travelled clasts. Compared to last-glacial PSD, those of the Rinikerfeld are strikingly thick, suggesting intensive subaerial erosion and redeposition during the time of their deposition (Mailänder and Veit, 2001).

Preconsolidation pressures determined for five sediment samples of the Rinikerfeld Paleolake are significantly higher than the present-day overload (Fig. IV-6, Table IV-S5). The three intermediate samples, recovered by wireline coring, show preconsolidation pressures that exceed their overload by >500 kN/m^2 or >250 %. These values can be explained by overconsolidation under >20/40 m of dry/water-saturated sediment that has since been eroded, or >50 m of glacier ice (O'Regan *et al.*, 2016; Van Gelder *et al.*, 1990). The topmost (9.65 m) and lowermost sample (31.88 m), recovered by pneumatic hammering, exceed the respective overload by ~200 kN/m^2 or 60-130 %, corresponding to ~10/20 m of dry/water-saturated sediment or ~20 m of glacier ice.

The overconsolidation recorded in the lacustrine deposits is enigmatic as we observe neither sedimentological indication for loading by ice (*e.g.* ice-contact deposits, glaciotectonism, fluid-escape structures; O'Regan *et al.*, 2016; Van der Meer *et al.*, 2009), nor potential gaps in the seemingly continuous Quaternary succession (see discussion above). It is possible that the overconsolidation is a result of freezing and thawing of the sediment (Alkire, 1981; Chamberlain, 1981; Qi *et al.*, 2006), which could also account for the shear-strength pattern that shows a distinct peak at the LFA 4b/4c boundary (Fig. IV-6), where generally lowering and fluctuating water levels are inferred.

6.3. Chronology

Several stratigraphic units of the Lower Aare Valley have recently been luminescence-dated by Mueller *et al.* (2020, in prep.), based on a combined approach analysing quartz, feldspar, and polymineral fractions. These studies revealed that the record of both, the overdeepened Gebenstorf-Stilli Trough (GST, Remigen Gravel) and the Habsburg-Rinikerfeld Paleochannel (HRPC; Gebenstorf Sand and Stilli Delta Gravel), reach back to at least MIS 10 (Fig. IV-12; Mueller *et al.*, in prep.).

Combining luminescence ages with sedimentology and sediment petrography, the Mid-Pleistocene environmental history of the Lower Aare Valley, and the confluence area with Reuss and Limmat, can be reconstructed. The minimum MIS 10 age of the GST incision suggests that the formation of the Birrfeld Basin started latest in MIS 12 (Graf, 2009b). Similarly, the Habsburg Gravel underlying the Remigen Gravel (see below), the supposedly correlative Rinikerfeld Basal Till, as well as the HRPC itself likely date back to MIS 12 or earlier (Graf, 2009b; Preusser *et al.*, 2011). The Aare-dominated petrography of the Habsburg Gravel identifies the HRPC as an ancient Aare riverbed (Fig. IV-7; Graf, 2009b), and the Rinikerfeld Basal Till indicates a pre-MIS 10 (MIS 12?) advance of the Aare glacier into the paleochannel.

The oldest directly dated deposits of the Lower Aare Valley have been deposited during MIS 10 (Habsburg Glaciation?; Mueller *et al.*, in prep.). These include the majority of the GST infill as well as the Remigen Gravel (1) of Alpberg (Rinikerfeld; Fig. IV-12).

It is noteworthy that the Habsburg Gravel predates the Remigen Gravel and thus, according to these new data, also the period tentatively referred to as Habsburg Glaciation (Graf, 2009b; Preusser *et al.*, 2021; Preusser *et al.*, 2011). The excavation of the GST requires a minimum ice extent beyond the trough terminus that is in accordance with intercalated tills in the Alpberg gravel pit (Fig. IV-1). Along the GST, we observe a change in sediment composition from an Aare/Reuss dominance (QGBR, QGVO) to a Limmat signal (QUST; see section 5.2.2, Table IV-S4). This suggests that the confluence of the Limmat catchment with the Aare/Reuss catchment occurred close to its present-day location (Figs. IV-1, -12; see also Gegg *et al.*, 2021).

The Remigen Gravel (2) in the Götschtel pit as well as the Upper High Terrace at Hönger have been dated to MIS 8 (Hagenholz Glaciation?; Fig. IV-12; Mueller *et al.*, in prep.). It appears that the Remigen Gravel comprises sediments related to at least two different glaciations (Fig. IV-12). The sediment at both localities is comparatively well sorted with pure sand layers, and no intercalated tills occur, compatible with a moderate ice extent inside the LGM as suggested by Graf (2009b). Gravel compositions of the Remigen Gravel suggest that these deposits generally represent a variable, mixed Reuss/Limmat facies. Our limited petrographic data indicate that the supposedly older (MIS 10) deposit could tend more towards a Reuss, and the younger (MIS 8) deposit more towards a Limmat composition (Figs. IV-7, -S1, -S2, Table IV-S4), but more samples would be needed to test this hypothesis. Further, it is questionable how Limmat-derived material could be deposited as far west as at the Götschtel site (Fig. IV-1).

An MIS 6 age has been inferred for one gravel sample below the Niederterrasse of QUST (Fig. IV-12; Mueller *et al.*, in prep.). We interpret this by the excavation of an inlaid basin inside the GST, and correlate the respective interval to the Vogelsang Gravel and Sand of QGVO (Fig. IV-9). The gravel petrography of the respective deposits indicates that this inlaid basin was mainly excavated by and infilled from the Reuss Glacier (Figs. IV-7, -S1, -S2).

A minimum glacier extent near Stilli (Fig. IV-1) is thus inferred for the Beringen Glaciation, but the MIS 6 glaciers advanced over the entire study area and beyond the Hochrhein (Fig. IV-12; Graf, 2009b; Preusser *et al.*, 2011), which is supported by glacigenic deposits at the top of the Hönger gravel pit (Upper Hochterrasse, Fig. IV-1). This makes it unlikely that the site of QGBR has not been overridden as well, and we suggest that the Gebenstorf Sand is - despite its fines content - not suitable for the determination of preconsolidation pressures (see section 6.1.5). Further MIS 6 ages are attributed to the Rinikerfeld Paleolake and Colluvium (Mueller *et al.*, 2020) that were deposited in the HRPC in a periglacial setting during/after ice retreat. To our knowledge, no younger glacial or glaciofluvial deposits exist within the paleochannel. Therefore, we hypothesize that, despite the GST being incised presumably already during MIS 10, the modern Aare Valley was deepened below the level of the HRPC, and the latter abandoned, only in late MIS 6.

The Niederterrasse of QGBR and QUST have been assigned MIS 4 and MIS 5d ages, respectively, the former thus correlating to the Mülligen Gravel of the Birrfeld Basin (Preusser and Graf, 2002). MIS 2 (LGM) ages have not been determined (Mueller *et al.*, in prep.).
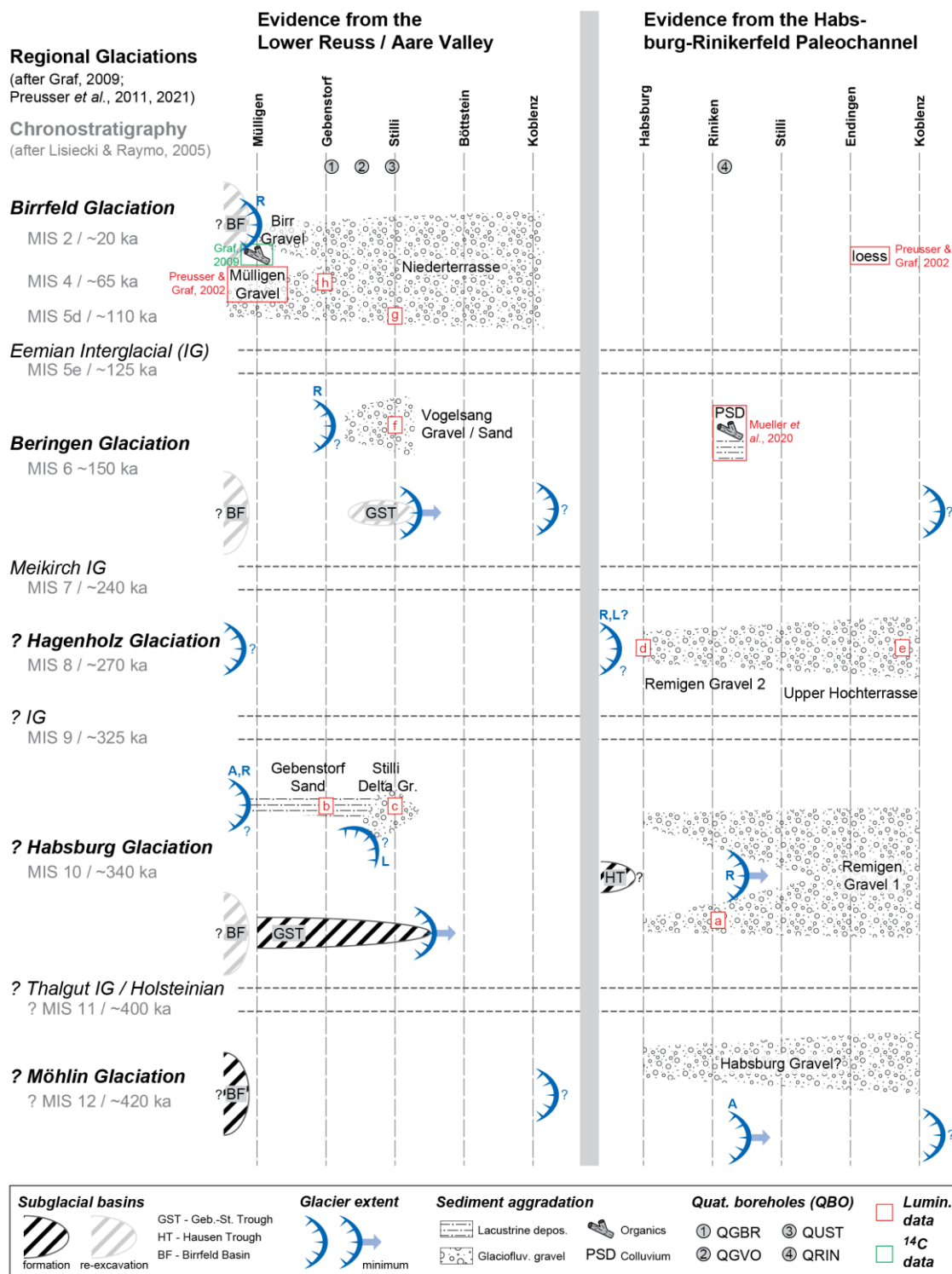
Fig. IV-12: Reconstruction of the glaciation history of the Lower Aare Valley area (scheme after Buechi *et al.*, 2017). Displayed are major phases of overdeepening erosion and sediment aggradation, and the respective reconstructed glacier extents (A: Aare, R: Reuss, L: Limmat). Chronological data a-h are taken from Mueller *et al.* (in prep.); a: Alpberg pit, b: QGBR 23.9-91.6 m depth, c: QUST 33.2-72.7 m, d: Götschtel pit, e: Hönger pit, f: QUST 19.2 m, g: QUST 13.2 m, h: QGBR 11.2 m. For locations, please refer to Fig. IV-1.

172

7. Synthesis

7.1. Integration into the regional stratigraphic record

The ample Quaternary record of the Lower Aare Valley complements and significantly expands our knowledge of the regional landscape and glaciation history (Graf, 2009b; Preusser *et al.*, 2011), as it comprises some of the first deposits of the Swiss Alpine foreland confidently dated to Mid-Pleistocene glaciations predating the Beringen Glaciation (as old as MIS 10; Mueller *et al.*, in prep.). Beyond that, sediment units (Habsburg Gravel, Rinikerfeld Basal Till) and large-scale landforms (Birrfeld Basin, HRPC) exist that are presumably yet older (Graf, 2009b; Preusser *et al.*, 2011). For their formation, MIS 12, tentatively connected to the Möhlin Glaciation (*i.e.* the supposed Most Extensive Glaciation of the Swiss Alpine foreland, see Fig. IV-1; Preusser *et al.*, 2021), is a plausible candidate (Fig. IV-12).

The Remigen Gravel 1 at Alpberg as well as the Gebenstorf-Stilli Trough and large parts of its infill trace a major erosive Alpine ice advance into the foreland during the Habsburg (?) Glaciation (MIS 10) that exceeded the LGM ice limit in the study area by ≥10 km. Similar ice extent, as well as the erosion and infilling of an overdeepening, have been tentatively inferred for the Habsburg Glaciation in the Lower Glatt Valley (Buechi *et al.*, 2017). In the Thalgut gravel pit (Aare Valley south of Bern; Schlüchter, 1989a, b), lake deposits with an inferred MIS 11 age are conformably overlain by a glaciofluvial delta complex and waterlain till (Preusser *et al.*, 2005) that may thus also correlate to the Habsburg (?) Glaciation.

Despite the probably rather limited ice extent (Graf, 2009b; Preusser *et al.*, 2011), the Hagenholz (?) Glaciation (MIS 8) delivered large amounts of meltwater gravel into the Lower Aare Valley (Remigen Gravel 2 at Götschtel, Untere Hochterrasse at Hönger; Mueller *et al.*, in prep.). The same has been suggested by Buechi *et al.* (2017) for the Lower Glatt Valley, and by Claude *et al.* (2017) for the Hochrhein Valley near Basel. A possibly correlative waterlain till underlies an MIS 7-paleolake in the Meikirch borehole (Aare Valley north of Bern; Preusser *et al.*, 2005).

The Beringen Glaciation (MIS 6) is well represented in other foreland records in the shape of both glaciofluvial outwash and glaciolacustrine basin infills (Anselmetti *et al.*, 2010; Buechi *et al.*, 2017; Dehnert *et al.*, 2010, 2012; Preusser and Schlüchter, 2004). Petrographic evidence further indicates the build-up and expansion of local ice caps in the Jura Mountains (Graf *et al.*, 2015) and in the Black Forest (Graf, 2009b). The glaciofluvial gravels of the Klettgau (Hochrhein Valley) record an especially complex and dynamic Beringen Glaciation: here, Lowick *et al.* (2015) identified up to four different ice advances during MIS 6 (and possibly MIS 5d). In contrast, the Beringen Glaciation left only little remains behind in the Lower Aare Valley, namely the infill of a minor inlaid basin within the GST (Mueller *et al.*, in prep.) and periglacial lacustrine and colluvial deposits in the Rinikerfeld (Mueller *et al.*, 2020). However, we consider plausible that the HRPC was abandoned in late MIS 6 due to significant erosion along, and deepening of, the modern Lower Aare Valley in the Beringen Glaciation.

Two samples from the Niederterrasse of the Lower Aare Valley yielded MIS 5d and MIS 4 ages, but none corresponding to MIS 2 (LGM; Mueller *et al.*, in prep.). These dates support a trinity of Late Pleistocene ice advances in the Western Alps that are all associated with substantial sediment production and deposition in the foreland (Chaline and Jerz, 1984; Ivy-Ochs *et al.*, 2008; Preusser *et al.*, 2011). Further evidence for early and middle Late Pleistocene glaciofluvial activity has been presented by Preusser *et al.* (2003), Preusser and Schlüchter (2004), Lowick *et al.* (2015), and Preusser and Graf (2002), Preusser *et al.* (2007), respectively.

7.2. Implications of the local setting for Quaternary stratigraphy

The Lower Aare Valley area stands out from the majority of other Quaternary sites in the Swiss Alpine foreland due to its local geological and topographic setting. While many well-studied localities are situated in the Molasse Basin, the GST and HRPC lie within the southeastern foothills of the Jura mountains. Here, in diverse but generally rather erosion-resistant Mesozoic rocks, an area of considerably increased relief developed (Yanites *et al.*, 2017) with morphologically well-defined and stable valleys (Ziegler and Fraefel, 2009).

As a result, the Pleistocene ice advances and meltwater streams were not only topographically constrained (Gegg *et al.*, 2021) but also repeatedly directed along the same pathways. This is illustrated i) by the remnants of at least three, but likely four or more, different glaciations occurring in the HRPC, and by ii) the Limmat-Aare confluence being established at its present-day location already in MIS 10, as revealed by the infill of the GST.

One consequence of the repeated occupation of the same valleys is a complex, intertwined stratigraphy whose components are difficult to identify and resolve. This is well exemplified by the finding that the Remigen Gravel appears to comprise deposits of at least two separate glaciations. However, the comprehensiveness of the Quaternary record in our study area spanning four glacial cycles at the minimum is rather surprising in light of its special setting. One might expect that multiple phases of glacial and/or glaciofluvial reactivation could have effectively obliterated older Pleistocene deposits in the GST and HRPC (Buechi *et al.*, 2017; Hughes *et al.*, 2019; Merritt *et al.*, 2019), but in contrast, we could identify sediments that predate those at many other well-studied localities.

It remains questionable why both MIS 2 and MIS 6, the presumably most severe cold phases of the last ~200 ka (Cohen and Gibbard, 2011; Lisiecki and Raymo, 2005), apparently only left little traces in the Lower Aare Valley. Based on our results we suggest that the regional Quaternary record may be further expanded and the landscape history better understood by detailed sedimentological and petrographic analysis combined with state-of-the-art chronostratigraphy in other areas.

8. References

Alkire, B. D., 1981, Effect of variable-drainage freeze-thaw tests on post-thaw shear strength: Transportation Research Record, v. 809, p. 13-18.

Alley, R., Cuffey, K., Evenson, E., Strasser, J., Lawson, D., and Larson, G., 1997, How glaciers entrain and transport basal sediment: physical constraints: Quaternary Science Reviews, v. 16, no. 9, p. 1017-1038.

Alley, R., Cuffey, K., and Zoet, L., 2019, Glacial erosion: status and outlook: Annals of Glaciology, v. 60, no. 80, p. 1-13.

Anderson, R. Y., 1985, Meromictic lakes and varved lake sediments in North America: US Geological Survey Bulletin, v. 1607, 19 p.

Anselmetti, F. S., Drescher-Schneider, R., Furrer, H., Graf, H. R., Lowick, S. E., Preusser, F., and Riedi, M. A., 2010, A~ 180,000 years sedimentation history of a perialpine overdeepened glacial trough (Wehntal, N-Switzerland): Swiss journal of geosciences, v. 103, no. 3, p. 345-361.

Asselman, N. E., and Middelkoop, H., 1995, Floodplain sedimentation: quantities, patterns and processes: Earth Surface Processes and Landforms, v. 20, no. 6, p. 481-499.

Becker, D., Crooks, J., Been, K., and Jefferies, M., 1987, Work as a criterion for determining in situ and yield stresses in clays: Canadian Geotechnical Journal, v. 24, no. 4, p. 549-564.

Bell, F., 2002, The geotechnical properties of some till deposits occurring along the coastal areas of eastern England: Engineering Geology, v. 63, no. 1-2, p. 49-68.

Benn, D. I., and Evans, D. J., 1996, The interpretation and classification of subglacially-deformed materials: Quaternary Science Reviews, v. 15, no. 1, p. 23-52.

Berner, R., 1985, Sulphate reduction, organic matter decomposition and pyrite formation: Philosophical Transactions of the Royal Society of London. Series A, Mathematical and Physical Sciences, v. 315, no. 1531, p. 25-38.

Bini, A., Buoncristiani, J. F., Couterrand, S., Ellwanger, D., Felber, M., Florineth, D., Graf, H. R., Keller, O., Kelly, M., and Schlüchter, C., 2009, Die Schweiz während des letzteiszeitlichen Maximums (LGM) 1:500'000: Bundesamt für Landestopographie swisstopo.

Bitterli-Dreher, P., Graf, H. R., Naef, H., Diebold, P., Matousek, F., Burger, H., and Pauli-Gabi, T., 2007, Geologischer Atlas der Schweiz 1:25'000. Blatt 1070 Baden. Erläuterungen, Wabern, Bundesamt für Landestopogaphie swisstopo, 152 p.

Bitterli, T., Graf, H. R., Matousek, F., and Wanner, M., 2000, Geologischer Atlas der Schweiz 1:25'000. Blatt 1050 Zurzach. Erläuterungen, Geologischer Atlas der Schweiz 1:25'000, 89 p.

Boulton, G., and Paul, M., 1976, The influence of genetic processes on some geotechnical properties of glacial tills: Quarterly Journal of Engineering Geology, v. 9, no. 3, p. 159-194.

Buechi, M. W., Graf, H. R., Haldimann, P., Lowick, S. E., and Anselmetti, F. S., 2017, Multiple Quaternary erosion and infill cycles in overdeepened basins of the northern Alpine foreland: Swiss Journal of Geosciences, v. 111, p. 1-34.

Bugmann, E., 1961, Beiträge zur Gliederung der Risszeitlichen Bildungen in der Nordschweiz: Mitteilungen der aargauischen Naturforschenden Gesellschaft, v. 26, p. 105-119.

Burkhard, M., 1990, Aspects of the large-scale Miocene deformation in the most external part of the Swiss Alps (sub-Alpine molasse to Jura fold belt): Eclogae Geologicae Helvetiae, v. 83, no. 3, p. 559-583.

Burkhard, M., and Sommaruga, A., 1998, Evolution of the western Swiss Molasse basin: structural relations with the Alps and the Jura belt: Geological Society, London, Special Publications, v. 134, no. 1, p. 279-298.

Carrivick, J. L., and Tweed, F. S., 2013, Proglacial lakes: character, behaviour and geological importance: Quaternary Science Reviews, v. 78, p. 34-52.

Casagrande, A., 1948, Classification and identification of soils: Transactions of the American Society of Civil Engineers, v. 113, no. 1, p. 901-930.

Chaline, J., and Jerz, H., 1984, Arbeitsergebnisse der Subkommission für Europäische Quartärstratigraphie: Stratotypen des Würm-Glazials (Bericht der SEQS 5): Eiszeitalter und Gegenwart, v. 34, p. 185-206.

Chamberlain, E. J., 1981, Overconsolidation effects of ground freezing: Engineering geology, v. 18, no. 1-4, p. 97-110.

Chiverrell, R., Smedley, R., Small, D., Ballantyne, C., Burke, M., Callard, S., Clark, C., Duller, G., Evans, D., and Fabel, D., 2018, Ice margin oscillations during deglaciation of the northern Irish Sea Basin: Journal of Quaternary Science, v. 33, no. 7, p. 739-762.

Claude, A., Akçar, N., Ivy-Ochs, S., Schlunegger, F., Rentzel, P., Pümpin, C., Tikhomirov, D., Kubik, P. W., Vockenhuber, C., and Dehnert, A., 2017, Chronology of Quaternary terrace deposits at the locality Hohle Gasse (Pratteln, NW Switzerland): Swiss journal of geosciences, v. 110, no. 3, p. 793-809.

Cohen, K., and Gibbard, P., 2011, Global chronostratigraphical correlation table for the last 2.7 million years.

Cook, S. J., and Swift, D. A., 2012, Subglacial basins: Their origin and importance in glacial systems and landscapes: Earth-Science Reviews, v. 115, no. 4, p. 332-372.

Dehnert, A., Lowick, S. E., Preusser, F., Anselmetti, F. S., Drescher-Schneider, R., Graf, H. R., Heller, F., Horstmeyer, H., Kemna, H. A., and Nowaczyk, N. R., 2012, Evolution of an overdeepened trough in the northern Alpine Foreland at Niederweningen, Switzerland: Quaternary Science Reviews, v. 34, p. 127-145.

Dehnert, A., Preusser, F., Kramers, J. D., Akcar, N., Kubik, P. W., Reber, R., and Schluechter, C., 2010, A multi-dating approach applied to proglacial sediments attributed to the Most Extensive Glaciation of the Swiss Alps: Boreas, v. 39, no. 3, p. 620-632.

Dick, K., Graf, H., Müller, B., Hartmann, P., and Schlüchter, C., 1996, Das nordalpine Wasserschloss und seine eiszeitgeologische Umgebung: Eclogae Geologicae Helvetiae, v. 89, p. 635-645.

Dietze, E., and Dietze, M., 2019, Grain-size distribution unmixing using the R package EMMAgeo: E & G Quaternary Science Journal, v. 68, no. 1, p. 29-46.

Dr. H. Jäckli AG, and DMT GmbH & Co. KG, 2012, 2D-Seismik Nordschweiz 2011/12: Geologische Aufnahme der Aufzeitbohrungen (Teil 1) und Aufzeitmessungen (Teil 2): Nagra Arbeitsbericht NAB 12-22, 31 p.

Dürst Stucki, M., and Schlunegger, F., 2013, Identification of erosional mechanisms during past glaciations based on a bedrock surface model of the central European Alps: Earth and Planetary Science Letters, v. 384, p. 57-70.

Evans, D., Phillips, E., Hiemstra, J., and Auton, C., 2006, Subglacial till: formation, sedimentary characteristics and classification: Earth-Science Reviews, v. 78, no. 1-2, p. 115-176.

Evans, D. J. A., 2007, Glacial landfoms, sediments - Tills, in Elias, S., ed., Encyclopedia of Quaternary Science: Amsterdam, Elsevier, p. 959–975.

Eyles, N., Eyles, C. H., and Miall, A. D., 1983, Lithofacies types and vertical profile models; an alternative approach to the description and environmental interpretation of glacial diamict and diamictite sequences: Sedimentology, v. 30, no. 3, p. 393-410.

Fleisher, P. J., 1986, Dead-ice sinks and moats: environments of stagnant ice deposition: Geology, v. 14, no. 1, p. 39-42.

Gaar, D., Graf, H. R., and Preusser, F., 2019, New chronological constraints on the timing of Late Pleistocene glacier advances in northern Switzerland: E&G Quaternary Science Journal, v. 68, no. 1, p. 53-73.

Gegg, L., Buechi, M. W., Ebert, A., Deplazes, G., Madritsch, H., and Anselmetti, F. S., 2020, Brecciation of glacially overridden palaeokarst (Lower Aare Valley, northern Switzerland): result of subglacial water-pressure peaks?: Boreas, v. 49, no. 4, p. 813–827.

Gegg, L., Deplazes, G., Keller, L., Madritsch, H., Spillmann, T., Anselmetti, F. S., and Buechi, M. W., 2021, 3D morphology of a glacially overdeepened trough controlled by underlying bedrock geology: Geomorphology, v. 394, DOI 10.1016/j.geomorph.2021.107950.

Gegg, L., Kuster, A. M., Amschwand, D., Huber, M., Deplazes, G., Madritsch, H., and Buechi, M. W., 2019a, Quaternary Borehole QBO Gebenstorf-Vogelsang (QGVO) Data Report: Nagra Arbeitsbericht NAB 19-03, 8 p.

Gegg, L., Kuster, A. M., Deplazes, G., Madritsch, H., and Buechi, M. W., 2019b, Quaternary Borehole QBO Gebenstorf-Brüel (QGBR) Data Report: Nagra Arbeitsbericht NAB 19-02, 8 p.

Gegg, L., Kuster, A. M., Schmid, D., and Buechi, M. W., 2018, Quaternary Boreholes QBO Riniken-1 & -2 (QRIN1 & QRIN2) Data Report: Nagra Arbeitsbericht NAB 18-40, 8 p.

Gegg, L., Kuster, A. M., Schmid, D., Lemke, K., Deplazes, G., Madritsch, H., and Buechi, M. W., 2019c, Quaternary Borehole QBO Untersiggenthal (QUST) Data Report: Nagra Arbeitsbericht NAB 19-01, 8 p.

Gilbert, G. L., Cable, S., Thiel, C., Christiansen, H. H., and Elberling, B., 2017, Cryostratigraphy, sedimentology, and the late Quaternary evolution of the Zackenberg River delta, northeast Greenland: The Cryosphere, v. 11, no. 3, p. 1265-1282.

Graf, A., Akçar, N., Ivy-Ochs, S., Strasky, S., Kubik, P. W., Christl, M., Burkhard, M., Wieler, R., and Schlüchter, C., 2015, Multiple advances of Alpine glaciers into the Jura Mountains in the Northwestern Switzerland: Swiss journal of geosciences, v. 108, no. 2, p. 225-238.

Graf, H. R., 1993, Die Deckenschotter der zentralen Nordschweiz: PhD thesis, ETH Zurich, 151 p.

-, 2009a, Stratigraphie und Morphogenese von frühpleistozänen Ablagerungen zwischen Bodensee und Klettgau: Quaternary Science Journal, v. 58, no. 1, p. 12-53.

-, 2009b, Stratigraphie von Mittel-und Spätpleistozän in der Nordschweiz, Beiträge zur Geologischen Karte der Schweiz, 198 p.

Graf, H. R., Bitterli-Dreher, P., Burger, H., Bitterli, T., Diebold, P., and Naef, H., 2006, Geologischer Atlas der Schweiz 1:25'000, Blatt 1070 Baden: Bundesamt für Landestopografie swisstopo, Wabern, Switzerland.

Graf, H. R., and Burkhalter, R., 2016, Quaternary deposits: concept for a stratigraphic classification and nomenclature—an example from northern Switzerland: Swiss Journal of Geosciences, v. 109, no. 2, p. 137-147.

Hammer, Ø., 2018, PAST – PAleontological STatistics: reference manual version 3.20: Oslo: Natural History Museum, University of Oslo, 262 p.

Hammer, Ø., Harper, D. A., and Ryan, P. D., 2001, PAST: Paleontological statistics software package for education and data analysis: Palaeontologia electronica, v. 4, no. 1, 9 p.

Hantke, R., 1978, Eiszeitalter. Die jüngste Erdgeschichte der Schweiz und ihrer Nachbargebiete. Band 1 - Klima, Flora, Fauna, Mensch, Alt-und Mittel-Pleistozän, Vogesen, Schwarzwald, Schwäbische Alb, Adelegg, Thun, Ott Verlag, 468 p.

He, Q., and Walling, D., 1998, An investigation of the spatial variability of the grain size composition of floodplain sediments: Hydrological Processes, v. 12, no. 7, p. 1079-1094.

Hughes, P. D., Gibbard, P. L., and Ehlers, J., 2019, The "missing glaciations" of the Middle Pleistocene: Quaternary Research, v. 96, p. 161–183.

Huybrechts, W., 2000, Post-pleniglacial floodplain sediments in Central Belgium: Geologica Belgica, v. 2, no. 3-4, p. 29-37.

International Organization for Standardization, 2004, ISO/TS 17892-5:2004. Geotechnical investigation and testing — Laboratory testing of soil — Part 5: Incremental loading oedometer test, 26 p.

Ivy-Ochs, S., Kerschner, H., Reuther, A., Preusser, F., Heine, K., Maisch, M., Kubik, P. W., and Schlüchter, C., 2008, Chronology of the last glacial cycle in the European Alps: Journal of Quaternary Science: Published for the Quaternary Research Association, v. 23, no. 6-7, p. 559-573.

Jordan, P., Wetzel, A., and Reisdorf, A., 2008, Swiss Jura Mountains, in McCann, T., ed., The Geology of Central Europe, Volume 2, Geological Society of London, p. 823-923.

Karlén, W., and Matthews, J. A., 1992, Reconstructing Holocene glacier variations from glacial lake sediments: studies from Nordvestlandet and Jostedalsbreen-Jotunheimen, southern Norway: Geografiska Annaler: Series A, Physical Geography, v. 74, no. 4, p. 327-348.

Keller, O., and Krayss, E., 2010, Mittel-und spätpleistozäne Stratigraphie und Morphogenese in Schlüsselregionen der Nordschweiz: E&G: Quaternary Science Journal, v. 59, no. 1-2, p. 88-119.

Krüger, J., Kjær, K. H., and Schomacker, A., 2010, 7 Dead-Ice Environments: A Landsystems Model for a Debris-Charged, Stagnant Lowland Glacier Margin, Kötlujökull: Developments in Quaternary Sciences, v. 13, p. 105-126.

Laubscher, H. P., 1962, Die Zweiphasenhypothese der Jurafaltung: Eclogae Geologicae Helvetiae, v. 55, p. 1-22.

Leonard, E. M., 1986, Varve studies at Hector Lake, Alberta, Canada, and the relationship between glacial activity and sedimentation: Quaternary Research, v. 25, no. 2, p. 199-214.

Lisiecki, L. E., and Raymo, M. E., 2005, A Pliocene-Pleistocene stack of 57 globally distributed benthic δ^{18}O records: Paleoceanography, v. 20, no. 1, PA1003.

Loepfe, R., *et al.*, in prep., Digitales Höhenmodell Basis Quartär der Nordschweiz – Version 2021 und ausgewählte Auswertungen: Nagra Arbeitsbericht.

Lowick, S. E., Buechi, M. W., Gaar, D., Graf, H. R., and Preusser, F., 2015, Luminescence dating of M iddle P leistocene proglacial deposits from northern S witzerland: methodological aspects and stratigraphical conclusions: Boreas, v. 44, no. 3, p. 459-482.

Mailänder, R., and Veit, H., 2001, Periglacial cover-beds on the Swiss Plateau: indicators of soil, climate and landscape evolution during the Late Quaternary: Catena, v. 45, no. 4, p. 251-272.

Matousek, F., Wanner, M., Baumann, A., Graf, H., Nüesch, R., and Bitterli, T., 2000, Geologischer Atlas der Schweiz 1:25'000. Blatt 102 Zurzach Bundesamt für Landestopografie swisstopo, Wabern, Switzerland.

Merritt, J. W., Gordon, J. E., and Connell, E. R., 2019, Late Pleistocene sediments, landforms and events in Scotland: a review of the terrestrial stratigraphic record: Earth and Environmental Science Transactions of the Royal Society of Edinburgh, v. 110, no. 1-2, p. 39-91.

Mills, P. C., 1983, Genesis and diagnostic value of soft-sediment deformation structures—a review: Sedimentary Geology, v. 35, no. 2, p. 83-104.

Moscariello, A., Schneider, A. M., and Filippi, M. L., 1998, Late glacial and early Holocene palaeoenvironmental changes in Geneva Bay (Lake Geneva, Switzerland): Palaeogeography, Palaeoclimatology, Palaeoecology, v. 140, no. 1-4, p. 51-73.

Mueller, D., Fuelling, A., Gegg, L., Buechi, M. W., Deplazes, G., and Preusser, F., in prep., Luminescence dating of Middle Pleistocene sedimentary deposits from the Lower Aare Valley region, northern Switzerland.

Mueller, D., Preusser, F., Buechi, M. W., Gegg, L., and Deplazes, G., 2020, Luminescence properties and dating of glacial to periglacial sediments from northern Switzerland: Geochronology, v. 2, no. 2, p. 305-323.

Nitsche, F., Monin, G., Marillier, F., Graf, H., and Ansorge, J., 2001, Reflection seismic study of Cenozoic sediments in an overdeepened valley of northern Switzerland: the Birrfeld area: Eclogae Geologicae Helvetiae, v. 94, no. 3, p. 363-371.

O'Regan, M., Greenwood, S. L., Preto, P., Swärd, H., and Jakobsson, M., 2016, Geotechnical and sedimentary evidence for thick-grounded ice in southern Lake Vättern during deglaciation: GFF, v. 138, no. 2, p. 355-366.

Peach, P. A., and Perrie, L. A., 1975, Grain-size distribution within glacial varves: Geology, v. 3, no. 1, p. 43-46.

Pfiffner, O. A., 1986, Evolution of the north Alpine foreland basin in the Central Alps: Special Publications of the International Association of Sedimentologists, v. 8, p. 219-228.

Pietsch, J., and Jordan, P., 2014, Digitales Höhenmodell Basis Quartär der Nordschweiz - Version 2014 und ausgewählte Auswertungen: Nagra Arbeitsbericht NAB 14-02, 69 p.

Pisarska-Jamrozy, M., and Weckwerth, P., 2013, Soft-sediment deformation structures in a Pleistocene glaciolacustrine delta and their implications for the recognition of subenvironments in delta deposits: Sedimentology, v. 60, no. 3, p. 637-665.

Preusser, F., 2004, Towards a chronology of the Late Pleistocene in the northern Alpine Foreland: Boreas, v. 33, no. 3, p. 195-210.

Preusser, F., Blei, A., Graf, H., and Schlüchter, C., 2007, Luminescence dating of Würmian (Weichselian) proglacial sediments from Switzerland: methodological aspects and stratigraphical conclusions: Boreas, v. 36, no. 2, p. 130-142.

Preusser, F., Büschelberger, M., Kemna, H. A., Miocic, J., Mueller, D., and May, J.-H., 2021, Exploring possible links between Quaternary aggradation in the Upper Rhine Graben and the glaciation history of northern Switzerland: International Journal of Earth Sciences, v. 110, p. 1827–1846.

Preusser, F., Drescher-Schneider, R., Fiebig, M., and Schlüchter, C., 2005, Re-interpretation of the Meikirch pollen record, Swiss Alpine Foreland, and implications for Middle Pleistocene chronostratigraphy: Journal of Quaternary Science, v. 20, no. 6, p. 607-620.

Preusser, F., Geyh, M. A., and Schlüchter, C., 2003, Timing of Late Pleistocene climate change in lowland Switzerland: Quaternary science reviews, v. 22, no. 14, p. 1435-1445.

Preusser, F., and Graf, H., 2002, Erste Ergebnisse von Lumineszenzdatierungen eiszeitlicher Ablagerungen der Nordschweiz: Jahresberichte und Mitteilungen des Oberrheinischen Geologischen Vereins, p. 419-438.

Preusser, F., Graf, H. R., Keller, O., Krayss, E., and Schlüchter, C., 2011, Quaternary glaciation history of northern Switzerland: E&G Quaternary Science Journal, v. 60, p. 282-305.

Preusser, F., Reitner, J. M., and Schlüchter, C., 2010, Distribution, geometry, age and origin of overdeepened valleys and basins in the Alps and their foreland: Swiss Journal of Geosciences, v. 103, no. 3, p. 407-426.

Preusser, F., and Schlüchter, C., 2004, Dates from an important early Late Pleistocene ice advance in the Aare valley, Switzerland: Eclogae Geologicae Helvetiae, v. 97, no. 2, p. 245-253.

Qi, J., Vermeer, P. A., and Cheng, G., 2006, A review of the influence of freeze-thaw cycles on soil geotechnical properties: Permafrost and periglacial processes, v. 17, no. 3, p. 245-252.

Raab, T., Leopold, M., and Völkel, J., 2007, Character, age, and ecological significance of Pleistocene periglacial slope deposits in Germany: Physical Geography, v. 28, no. 6, p. 451-473.

Regnéll, C., Haflidason, H., Mangerud, J., and Svendsen, J. I., 2019, Glacial and climate history of the last 24 000 years in the Polar Ural Mountains, Arctic Russia, inferred from partly varved lake sediments: Boreas, v. 48, no. 2, p. 432-443.

Rickard, D., Mussmann, M., and Steadman, J. A., 2017, Sedimentary Sulfides: Elements, v. 13, no. 2, p. 117-122.

Schlüchter, C., 1984, Geotechnical properties of ZüBO-sediments: Contributions to Sedimentology, v. 13, p. 135-140.

-, 1989a, The most complete Quaternary record of the Swiss Alpine Foreland: Palaeogeography, Palaeoclimatology, Palaeoecology, v. 72, p. 141-146.

-, 1989b, Thalgut-A comprehensive Quaternary record of the northern Swiss alpine foreland: Eclogae Geologicae Helvetiae, v. 82, no. 1, p. 277-284.

-, 1997, Sedimente des Gletschers (Teil I): Bulletin für angewandte Geologie, v. 2, no. 2, p. 99-112.

Schlüchter, C., Akçar, N., and Ivy-Ochs, S., 2021, The Quaternary Period in Switzerland, Landscapes and Landforms of Switzerland, Springer, p. 47-69.

Schultheiss, P., and Weaver, P., Multi-sensor core logging for science and industry, in Proceedings OCEANS'92. Mastering the Oceans Through Technology. Proceedings.1992, Volume 2, IEEE, p. 608-613.

Seguinot, J., Ivy-Ochs, S., Jouvet, G., Huss, M., Funk, M., and Preusser, F., 2018, Modelling last glacial cycle ice dynamics in the Alps: The Cryosphere, v. 12, no. 10, p. 3265-3285.

Seidel, M., and Hlawitschka, M., 2015, An R-based function for modeling of end member compositions: Mathematical Geosciences, v. 47, no. 8, p. 995-1007.

Serra, O., and Sulpice, L., Sedimentological analysis of shale-sand series from well logs, 16th Annual Logging Symposium1975, Society of Petrophysicists and Well-Log Analysts.

Smedley, R., Chiverrell, R. C., Ballantyne, C. K., Burke, M., Clark, C., Duller, G., Fabel, D., McCarroll, D., Scourse, J., and Small, D., 2017, Internal dynamics condition centennial-scale oscillations in marine-based ice-stream retreat: Geology, v. 45, no. 9, p. 787-790.

Suits, N. S., and Wilkin, R. T., 1998, Pyrite formation in the water column and sediments of a meromictic lake: Geology, v. 26, no. 12, p. 1099-1102.

Svendsen, J. I., Færseth, L. M. B., Gyllencreutz, R., Haflidason, H., Henriksen, M., Hovland, M. N., Lohne, Ø. S., Mangerud, J., Nazarov, D., and Regnéll, C., 2019, Glacial and environmental changes over the last 60 000 years in the Polar Ural Mountains, Arctic Russia, inferred from a high-resolution lake record and other observations from adjacent areas: Boreas, v. 48, no. 2, p. 407-431.

Swiss Association of Road and Transportation Experts, 2008, SN 670 345b. Böden – Konsistenzgrenzen, 7 p.

Trenter, N., 1999, Engineering in glacial tills, CIRIA Report C504: London: Construction Research and Information Association, 248 p.

Urban, B., and Bigga, G., 2015, Environmental reconstruction and biostratigraphy of late Middle Pleistocene lakeshore deposits at Schöningen: Journal of Human Evolution, v. 89, p. 57-70.

Van der Meer, J. J., Kjær, K. H., Krüger, J., Rabassa, J., and Kilfeather, A., 2009, Under pressure: clastic dykes in glacial settings: Quaternary Science Reviews, v. 28, no. 7-8, p. 708-720.

Van Dijk, D., Hobday, D. K., and Tankard, A., 1978, Permo-Triassic Lacustrine Deposits in the Eastern Karoo Basin, Natal, South Africa: Modern and Ancient Lake Sediments, p. 225-239.

Van Gelder, G., de Graaff, L., and Schurink, E., 1990, Subglacial consolidation of fine-grained stratified sediments: a neglected tool in reconstructing ice-thickness in Pleistocene valley glaciers: Arctic and Alpine Research, p. 329-340.

Veit, H., Trauerstein, M., Preusser, F., Messmer, T., Gnägi, C., Zech, R., and Wüthrich, L., 2017, Late Glacial/Early Holocene slope deposits on the Swiss Plateau: Genesis and palaeo-environment: Catena, v. 158, p. 102-112.

Vogel, H., Wagner, B., Zanchetta, G., Sulpizio, R., and Rosén, P., 2010, A paleoclimate record with tephrochronological age control for the last glacial-interglacial cycle from Lake Ohrid, Albania and Macedonia: Journal of Paleolimnology, v. 44, no. 1, p. 295-310.

Wennrich, V., Minyuk, P., Borkhodoev, V., Francke, A., Ritter, B., Nowaczyk, N. R., Sauerbrey, M., Brigham-Grette, J., and Melles, M., 2014, Pliocene to Pleistocene climate and environmental history of Lake El'gygytgyn, Far East Russian Arctic, based on high-resolution inorganic geochemistry data: Climate of the Past, v. 10, no. 4, p. 1381-1399.

Yanites, B. J., Becker, J. K., Madritsch, H., Schnellmann, M., and Ehlers, T. A., 2017, Lithologic effects on landscape response to base level changes: A modeling study in the context of the Eastern Jura Mountains, Switzerland: Journal of Geophysical Research: Earth Surface, v. 122, no. 11, p. 2196-2222.

Ziegler, P. A., and Fraefel, M., 2009, Response of drainage systems to Neogene evolution of the Jura fold-thrust belt and Upper Rhine Graben: Swiss journal of geosciences, v. 102, no. 1, p. 57-75.

Zolitschka, B., Francus, P., Ojala, A. E., and Schimmelmann, A., 2015, Varves in lake sediments–a review: Quaternary Science Reviews, v. 117, p. 1-41.

9. Supplementary material

Table IV-S1: List of sampled outcrops. GA25: Graf *et al.*, 2006; Matousek *et al.*, 2000.

[1]: attributed to Remigen Gravel in Graf, 2009.

No.	Outcrop name	Coordinates	Stratigraphic unit (GA25)	Outcrop description	Samples with elevation
1	Hinterrein former gr. pit	47°30'09" N, 8°13'02" E	Tiefere Deckenschotter	~10 m-long outcrop of crudely bedded sandy gravel with horizontally aligned, poorly cemented, rounded clasts	TDS-Hr ~455 m a.s.l.
2	Wasserschloss-blick footpath	47°30'07" N, 8°13'36" E		Several isolated outcrops (few meters) of medium-coarse gravel with horizontally aligned, rounded clasts cemented by calcite	TDS-Wb ~480 m a.s.l.
3	Chilhalde former gr. pit	47°29'07" N, 8°11'31" E		Large (~150 m) but mostly overgrown outcrop of bedded gravels with varying grain sizes and degrees of sorting, generally sandy but without distinct sand layers, locally cemented, overlain by diamict with striated clasts	HS-Ch1 ~395 m a.s.l. HS-Ch2 ~390 m a.s.l.
4	Galgenhübel former gr. pit	47°28'21" N, 8°12'08" E		Small (~10 m) outcrop of cemented sandy gravel with decametre-scale bedding, horizontally aligned, with frequent large cobbles	HS-GhN ~370 m a.s.l.
5	Götschtel former gr. pit[1]	47°27'04" N, 8°10'27" E	Hochterrasse, Habsburg Gravel	~100 m-wide outcrop of bedded sandy gravel with well-sorted, decimetre-thick sand layers, stratigraphy deformed and folded, clasts are generally well rounded, mostly horizontally aligned or imbricated, occasional crushed grains	HS-Göl ~390 m a.s.l. HS-Gö2 ~395 m a.s.l.
6	Hansfluhsteig foodpath	47°29'20" N, 8°12'31" E		Several small outcrops of relatively well-sorted coarse gravel, cemented, with decimetre-scale eastward-inclined bedding, individual crushed grains	HS-Hfs ~400 m a.s.l.
7	Müligässli foodpath	47°29'11" N, 8°12'01" E		Several small, overgrown outcrops of well-rounded gravel, slightly cemented, soil formation: brown, organic-rich matrix	HS-Mg ~375 m a.s.l.
8	Tandlirai former gr. pit	47°30'41" N, 8°13'06" E		~25 m-wide outcrop, mostly overgrown, of cemented sandy gravel, moderately sorted with large cobbles, well-rounded clasts, locally ochre-brown	HS-Tr1 ~365 m a.s.l. HS-Tr2 ~375 m a.s.l.
9	Haselloch former gr. pit	47°30'57"N, 8°12'29"E		Former pit is today a pond, with a small isolated outcrop at the upslope bank: well-rounded coarse gravel with individual striated clasts, soil formation: ochre-brown matrix	HS-Zh ~385 m a.s.l.
10	Alpberg (W) former gr. pit	47°30'45"N, 8°11'00"E	Hochterrasse, Remigen Gravel	Two former neighbouring gravel pits, western pit with better exposures: well-bedded (decimetre-scale, locally cross-bedded) gravel with loose laminated sand layers, gravel mostly fine- to medium-grained, with orange-beige cement, toppled blocks at the base of the pit; Gravels in the neighbouring pit to the east (47°30'39" N; 8°11'12" E) less well exposed but overlain by sandy-silty diamict	RS-Re ~415 m a.s.l.

Table IV-S1 (continued): List of sampled outcrops. GA25: Graf *et al.,* 2006; Matousek *et al.,* 2000. [2]: correlative unit after Graf, 2009.

No.	Outcrop name	Coordinates	Stratigraphic unit (GA25)	Outcrop description	Samples with elevation
11	Wuest former gr. pit	47°27′10″ N 8°11′30″ E	Hochterrasse, Remigen Gravel	Several outcrops in ~50 m wide, mostly overgrown former gravel pit; well-rounded, very sandy gravel, horizontally aligned and faintly bedded, locally strongly cemented: toppled conglomeratic blocks at the base of the pit	RS-Wu1 ~415 m a.s.l. RS-Wu2 ~415 m a.s.l.
12	Remigersteig road cut	47°29′12″ N 8°12′05″ E		Few small (~1 m) outcrops of cemented, crudely bedded and poorly sorted sandy gravel at the side of the road	RS-Rs ~380 m a.s.l.
13	Hönger former gr. pit	47°35′14″ N 8°14′46″ E	Upper Hochterrasse (~Habsburg Gr.[2])	Large and high (~100*30 m^2) outcrop of loose, bedded (decimetre-scale, with trough cross-stratification) sandy gravel with well-sorted sand layers; gravel fraction mostly well sorted, clasts generally rounded, horizontally aligned or imbricated; polished and striated blocks of conglomerate above the pit wall	uHT-Hö ~385 m a.s.l.
14	Tüftel former gr. pit	47°36′39″ N 8°15′18″ E		Few isolated outcrops of fine to medium, well-bedded and cemented sandy gravel in overgrown former gravel pit, with individual thin (few cm) sand layers	uHT-Tü ~355 m a.s.l.
15	Surb bank Unterendingen	47°33′03″ N 8°17′11″ E	Middle Hochterrasse (~Ruckfeld Gr.[2])	20 m-wide/high outcrop of cemented, crudely bedded (with trough cross-stratification) sandy gravel at a cut bank of the Surb creek, with meter-sized toppled blocks at the stream bed; note: sample RU-Ue collected from toppled block	mHT-Ue ~375 m a.s.l.
16	Langgrabe road cut	47°33′44″ N 8°15′29″ E	Lower Hochterrasse (~Remigen Gr.[2])	Large (~100 m) but mostly overgrown outcrop of strongly cemented, crudely bedded sandy gravel, horizontally aligned, rounded clasts	lHT-La ~360 m a.s.l.
17	Amsler AG gravel pit	47°27′16″ N 8°08′59″ E	Niederterrasse (Aare Valley)	Large (>200 m) outcrop of alternating sequences of well-bedded (including trough cross-stratification), moderately to well sorted gravel with decimetre-thick laminated and graded sand lenses	NT-A-Am ~350 m a.s.l.
18	Im Feld road cut	47°26′22″ N 8°10′03″ E		~50 m-wide outcrop of bedded (decimetre-scale) sandy gravel with horizontally aligned or imbricated, mostly rounded clasts	NT-A-If ~355 m a.s.l.
19	Notter AG gravel pit	47°23′42″ N 8°19′02″ E	Niederterrasse (Reuss Valley)	Large (~100 m) outcrop of compacted, poorly sorted (partly matrix-supported) and crudely thick-bedded gravel below diamicton with meter-sized blocks and interbedded fine deposits; no obvious preferred clast orientation	NT-R-No ~400 m a.s.l.
20	Reuss river bank W' Birmenstorf	47°27′47″ N 8°13′55″ E		Large (~100 m) natural outcrop of the Niederterrasse undercut by the Reuss river; loose, poorly sorted, sandy gravel, horizontally aligned; poorly accessible	NT-R-Bi ~340 m a.s.l.

Table IV-S1 (continued): List of sampled outcrops. GA25: Graf *et al.,* 2006; Matousek *et al.,* 2000.

No.	Outcrop name	Coordinates	Stratigraphic unit (GA25)	Outcrop description	Samples with elevation
21	Agir AG gravel pit	47°27'01" N 8°21'01" E	Niederterrasse (Limmat Valley)	Large (~100 m) outcrop of loose, crudely bedded and poorly sorted gravel with sand interbeds; clasts horizontally aligned and frequently subangular	NT-L-Ag ~390 m a.s.l.
22	Tägerhard AG gravel pit	47°27'23" N 8°20'57" E		Large (~100 m) outcrop of well bedded gravel with layered, fine-grained lenses; clasts horizontally aligned and frequently subangular	NT-L-Th ~410 m a.s.l.

Table IV-S2: Lithology groups as input for statistical analysis.

Lithology group	Lithologies
Alpine limestones	dark grey limestone, light grey limestone, other limestone
Siliceous Alpine limestones	dark grey siliceous limestone, light grey siliceous limestone, dark granular limestone
Jura Mountains limestones	beige limestone, angular beige limestone, patterned beige limestone
Dolostones	dolostone
Sandstones and conglomerates	sandstone general, glauconitic sandstone, conglomerate general, breccia general, rauhwacke-type breccia,
Red sandstones	red sandstone, red conglomerate
Taveyannaz sandstones	Taveyannaz sandstone
Quartzites	quartzite, vein quartz
Cherts	chert, radiolarite
Plutonics, undiff.	granitoid, dioritoid, gabbroid, foidite
Rhyolites	rhyolite
Further volcanics	green/yellow volcanic, purple volcanic, other volcanic
Metamorphics, undiff.	gneiss, schist, amphibolite, serpentinite

Table IV-S3: Petrographic composition of selected core intervals. [1]: Bulk sample integrating 5 m of poorly recovered core.

	Sum	127	143	109	63	154	136	89	224	134	58	137	102	166
amphibolite		0	0	0	0	0	0	0	0	0	0	0	0	0
schist		0	5	0	0	0	0	0	0	0	0	0	0	1
gneiss		2	1	1	1	1	0	5	2	0	0	0	0	4
other volcanic		0	0	0	0	0	0	0	0	0	0	0	0	0
purple volcanic		0	0	0	0	0	0	0	0	0	0	0	0	0
green/yellow volcanic		0	1	4	0	0	0	0	1	0	0	0	0	1
rhyolite		0	0	1	0	0	0	0	0	1	0	0	0	1
gabbroid		0	0	1	0	0	1	0	0	0	0	0	0	2
dioritoid		0	0	0	0	0	0	0	0	0	0	1	0	1
granitoid		12	9	5	0	4	1	2	10	2	1	2	3	10
radiolarite		1	0	1	0	5	2	2	2	3	0	0	0	1
chert		2	1	0	0	0	0	0	0	2	1	2	0	0
vein quartz		1	9	8	2	1	1	2	1	1	1	7	5	3
quartzite		17	24	28	16	12	17	6	27	19	9	19	28	47
rauhwacke-type breccia		0	0	0	0	0	1	0	0	0	0	0	0	0
breccia, general		0	1	0	1	0	0	0	2	1	0	0	0	2
red conglomerate		0	0	0	0	0	1	0	0	0	0	0	0	0
conglomerate, general		2	0	0	0	5	0	0	0	0	0	0	0	0
glauconitic sandstone		0	0	0	0	0	2	0	0	0	0	0	0	1
Taveyannaz sandstone		3	2	1	0	7	6	3	4	3	0	2	2	2
red sandstone		0	0	0	0	7	0	0	0	0	0	0	0	0
sandstone, general		24	23	19	11	29	18	23	38	17	2	27	14	21
dolostone		0	0	0	0	0	0	0	0	0	0	0	0	0
other limestone		0	1	0	0	0	2	0	1	0	0	0	0	0
patterned beige lst.		0	0	0	0	0	0	0	0	0	0	0	0	1
beige lst., angular		8	1	0	5	0	0	0	2	8	15	3	5	12
beige limestone		7	8	5	4	8	2	7	16	11	16	22	2	7
dark granular limestone		1	0	0	1	0	5	0	12	6	0	2	1	2
light grey siliceous lst.		38	25	28	12	51	21	26	40	25	7	32	20	12
light grey limestone		6	5	0	2	10	12	0	9	2	2	4	3	7
dark gey siliceous lst.		2	23	7	8	11	32	12	50	33	4	14	19	27
dark grey limestone		1	4	0	0	3	12	1	7	0	0	0	0	1
Sample: borehole, depth [m]		QGBR 12-13	QGBR 16-17	QGBR 21-22	QGBR 109-111	QGVO 10-11	QGVO 15-16	QGVO 27-28	QGVO 57-58	QGVO 63-64	QRIN 6.5-7.5	QRIN 36.1-37.1	QRIN 39.1-40.1	QRIN 36-41[1]

Table IV-S3 (continued): Petrographic composition of selected core intervals.

	QUST 4-5	QUST 12-13	QUST 16-17	QUST 19-20	QUST 24-25	QUST 30-31	QUST 36-37	QUST 43-44	QUST 49-50	QUST 52-53	QUST 57-58	QUST 62-63	QUST 65-66	QUST 74-75
Sum	126	114	177	117	139	137	124	131	153	67	158	108	133	99
amphibolite	0	0	1	0	0	0	1	0	1	1	0	0	0	1
schist	0	1	0	0	0	0	0	1	0	0	0	0	0	0
gneiss	2	2	3	3	1	2	2	0	3	0	1	2	0	2
other volcanic	1	0	0	1	0	0	0	0	0	0	0	0	0	0
purple volcanic	1	1	0	0	2	1	0	0	0	0	0	0	0	0
green/yellow volcanic	0	0	3	0	1	1	0	0	1	0	1	1	0	1
rhyolite	0	0	1	0	0	0	0	0	0	0	0	0	1	0
gabbroid	1	0	0	0	0	1	0	0	0	0	0	0	0	0
dioritoid	1	1	0	0	0	0	0	1	0	0	0	0	0	0
granitoid	2	2	8	1	1	3	1	3	0	0	2	6	1	2
radiolarite	0	4	3	1	0	2	1	0	0	0	1	3	2	2
chert	2	0	2	1	1	0	0	5	3	1	2	3	1	2
vein quartz	5	2	8	5	1	0	1	3	2	2	2	1	8	3
quartzite	8	22	19	6	10	8	10	10	14	10	11	7	15	7
rauhwacke-type breccia	0	0	0	0	0	1	0	0	0	0	0	0	1	1
breccia, general	0	0	0	0	1	0	0	0	0	0	0	0	0	0
red conglomerate	0	0	0	1	0	0	0	0	0	0	0	0	0	0
conglomerate, general	0	0	1	0	1	2	0	0	1	0	0	1	0	0
glauconitic sandstone	4	0	1	3	0	1	0	0	1	0	0	0	0	0
Taveyannaz sandstone	1	3	0	4	2	3	6	2	1	1	1	2	1	1
red sandstone	3	0	0	2	1	0	1	3	1	0	0	1	0	1
sandstone, general	23	14	14	11	31	23	27	23	31	9	37	15	25	14
dolostone	0	0	0	0	1	4	0	0	0	0	0	1	0	1
other limestone	0	0	0	7	0	0	0	0	1	5	1	1	0	0
patterned beige lst.	0	0	1	0	0	0	0	0	0	0	0	0	0	0
beige lst., angular	0	2	2	0	0	0	4	7	0	0	1	0	0	0
beige limestone	3	1	7	5	4	6	5	7	5	7	13	8	7	4
dark granular limestone	9	11	26	3	3	2	0	9	12	4	7	8	8	9
light grey siliceous lst.	19	12	17	23	22	37	36	9	8	10	15	17	19	11
light grey limestone	5	7	15	8	7	5	2	4	11	4	8	8	12	6
dark gey siliceous lst.	31	27	27	25	44	33	27	41	51	12	38	21	26	29
dark grey limestone	5	2	18	7	5	2	0	3	6	1	17	2	6	2

188

Table IV-S3 (continued): Petrographic composition of selected core intervals (percentage).
[1]: Bulk sample integrating 5 m of poorly recovered core.

Sample: borehole, depth [m]	QGBR 12-13	QGBR 16-17	QGBR 21-22	QGBR 109-111	QGVO 10-11	QGVO 15-16	QGVO 27-28	QGVO 57-58	QGVO 63-64	QRIN 6.5-7.5	QRIN 36.1-37.1	QRIN 39.1-40.1	QRIN 36-41[1]
Sum	100	100	100	100	100	100	100	100	100	100	100	100	100
amphibolite	0.0	0.0	0.0	0.0	0.0	0.0	0.0	0.0	0.0	0.0	0.0	0.0	0.0
schist	0.0	3.5	0.0	0.0	0.0	0.0	0.0	0.0	0.0	0.0	0.0	0.0	0.6
gneiss	1.6	0.7	0.9	1.6	0.6	0.0	5.6	0.9	0.0	0.0	0.0	0.0	2.4
other volcanic	0.0	0.0	0.0	0.0	0.0	0.0	0.0	0.0	0.0	0.0	0.0	0.0	0.0
purple volcanic	0.0	0.0	0.0	0.0	0.0	0.0	0.0	0.0	0.0	0.0	0.0	0.0	0.0
green/yellow volcanic	0.0	0.7	3.7	0.0	0.0	0.0	0.0	0.4	0.0	0.0	0.0	0.0	0.6
rhyolite	0.0	0.0	0.9	0.0	0.0	0.0	0.0	0.0	0.7	0.0	0.0	0.0	0.6
gabbroid	0.0	0.0	0.9	0.0	0.0	0.7	0.0	0.0	0.0	0.0	0.0	0.0	1.2
dioritoid	0.0	0.0	0.0	0.0	0.0	0.0	0.0	0.0	0.0	0.0	0.7	0.0	0.6
granitoid	9.4	6.3	4.6	0.0	2.6	0.7	2.2	4.5	1.5	1.7	1.5	2.9	6.0
radiolarite	0.8	0.0	0.9	0.0	3.2	1.5	2.2	0.9	2.2	0.0	0.0	0.0	0.6
chert	1.6	0.7	0.0	0.0	0.0	0.0	0.0	0.0	1.5	1.7	1.5	0.0	0.0
vein quartz	0.8	6.3	7.3	3.2	0.6	0.7	2.2	0.4	0.7	1.7	5.1	4.9	1.8
quartzite	13	17	26	25	7.8	13	6.7	12	14	16	14	27	28
rauhwacke-type breccia	0.0	0.0	0.0	0.0	0.0	0.7	0.0	0.0	0.0	0.0	0.0	0.0	0.0
breccia, general	0.0	0.7	0.0	1.6	0.0	0.0	0.0	0.9	0.7	0.0	0.0	0.0	1.2
red conglomerate	0.0	0.0	0.0	0.0	0.0	0.7	0.0	0.0	0.0	0.0	0.0	0.0	0.0
conglomerate, general	1.6	0.0	0.0	0.0	3.2	0.0	0.0	0.0	0.0	0.0	0.0	0.0	0.0
glauconitic sandstone	0.0	0.0	0.0	0.0	0.0	1.5	0.0	0.0	0.0	0.0	0.0	0.0	0.6
Taveyannaz sandstone	2.4	1.4	0.9	0.0	4.5	4.4	3.4	1.8	2.2	0.0	1.5	2.0	1.2
red sandstone	0.0	0.0	0.0	0.0	4.5	0.0	0.0	0.0	0.0	0.0	0.0	0.0	0.0
sandstone, general	19	16	17	18	19	13	26	17	13	3.4	20	14	13
dolostone	0.0	0.0	0.0	0.0	0.0	0.0	0.0	0.0	0.0	0.0	0.0	0.0	0.0
other limestone	0.0	0.7	0.0	0.0	0.0	1.5	0.0	0.4	0.0	0.0	0.0	0.0	0.0
patterned beige lst.	0.0	0.0	0.0	0.0	0.0	0.0	0.0	0.0	0.0	0.0	0.0	0.0	0.6
beige lst., angular	6.3	0.7	0.0	7.9	0.0	0.0	0.0	0.9	6.0	26	2.2	4.9	7.2
beige limestone	5.5	5.6	4.6	6.3	5.2	1.5	7.9	7.1	8.2	28	16	2.0	4.2
dark granular limestone	0.8	0.0	0.0	1.6	0.0	3.7	0.0	5.4	4.5	0.0	1.5	1.0	1.2
light grey siliceous lst.	30	17	26	19	33	15	29	18	19	12	23	20	7.2
light grey limestone	4.7	3.5	0.0	3.2	6.5	8.8	0.0	4.0	1.5	3.4	2.9	2.9	4.2
dark gey siliceous lst.	1.6	16	6.4	13	7.1	24	13	22	25	6.9	10	19	16
dark grey limestone	0.8	2.8	0.0	0.0	1.9	8.8	1.1	3.1	0.0	0.0	0.0	0.0	0.6

Table IV-S3 (continued): Petrographic composition of selected core intervals (percentage).

Sample: borehole, depth [m]	QUST 4-5	QUST 12-13	QUST 16-17	QUST 19-20	QUST 24-25	QUST 30-31	QUST 36-37	QUST 43-44	QUST 49-50	QUST 52-53	QUST 57-58	QUST 62-63	QUST 65-66	QUST 74-75
Sum	100	100	100	100	100	100	100	100	100	100	100	100	100	100
amphibolite	0.0	0.0	0.6	0.0	0.0	0.0	0.8	0.0	0.7	1.5	0.0	0.0	0.0	1.0
schist	0.0	0.9	0.0	0.0	0.0	0.0	0.0	0.8	0.0	0.0	0.0	0.0	0.0	0.0
gneiss	1.6	1.8	1.7	2.6	0.7	1.5	1.6	0.0	2.0	0.0	0.6	1.9	0.0	2.0
other volcanic	0.8	0.0	0.0	0.9	0.0	0.0	0.0	0.0	0.0	0.0	0.0	0.0	0.0	0.0
purple volcanic	0.8	0.9	0.0	0.0	1.4	0.7	0.0	0.0	0.0	0.0	0.0	0.0	0.0	0.0
green/yellow volcanic	0.0	0.0	1.7	0.0	0.7	0.7	0.0	0.0	0.7	0.0	0.6	0.9	0.0	1.0
rhyolite	0.0	0.0	0.6	0.0	0.0	0.0	0.0	0.0	0.0	0.0	0.0	0.0	0.8	0.0
gabbroid	0.8	0.0	0.0	0.0	0.0	0.7	0.0	0.0	0.0	0.0	0.0	0.0	0.0	0.0
dioritoid	0.8	0.9	0.0	0.0	0.0	0.0	0.0	0.8	0.0	0.0	0.0	0.0	0.0	0.0
granitoid	1.6	1.8	4.5	0.9	0.7	2.2	0.8	2.3	0.0	0.0	1.3	5.6	0.8	2.0
radiolarite	0.0	3.5	1.7	0.9	0.0	1.5	0.8	0.0	0.0	0.0	0.6	2.8	1.5	2.0
chert	1.6	0.0	1.1	0.9	0.7	0.0	0.0	3.8	2.0	1.5	1.3	2.8	0.8	2.0
vein quartz	4.0	1.8	4.5	4.3	0.7	0.0	0.8	2.3	1.3	3.0	1.3	0.9	6.0	3.0
quartzite	6.3	19	11	5.1	7.2	5.8	8.1	7.6	9.2	15	7.0	6.5	11	7.1
rauhwacke-type breccia	0.0	0.0	0.0	0.0	0.0	0.7	0.0	0.0	0.0	0.0	0.0	0.0	0.8	1.0
breccia, general	0.0	0.0	0.0	0.0	0.7	0.0	0.0	0.0	0.0	0.0	0.0	0.0	0.0	0.0
red conglomerate	0.0	0.0	0.0	0.9	0.0	0.0	0.0	0.0	0.0	0.0	0.0	0.0	0.0	0.0
conglomerate, general	0.0	0.0	0.6	0.0	0.7	1.5	0.0	0.0	0.7	0.0	0.0	0.9	0.0	0.0
glauconitic sandstone	3.2	0.0	0.6	2.6	0.0	0.7	0.0	0.0	0.7	0.0	0.0	0.0	0.0	0.0
Taveyannaz sandstone	0.8	2.6	0.0	3.4	1.4	2.2	4.8	1.5	0.7	1.5	0.6	1.9	0.8	1.0
red sandstone	2.4	0.0	0.0	1.7	0.7	0.0	0.8	2.3	0.7	0.0	0.0	0.9	0.0	1.0
sandstone, general	18	12	7.9	9.4	22	17	22	18	20	13	23	14	19	14
dolostone	0.0	0.0	0.0	0.0	0.7	2.9	0.0	0.0	0.0	0.0	0.0	0.9	0.0	1.0
other limestone	0.0	0.0	0.0	6.0	0.0	0.0	0.0	0.0	0.7	7.5	0.6	0.9	0.0	0.0
patterned beige lst.	0.0	0.0	0.6	0.0	0.0	0.0	0.0	0.0	0.0	0.0	0.0	0.0	0.0	0.0
beige lst., angular	0.0	1.8	1.1	0.0	0.0	0.0	3.2	5.3	0.0	0.0	0.6	0.0	0.0	0.0
beige limestone	2.4	0.9	4.0	4.3	2.9	4.4	4.0	5.3	3.3	10	8.2	7.4	5.3	4.0
dark granular limestone	7.1	9.6	15	2.6	2.2	1.5	0.0	6.9	7.8	6.0	4.4	7.4	6.0	9.1
light grey siliceous lst.	15	11	9.6	20	16	27	29	6.9	5.2	15	9.5	16	14	11
light grey limestone	4.0	6.1	8.5	6.8	5.0	3.6	1.6	3.1	7.2	6.0	5.1	7.4	9.0	6.1
dark gey siliceous lst.	25	24	15	21	32	24	22	31	33	18	24	19	20	29
dark grey limestone	4.0	1.8	10	6.0	3.6	1.5	0.0	2.3	3.9	1.5	11	1.9	4.5	2.0

190

Table IV-S4: Petrographic composition of field-collected samples (see Table IV-S1 for descriptions and coordinates).

Sample	TDS-Hr	TDS-Wb	HS-Ch1	HS-Ch2	HS-GhN	HS-Göl	HS-Gö2	HS-Hfs	HS-Mg	HS-Tr1	HS-Tr2	HS-Zh	RS-Re	RS-Wu1	RS-Wu2	RS-Rs	uHT-Hö	uHT-Tü	mHT-Ue	IHT-La	NT-A-Am	NT-A-If	NT-R-No	NT-R-Bi	NT-L-Ag	NT-L-Th
Sum	161	103	152	161	154	149	189	118	131	227	97	92	156	92	126	196	159	149	123	196	229	161	147	157	142	207
serpentinite	0	0	0	0	0	0	0	0	0	0	0	0	0	0	0	0	1	0	0	0	0	0	0	0	0	0
amphibolite	0	1	0	0	0	0	0	0	0	1	1	1	0	0	0	0	0	0	0	1	0	0	0	0	1	0
schist	0	0	0	0	0	0	1	1	0	2	1	2	0	0	2	0	3	2	1	1	0	0	0	2	0	0
gneiss	0	3	0	3	1	1	3	2	2	3	1	1	4	2	0	3	0	0	0	2	4	5	0	0	0	1
other volcanic	0	0	1	0	0	0	1	0	0	0	1	0	0	0	0	0	0	0	0	0	0	0	0	0	0	1
purple volcanic	0	0	0	0	0	0	0	0	0	0	0	0	0	0	0	0	0	0	0	0	0	0	0	0	1	0
green/yellow volcanic	0	0	0	0	2	1	0	1	2	0	0	2	0	0	0	0	2	2	1	0	0	0	0	0	0	2
rhyolite	3	0	0	0	1	1	1	0	0	2	0	0	2	0	0	0	2	0	0	1	0	3	1	0	0	3
foidite (?)	0	0	0	0	0	0	0	0	0	1	0	0	0	0	0	0	0	0	0	0	0	0	0	0	0	0
gabbroid	0	0	0	0	0	0	0	0	0	0	0	1	0	0	0	0	0	0	0	0	0	0	0	0	0	0
dioritoid	1	0	1	0	0	1	0	0	3	0	0	0	0	0	4	0	5	0	0	2	3	0	0	1	0	1
granitoid	4	0	3	4	2	3	9	3	6	10	3	5	3	3	6	10	1	2	1	2	7	11	4	5	4	3
radiolarite	0	0	1	0	0	0	1	0	0	4	0	2	0	0	6	0	5	4	0	5	8	2	1	1	4	5
chert	1	0	0	1	0	2	1	0	0	0	0	0	2	3	0	4	5	4	1	1	1	0	0	0	0	3
vein quartz	6	2	11	0	7	1	0	2	0	5	0	6	2	0	0	0	6	7	0	4	9	10	2	4	4	1
quartzite	8	8	18	24	30	1	6	4	18	24	8	12	4	2	2	9	21	13	11	23	39	17	6	20	17	13
rauhwacke-type breccia	0	0	0	0	0	0	0	0	0	0	0	0	2	0	0	0	1	0	0	0	0	0	0	0	0	0
breccia, general	0	0	0	0	0	0	0	0	0	0	0	0	1	0	0	0	0	1	0	2	0	0	0	0	1	0
red conglomerate	0	0	0	0	0	2	1	0	0	1	0	0	0	0	0	0	0	0	0	2	0	1	0	0	2	7
conglomerate, general	0	0	2	0	0	2	0	0	0	1	1	0	0	0	0	0	0	1	0	1	2	1	2	4	0	4
glauconitic sandstone	1	0	0	0	0	0	0	0	0	0	0	0	0	0	0	0	0	0	0	0	0	1	0	0	0	0
Taveyannaz sandstone	1	0	2	2	0	11	3	1	0	7	2	3	1	2	6	3	0	0	1	2	1	2	5	1	2	3
red sandstone	1	0	1	1	0	3	4	1	0	1	0	0	1	0	0	1	1	1	0	3	0	1	0	0	6	3
sandstone, general	34	19	32	39	26	27	33	20	19	48	19	24	15	28	25	41	24	9	26	31	42	34	23	34	15	30
dolostone	1	0	0	0	0	1	0	0	0	1	0	1	0	0	0	0	0	0	0	0	1	0	0	1	2	1
other limestone	1	1	0	0	0	4	0	0	0	4	1	0	2	0	0	0	1	6	0	4	5	1	2	2	1	0
patterned beige lst.	0	0	0	0	0	2	21	0	0	0	0	1	3	0	0	0	0	1	0	1	0	0	1	1	2	1
beige lst., angular	0	0	0	0	0	0	0	0	0	0	0	7	0	0	0	0	0	0	0	0	2	0	0	0	0	0
beige limestone	3	5	2	8	15	2	12	5	6	5	5	4	5	3	3	6	9	25	5	15	11	8	4	5	10	8
dark granular limestone	0	0	8	0	0	6	5	0	0	0	0	0	14	0	0	0	13	11	0	14	0	0	0	0	0	0
light grey siliceous lst.	63	46	25	68	55	30	27	59	50	88	38	15	47	27	22	93	19	37	59	31	69	51	58	44	49	83
light grey limestone	8	6	10	1	5	7	8	8	1	19	1	0	4	0	13	14	10	15	2	15	3	2	8	4	7	19
dark gey siliceous lst.	19	11	32	10	10	37	44	11	23	0	15	2	40	22	33	10	30	6	15	26	24	9	28	27	12	13
dark grey limestone	6	1	3	0	0	4	8	0	1	0	0	3	2	0	4	2	1	1	0	7	0	0	2	1	2	2

Table IV-S4 (continued): Petrographic composition of field-collected samples (percentage; see Table IV-S1 for descriptions and coordinates).

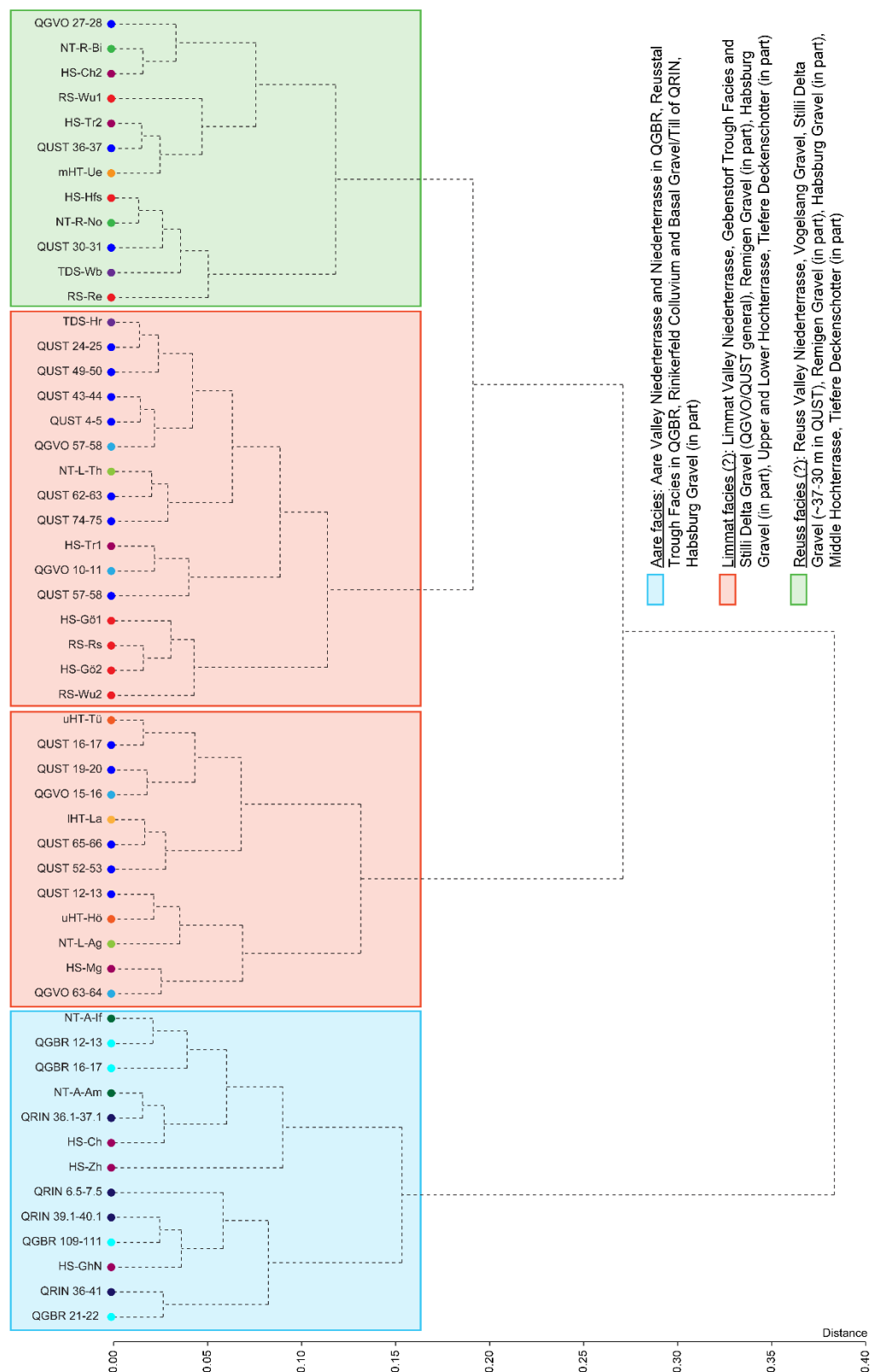| Sample	TDS-Hr	TDS-Wb	HS-Ch1	HS-Ch2	HS-GhN	HS-Göl	HS-Gö2	HS-Hfs	HS-Mg	HS-Tr1	HS-Tr2	HS-Zh	RS-Re	RS-Wu1	RS-Wu2	RS-Rs	uHT-Hö	uHT-Tü	mHT-Ue	lHT-La	NT-A-Am	NT-A-If	NT-R-No	NT-R-Bi	NT-L-Ag	NT-L-Th
Sum	100	100	100	100	100	100	100	100	100	100	100	100	100	100	100	100	100	100	100	100	100	100	100	100	100	100
serpentinite	0.0	0.0	0.0	0.0	0.0	0.0	0.0	0.0	0.0	0.0	0.0	0.0	0.0	0.0	0.0	0.0	0.0	0.7	0.0	0.0	0.0	0.0	0.0	0.0	0.0	0.0
amphibolite	0.0	1.0	0.0	0.0	0.0	0.0	0.0	0.0	0.0	0.4	1.0	1.1	0.0	0.0	0.0	0.0	0.0	0.0	0.5	0.0	0.0	0.0	0.0	0.0	0.7	0.0
schist	0.0	0.0	0.0	0.0	0.0	0.0	0.5	0.8	0.0	0.9	1.0	2.2	0.0	1.6	0.0	1.9	1.3	0.8	0.5	0.0	0.0	0.0	1.3	0.0	0.0	0.0
gneiss	0.0	2.9	0.0	1.9	0.6	0.7	1.6	1.7	1.5	1.3	1.0	1.1	2.6	2.2	0.0	1.5	0.0	0.0	0.0	1.0	1.7	3.1	0.0	0.0	0.0	0.5
other volcanic	0.0	0.0	0.7	0.0	0.0	0.0	0.5	0.0	0.0	0.0	1.0	0.0	0.0	0.0	0.0	0.0	0.0	0.0	0.0	0.0	0.0	0.0	0.0	0.0	0.0	0.5
purple volcanic	0.0	0.0	0.0	0.0	0.0	0.0	0.0	0.0	0.0	0.0	0.0	0.0	0.0	0.0	0.0	0.0	0.0	0.0	0.0	0.0	0.0	0.0	0.0	0.0	0.7	0.0
green/yellow volcanic	0.0	0.0	0.0	0.0	1.3	0.7	0.0	0.8	1.5	0.0	2.2	0.0	0.0	0.0	0.0	0.0	1.3	1.3	0.8	0.0	0.0	0.0	0.0	0.0	0.0	1.0
rhyolite	1.9	0.0	0.0	0.0	0.6	0.7	0.5	0.0	0.0	0.9	0.0	0.0	1.3	0.0	0.0	0.5	1.3	0.0	0.0	0.5	0.0	1.9	0.7	0.0	0.0	1.4
foidite (?)	0.0	0.0	0.0	0.0	0.0	0.0	0.0	0.0	0.0	0.4	0.0	0.0	0.0	0.0	0.0	0.0	0.0	0.0	0.0	0.0	0.0	0.0	0.0	0.0	0.0	0.0
gabbroid	0.0	0.0	0.0	0.0	0.0	0.0	0.0	0.0	0.0	0.0	1.1	0.0	0.0	0.0	0.0	0.0	0.0	0.0	0.0	0.0	0.0	0.0	0.0	0.0	0.0	0.0
dioritoid	0.6	0.0	0.7	0.0	0.0	0.7	0.0	0.0	2.3	0.0	0.0	0.0	0.0	0.0	3.2	0.0	3.1	0.0	0.0	1.0	1.3	0.0	0.0	0.6	0.0	0.5
granitoid	2.5	0.0	2.0	2.5	1.3	2.0	4.8	2.5	4.6	4.4	3.1	5.4	1.9	3.3	4.8	5.1	0.6	1.3	0.8	1.0	3.1	6.8	2.7	3.2	2.8	1.4
radiolarite	0.0	0.0	0.7	0.0	0.0	0.0	0.5	0.0	0.0	1.8	0.0	2.2	0.0	0.0	4.8	0.0	3.1	2.7	0.0	2.6	3.5	1.2	0.7	0.6	2.8	2.4
chert	0.6	0.0	0.0	0.6	0.0	1.3	0.5	0.0	0.0	0.0	0.0	0.0	1.3	3.3	0.0	2.0	3.1	2.7	0.8	0.5	0.4	0.0	0.0	0.0	0.0	1.4
vein quartz	3.7	1.9	7.2	0.0	4.5	0.7	0.0	1.7	0.0	2.2	0.0	6.5	1.3	0.0	0.0	0.0	3.8	4.7	0.0	2.0	3.9	6.2	1.4	2.5	2.8	0.5
quartzite	5.0	7.8	12	15	19	0.7	3.2	3.4	14	11	8.2	13	2.6	2.2	1.6	4.6	13	8.7	8.9	12	17	11	4.1	13	12	6.3
rauhwacke-type breccia	0.0	0.0	0.0	0.0	0.0	0.0	0.0	0.0	0.0	0.0	0.0	0.0	1.3	0.0	0.0	0.0	0.6	0.0	0.0	0.0	0.0	0.0	0.0	0.0	0.0	0.0
breccia, general	0.0	0.0	0.0	0.0	0.0	0.0	0.0	0.0	0.0	0.0	0.0	0.0	0.6	0.0	0.0	0.0	0.7	0.0	1.0	0.0	0.0	0.0	0.0	0.7	0.0	0.0
red conglomerate	0.0	0.0	0.0	0.0	0.0	1.3	0.5	0.0	0.0	0.4	0.0	0.0	0.0	0.0	0.0	0.0	0.0	0.0	0.0	1.0	0.0	0.6	0.0	0.0	1.4	3.4
conglomerate, general	0.0	0.0	1.3	0.0	0.0	1.3	0.0	0.0	0.0	0.4	1.0	0.0	0.0	0.0	0.0	0.0	0.0	0.7	0.0	0.5	0.9	0.6	1.4	2.5	0.0	1.9
glauconitic sandstone	0.6	0.0	0.0	0.0	0.0	0.0	0.0	0.0	0.0	0.0	0.0	0.0	0.0	0.0	0.0	0.0	0.0	0.0	0.0	0.0	0.0	0.6	0.0	0.0	0.0	0.0
Taveyannaz sandstone	0.6	0.0	1.3	1.2	0.0	7.4	1.6	0.8	0.0	3.1	2.1	3.3	0.6	2.2	4.8	1.5	0.0	0.0	0.8	1.0	0.4	1.2	3.4	0.6	1.4	1.4
red sandstone	0.6	0.0	0.7	0.6	0.0	2.0	2.1	0.8	0.0	0.4	0.0	0.0	0.6	0.0	0.0	0.5	0.6	0.7	0.0	1.5	0.0	0.6	0.0	0.0	4.2	1.4
sandstone, general	21	18	21	24	17	18	17	17	15	21	20	26	9.6	30	20	21	15	6.0	21	16	18	21	16	22	11	14
dolostone	0.6	0.0	0.0	0.0	0.0	0.7	0.0	0.0	0.0	0.4	0.0	1.1	0.0	0.0	0.0	0.0	0.0	0.0	0.0	0.0	0.4	0.0	0.0	0.6	1.4	0.5
other limestone	0.6	1.0	0.0	0.0	0.0	2.7	0.0	0.0	0.0	1.8	1.0	0.0	1.3	0.0	0.0	0.0	0.6	4.0	0.0	2.0	2.2	0.6	1.4	1.3	0.7	0.0
patterned beige lst.	0.0	0.0	0.0	0.0	0.0	1.3	11	0.0	0.0	0.0	1.1	1.9	0.0	0.0	0.0	0.0	0.0	0.7	0.0	0.5	0.0	0.0	0.7	0.6	1.4	0.5
beige lst., angular	0.0	0.0	0.0	0.0	0.0	0.0	0.0	0.0	0.0	0.0	0.0	7.6	0.0	0.0	0.0	0.0	0.0	0.0	0.0	0.0	0.0	1.2	0.0	0.0	0.0	0.0
beige limestone	1.9	4.9	1.3	5.0	9.7	1.3	6.3	4.2	4.6	2.2	5.2	4.3	3.2	3.3	2.4	3.1	5.7	17	4.1	7.7	4.8	5.0	2.7	3.2	7.0	3.9
dark granular limestone	0.0	0.0	5.3	0.0	0.0	4.0	2.6	0.0	0.0	0.0	0.0	0.0	9.0	0.0	0.0	0.0	8.2	7.4	0.0	7.1	0.0	0.0	0.0	0.0	0.0	0.0
light grey siliceous lst.	39	45	16	42	36	20	14	50	38	39	39	16	30	29	17	47	12	25	48	16	30	32	39	28	35	40
light grey limestone	5.0	5.8	6.6	0.6	3.2	4.7	4.2	6.8	0.8	8.4	1.0	0.0	2.6	0.0	10	7.1	6.3	10	1.6	7.7	1.3	1.2	5.4	2.5	4.9	9.2
dark gey siliceous lst.	12	11	21	6.2	6.5	25	23	9.3	18	0.0	15	2.2	26	24	26	5.1	19	4.0	12	13	10	5.6	19	17	8.5	6.3
dark grey limestone	3.7	1.0	2.0	0.0	0.0	2.7	4.2	0.0	0.8	0.0	0.0	3.3	1.3	0.0	3.2	1.0	0.6	0.7	0.0	3.6	0.0	0.0	1.4	0.6	1.4	1.0

Fig. IV-S1: Results of a cluster analysis of the petrographic samples (Ward's method, Euclidean distance matrix). Facies groups are identified based on reference samples from the Niederterrasse, and generally agree well with principal component analysis as well as previous studies (see text).
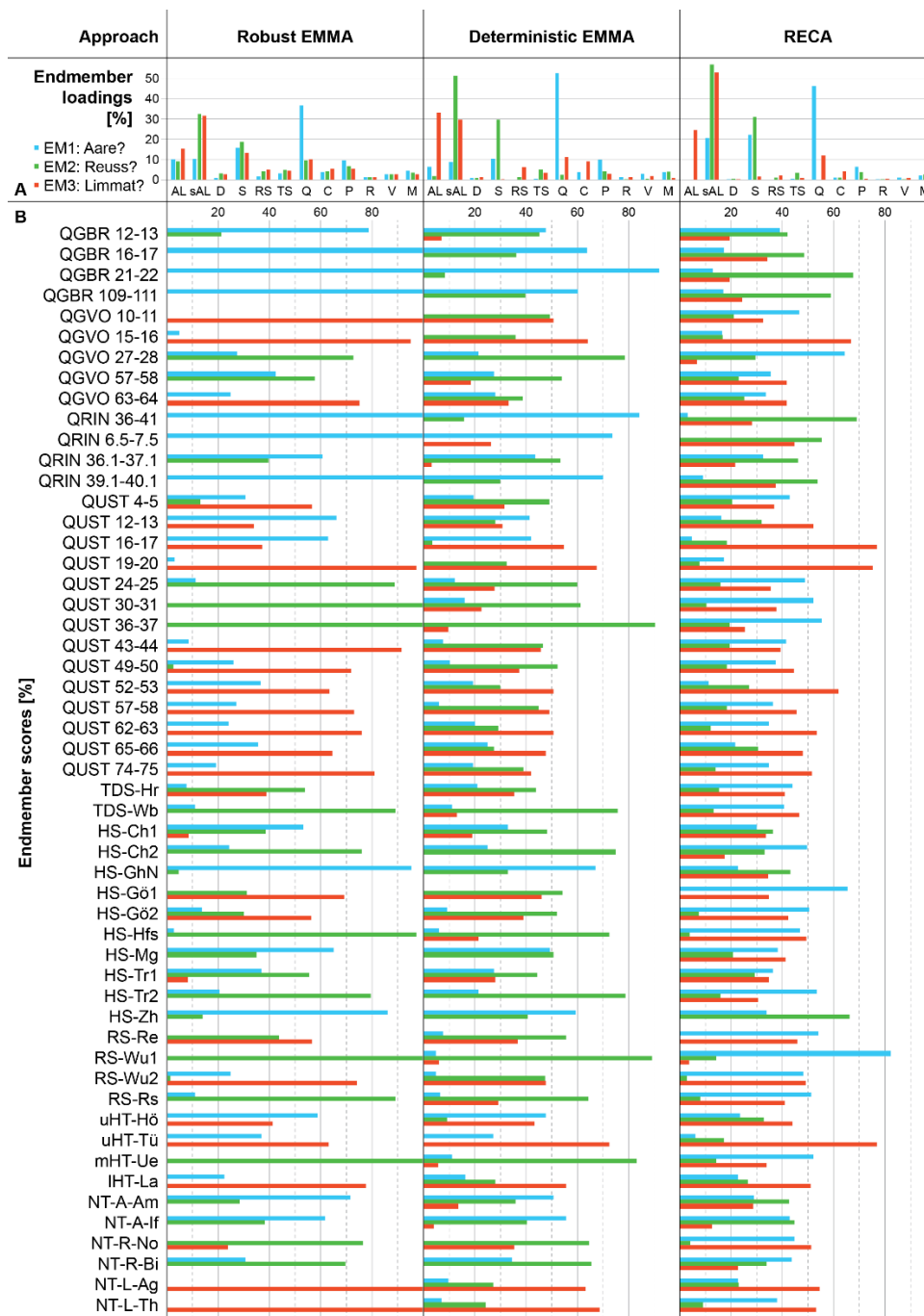
Fig. IV-S2: Results of three different endmember (EM) analyses (Robust EMMA; deterministic EMMA with 3 EM; RECA with 3 EM, convexity threshold -6, and weighing exponent 1). All approaches produce a quartz-rich EM (EM1, tentatively correlated with an Aare input; S2A), a siliceous Alpine limestone-rich EM (EM2, ~Reuss?), and a third EM rich in non-siliceous Alpine limestone (EM3, ~Limmat?). The EM scores of Niederterrasse reference samples (last 6 lines; S2B) suggests that in our case the EMMAgeo package performs better than the RECA package. The calculated EM scores of the EMMA analyses generally agree well with principal component analysis, clustering, and previous studies (see text, Fig. IV-S1).

194

Table IV-S5: Oedometer measurement data (sample compaction in response to applied vertical load) and work done per unit volume after Becker *et al.* (1987). Initial thickness of all samples is 20 mm.

sample	QGBR, 43.10 m		QGBR, 63.90 m		QGBR, 68.90 m		QGBR, 74.90 m		QGBR, 78.90 m	
load [kN/m2]	compact. [mm]	Δ work [kN/m]	compact. [mm]	Δ work [kN/m]	compact. [mm]	Δ work [kN/m]	compact. [mm]	Δ work [kN/m]	compact. [mm]	Δ work [kN/m]
12.5	0.18	-	0.14	-	0.14	-	0.16	-	0.15	-
25	0.24	63	0.20	58	0.20	60	0.18	21	0.19	45
50	0.32	155	0.29	181	0.32	227	0.24	120	0.28	169
100	0.44	447	0.42	496	0.50	697	0.38	515	0.40	457
200	0.57	994	0.59	1316	0.71	1636	0.45	563	0.56	1235
400	0.75	2943	0.81	3495	0.91	3259	0.60	2357	0.80	3758
800	0.97	6990	1.03	7262	1.25	11049	0.79	5898	1.11	10118
1600	1.22	16579	1.32	19046	1.59	23008	1.02	14900	1.39	18817
3200	1.54	43091	1.65	44225	2.05	63693	1.34	41631	1.74	47775

sample	QGBR, 84.90 m		QGBR, 96.90 m		QGBR, 100.90 m		QGBR, 106.90 m	
load [kN/m2]	compact. [mm]	Δ work [kN/m]	compact. [mm]	Δ work [kN/m]	compact. [mm]	Δ work [kN/m]	compact. [mm]	Δ work [kN/m]
12.5	0.13	-	0.12	-	0.30	-	0.22	-
25	0.17	37	0.33	194	0.36	64	0.31	87
50	0.27	195	0.64	610	0.50	276	0.43	240
100	0.39	474	0.80	703	0.69	767	0.59	634
200	0.59	1588	1.01	1891	0.93	2063	0.80	1756
300	0.68	1409	1.13	2253	1.07	2388	0.94	2289
400	0.76	1816	1.21	2652	1.18	3143	1.05	2798
600	0.91	4627	1.36	5939	1.39	7459	1.33	8816
800	0.98	4048	1.44	6477	1.48	7068	1.43	7248
1200	1.14	10931	1.60	14153	1.67	16145	1.71	20565
1600	1.24	12386	1.69	16574	1.80	20607	1.85	21568
2400	1.42	27401	1.87	35021	2.05	44660	2.10	46249
3200	1.59	40685	2.00	47449	2.20	56347	2.25	58473

Table IV-S5 (continued): Oedometer measurement data (sample compaction in response to applied vertical load) and work done per unit volume after Becker *et al.* (1987). Initial thickness of all samples is 20 mm ([1]: 19.1 mm; [2]: sample QRIN, 20.89 m).

sample	QRIN, 9.65 m [1]		QRIN, 16.26 m		QRIN, 20.89 m		QRIN, 29.15 m [2]		QRIN, 31.88 m	
load [kN/m2]	compact. [mm]	Δ work [kN/m]	compact. [mm]	Δ work [kN/m]	compact. [mm]	Δ work [kN/m]	compact. [mm]	Δ work [kN/m]	compact. [mm]	Δ work [kN/m]
12.5	0.39	-	-	-	0.09	-	0.09	-	0.19	-
25	0.57	188	0.34	-	0.15	57	0.17	75	0.28	85
50	0.79	480	0.43	194	0.27	233	0.40	44	0.42	270
100	1.06	1240	0.64	829	0.45	687	0.73	1269	0.61	776
200 ([2] 175)	1.36	2984	0.83	1466	0.68	1695	1.09	2928	0.86	1863
300 ([2] 275)	-	-	0.96	1983	0.84	2109	-	-	1.01	2275
400 ([2] 375)	1.70	7387	1.08	2835	0.96	2682	1.52	7134	1.10	2383
600	-	-	1.32	7790	1.23	8045	-	-	1.32	7261
800	2.11	19355	1.54	11419	1.41	9380	2.03	17712	1.49	9603
1200	-	-	1.94	28210	1.74	23055	-	-	1.66	14911
1600	-	-	2.24	37817	1.98	30622	2.59	41086	1.81	22357
2400	-	-	2.72	82253	2.40	67253	-	-	2.08	47500
3200	-	-	3.01	106820	2.67	89902	3.18	92312	2.26194	61577

Table IV-S6: Water contents and Atterberg limits determined from samples from QGBR and QRIN.

QGBR				QRIN			
Depth [m]	**Water content**	**Liquid limit**	**Plastic limit**	**Depth [m]**	**Water content**	**Liquid limit**	**Plastic limit**
68.90	16%	18%	15%	9.65	25%	25%	14%
106.90	19%	19%	14%	16.26	23%	34%	17%
109.80	14%	18%	11%	20.89	22%	34%	16%
Note: samples from 43.10, 63.90, 74.90, 78.90, 84.90, 96.90, 100.90 m depth not sufficiently cohesive.				29.15	20%	24%	16%
				31.88	21%	31%	14%
				39.88	9%	18%	13%

This page is intentionally left blank.
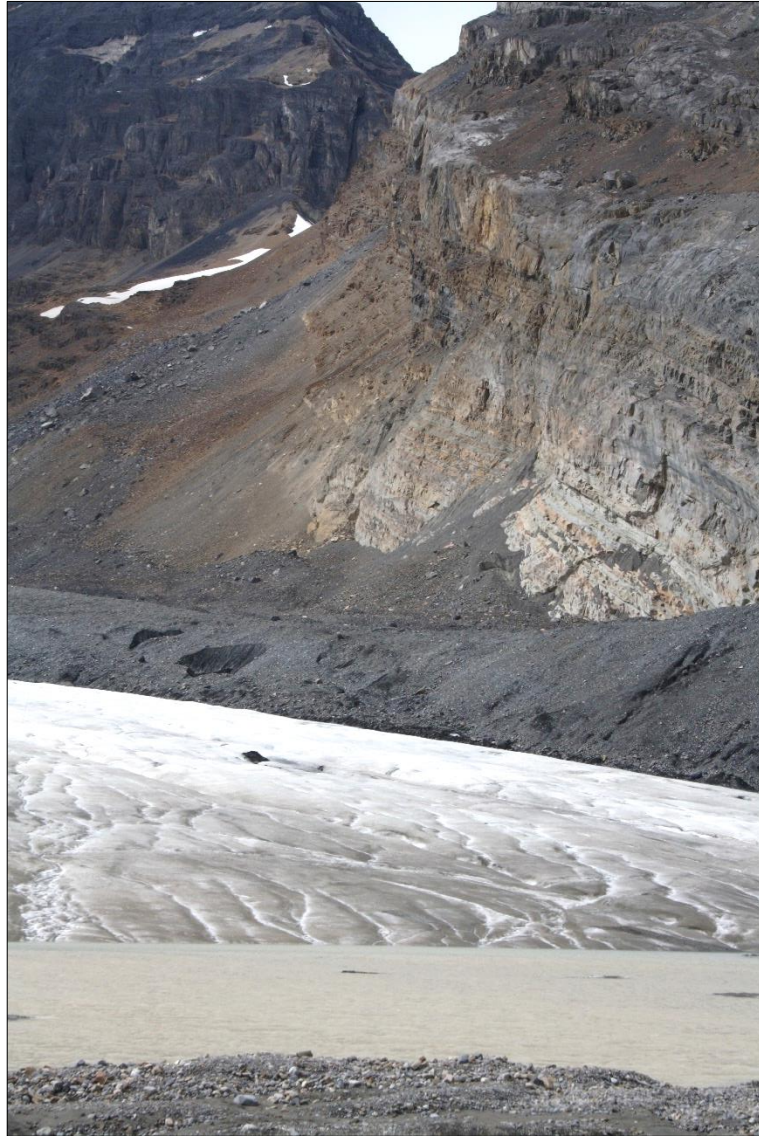
Terminus of the Athabasca Glacier (British Columbia, Canada).

V. Conclusions and Outlook

The present thesis sheds light on the process of overdeepening erosion and the associated subglacial conditions, as well as on the sedimentary archive contained in the resulting basin. This is done by the example of the Lower Aare Valley in northern Switzerland, which has been targeted by a scientific drilling campaign.

For the second chapter, borehole data were complemented with a geophysical survey based on the analysis of surface waves, a cost-effective approach found well-suited for subsurface mapping of the overdeepened Gebenstorf-Stilli Trough. It revealed an unexpected, complex trough shape that could be linked to the study area's regionally unique bedrock architecture, and shows that varying rock erodibilities exert major control on the efficiency of overdeepening erosion. This suggests that the morphologic complexity of overdeepenings in heterogeneous bedrock may have been considerably underestimated (*e.g.* in Linsbauer *et al.*, 2016; Patton *et al.*, 2016; Pietsch & Jordan, 2014). The presented results further indicate that subglacial water played a significant, possibly the leading, role in the erosion of the trough, and thus that the overdeepenings of mountain forelands may be appropriately regarded as analogues of tunnel valleys (Cofaigh, 1996; Dürst Stucki and Schlunegger, 2013; Van der Vegt *et al.*, 2012).

The role of fluid water in overdeepening erosion is further exemplified by the findings of the third chapter. There, surficial brecciation in sediment-filled paleokarst walls underneath the overdeepened trough was identified as the result of hydrofracturing, illustrating the occurrence of high water-pressure events. In contrast to typical hydrofractures (*e.g.* Phillips *et al.*, 2013; Rijsdijk *et al.*, 1999) however, no macroscopic, microscopic or mineralogical evidence was encountered for water flow through the paleokarst or the newly formed fractures, indicating that they did not act as 'safety valves' (Van der Meer *et al.*, 2009) and that the pressurised water could not escape from the base of the overdeepening. In spite – or exactly because – of that, subglacial hydrofracturing may be an important but yet underestimated mechanism of subglacial overdeepening erosion.

The sedimentary archive of the Gebenstorf-Stilli Trough, as well as further Pleistocene deposits in its vicinity, are the main focus of the fourth chapter. Borehole logs, detailed sedimentological characterisation and gravel petrographic compositions prove to be valuable stratigraphic tools in both the overdeepening and neighbouring glaciofluvial paleovalleys (Graf, 2009). That way, discernible sediment bodies are recognised, material inputs from the individual confluent glaciers (Aare, Reuss, Limmat) are identified, and several phases of glacial and/or glaciofluvial reactivation are reconstructed. An integration of luminescence ages shows that the Pleistocene deposits of the Lower Aare Valley represent large parts of the Middle and Late Pleistocene (MIS 10-4 at minimum), and allows to tie them into the regional framework, where evidence of the early Mid-Pleistocene has previously been very scarce (Preusser *et al.*, 2011). However, the results of this study indicate that detailed multi-method investigations at other key sites have the potential to further expand the regional record.

At the time of completion of this thesis, overdeepened basins and their infills are the target of several independent projects under Bernese lead or participation. With scientific drillings completed in central northern Switzerland (QBO; Fig. I-7) and further upstream the Aare Valley (Schwenk *et al.*, 2020), and ongoing in the Lake Constance area (ICDP DOVE: Anselmetti *et al.*, 2016), many hundred meters of cores are undergoing or awaiting analysis. Further valuable insights are to be expected from palynological analysis of the recovered records (Schläfli *et al.*, 2020), as well as from gravimetric mapping of overdeepenings (Bandou *et al.*, 2020), and regional-scale models (Magrani *et al.*, 2020). There is therefore all reason to be curious about the future…

References

Anselmetti, F. S., Preusser, F., Crouzet, C., Fiebig, M., Gabriel, G., and Ravazzi, C., 2016, Drilling Overdeepened Alpine Valleys (DOVE): ICDP Full Proposal 2016/04, 174 p.

Bandou, D., Schläfli, P., Schwenk, M., Douillet, G., Kissling, E., and Schlunegger, F., 2020, Overdeepenings modelled with gravimetry-based data: EGU General Assembly Conference Abstracts, 15807.

Dürst Stucki, M., and Schlunegger, F., 2013, Identification of erosional mechanisms during past glaciations based on a bedrock surface model of the central European Alps: Earth and Planetary Science Letters, v. 384, p. 57-70.

Cofaigh, C. Ó., 1996, Tunnel valley genesis: Progress in physical geography, v. 20, no. 1, p. 1-19.

Graf, H. R. 2009: Stratigraphie von Mittel-und Spätpleistozän in der Nordschweiz: Bundesamt für Landestopographie, Wabern, 198 p.

Linsbauer, A., Frey, H., Haeberli, W., Machguth, H., Azam, M., and Allen, S., 2016, Modelling glacier-bed overdeepenings and possible future lakes for the glaciers in the Himalaya—Karakoram region: Annals of Glaciology, v. 57, no. 71, p. 119-130.

Magrani, F., Valla, P., Gribenski, N., and Serra, E., 2020, Glacial overdeepenings in the Swiss Alps and foreland: Spatial distribution and morphometrics: Quaternary Science Reviews, v. 243.

Patton, H., Swift, D., Clark, C., Livingstone, S. J., and Cook, S. J., 2016, Distribution and characteristics of overdeepenings beneath the Greenland and Antarctic ice sheets: Implications for overdeepening origin and evolution: Quaternary Science Reviews, v. 148, p. 128-145.

Phillips, E., Everest, J., and Reeves, H., 2013, Micromorphological evidence for subglacial multiphase sedimentation and deformation during overpressurised fluid flow associated with hydrofracturing: Boreas, v. 42, no. 2, p. 395-427.

Pietsch, J., and Jordan, P., 2014, Digitales Höhenmodell Basis Quartär der Nordschweiz - Version 2014 und ausgewählte Auswertungen: Nagra Arbeitsbericht NAB 14-02, 69 p.

Preusser, F., Graf, H. R., Keller, O., Krayss, E., and Schlüchter, C., 2011, Quaternary glaciation history of northern Switzerland: E&G Quaternary Science Journal, v. 60, p. 282-305.

Rijsdijk, K. F., Owen, G., Warren, W. P., McCarroll, D., and van der Meer, J. J., 1999, Clastic dykes in over-consolidated tills: evidence for subglacial hydrofracturing at Killiney Bay, eastern Ireland: Sedimentary Geology, v. 129, no. 1-2, p. 111-126.

Schläfli, P., Gobet, E., Tinner, W., van Leeuwen, J., Vescovi, E., Douillet, G., Schwenk, M., Bandou, D., and Schlunegger, F., 2020, Biostratigraphic dating of palaeolake deposits from an overdeepening in the Swiss Northern Alpine Foreland by numerical assessments of vegetation composition and the role of species dynamics: EGU General Assembly Conference Abstracts, 8287.

Schwenk, M. A., Bandou, D., Schläfli, P., Douillett, G. A., and Schlunegger, F., 2020, Drilling into mid-Pleistocene sediments in the overdeepened Aare Valley, CH: EGU General Assembly Conference Abstracts, 5214.

Van der Meer, J. J., Kjær, K. H., Krüger, J., Rabassa, J., and Kilfeather, A., 2009, Under pressure: clastic dykes in glacial settings: Quaternary Science Reviews, v. 28, no. 7-8, p. 708-720.

Van der Vegt, P., Janszen, A., and Moscariello, A., 2012, Tunnel valleys: current knowledge and future perspectives: Geological Society, London, Special Publications, v. 368, no. 1, p. 75-97.

This page is intentionally left blank.

Sedimentary structures in glaciofluvial gravel and sand (Lower Aare Valley, Switzerland).

Appendix A: Beyond the scope

1. Introduction

During the process of sample analysis and interpretation, and writing of the thesis at hand, much more data have been acquired than could reasonably be integrated into the main chapters. Here, some of the data that did not make it into these manuscripts are presented and tentatively interpreted. The following section thus provides further insights into very specific topics, and is intended as a basis for future work.

2. Approaches towards bedrock erodibility quantification

In chapter II, evidence for strong lithological control on the efficiency of subglacial overdeepening erosion in the Wasserschloss area was provided. The results of this study indicate that the Upper Jurassic limestones (Villigen Fm.) of the Jura Mountains are significantly more resistant to overdeepening erosion than underlying marls (Wildegg Fm.) and overlying Molasse deposits. A quantification of this erodibility contrast however is difficult (Zhang, 2010). In applied geology, several attempts have been made to assess rock mass strength (RMS), *i.e.* the macroscale strength of a natural, jointed rock body, based on outcrop and drill core evaluation (*e.g.* Bieniawski, 1973; Deere, 1963; Marinos and Hoek, 2000; see also Edelbro, 2003). It has been suggested that RMS is among the primary controls on subaerial hillslope denudation, and that slope angles that are not predefined by distinct fracture sets will tend towards a 'strength equilibrium' (Selby, 1982; see also *e.g.* Augustinus, 1992; Brook and Tippett, 2002; Moore *et al.*, 2009). Therefore, an assessment of RMS via analysis of digital elevation data could be a viable approach.

Thus, LiDAR surface elevation data with a spatial resolution of 2 m (Swisstopo, 2013) were analysed in order to better characterise the resilience of the above-mentioned lithologies, and of further stratigraphic units in the vicinity. Based on the 1 : 25'000-scale Geologic Atlas of Switzerland (Graf *et al.*, 2006), outcrop areas of the bedrock units were mapped, and slope angle histograms of these areas were computed (Fig. A-1). On average, higher slope angles should correspond to higher RMS and thus reduced erodibility. However, the interpretation of the diagrams on Fig. A-1 is not straightforward due to the tectonic setting: Dip angles of the bedrock strata vary strongly throughout the study area (see chapter II) and may result in an overrepresentation of certain slope angles. As an example, the sub-horizontal Villigen Fm. limestones of the Tabular Jura form plateaus that reduce the average/median hillslope angle. Therefore, it may be more appropriate to compare the abundances of steep hillslopes, which are here defined by an angle of >30° (DiBiase *et al.*, 2017; Tian *et al.*, 2017).

The results suggest relatively low RMS / high erodibility for Molasse and Opalinus Clay (≤5% >30°), intermediate RMS / erodibility for Wildegg Fm., Staffelegg Fm. and Klettgau/Bänkerjoch Fm. (5-10% >30°), and relatively high RMS / low erodibility for Villigen Fm., PKI, and Schinznach Fm. (>10% >30°). This is in qualitative agreement with conclusions by Ludwig (2018).

The incision of the Gebenstorf-Stilli Trough through the Folded Jura allows for a second approach targeting the differences of RMS. As described in chapter II, the cross section of the buried trough remains largely constant throughout the FJ despite the bedrock lithologies changing repeatedly over short distances. However, the exposed valley slopes above the trough infill have been subject to continued erosion and slope retreat whose extent shows considerable differences (Fig. A-2). On average, estimated values range from <300 m in the presumably resistant Villigen Fm. and Schinznach Fm., to >500 m in the weaker Opalinus Clay. In the Wildegg Fm., PKI, and Klettgau/Bänkerjoch Fm., intermediate values (350-420 m on average) are determined, whereas the Molasse beyond the FJ is almost entirely levelled off (Fig. A-2). While these results generally agree with the considerations above, they have to be again interpreted cautiously, as a direct conversion of estimated slope retreat to RMS would likely be a gross oversimplification. Locally, slope retreat may have been enhanced through weakening by faults (Graf *et al.*, 2006) or through undercutting by the meandering Reuss river, leading to an underestimation of the respective RMS. In addition, some of the stratigraphic units, especially the aggregated PKI and Klettgau/Bänkerjoch Fm., are lithologically diverse and likely not appropriately characterised by a single RMS value.

As a concluding remark, it needs to be emphasised that LiDAR data, like most digital elevation data, only provide insights into the non-overdeepened realm. Therefore, an assessment of rock resilience via DEMs, and conclusions drawn from it, are restricted to the corresponding erosion processes, which are likely different from the prevailing processes in overdeepening erosion (see chapter II). The analysed hillslopes have not been glaciated for ~150 ka (Bini *et al.*, 2009; Preusser *et al.*, 2011), and their present-day morphology is a product of subaerial denudation. It is not clear and needs to be a focus of future work in how far subaerial erodibilities can be applied to the overdeepening process.

Appendix A
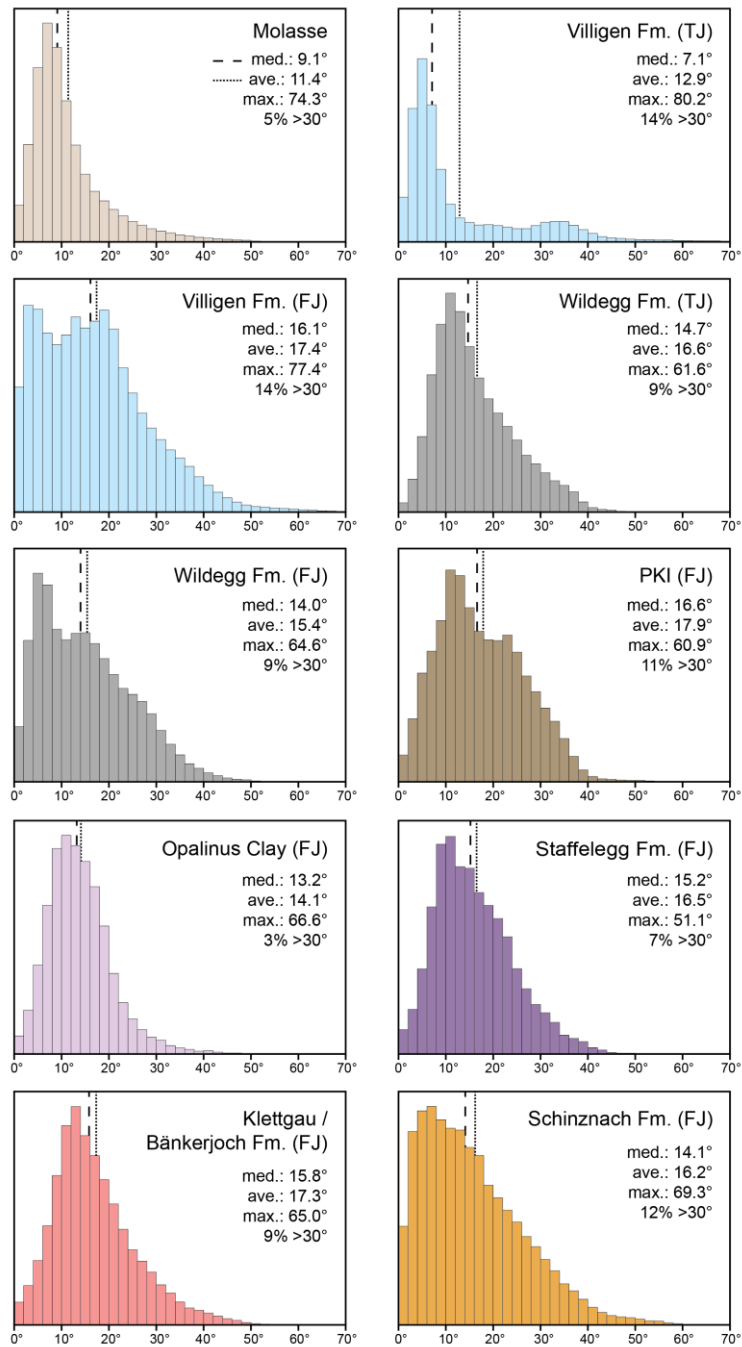
Fig. A-1: Slope histograms for outcrop areas of the bedrock strata in the Wasserschloss area, distinguishing between Tabular (TJ) and Folded Jura (FJ).
Med. = median (dashed line), ave. = average (dotted line), max. = maximum values.

Fig. A-2 (next page): Cross sections of the buried Gebenstorf-Stilli Trough and the modern valley flanks through the Folded Jura from south (bottom) to north (top). With dashed lines, the post-incisional slope retreat of the exposed valley walls is estimated.
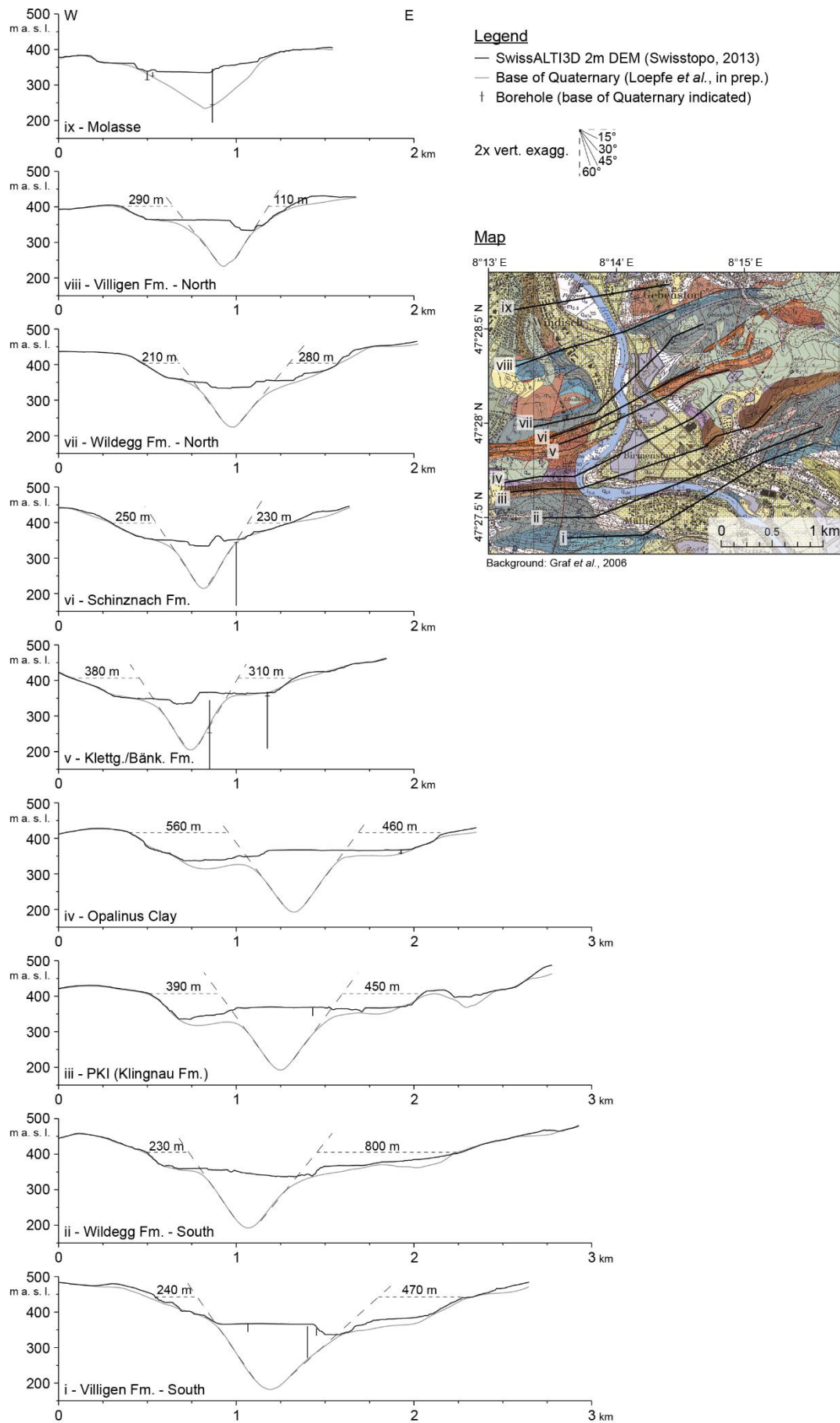
Appendix A

Appendix A

3. Further thoughts on gravel petrography

Gravel petrographic compositions are a valuable tool to subdivide individual sediment bodies and to infer material provenance (chapter IV; Gerth and Becker-Haumann, 2007; Graf, 2009; Schlüchter, 1975). In contrast to the sand fraction that predominantly reflects local bedrock erosion, for example in heavy mineral spectra, coarser-grained components of Pleistocene deposits of Switzerland have been shown to better preserve a source signal (Gasser and Nabholz, 1969; Graf, 2009). In the Wasserschloss area, sediment petrography and provenance can be especially powerful tools for Quaternary geology. On the one hand, petrographic analysis allows a distinction of sediments delivered from Aare, Reuss, and Limmat. On the other hand, especially the Stilli Delta Gravel contains a comparatively long and continuous record to explore (see chapter IV), which cannot be expected in a glaciofluvial setting.

Pitfalls of petrographic analysis can lie in mixing of different deposits, *e.g.* by reworking of older glaciofluvial gravels or Molasse deposits (Weltje and von Eynatten, 2004). Thus, individual clasts of certain lithologies, especially of index lithologies, must be interpreted with caution and under consideration of complex transport pathways. Further complication can arise from sediment modification during and after transport, *e.g.* by the erosion of non-resistant clasts that end up being underrepresented (Weltje and von Eynatten, 2004). In the Wasserschloss area, potential examples include dolostones and certain sandstones and granitoids that are occasionally encountered in a weathered, disintegrating shape (see Graf, 2009). Finally, inferring the provenance of old deposits through gravel petrography may be difficult as the surface geology in the source areas may change with ongoing erosion, distorting its specific fingerprint over time (Schlüchter, 1975).

In chapter IV, the results of principal component analysis (PCA) were presented, and it was inferred that principal component (PC) 1 is indicative for the sediment-delivering catchments, which PC2 appears not to be. PC2 separates primarily samples rich in Alpine limestones (high PC2) from samples rich in sandstones (low PC2; correlation coefficient -0.40; Fig. A-3). I assume that PC2 could contain information on the dominant sediment source in terms of tectonic units, with low PC2 values indicating erosion focused in the Molasse basin, *i.e.* the mountain foreland, and high PC2 values indicating predominantly inner-Alpine erosion. This could be linked to peak glacial conditions vs. conditions of rather limited ice extent, respectively.
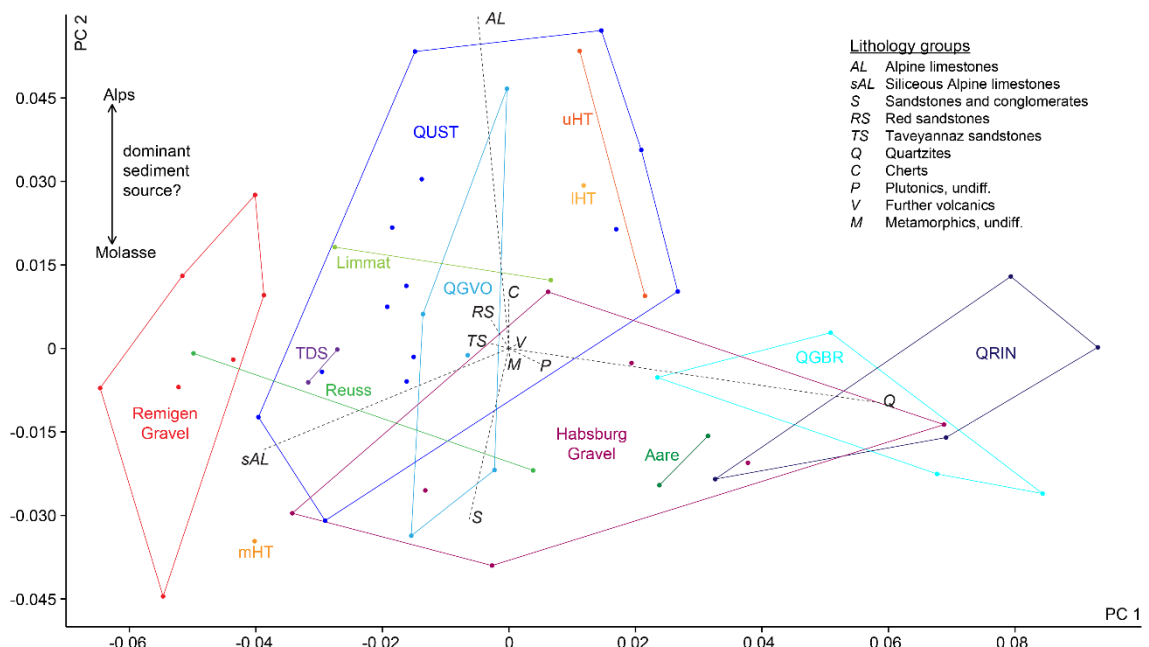
Fig. A-3: Results of a principal component analysis (PCA) of gravel petrographic data including all lithology groups except from locally derived (Jura Mountains) limestones. For details, please see chapter IV.

It is noteworthy that the PC2 (and PC1) scores of QUST do not display a random scatter but several distinct trends whose breaks lie at the approximate locations of unit boundaries, some of which are presumably associated with hiati (Fig. A-4). This gives the impression that both PC have, in fact, geological implications.

Appendix A

Applying the above-mentioned considerations, the first increasing and then decreasing PC2 scores in the Gebenstorf Trough Diamict and Stilli Delta Gravel could indicate ice retreat followed by a re-advance, which could be connected with, and supported by, presumed dropstones encountered towards the top of the Gebenstorf Sand in QGBR and QGVO (see chapter IV). Increasing PC2 scores in the Vogelsang Gravel would thus suggest its deposition during ice retreat, while the decreasing scores in the Niederterrasse would point towards deposition during ice advance (Fig. A-4).

Further, a positive correlation of PC1 and PC2 is observed in QUST (correlation coefficient 0.56; Fig. A-4), indicating that larger glacier distances coincided with relatively increased sediment input from the Aare catchment (high PC1, see chapter IV). This is not readily explained. Different magnitudes of local redeposition as opposed to the delivery of fresh sediment from outside of the study area may, for example, play a role.

Generally, these considerations at their present stage require significantly more discussion to be viable. Several important points of uncertainty exist and will have to be addressed. i) Considerable contributions of, among others, siliceous Alpine limestones and quartzites (Reuss and Aare signals?) to PC2 suggest that its significance is more complex and that it should be interpreted with caution. ii) While sediment in the subglacial drainage network is presumably transported into the terminal overdeepening relatively quickly, clasts that fall onto or are entrained into the glacier may be deposited only after a significant delay. Different debris pathways between erosion and deposition will have to be characterised and discussed (Boulton, 1978; Kirkbride, 2002). iii) The previously proposed connection of sandstones with the Molasse Basin as sediment source is an oversimplification, as several Alpine sandstones (*e.g.* derived from Flysch or the Helvetic Garschella Fm.; Meyer, 2013) are also classified into this group. A refinement of the lithology groups with a stronger emphasis on the clast stratigraphy would help to better resolve source signals.
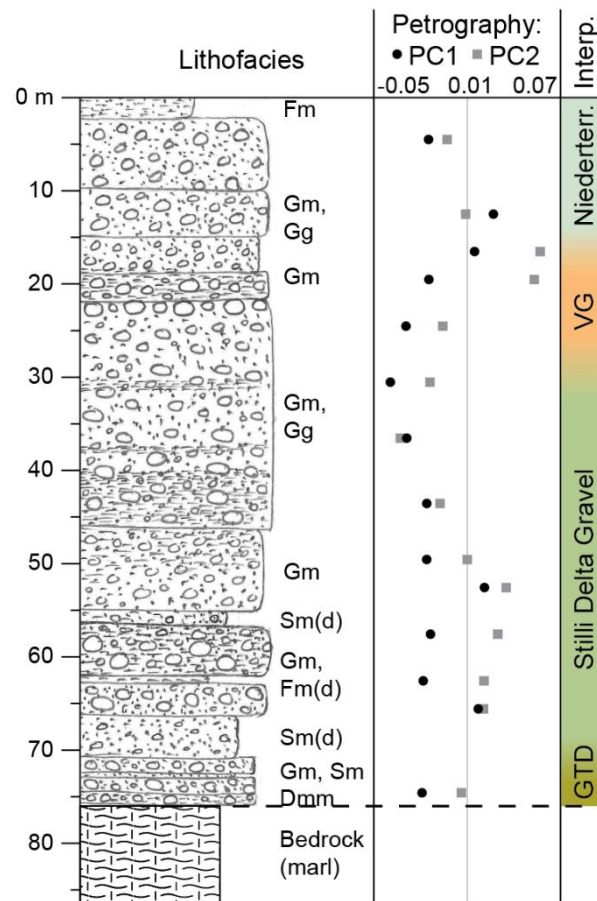
Fig. A-4: Principal components of petrography samples from QUST, with interpretation based on chapter IV (VG: Vogelsang Gravel, GTD: Gebenstorf Trough Diamict). Lithofacies codes refer to Eyles *et al.* (1983).

4. The Rinikerfeld Paleolake: detailed insights

4.1. Elementary analysis

X-ray fluorescence (XRF) scanning provides high-resolution insights into the elementary composition of fine-grained sediments that can be diagnostic for a variety of sedimentary and climatic processes (*e.g.* Croudace *et al.*, 2019, and references therein). XRF scans of the Rinikerfeld Paleolake (see chapter IV) deposits were acquired and tentatively interpreted under guidance from Hendrik Vogel (University of Bern).

The interval between 28.6 and 23.1 m depth brackets the gradual sedimentary change from LFA 4b to 4c (26.1-23.4 m depth; see chapter IV) and was considered of special interest. The respective core sections were analysed with a Cox Ltd. Itrax x-ray fluorescence (XRF) core scanner (Cr tube, 30 kV, 50 mA, 20 s integration time) at the Institute of Geological Sciences, University of Bern. Relative element abundances were determined in a resolution of 2500 μm, and 500 μm in selected intervals.

No systematic variations are evident within the rhythmically banded fine-grained deposits of LFA 4b below 26.1 m depth: The presumed summer and winter layers are not distinguishable by XRF data. Only occasional sandy interbeds are relatively enriched in Si and Zr/Rb, and depleted in K, Ti, and Fe. The rhythmic occurrence of orange-brown laminated packages (LFA 4c) starting at 26.1 m depth is interpreted as indicative for repeated episodes of bottom water oxygenation that became continuous at 23.4 m below ground (see chapter IV). This is supported by a slight decrease in Fe/Mn (Fig. A-5; Naeher *et al.*, 2013; Żarczyński *et al.*, 2019) and S (Holmer and Storkholm, 2001). Over the LFA 4b-4c transition, the deposits become progressively richer in Ca and accordingly, $CaCO_3$ content inreases from ~45% to ~55% as inferred from combustion gas analysis. A concurring decrease in Zr/Rb indicates that the clay mineral content decreased (Dypvik and Harris, 2001), as can also be inferred from the gamma log. This supports the interpretation of a significant change in sediment input into the lake that may reflect the transition from a glacier-fed towards a locally dominated lake, fed by runoff from the Jura Mountains (see chapter IV).
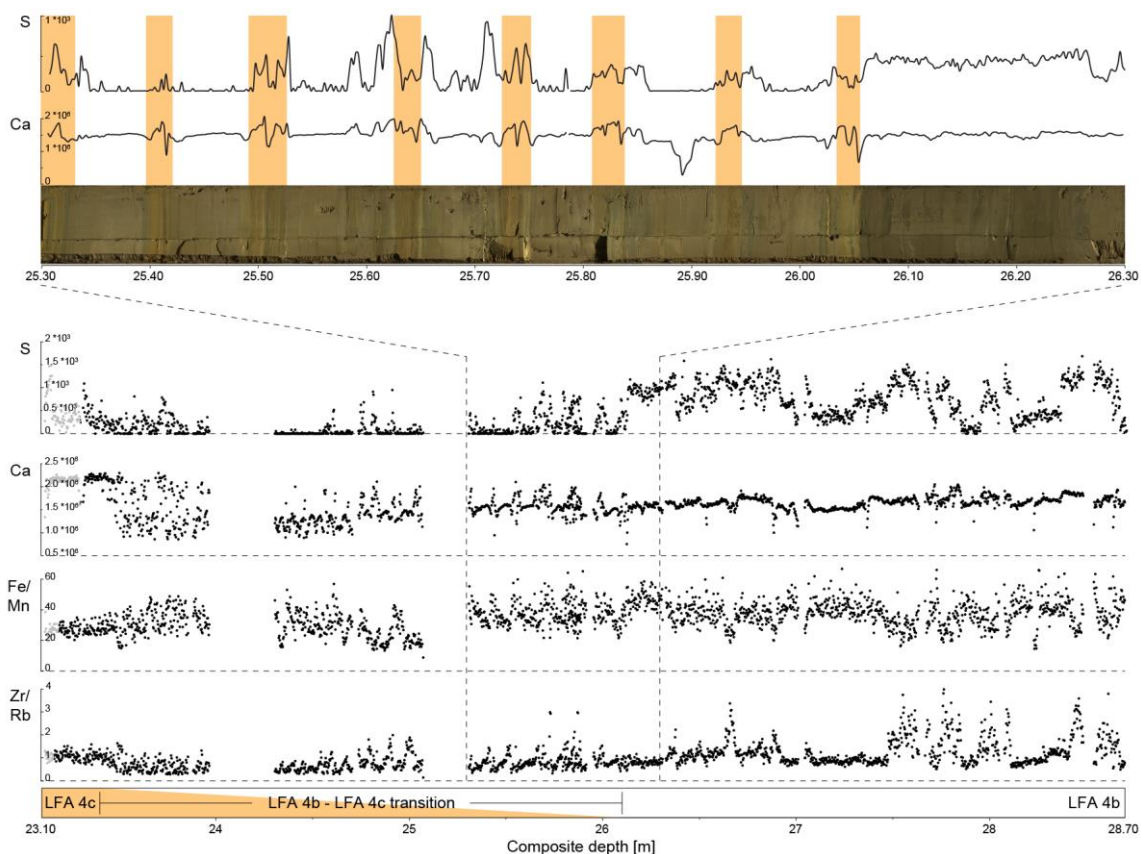
Fig. A-5: XRF data of the upper LFA 4b and transition to LFA 4c (shaded orange), illustrating changes in sediment input and redox conditions. Top: Zoom-in on drill core QRIN1, 25.3-26.3 m (photograph).

4.2. Palynology

The pollen content of the Rinikerfeld Paleolake was identified and interpreted by Maria Knipping (University of Hohenheim), who provided a detailed report on her findings to Nagra. I contributed to this study by selecting the samples to be analysed, and in the following provide a brief summary of the findings. They offer valuable information about the environmental conditions and floral evolution during the lifetime of the paleolake.

Material from 8 bulk sediment samples of QRIN was processed and analysed at the palynology laboratory at the Institute of Botany, University of Hohenheim (Germany). Palynomorphs were extracted from the sediment by subsequent leaching with HCl, NaOH/KOH, and HF, followed by chemical drying with acetic acid and acetolysis with acetic anhydride and H_2SO_4 (Eisele *et al.*, 1994; Knipping *et al.*, 2008). The separated palynomorphs were spiked with non-endemic *Lycopodium* spores and sieved to ≤7 μm. In aliquots of the so-treated samples, pollen grains were identified under a binocular with 500x and 1250x magnification (Beug, 2004; Moore *et al.*, 1991), and the respective state of pollen preservation was noted.

Sedimentary facies and TOC contents in the Rinikerfeld Paleolake indicate sediment deposition in a cold – glacial or stadial – lake under gradually ameliorating climate (see chapter IV). This trend towards more temperate conditions is also evident by the pollen content of the lake deposits that strongly increase upwards (Table A-1, Fig. A-6). LFA 4a and 4b (33.5-23.4 m depth) contain only few, mostly arboreal pollen, *e.g. Pinus, Picea, Abies*, that are likely allochthonous or contaminated (<10 grains per aliquot, projected to approx. 15, 70 and 140 grains per cm^3, respectively). However, the low pollen concentrations of LFA 4a and 4b are also a consequence of the presumed high sedimentation rates of few cm/yr. In the basal LFA 4c, starting at 21.39 m, concentrations of Pleistocene pollen (~400 grains per cm^3) increase considerably (Table A-1). Poaceae and Cyperaceae indicate an open steppe-tundra (Starnberger *et al.*, 2013) that becomes progressively more diverse. However, throughout LFA 4c, no more than ~25% arboreal pollen are encountered, and light-demanding taxa such as *Artemisia, Botrychium, Hippophae, Selaginella selaginoides* and Plumbaginaceae further support a continuously open vegetation with small shrubs (*e.g. Salix, Juniperus*; Lang, 1994; Sebald *et al.*, 1990). The presence of Hippophae suggests summer temperatures as high as 11.5 °C (Kolstrup, 1980), and individual findings of *Batrachium* and *Sparganium* as well as *Botryococcus* and *Pediastrum* indicate the presence of a sparse aquatic flora.

Table A-1: Pollen contents of samples from borehole QRIN. Data provided by Maria Knipping.

Sample depth [m]	6.90	10.80	14.49	16.58	21.39	25.90	30.58	34.75
Counted grains in aliquot	466	485.5	392.5	335.5	97	8.5	6	2
Pinus (arboreal taxa, a. t.)	56	51	64	69	18	1.5	0.5	0
Pinus cembra type	0	2	8	1	2	0	0	0
Betula	13	18	2	3	2	1	0	1
Betula cf. nana type	9	43	2	2	0	0	0	0
Salix	1	4	2	1	1	0	0	0
Alnus viridis type	0	1	0	0	0	0	0	0
Juniperus	1	0	3	1	1	0	0	0
Hippophae	1	4	0	1	1	0	0	0
Ephedra distachya	2	1	1	3	0	0	0	0
Ephedra fragilis type	0	0	0	2	0	0	0	0
Corylus (a. t., likely reworked)	0	0	0	0	0	0	1	0
Quercus	1	0	cf	0	0	0	0	0
Alnus glutinosa type	4	0	0	2	0	0	1	0
Picea	0	?	5	4.5	2.5	3.5	1.5	0
Abies	0	0	1	1	0	1.5	1	0
Poaceae	53	160	54	59	17	1	1	1
Cyperaceae	138	122	189	151	37	0	0	0
Artemisia	53	8	15	7	4	0	0	0
Chenopodiaceae	15	2	7	8	2	0	0	0
Helianthemum	16	20	3	2	0	0	0	0
Saxifraga aizoides group	4	6	4	2	0	0	0	0
Thalictrum	23	6	6	8	3	0	0	0
Caryophyllaceae	8	2	2	1	2	0	0	0
Cerastium type	1	0	0	0	0	0	0	0
Gipsophila	2	3	0	0	0	0	0	0
Silene type	1	0	0	1	0	0	0	0
Plumbaginaceae	0	1	0	0	0	0	0	0
Rubiaceae	4	3	0	0	0	0	0	0
Plantago tenuiflora type	0	1	0	0	0	0	0	0
Plantago sp.	0	2	1	0	1	0	0	0
Achillea type	3	1	3	1	0	0	0	0
Solidago type	2	1	0	0	0	0	0	0
Cichoriaceae	5	3	5	4	2	0	0	0
Brassicaceae	7	4	4	1	0	0	0	0
Apiaceae	0	1	0	0	0	0	0	0
Rosaceae	0	1	0	0	0	0	0	0
Ranunculaceae	1	0	0	0	0	0	0	0
Ranunculus type	1	0	0	0	0	0	0	0
Valeriana	0	1	0	0	0	0	0	0
Botrychium	2	2	0	0	1	0	0	0
Selaginella selaginoides	28	11	9	1	0	0	0	0
Varia	11	1	3	0	1	0	0	0
Indeterminata	++	+	+	+	+++	+	+	(+)
Sparganium type (aquatic taxa)	1	0	0	0	0	0	0	0
cf. Batrachium type	0	0	0	1	0	0	0	0
cf. Triglochin	0	4	0	0	0	0	0	0
Pediastrum	0	0	0	0	1	0	0	0
Botryococcus	2	1	2	7	1	0	0	0
monolete spores	0	0	1	0	0	0	0	0
Sphagnum	1	0	0	1	0	0	0	0
pre-Quaternary taxa	++	+	+	++	+++	+	(+)	(+)
marine taxa	++	++	+	+	0	+	0	(+)
Terrestrial pollen per cm³	2583	7223	1768	1286	414	142	68	16
Arboreal taxa [%]	18.9	25.4	22.3	26.7	27.8	88.2	83.3	50.0
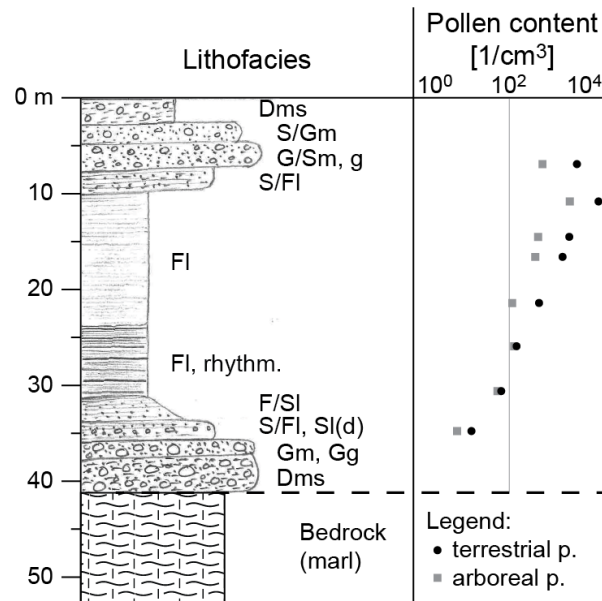
Fig. A-6: Total pollen contents in the Rinikerfeld Paleolake of QRIN. For details, please refer to Table A-1. Lithofacies codes refer to Eyles *et al.* (1983).

The observed pollen assemblage is similar to other Pleistocene records of the northern Alpine foreland (Knipping, 1990; Lang, 1985; Müller, 2001) but not diagnostic for a certain glaciation. Abundant reworked palynomorphs, including marine taxa (Table A-1), indicate intensive erosion in the catchment, whereas individual thermophile pollen (*e.g. Abies, Corylus, Quercus*) are likely the result of contamination during drilling and/or core handling.

5. Pleistocene deposits as archives of neotectonism – the Ruckfeld case

5.1. Project and motivation

Neotectonic activity in the northern Alpine foreland is generally associated with low deformation rates and therefore moderate seismicity (Isler, 1985). While the present-day stress field and mild earthquakes can be registered with precision instruments (Wiget *et al.*, 2007), the field study of pre-historic neotectonic events is challenging. Natural as well as anthropogenic processes effectively obliterate the surface expression of mild movements, and thick and extensive unconsolidated deposits, for example glaciofluvial gravels, cover large areas of the northern Alpine foreland, blanketing and compensating underlying deformations (Isler, 1985). However, these gravels are also a valuable potential archive of neotectonic deformations. As a prominent example, the Deckenschotter west of the Aare record the cut-off of a major glaciofluvial channel that is likely due to a re-activation of the Mandach Thrust at ~1 Ma (Bitterli *et al.*, 2000; Graf, 1993; Knudsen *et al.*, 2020).

Based on high-resolution reflection seismic data, the Mid-Pleistocene Ruckfeld gravel plain in Northern Switzerland was investigated in close cooperation with Herfried Madritsch (Swiss National Cooperative for the Disposal of Radioactive Waste Nagra) and considering previous interpretations by Bernd Fiebig, Louis Hauvette, and Rodolpho Lathion (University of Geneva). Special focus lay on displacements of the Pleistocene sediments that could hint at neotectonic deformation since roughly 0.5 Ma (Graf, 2009). Elevated ~100 m above today's Aare river level, the Ruckfeld plain lies at the eastern termination of the Mandach Thrust, a major thin-skinned overthrust and the northernmost extension of the Jura fold-and-thrust belt (Fig. A-7; Bitterli-Brunner, 1987; Bitterli *et al.*, 2000).

The Mandach Thrust is only the youngest component of a threefold superimposed tectonic structure: It is situated above a major transverse fault zone in the crystalline basement that forms the northern margin of a several kilometre-deep variscan sedimentary basin (Permo-Carboniferous Trough; Bitterli-Brunner, 1987; Laubscher, 1986). It was buried by several hundred meters of sediments deposited on an epicontinental platform, today referred to as Tabular Jura, during early Triassic through late Jurassic (Bitterli *et al.*, 2000; Jordan and Deplazes, 2019).

The fault zone was later reactivated first in an extensional regime during the early Cenozoic, and a second time during the Miocene in a now compressional stress field, resulting in the Mandach Flexure and the superimposed Mandach Thrust, respectively (Laubscher, 1986).

During the Pleistocene, the northern Alpine foreland was intensively dissected by glaciofluvial activity, and the valleys infilled with meltwater gravels. The Ruckfeld plain lies in elongation of the Habsburg-Rinikerfeld paleochannel, presumably the oldest mid-Pleistocene draw in the lower Aare valley area (Bitterli-Dreher *et al.*, 2007; Graf, 2009), and its stratigraphy consists of basal diamicts overlain by several decametres of Hochterrasse gravel (Middle Pleistocene glaciofluvial deposits) that are in turn covered by colluvium and last-glacial loess (Graf, 2009; Preusser and Graf, 2002). It is a promising location to study potential neotectonic dislocations near the transition between the Tabular Jura and the Jura fold-and-thrust belt (Fig. A-7).
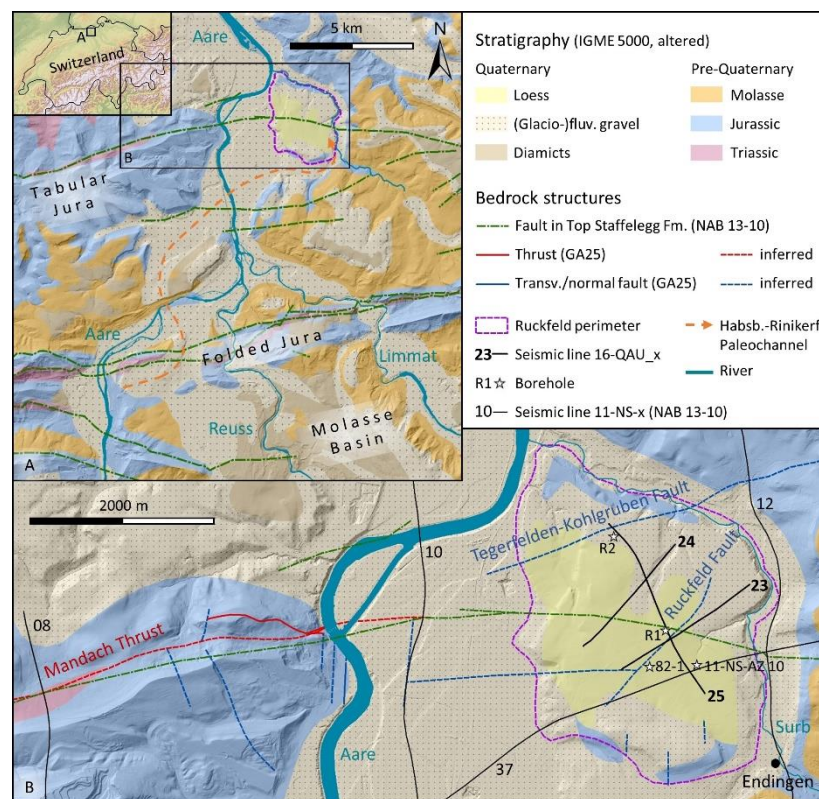
Fig. A-7: Map of the study area in the regional (A) and local (B) tectonic context, including boreholes and seismic acquisition lines. IGME 2005: Commission for the Geological Map of the World *et al.* (2005); NAB 13-10: Madritsch *et al.* (2013); GA25: Matousek *et al.* (2000), Graf *et al.* (2006). Background: Swisstopo (2013).

5.2. Seismic data and interpretation

Three high-resolution 2D seismic lines of the Ruckfeld were acquired by Nagra in 2016: 16-QAU_23 ('line 23'), 16-QAU_24 ('line 24', both oriented SW-NE), and 16-QAU_25 ('line 25' oriented SE-NW; Fig. A-7). These are 1.5-2.2 km long and image the Mesozoic and Cenozoic strata up to ca. 0.9 s two-way travel time (TWT) in depth. The data were analysed in IHS KingdomSuite and DMNG SeiSee in stacked form, with focus on sedimentary architecture as well as potential tectonic displacements.

Line 25 passes through the site of Ruckfeld R1 (latitude 47°32'58" N, longitude 8°16'30" E), an >700 m deep well. The depths of major geological boundaries from R1 (Bitterli *et al.*, 2000) were converted into TWT with help of literature values for the respective seismic velocities (Table A-2). The resulting values were plotted into seismic line 25 at the site of R1 (at ~800 m) and, with exception of the Middle Jurassic Passwang Fm., all contacts coincided with more or less distinct reflectors that could be confidently followed through the seismic line. The results agree with the stratigraphy recorded in well Ruckfeld R2 (47°33'31" N, 8°16'3" E) located further northwest (at ~2000 m), and were transferred to lines 23 and 24. Stratigraphy, discontinuities and dislocations were then mapped in consideration of further boreholes (R2, 82-1, 11-NS-AZ 10; Fig. A-7; Nagra borehole database) as well as known and inferred fault locations (Madritsch *et al.*, 2013; Matousek *et al.*, 2000; Sprecher and Müller, 1986).

5.3. Preliminary results

5.3.1. Seismic stratigraphy

The reflection seismic data image the sedimentary architecture of the Ruckfeld to a depth of ~0.9 s TWT (Fig. A-8). From top to bottom, three major seismic facies (SF) are distinguished (Fig. A-9): SF A (above ~0.2 s TWT) is characterised by overall low amplitudes and continuous as well as discontinuous reflections. In the lower part of SF A (~0.1-0.2 s TWT) our data image distinct, 100-500 m wide packages of moderate amplitude, discontinuous internal reflections. The base of SF A is formed by a prominent horizontal reflection that coincides with an angular unconformity.

SF B (~0.2-0.6 s TWT) consists of horizontal to slightly southward-dipping continuous reflections. Amplitudes within SF B are moderate to high, with prominent reflections at ~0.3 and ~0.4 s TWT, and a thick package of well-imaged, high-amplitude reflections between ~0.4 and ~0.5 s TWT. In SF C, reflections are again significantly lower in amplitude and mainly discontinuous to chaotic.

<u>Pre-Quaternary</u> – The prominent reflector at ~0.2 s TWT marks the base of the Quaternary strata that unconformably overlie the Mesozoic deposits of the Tabular Jura. Major internal reflectors of the Mesozoic likely represent the base of the Middle Jurassic Klingnau Fm. (~0.3 s TWT) and the base of the Lower Jurassic Staffelegg Fm. (~0.4 s TWT), the latter being underlain by well-developed high-amplitude reflectors of the Upper Triassic Bänkerjoch Fm. This is in qualitative agreement with regional seismic interpretation by Madritsch *et al.* (2013), whereas Malz *et al.* (2020) chose a slightly different interpretation attributing the package of high-amplitude reflectors partly to the underlying Middle Triassic.

Table A-2: Stratigraphy in well Ruckfeld R1 and expected TWT of lithological contacts.
[1] Dr. H. Jäckli AG and DMT GmbH & Co. KG (2012), well 11-NS-AZ 10; [2] Sprecher and Müller (1986), well Weiach, Fig. 23; [3] Bitterli *et al.* (2000), Fig. 11.

Sedimentary unit		Seismic velocity [m/s]	Base in R1 [m depth][3]	Base in R1 [s TWT]	Base below datum [s TWT]
Pleistocene		1320[1]	85	0.129	0.206
Upper Jur., Wildegg Fm.		3050[2]	159	0.177	0.254
Middle Jurassic	Klingnau Fm.	3050[2]	233	0.226	0.303
	Passwang Fm.	3050[2]	280	0.257	0.334
	Opalinus Clay	3150[2]	417	0.344	0.421
Lower Jur., Staffelegg Fm.		3150[2]	459	0.370	0.447
Upper Triassic, Bänkerjoch Fm.		3150[2]	608	0.465	0.542
Middle Triassic, Schinznach Fm.		3150[2]	682	0.512	0.589
Lower Triassic, Dinkelberg Fm.		3150[2]	748	0.554	0.631
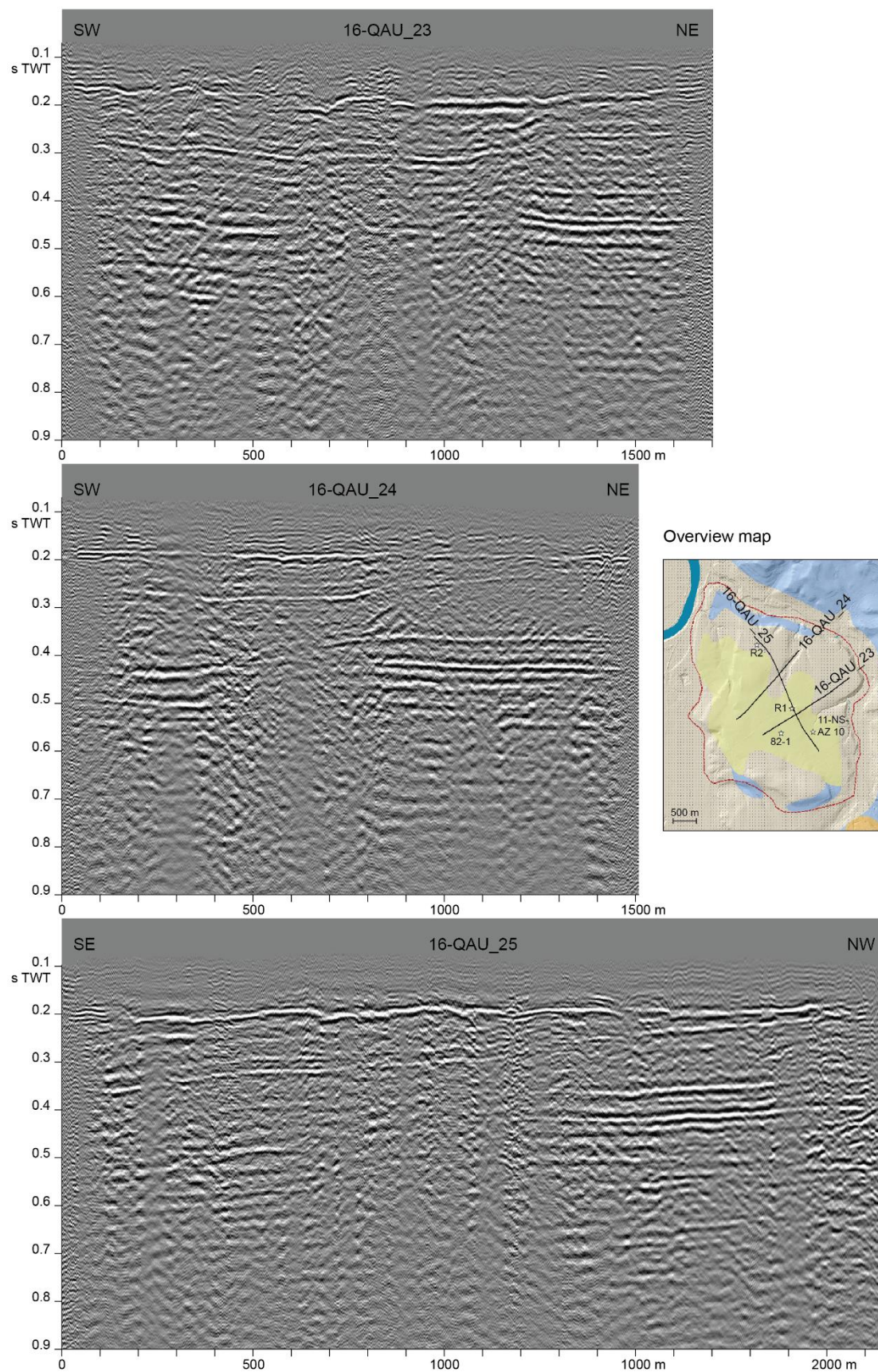
Fig. A-8: Seismic lines 23, 24, and 25 imaging the sedimentary architecture of the Ruckfeld.

Appendix A
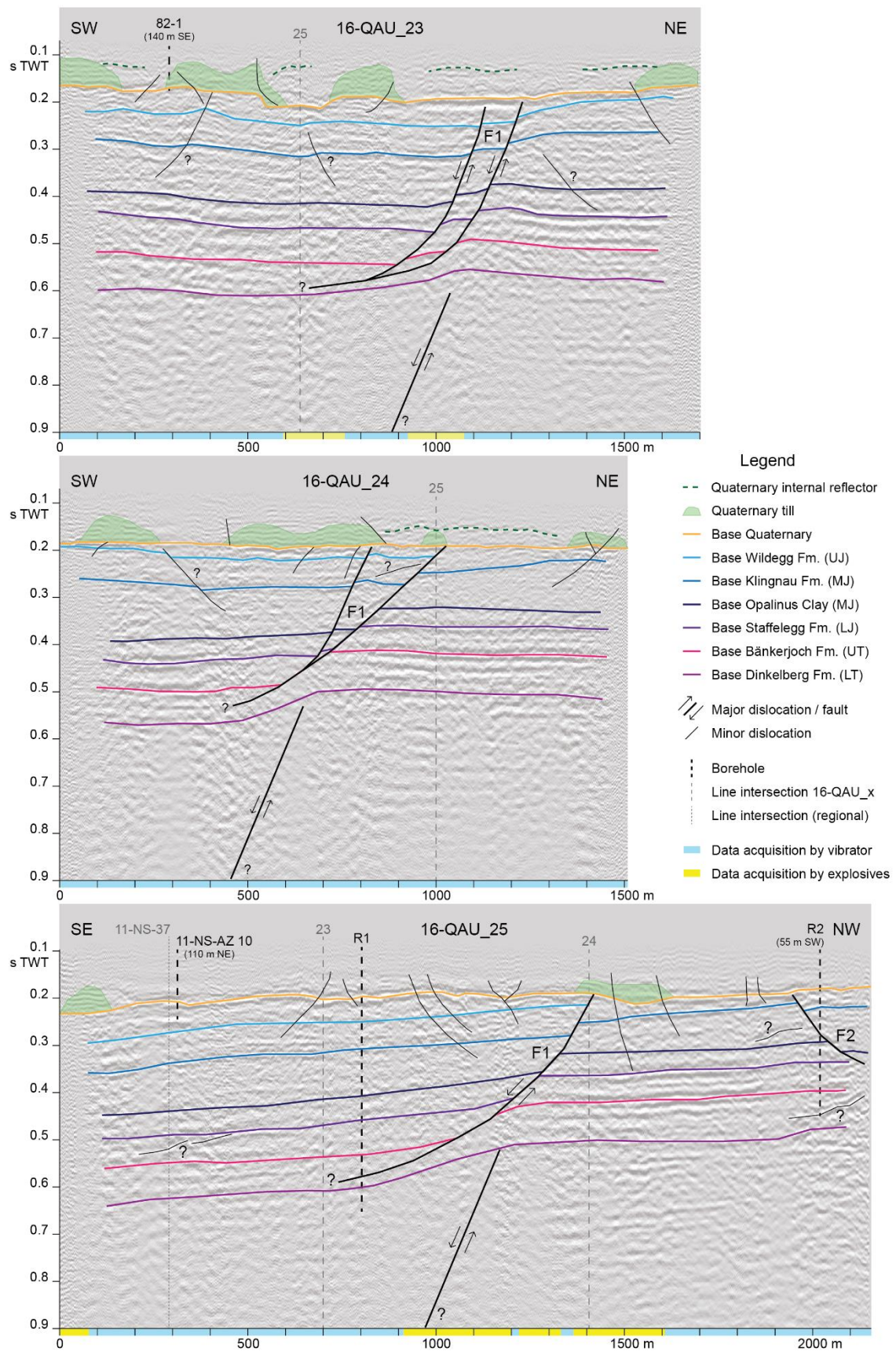
Fig. A-9: Interpretation of seismic lines 23, 24, and 25.

Appendix A

<u>Quaternary</u> – The base of the Quaternary below the Ruckfeld appears to be mostly flat and smooth on the SW-NE lines, with the exception of a distinct U-shaped depression on line 23 (at 500-800 m), while it has slightly more relief on the SE-NW line 25 (Fig. A-9). The angular unconformity towards the underlying bedrock identifies it as an erosional boundary. With a bedrock elevation of <330 m a.s.l., the Ruckfeld is interpreted as the northward continuation of the early Mid-Pleistocene Habsburg-Rinikerfeld channel (Graf, 2009; Pietsch and Jordan, 2014). Due to its gentle downstream gradient it is presumed to be a (glacio-)fluvially eroded valley (Bitterli-Dreher *et al.*, 2007), and the depression on line 23 could thus be the cross-section of an individual fluvial channel, possibly eroded along a zone of weakness within the underlying Mesozoic (see following section).

Internally, the Pleistocene is largely seismically transparent on the seismic data with few discontinuous packages of high-amplitude reflectors in the lower part. All available boreholes are located within the transparent seismic facies or at its margin. Borehole 82-1 records >50 m of Hochterrasse gravel overlying 1.5 m of glacial till and overlain by ~10 m of loess, while 11-NS-AZ 10 (Dr. H. Jäckli AG and DMT GmbH & Co. KG, 2012) records 70 m of Hochterrasse gravel. In R1 and R2 the Pleistocene was not described. The transparent portions of the Quaternary are thus interpreted as glaciofluvial gravel, while the high-amplitude packages could represent glacigenic diamicts (till; Fig. A-9; *cf.* Graf, 2009). Comparable seismic facies are connected to similar lithologies for example in the Tannwald Basin in Southern Germany (~100 km ENE; Burschil *et al.*, 2018). The presumed till bodies could be part of distinct moraine ridges or of a glaciofluvially dissected ice decay landscape. On seismic line 23 and the northeastern half of line 24 one relatively prominent and continuous internal reflector within the Pleistocene is imaged, which lies approximately at the top of the presumed till packages at ~0.1 s TWT. It could be the expression of an erosional boundary and thus indication for a two-phase origin of the Ruckfeld gravel plain, as hypothesized by Bitterli *et al.* (2000).

5.3.2. Structures

<u>Large-scale structures</u> – The seismic data image several distinct extensional flexures within the Mesozoic deposits that indicate underlying normal faults (Fig. A-9). Above these flexures, larger-scale dislocations of the Mesozoic strata below the Ruckfeld could be identified on all seismic lines (line 23 at 900-1400 m, line 24 at 500-1000 m, line 25 at 800-1400 m; Fig. A-9). These dislocations originate in a depth of ~0.6 s TWT, are inclined towards north, and can be traced up to the base of Quaternary at ~0.2 s TWT. A further dislocation at the northwestern end of line 25 is only partly imaged and appears to dip towards north, which is however not entirely clear (Fig. A-9).

The flexures on lines 23, 24, and 25 can be connected to one continuous W-E striking structure (Mandach Flexure). Analogously, the southward-dipping dislocations represent one W-E striking fault F1 (Fig. A-9) that lies approximately in elongation of the Mandach Thrust as shown on Fig. A-7. Near the Aare, the Mandach Thrust dips towards south with an angle of ~30°, and accounts for a shortening of ~150 m (Madritsch *et al.*, 2013, line 11-NS-10). In contrast, tracing the bedrock contacts on lines 23-25 indicates that F1 is a pure normal fault, which is supported by the findings of well R1 (Bitterli *et al.*, 2000). Extension along F1 is on the order of ~50 m, and its dip angle of ~55° in the western Ruckfeld (lines 24, 25) appears to increase towards east to ~65° (line 23). F1 corresponds thus likely to the Unterendingen Fault identified east of the Ruckfeld by Madritsch *et al.* (2013, line 10-NS-12). The dislocation at the northwestern end of line 25 (F2; Fig. A-9) could correspond to the Tegerfelden-Kohlgruben (normal) Fault (Fig. A-7; Bitterli *et al.*, 2000) that is however not expressed in the data of Madritsch *et al.* (2013).

Evidence for a reverse reactivation of F1, or another major overthrust, as it has been imaged near the Aare (Mandach Thrust) is therefore neither identified below the Ruckfeld, nor further east (see Bitterli *et al.*, 2000; Madritsch *et al.*, 2013, line 10-NS-12). Only ~3 km to the south, near Endingen (Fig. A-7), a major thrust wedge is located on the eastern side of the Aare (Madritsch *et al.*, 2013, line 10-NS-12). This situation has previously been tentatively explained by the existence of a larger transverse Ruckfeld Fault that dislocates both the Mandach Flexure and Thrust to the south (Amsler, 1915; Bitterli *et al.*, 2000).

The SW-NE trend of the Ruckfeld Fault as inferred by Matousek *et al.* (2000; Fig. A-7) coincides with a prominent U-shaped depression in the base of the Quaternary on line 23 (at 500-800 m; and with a slight dislocation on line 25 at ~700 m). This depression could be due to (*e.g.* glaciofluvial) incision into the underlying Mesozoic along a weak zone, and it is therefore plausible that a fault exists at this location. However, the seismic data indicate that this fault is not of regional-tectonic significance. The Mandach Flexure crosses below the Ruckfeld seemingly undisturbed (*cf.* Madritsch *et al.*, 2013, lines 11-NS-10/-12), while the Mandach Thrust appears to terminate abruptly between the Aare and the Ruckfeld. If the thrust wedge at Endingen is in fact to be regarded as the Mandach Thrust's eastward continuation, the dislocation between these two thrust segments must lie in a narrow corridor close to the present-day Aare river (*cf.* chapter II, section 6.1.2; faults mapped by Matousek *et al.*, 2000).

Neotectonism – The Pleistocene strata, and seemingly also the base of the Quaternary as well as the underlying Mesozoic, display a series of smaller-scale discontinuities (down to depths of ~0,4 s TWT; Fig. A-9). It is striking that many of these structures are associated with the high-amplitude reflector packages tentatively identified as till bodies. These discontinuities could be artefacts related to the contrast in seismic properties between till and adjacent gravel, or the result of heterogeneities within the till. Both can however not account for deformations offside the till packages, *e.g.* on line 25 at 600-1200 m.

Some dislocations could be explained by sagging of loose sediment due to differences in compaction between gravel and till, especially in the case of overconsolidated subglacial till (Bitterli *et al.*, 2000), *e.g.* on line 23 at 500 m. However, intra-Quaternary sagging cannot explain dislocations that can well be traced into the Mesozoic. The same applies to periglacial surface processes such as solifluction, which has been previously observed on the Ruckfeld plain (Graf, 2009). In addition, the majority of the dislocations appear to be the result of compressive deformation. Considering indication for a multiphase origin of the Ruckfeld gravel plain, glaciotectonism below an overriding glacier could explain deformation and thrusting, but likely not in bedrock below decametres of soft sediment.

It appears possible that small-scale dislocations of the Pleistocene deposits and of the base of the Quaternary could in fact be the result of minor neotectonic activity. The steepness of some dislocations (*e.g.* at 1400-1700 m on line 25) would fit an oblique-slip motion with considerable transverse component that is consistent with the present day stress field (Deichmann *et al.*, 2000; Heidbach and Reinecker, 2013). It is noteworthy though that no evidence for deformation of the Pleistocene strata is observed above the subcrop of fault F1. Thus, it appears that minor neotectonic activity may have occurred, but that the major tectonic structure below the Ruckfeld was quiescent over the last ~0.5 Myr.

Appendix A

6. References

Amsler, A., 1915, Tektonik des Staffelegg-Gebietes und Betrachtungen über Bau und Entstehung des Jura-Ostendes: Eclogae Geologicae Helvetiae, v. 13, no. 4, p. 377-484.

Augustinus, P. C., 1992, The influence of rock mass strength on glacial valley cross-profile morphometry: A case study from the Southern Alps, New Zealand: Earth Surface Processes and Landforms, v. 17, no. 1, p. 39-51.

Beug, H., 2004, Leitfaden der Pollenbestimmung für Mitteleuropa und angrenzende Gebiete, Munich, Verlag Dr. Friedrich Pfeil, 542 p.

Bieniawski, Z. T., 1973, Engineering classification of jointed rock masses: Transactions of the South African Institution of Civil Engineers, no. 15, p. 335-344.

Bitterli-Brunner, P., 1987, Die Mandacher und Mettauer Aufschiebungen (Aargauer Tafeljura) aufgrund neuer Untersuchungen: Bulletin der Vereinigung Schweizerischen Petroleum-Geologen und -Ingenieure, v. 53, no. 124, p. 23-26.

Bitterli-Dreher, P., Graf, H. R., Naef, H., Diebold, P., Matousek, F., Burger, H., and Pauli-Gabi, T., 2007, Geologischer Atlas der Schweiz 1:25'000. Blatt 1070 Baden. Erläuterungen, Wabern, Bundesamt für Landestopogaphie swisstopo, 152 p.

Bitterli, T., Graf, H. R., Matousek, F., and Wanner, M., 2000, Geologischer Atlas der Schweiz 1:25'000. Blatt 1050 Zurzach. Erläuterungen, Geologischer Atlas der Schweiz 1:25'000, 89 p.

Bini, A., Buoncristiani, J. F., Couterrand, S., Ellwanger, D., Felber, M., Florineth, D., Graf, H. R., Keller, O., Kelly, M., and Schlüchter, C., 2009, Die Schweiz während des letzteiszeitlichen Maximums (LGM) 1:500'000: Bundesamt für Landestopographie swisstopo.

Boulton, G., 1978, Boulder shapes and grain-size distributions of debris as indicators of transport paths through a glacier and till genesis: Sedimentology, v. 25, no. 6, p. 773-799.

Brook, M., and Tippett, J., 2002, The influence of rock mass strength on the form and evolution of deglaciated valley slopes in the English Lake District: Scottish Journal of Geology, v. 38, no. 1, p. 15-20.

Burschil, T., Buness, H., Tanner, D. C., Wielandt-Schuster, U., Ellwanger, D., and Gabriel, G., 2018, High-resolution reflection seismics reveal the structure and the evolution of the Quaternary glacial Tannwald Basin: Near Surface Geophysics, v. 16, no. 6, p. 593-610.

Commission for the Geological Map of the World, Asch, K., and Bellenberg, S., 2005, The 1:5 million international geological map of Europe and adjacent areas (IGME 5000), Hannover, Bundesanstalt für Geowissenschaften und Rohstoffe.

Croudace, I. W., Löwemark, L., Tjallingii, R., and Zolitschka, B., 2019, Current perspectives on the capabilities of high resolution XRF core scanners: Quaternary international, v. 514, p. 5-15.

Deere, D. U., 1963, Technical description of rock cores for engineering purpose: Rock Mechanics and Engineering Geology, v. 1, no. 1, p. 16-22.

Deichmann, N., Ballarin Dolfin, D., and Kastrup, U., 2000, Seismizität der Nord- und Zentralschweiz: Nagra Technischer Bericht NTB 00-05, 113 p.

DiBiase, R. A., Lamb, M. P., Ganti, V., and Booth, A. M., 2017, Slope, grain size, and roughness controls on dry sediment transport and storage on steep hillslopes: Journal of Geophysical Research: Earth Surface, v. 122, no. 4, p. 941-960.

Dr. H. Jäckli AG, and DMT GmbH & Co. KG, 2012, 2D-Seismik Nordschweiz 2011/12: Geologische Aufnahme der Aufzeitbohrungen (Teil 1) und Aufzeitmessungen (Teil 2): Nagra Arbeitsbericht NAB 12-22, 31 p.

Appendix A

Dypvik, H., and Harris, N. B., 2001, Geochemical facies analysis of fine-grained siliciclastics using Th/U, Zr/Rb and (Zr+ Rb)/Sr ratios: Chemical geology, v. 181, no. 1-4, p. 131-146.

Edelbro, C., 2003, Rock Mass Strength - a Review: Lulea University Technical Report, 92 p.

Eisele, G., Haas, K., and Liner, S., 1994, Methode zur Aufbereitung fossilen Pollens aus minerogenen Sedimenten: Über Probleme der holozänen Vegetationsgeschichte Osttibets. Göttinger Geographische Abhandlungen, v. 95, p. 165-166.

Eyles, N., Eyles, C. H., and Miall, A. D., 1983, Lithofacies types and vertical profile models; an alternative approach to the description and environmental interpretation of glacial diamict and diamictite sequences: Sedimentology, v. 30, no. 3, p. 393-410.

Gasser, U., and Nabholz, W. K., 1969, Zur Sedimentologie der Sandfraktion im Pleistozän des schweizerischen Mittellandes: Eclogae Geologicae Helvetiae, v. 62, no. 2, p. 467-516.

Gerth, A., and Becker-Haumann, R., 2007, Sedimentuntersuchungen an unterpleistozänen Schmelzwasserablagerungen und Periglazialschottern im Riß-Iller-Gebiet, deutsches Alpenvorland: E&G Quaternary Science Journal, v. 56, no. 3, p. 186-211.

Graf, H. R., 1993, Die Deckenschotter der zentralen Nordschweiz: PhD thesis, ETH Zurich, 151 p.

Graf, H. R., 2009, Stratigraphie von Mittel-und Spätpleistozän in der Nordschweiz, Beiträge zur Geologischen Karte der Schweiz, 198 p.

Graf, H. R., Bitterli-Dreher, P., Burger, H., Bitterli, T., Diebold, P., and Naef, H., 2006, Geologischer Atlas der Schweiz 1:25'000, Blatt 1070 Baden: Bundesamt für Landestopografie swisstopo, Wabern, Switzerland.

Heidbach, O., and Reinecker, J., 2013, Analyse des rezenten Spannungsfeldes der Nordschweiz: Nagra Arbeitsbericht NAB 12-05, 123 p.

Holmer, M., and Storkholm, P., 2001, Sulphate reduction and sulphur cycling in lake sediments: a review: Freshwater Biology, v. 46, no. 4, p. 431-451.

Isler, A., 1985, Literaturzusammenstellung zur Neotektonik: Nagra Technischer Bericht NTB 84-29, 187 p.

Jordan, P., and Deplazes, G., 2019, Lithostratigraphy of Consolidated Rocks expected in the Jura Ost, Nördlich Lägern and Zürich Nordost Regions: Nagra Arbeitsbericht NAB 19-14, p. 176 p.

Kirkbride, M. P., 2002, Processes of glacial transportation: Modern and past glacial environments, p. 147-169.

Knipping, M., 1989, Zur spät-und postglazialen Vegetationsgeschichte des-Oberpfälzer Waldes: Dissertationes Botanicae, v. 140, 209 p.

Knipping, M., Müllenhoff, M., and Brückner, H., 2008, Human induced landscape changes around Bafa Gölü (western Turkey): Vegetation History and Archaeobotany, v. 17, no. 4, p. 365-380.

Knudsen, M. F., Nørgaard, J., Grischott, R., Kober, F., Egholm, D. L., Hansen, T. M., and Jansen, J. D., 2020, New cosmogenic nuclide burial-dating model indicates onset of major glaciations in the Alps during Middle Pleistocene Transition: Earth and Planetary Science Letters, v. 549, 116491.

Kolstrup, E., 1980, Climate and stratigraphy in northwestern Europe between 30,000 BP and 13,000 BP with special reference to the Netherlands: Mededelingen Rijks Geologische Dienst, v. 32, p. 181-253.

Lang, G., 1985, Swiss lake and mire environments during the last 15000 years: Dissertationes Botanicae, v. 87, 482 p.

-, 1994, Quartäre Vegetationsgeschichte Europas: Methoden und Ergebnisse, Jena/Stuttgart/New York, Gustav Fischer Verlag, 462 p.

Laubscher, H. P., 1986, The eastern Jura: relations between thin-skinned and basement tectonics, local and regional: Geologische Rundschau, v. 75, no. 3, p. 535-553.

Ludwig, A., 2018, Local topography and hillslope processes in the Jura Ost siting region (and surrounding areas): Nagra Arbeitsbericht NAB 17-42, 59 p.

Madritsch, H., Meier, B., Kuhn, P., Roth, P., Zingg, O., Heuberger, S., Naef, H., and Birkhäuser, P., 2013, Regionale strukturgeologische Zeitinterpretation der Nagra 2D-Seismik 2011/12: Nagra Arbeitsbericht NAB 13-10, 100 p.

Malz, A., Madritsch, H., Jordan, P., Meier, B., and Kley, J., 2020, Along-strike variations in thin-skinned thrusting style controlled by pre-existing basement structure in the easternmost Jura Mountains (Northern Switzerland): Geological Society, London, Special Publications, v. 490, no. 1, p. 199-220.

Marinos, P., and Hoek, E., 2000, GSI: a geologically friendly tool for rock mass strength estimation, in Proceedings ISRM International Symposium, International Society for Rock Mechanics and Rock Engineering.

Matousek, F., Wanner, M., Baumann, A., Graf, H., Nüesch, R., and Bitterli, T., 2000, Geologischer Atlas der Schweiz 1:25'000. Blatt 102 Zurzach Bundesamt für Landestopografie swisstopo, Wabern, Switzerland.

Meyer, J., 2013, Gesteine der Schweiz - Der Feldführer, Bern, Haupt Verlag, 448 p.

Moore, J. R., Sanders, J. W., Dietrich, W. E., and Glaser, S. D., 2009, Influence of rock mass strength on the erosion rate of alpine cliffs: Earth Surface Processes and Landforms, v. 34, no. 10, p. 1339-1352.

Moore, P. D., Webb, J. A., and Collison, M. E., 1991, Pollen analysis, Oxford, Blackwell scientific publications, 216 p.

Müller, U., 2001, Die Vegetations-und Klimaentwicklung im jüngeren Quartär anhand ausgewählter Profile aus dem südwestdeutschen Alpenvorland, Tübinger Geowissenschaftliche Arbeiten, 118 p.

Naeher, S., Gilli, A., North, R. P., Hamann, Y., and Schubert, C. J., 2013, Tracing bottom water oxygenation with sedimentary Mn/Fe ratios in Lake Zurich, Switzerland: Chemical Geology, v. 352, p. 125-133.

Pietsch, J., and Jordan, P., 2014, Digitales Höhenmodell Basis Quartär der Nordschweiz - Version 2014 und ausgewählte Auswertungen: Nagra Arbeitsbericht NAB 14-02, 69 p.

Preusser, F., and Graf, H., 2002, Erste Ergebnisse von Lumineszenzdatierungen eiszeitlicher Ablagerungen der Nordschweiz: Jahresberichte und Mitteilungen des Oberrheinischen Geologischen Vereins, p. 419-438.

Preusser, F., Graf, H. R., Keller, O., Krayss, E., and Schlüchter, C., 2011, Quaternary glaciation history of northern Switzerland: E&G Quaternary Science Journal, v. 60, p. 282-305.

Schlüchter, C., 1975, Schotterpetrologie und deren relativ-stratigraphische Anwendbarkeit im Aaretal südlich von Bern (Schweiz): Eiszeitalter und Gegenwart E&G/Quaternary science journal, v. 26, no. 1, p. 74-81.

Sebald, O., Seybold, S., and Philippi, G., 1990, Die Farn-und Blütenpflanzen Baden-Württembergs (8 volumes), Stuttgart, Ulmer Verlag.

Selby, M., 1982, Controls on the stability and inclinations of hillslopes formed on hard rock: Earth Surface Processes and Landforms, v. 7, no. 5, p. 449-467.

Sprecher, C., and Müller, W., 1986, Geophysikalisches Untersuchungsprogramm Nordschweiz: Reflexionsseismik 82: Nagra Technischer Bericht NTB 84-15, 168 p.

Appendix A

Starnberger, R., Drescher-Schneider, R., Reitner, J. M., Rodnight, H., Reimer, P. J., and Spötl, C., 2013, Late Pleistocene climate change and landscape dynamics in the Eastern Alps: the inner-alpine Unterangerberg record (Austria): Quaternary Science Reviews, v. 68, p. 17-42.

Swisstopo, 2013, swissALTI3D, Federal Office of Topography swisstopo Wabern, Switzerland.

Tian, P., Xu, X., Pan, C., Hsu, K., and Yang, T., 2017, Impacts of rainfall and inflow on rill formation and erosion processes on steep hillslopes: Journal of Hydrology, v. 548, p. 24-39.

Weltje, G. J., and von Eynatten, H., 2004, Quantitative provenance analysis of sediments: review and outlook: Sedimentary Geology, v. 171, no. 1-4, p. 1-11.

Wiget, A., Schlatter, A., Brockmann, E., Ineichen, D., Marti, U., and Egli, R., 2007, GPS-Netz NEOTEKTONIK Nordschweiz 2004: Messkampagne im Auftrag der Nagra und Deformationsanalyse 1988-1995-2004: Nagra Arbeitsbericht NAB 06-04, 76 p.

Żarczyński, M., Wacnik, A., and Tylmann, W., 2019, Tracing lake mixing and oxygenation regime using the Fe/Mn ratio in varved sediments: 2000 year-long record of human-induced changes from Lake Żabińskie (NE Poland): Science of the Total Environment, v. 657, p. 585-596.

Zhang, L., 2010, Estimating the strength of jointed rock masses: Rock mechanics and rock engineering, v. 43, no. 4, p. 391-402.

Appendix A

Appendix B: Large-scale sections

Longitudinal and cross sections are an important tool for the interpretation of landscapes with a complex geological architecture. In the Lower Aare Valley, three profile lines have been defined (B-2, B-3 (a and b), B-4 (with auxiliary line B-4*); Fig. B-1). Along these lines, sections have been constructed considering a variety of different input data (Table B-1). Excerpts of the respective sections are included in chapters II and IV, and the full sections are plotted on Fig. B-2 to B-4.
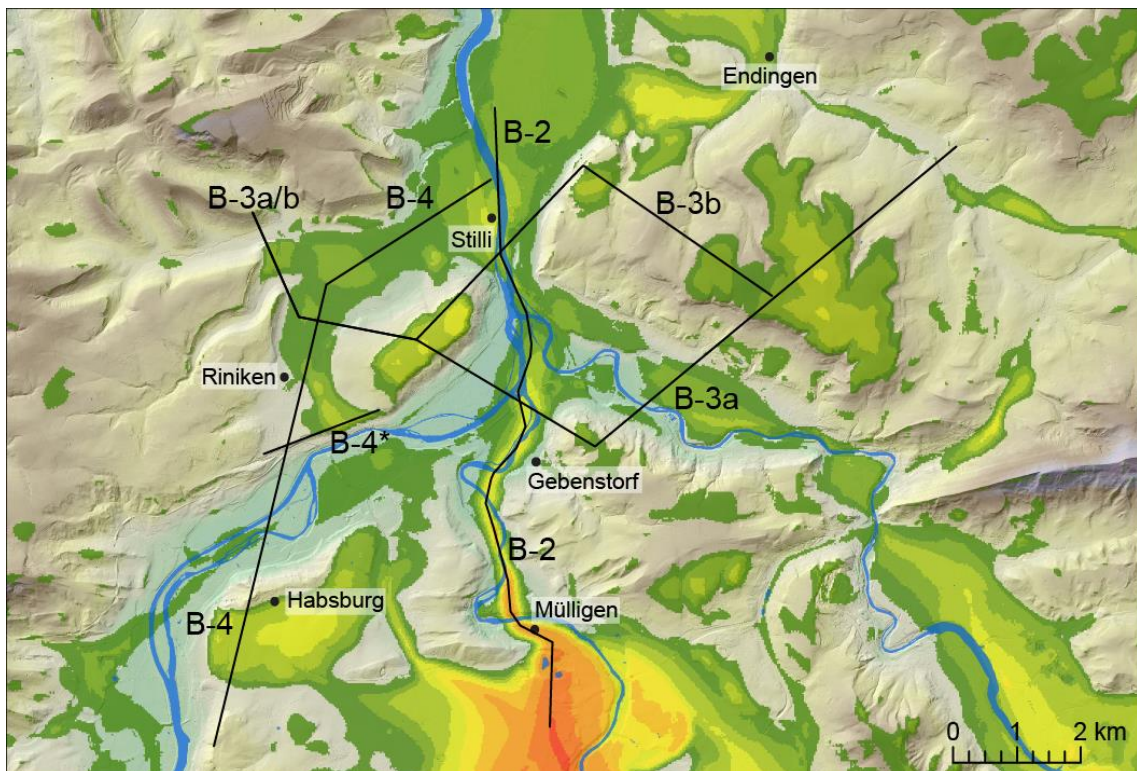
Fig. B-1: Layout of profile lines. For an explanation of the base map, please refer to Fig. I-7.

Table B-1: Input data for section construction. [1] Boreholes in the Gebenstorf-Stilli Trough and, generally, the Lower Aare Valley are projected onto the sections parallel to the isolines of the base of Quaternary-model by Pietsch and Jordan (2014).

Topography	Swisstopo (2013)
Quaternary and bedrock stratigraphy	Graf *et al.* (2006), Loepfe *et al.* (in prep.), Nitsche *et al.* (2001), Pietsch and Jordan (2014), Nagra borehole database (version 11/2018)[1]
Structural and morphological concept	Diebold *et al.* (1992), Heuberger (unpubl.), Madritsch *et al.* (2013), Malz *et al.* (2015), Sprecher and Müller (1986)
Design	Naef *et al.* (2019)

References

Diebold, P., Naef, H., and Ammann, M., 1992, Zur Tektonik der zentralen Nordschweiz: Interpretation aufgrund regionaler Seismik, Oberflächengeologie und Tiefbohrungen: Nagra Technischer Bericht NTB 90-04, 277 p.

Graf, H. R., Bitterli-Dreher, P., Burger, H., Bitterli, T., Diebold, P., and Naef, H., 2006, Geologischer Atlas der Schweiz 1:25'000, Blatt 1070 Baden: Bundesamt für Landestopografie swisstopo, Wabern, Switzerland.

Heuberger, S., unpubl., Profile Unteres Aaretal.

Loepfe, R., *et al.*, in prep., Digitales Höhenmodell Basis Quartär der Nordschweiz – Version 2021 und ausgewählte Auswertungen: Nagra Arbeitsbericht.

Madritsch, H., Meier, B., Kuhn, P., Roth, P., Zingg, O., Heuberger, S., Naef, H., and Birkhäuser, P., 2013, Regionale strukturgeologische Zeitinterpretation der Nagra 2D-Seismik 2011/12: Nagra Arbeitsbericht NAB 13-10, 100 p.

Malz, A., Madritsch, H., and Kley, J., 2015, Improving 2D seismic interpretation in challenging settings by integration of restoration techniques: A case study from the Jura fold-and-thrust belt (Switzerland): Interpretation, v. 3, no. 4, p. SAA37-SAA58.

Naef, H., Büchi, M., Bläsi, H. R., Deplazes, G., and Gysi, M., 2019, Lithology Manual - Lithological description of drill cores and cuttings in Northern Switzerland: Nagra Arbeitsbericht NAB 19-11, 101 p.

Nitsche, F., Monin, G., Marillier, F., Graf, H., and Ansorge, J., 2001, Reflection seismic study of Cenozoic sediments in an overdeepened valley of northern Switzerland: the Birrfeld area: Eclogae Geologicae Helvetiae, v. 94, no. 3, p. 363-371.

Pietsch, J., and Jordan, P., 2014, Digitales Höhenmodell Basis Quartär der Nordschweiz - Version 2014 und ausgewählte Auswertungen: Nagra Arbeitsbericht NAB 14-02, 69 p.

Sprecher, C., and Müller, W., 1986, Geophysikalisches Untersuchungsprogramm Nordschweiz: Reflexionsseismik 82: Nagra Technischer Bericht NTB 84-15, 168 p.

Swisstopo, 2013, swissALTI3D, Federal Office of Topography swisstopo Wabern, Switzerland.
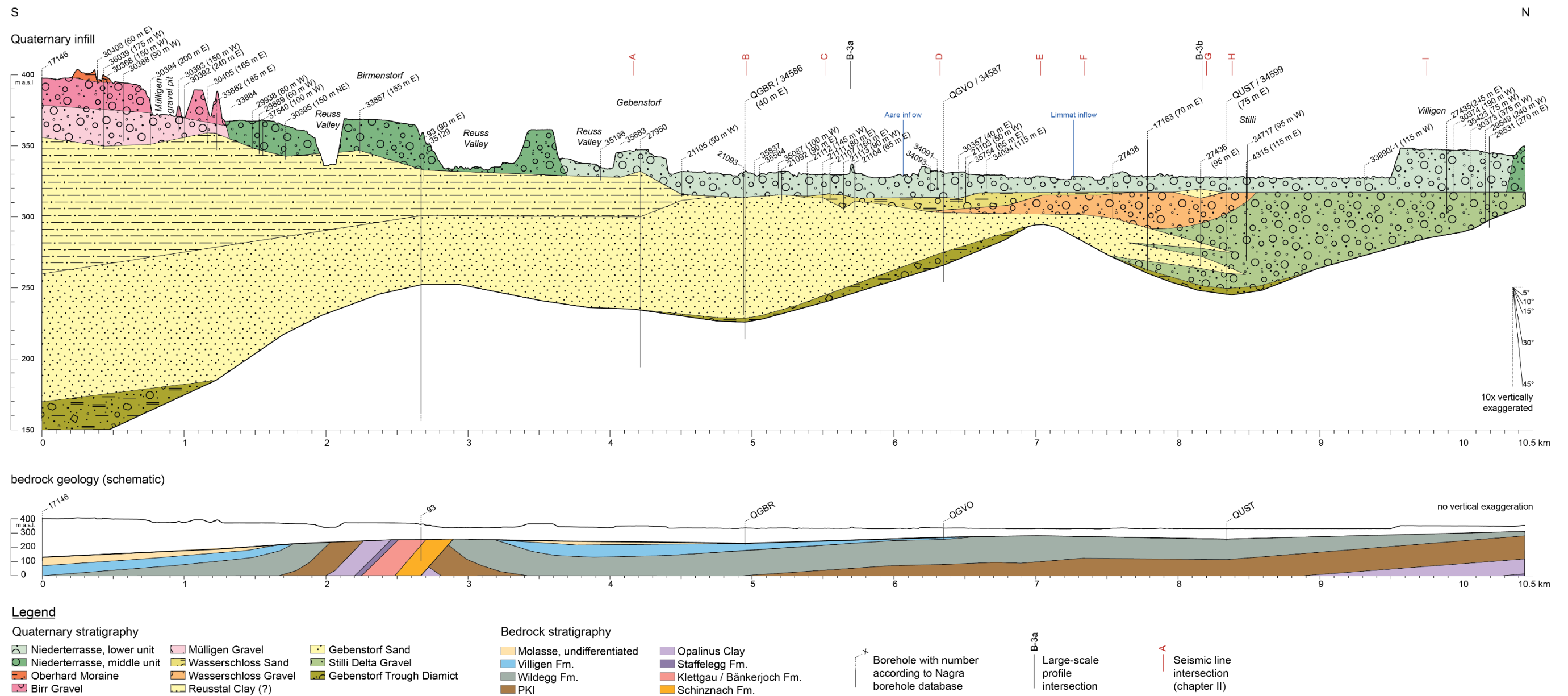
Fig. B-2: Section B-2 along the Gebenstorf-Stilli Trough (see Fig. B-1).

Appendix B

B-3a

W

E

600 m a.s.l.
550
500
450
400
350
300
250

Bützberg
Rinikerfeld
QRIN / 34550, 34551
Bruggerberg
Lower Aare Valley
Gebenstorfer Horn
Limmat Valley
Gländ
Surb Valley

SE WNW
B-4
ESE NW
B-2
SE SW

0   1   2   3   4   5   6   7   8   9   10   11   12   13   14 km

B-3b

600 m a.s.l.
550
500
450
400
350
300
250

Bützberg
Rinikerfeld
QRIN / 34550, 34551
Bruggerberg
Lower Aare Valley
Iberig
Hornrig

SE WNW
B-4
ESE SW
B-2
NE NW

QUST / 34599

0   1   2   3   4   5   6   7   8   9   10   11 km

Legend

Quaternary stratigraphy

- Niederterrasse, lower unit
- Niederterrasse, middle unit
- Niederterrasse, upper unit
- Wasserschloss Sand
- Wasserschloss Gravel
- Surbtal Gravel
- Rinikerfeld Colluvium
- Rinikerfeld Paleolake
- Gebenstorf Sand
- Stilli Delta Gravel
- Gebenstorf Trough Diamict
- Remigen Gravel
- Remigen Till
- Habsburg Gravel
- Rinikerfeld Basal Till
- Deeply weathered gravels/diamicts
- Tiefere Deckenschotter, undiff.
- Höhere Deckenschotter, lower unit
- Höhere Deckenschotter, upper unit

bedrock stratigraphy

- Upper Freshwater Molasse
- Upper Marine Molasse
- Lower Freshwater Molasse
- Villigen Fm.
- Wildegg Fm.

B-2
Large-scale profile intersection

Borehole with number according to Nagra borehole database

NE NW
Profile kink

5°
10°
15°
30°
45°

10x vertically exaggerated

Fig. B-3: Sections B-3a, B-3b across the study area (see Fig. B-1).

Appendix B

Fig. B-4: Section B-4, with auxiliary section B-4*, along the Habsburg-Rinikerfeld Paleochannel (see Fig. B-1).

Appendix B

Appendix C: Publication Mueller *et al.*, 2020

This study addresses the difficulties of luminescence-dating the Pleistocene deposits of the northern Alpine foreland, specifically of the Rinikerfeld Paleolake and Colluvium. The in-depth investigation and comparison of different luminescence signals gives confidence in sedimentary ages dating back to a least MIS 6. My contribution in the framework of this thesis consisted in characterising the regional geologic setting and providing sample material and illustrations. The manuscript has been published in Geochronology 2 under the Creative Commons Attribution 4.0 International license (open access) as

Mueller, D.[1], Preusser, F.[1], Buechi, M. W.[2], Gegg, L.[2], and Deplazes, G.[3], 2020, Luminescence properties and dating of glacial to periglacial sediments from northern Switzerland (DOI 10.5194/gchron-2-305-2020).

[1] Institute of Earth and Environmental Sciences, University of Freiburg, Alberstraße 23b, 79104 Freiburg, Germany

[2] Institute of Geological Sciences and Oeschger Centre for Climate Change Research, University of Bern, Baltzerstrasse 1+3, 3012 Bern, Switzerland

[3] National Cooperative for the Disposal of Radioactive Waste (Nagra), Hardstrasse 73, 5430 Wettingen, Switzerland

GEOCHRONOLOGY Open Access EGU

Luminescence properties and dating of glacial to periglacial sediments from northern Switzerland

Daniela Mueller[1], Frank Preusser[1], Marius W. Buechi[2], Lukas Gegg[2], and Gaudenz Deplazes[3]

[1]Institute of Earth and Environmental Sciences, University of Freiburg, 79104 Freiburg, Germany
[2]Institute of Geological Sciences, University of Bern, 3012 Bern, Switzerland
[3]Nationale Genossenschaft für die Lagerung radioaktiver Abfälle (NAGRA), 5430 Wettingen, Switzerland

Correspondence: Daniela Mueller (daniela.mueller@geologie.uni-freiburg.de)

Abstract. Luminescence dating has become a pillar of the understanding of Pleistocene glacial advances in the northern foreland of the Swiss Alps. However, both quartz and feldspar from the region are equally challenging as dosimeters with anomalous fading and partial bleaching being some of the obstacles to overcome for the establishment of decisive chronologies. In this study, luminescence properties of coarse- and fine-grained quartz, feldspar, and polymineral fractions of eight samples from a palaeovalley, Rinikerfeld in northern Switzerland, are systematically assessed. Standard performance tests are conducted on all four fractions. Deconvolution of luminescence signals of the quartz fractions is implemented and shows the dominance of stable fast components. Reader-specific low preheat temperatures are investigated on the infrared stimulated luminescence (IRSL) signal of feldspar. Thermal stability of this signal is found for low preheats, and thermal quenching could be excluded for higher preheats. However, anomalous fading is observed in the feldspar and polymineral IRSL signals and two correction approaches are applied. For one approach, fading corrected coarse-grained feldspar ages are consistent with those derived from quartz. In general, coarse-grained quartz and feldspar, as well as the fine-grained polymineral fraction of one sample, are in chrono-stratigraphic agreement and present negligible evidence for partial bleaching. However, ages derived from fine-grained quartz are found to underestimate those of the coarse-grained quartz fractions. Hence, the impact of alpha efficiency and water content on the dose rate and thus the ages are assessed. A finite explanation for the observed discrepancies remains lacking, but this systematic investigation of different luminescence signals allows for the establishment of a chronology for the palaeovalley fill dating back to at least Marine Isotope Stage 6 (MIS 6).

1 Introduction

Pleistocene glaciations in the northern foreland of the Swiss Alps have been studied since the early 19th century (summarised in Preusser et al., 2011). Whereas it appears that a minimum of eight glacial advances have shaped the lowlands, consensus on the exact number and timing is still lacking. During the last 3 decades, numerical dating has become a crucial component in the reconstruction of the environmental past of northern Switzerland (e.g. Preusser, 1999a; Graf et al., 2007; Kock et al., 2009; Dehnert et al., 2012). In particular, luminescence dating has become a pillar of chronostratigraphy and understanding of glacial advances (Preusser et al., 2011). However, luminescence dating of glacial and proglacial deposits can be complex (e.g. Duller, 1994, 2006; Spencer and Owen, 2004). For one, in such environments sediment sources and sinks are often within a short distance of each other and transport may occur in turbid waters, both of which reduces the chance for grains to experience sufficient sunlight exposure to reset or bleach any pre-existing luminescence signals. This effect will consequently lead to age overestimation and requires consideration in such deposits. The measurement of single grains or small aliquots has been advised to allow for monitoring of luminescence signal, commonly presented as equivalent dose (D_e) distributions and the isolation of a proportion of the D_e distributions that is considered well bleached (e.g. Olley et al., 2004;

Appendix C

Duller, 2006; Trauerstein et al., 2017). The optically stimulated luminescence (OSL) signal of quartz is more readily bleachable than that of feldspar (Godfrey-Smith et al., 1988; Murray et al., 2012), and hence it is favoured as a dosimeter (e.g. Lowick et al., 2015). But, to assess partial bleaching of samples from northern Switzerland, Trauerstein et al. (2017) have recommended the comparison of luminescence signals obtained from both dosimeters. However, quartz and feldspar from the region have found to be equally challenging for dating.

For quartz from the wider region, unstable components were reported for some (e.g. Klasen et al., 2016) but not all samples (e.g. Gaar et al., 2013). Moreover, laboratory dose response curves for quartz were often best fitted with a double-saturating exponential function that accounts for high dose responses beyond single exponential behaviour (Lowick et al., 2010; Dehnert et al., 2012). This phenomenon is also known for samples from other regions where luminescence ages are either in agreement (e.g. Murray et al., 2008; Pawley et al., 2010) or disagreement (e.g. Lai, 2010; Timar et al., 2010; Timar-Gabor et al., 2011) with independent age control. However, the physical reason for this behaviour has yet to be identified (Wintle, 2008). In northern Switzerland, quartz luminescence ages of up to (but not beyond) ca. 250 ka have been found to be reliable (Anselmetti et al., 2010; Dehnert et al., 2012; Lowick et al., 2015; Buechi et al., 2017). Hence, this approach is not suitable to establish an independent chronology for the recently modified Mid-Pleistocene glaciation history (Graf, 2009; Preusser et al., 2011).

While feldspar requires more time to reset the signal prior to deposition, it is known to saturate at higher doses and therefore often allows one to date much older deposits than quartz (cf. Duller, 1997). Yet, the infrared stimulated luminescence signal of feldspar measured at 50 °C (IRSL) often suffers from anomalous fading, contributing to age underestimation (Wintle, 1973; Spooner, 1994). Different approaches to determine and account for the loss of signal over time have been proposed (Huntley and Lamothe, 2001; Auclaire et al., 2003; Lamothe et al., 2003; Huntley, 2006; Kars et al., 2008). These approaches rely on observing signal loss over hours to days within laboratory experiments and from this data the signal loss that has occurred over geological timescales is deduced. In such storage tests, fading has been observed for most samples from northern Switzerland with g-values between 1 % and 3 % per decade (Dehnert et al., 2012; Lowick et al., 2012, 2015; Gaar and Preusser, 2012) and 2.7 ± 0.3 % per decade (normalised to 2 d; Buechi et al., 2017). However, (1) uncorrected IRSL D_e values were beyond the linear part of the dose response curve and therefore unsuited for most fading correction approaches, (2) corrected IRSL D_e values were close to saturation and consequently rejected for age determination, or (3) uncorrected feldspar ages were in better agreement with quartz ages and therefore favoured (Dehnert et al., 2012; Lowick et al., 2012, 2015; Gaar and Preusser, 2012; Buechi et al., 2017). Only Gaar et al. (2013) found

correcting for fading appropriate and necessary for samples < 100 ka. For dating of older samples, Lowick et al. (2012) tested alternative measurement protocols that target signals that are more stable than the IRSL signal, the post-infrared infrared stimulated luminescence signals (pIRIR). The pIRIR signals are measured at higher temperatures after an initial readout of IRSL signals at 50 °C (Thomsen et al., 2008; Buylaert et al., 2011; Thiel et al., 2011). While fading is expected to decrease or become negligible for the more stable pIRIR signals, these take longer to bleach by sunlight during transport. For the selected pIRIR$_{225}$ and pIRIR$_{290}$ signals, fading was still observed and age overestimations led to the conclusion that these approaches are not beneficial for the investigated water-lain sediments from northern Switzerland (Lowick et al., 2012).

Here, luminescence properties of samples from the Rinikerfeld in the northern foreland of the Swiss Alps are assessed. Scientific drilling was conducted at a stratigraphic key site within the former glacier forefield as part of a larger campaign. The campaign aims to acquire further insights into the long-term glacial and fluvial landscape evolution of northern Switzerland. Modelling of future erosion scenarios will be based on the gained knowledge and thereby assist in the assessment of the safest and most suitable location for a prospective Swiss nuclear waste depository. For this, the establishment of a chrono-stratigraphy is essential, and hence dating is a crucial component. Therefore, feldspar, polymineral, and fine- and coarse-grained quartz are investigated to exploit the dating potential of the samples from this site. Performance tests, signal intensity and composition of quartz, and signal and fading properties of feldspar are discussed, and two approaches to correct for fading are applied. Eventually ages are derived and discussed with regard to problems found for other studies of the region. For ease of reading, methods, results and discussion are jointly presented in aspect specific subsections.

2 Site setting and samples

The study site (Fig. 1) is located within the Rinikerfeld, at the eastern tail of the Jura Mountains, about 30 km NW of Zurich. Rinikerfeld is part of an extensive palaeovalley structure and situated in an elevated position, ca. 50 m above the nearby present-day Lower Aare Valley. At the site, the palaeovalley is carved into Mesozoic bedrock and presumed to be of Mid-Pleistocene age (Bitterli-Dreher et al., 2007; Graf, 2009). It was spared from glacial overprint during the Last Glacial Maximum (Bini et al., 2009); however, the outermost ice margins of preceding glaciations were found to the north of the study area (cf. Preusser et al., 2011), suggesting a glacial to periglacial sedimentary nature of the palaeovalley fill.

About 40 m of Quaternary sediments are overlying the bedrock (carbonaceous marl) and were recovered in a com-

Appendix C
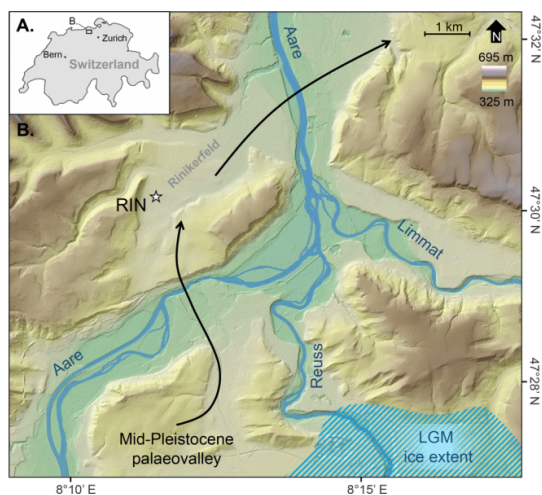
Figure 1. (a) Location of the study area within Switzerland. **(b)** Overview of the study area and drill site.

posite core (Fig. 2) within a scientific drilling campaign (Gegg et al., 2018). At its base, the composite core consists of about 4 m of glacial diamicton overlain by ca. 2 m of glacial or glacier-proximal sandy gravel that contains frequent angular, faceted and (in the lowest part) striated clasts. This unit transitions into ca. 24 m of lacustrine clay and silt. The interbedded gravelly sand and silt at the bottom of the lacustrine unit suggest an initial dominance of deposition by traction currents, possibly in a glaciolacustrine or deltaic setting. Relatively homogeneous laminated sediments in the rest of the lacustrine unit indicate suspension settling and low-energy currents. Towards the top, the lacustrine unit progressively coarsens and is capped by ca. 4.6 m of interbedded gravelly and sandy diamictons that are rich in locally derived angular clasts. This heterogeneous unit is likely to represent a mix of fluvial and colluvial deposits possibly deposited in a periglacial setting (Raab et al., 2007).

For luminescence dating, samples were obtained from ca. 10 cm diameter cores recovered in plastic liners (Table 1). A total of eight samples were taken: three samples from the gravelly to sandy diamicton unit (RIN1, 2, 3), one sample of lacustrine sands (RIN4), and one sample of gravelly sand and silt (RIN13). The two latter samples bracket the fine-grained lacustrine unit, whereof another three samples were taken (RIN5, 6, 8). Sample material was collected in ca. 10 cm segments, whereby the outer rind and the surface, exposed to daylight during core cutting and splitting, were allocated for dose rate determination, and the inner core was used for D_e determination.
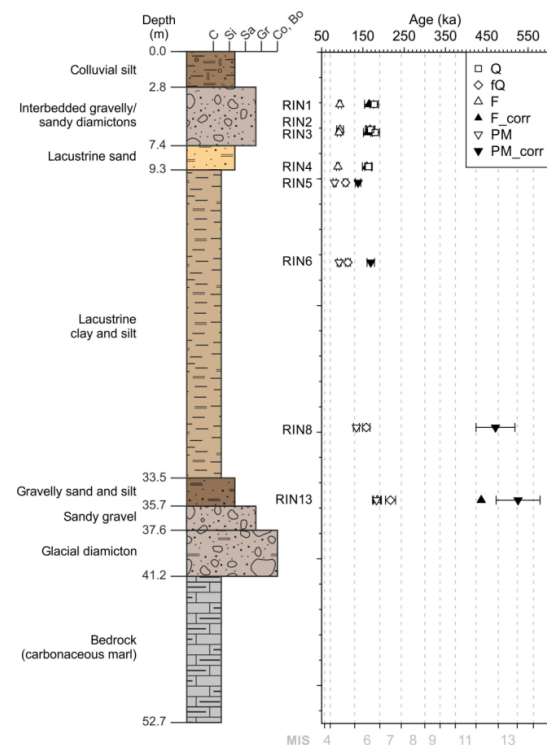
Figure 2. Core log and age–depth model of the investigated site. Ages for all minerals and fractions are presented with 1σ uncertainty. Fading corrected ages are calculated following Kars et al. (2008). Grain size fractions are subdivided into clay (C), silt (Si), sand (Sa), gravel (Gr), and a combined fraction of cobbles and boulders (Co, Bo).

3 Sample preparation, equipment and dose rate determination

To determine D_e values, samples were wet-sieved and treated with HCl and H_2O_2 to remove carbonates and organic matter, respectively. Of five samples (RIN1 to RIN4 and RIN13), coarse-grained (150–200 and 200–250 μm) potassium-rich feldspar (F) and quartz (Q) were separated using sodium polytungstate at densities of 2.58 and 2.7 g cm^{-3}. The outer rind of the quartz grains was etched in 40 % hydrofluoric acid (HF) for 1 h, followed by a 32 % HCl treatment for another hour to eliminate any fluoride precipitates. For the remaining three samples (RIN5, 6, 8) and RIN13, the fine-grained fraction (4–11 μm) was separated using settling under Stokes' Law. One half of the sample remained pristine as polymineral fraction (PM), while the other half was treated with hexafluorosilicic acid for 7 d in order to obtain purified quartz (fQ). The fine-grained fractions were suspended in acetone and settled onto cups of 9.8 mm in diameter ($> 10^6$ grains). For

Appendix C

Table 1. D_e values and derived ages for all samples; 1σ uncertainties are given. Presented values are obtained using the central age model (CAM, Galbraith et al., 1999). The number of accepted and measured aliquots is provided by n. The measured mineral, i.e. coarse-grained quartz (Q), fine-grained quartz (fQ), feldspar (F), and polymineral (PM), is given by M. Ages to be considered for chrono-stratigraphic interpretation are presented in bold.

Sample code	M	Grain size (μm)	n	OD[a] (%)	$2D_{0\_CAM}$ (Gy)	D_{e_CAM} (Gy)	$D_{e\_Lamothe}^{b}$ (Gy)	$D_{e\_Kars}^{c}$ (Gy)	Age_{CAM}^{d} (ka)	$Age_{Lamothe}^{b}$ (ka)	Age_{Kars}^{c} (ka)
RIN1	Q	200–250	30/31	24±3	316±17	150±7	–	–	**177±11**	–	–
	F	150–200	30/30	11±2	577±20	141±3	215±5	247±7	94±4	143±6	**165±7**
RIN2	Q	200–250	30/31	25±3	343±13	144±7	–	–	**169±10**	–	–
	F	200–250	30/30	14±2	626±22	158±4	242±8	280±9	95±4	145±7	**167±8**
RIN3	Q	200–250	30/30	25±3	317±15	146±7	–	–	**180±11**	–	–
	F	200–250	30/31	14±2	609±18	151±4	228±7	265±8	92±4	139±7	**162±8**
RIN4	Q	200–250	30/33	21±3	365±16	195±8	–	–	**164±9**	–	–
	F	150–200	30/30	6±1	641±26	167±2	256±4	297±6	90±4	137±6	**160±7**
RIN5	fQ	4–11	7/7	–	431±28	195±4[f]	–	–	>113±9[f]	–	
	PM	4–11	30/30	3±1	445±19	148±2	209±2	252±3	82±4	115±6	**138±7**
RIN6	fQ	4–11	7/7	–	459±31	227±5[f]	–	–	>117±9[f]	–	–
	PM	4–11	7/7	–	458±44	188±4	272±6	343±9	92±5	134±7	**169±9**
RIN8	fQ	4–11	7/7	–	577±27	365±10[f]	–	–	>163±13[f]	–	–
	PM	4–11	7/7	–	480±40	314±8	560±19	1101±97	134±7[h]	240±14[h]	471±47[h]
RIN13	Q	200–250	19/26	56±10	274±16	255±34[g]	–	–	>**183±26**[f,g]	–	–
	fQ	4–11	7/7	–	545±28	388±12[f]	–	–	>224±18[f]	–	–
	F	200–250	30/30	17±3	651±32	413±14	>695[e,h]	>974[e,h]	185±10	>311[e,h]	>437[e,h]
	PM	4–11	7/7	–	515±39	333±8	542±17	955±86[h]	183±10	299±17	526±53[h]

[a] Overdispersion was calculated using the CAM (Galbraith et al., 1999). [b] A g-value (normalised to 2 d) of 3.1 ± 0.6 was used for F of RIN1 to RIN4 and RIN13, and a g-value of 2.4 ± 0.6 was used for PM of RIN5 to RIN13. [c] A ρ'-value of 2.21×10^{-6} was used for F of RIN1 to RIN4 and RIN13, and a ρ'-value of 1.89×10^{-6} was used for PM of RIN5 to RIN13. [d] Ages were calculated using the weighted mean of the uncorrected D_e values derived with the CAM (Galbraith et al., 1999). [e] Out of 30 measured aliquots, 12 (Lamothe-corrected) and 19 (Kars-corrected) aliquots are in saturation following fading correction, and therefore the values shown are derived using a CAM on a truncated distribution. [f] Regarded to be minimum estimates due to chrono-stratigraphic reasons. [g] Derived CAM is based on a truncated distribution, and results should be considered as minima. [h] Based on D_e values beyond $2 \times D_0$.

the coarse-grained fractions, sample material was mounted onto cups using silicon oil stamps with diameters of 1 mm for feldspar and 4 mm for quartz (ca. 13 and 200 grains, respectively).

D_e values were obtained with a Freiberg Instruments Lexsyg Research reader using LEDs with peak emission at 458 nm (blue-light stimulated luminescence, BSL) for quartz and at 850 nm (IRSL) for feldspar and polymineral. BSL and IRSL signals were detected by an ET9235QB photomultiplier tube filtered through a 2.5 mm Hoya U-340 glass combined with a 5 mm Delta-BP 365/50 EX-interference filter or a 3 mm BG 39 Schott glass and a 3.5 mm HC 414/46-1 AHF Brightline interference filter (referred to as "410 nm filter combination"), respectively. Additionally, a cardboard barrier was mounted into the filter wheel for IRSL measurements (for details, see Sect. 4.2). Laboratory irradiation was given by a ^{90}Sr/^{90}Y beta source mounted into the reader. The beta source was calibrated using Risø calibration quartz batches 108 (4–11 μm) and 118 (180–250 μm) to ca. 0.10 and 0.11 Gy s^{-1}, respectively. Measurements with the electron-multiplying charge-coupled device (EMCCD) were conducted using an Andor iXon Ultra 897 camera mounted to the Lexsyg Research.

Notable is the preheat behaviour of the used Lexsyg Research reader (Lexsyg ID 090020): at a heating rate of $5\,°C\,s^{-1}$, the so-called $110\,°C$ thermoluminescence (TL) peak emerges at much lower temperatures than expected. For example, for Risø calibration quartz (batch 118) TL counts peak at $87 \pm 3\,°C$ during preheat. This is in agreement with observations made by Schmidt et al. (2018b), who compared the preheat behaviour of various OSL readers and discovered the appearance of the $110\,°C$ TL peak within a range of $60\,°C$. This has to be considered when assessing appropriate measurement protocols (see Sect. 4).

For dose rate determination (Table 2), sample material was dried and radionuclide content was determined via high-resolution gamma-ray spectrometry at VKTA (Dresden, Germany). In absence of evidence for radioactive disequilibrium (cf. Degering and Degering, 2020), only contents used for dose rate determination are presented in Table 2. A mean alpha efficiency factor of 0.04 ± 0.02 (a-value) was assumed for all fQ following Buechi et al. (2017). An a-value of 0.05 ± 0.01 was applied for the F and PM fractions (Preusser, 1999a, b; Preusser et al., 2001). For the two latter fractions an internal potassium content of $12.5\% \pm 0.5\%$ was used (Huntley and Baril, 1997). The cosmic contribution was de-

Appendix C

Table 2. Dosimetric data and total dose rates as used for age determination (all values are given with 1 σ uncertainties).

Sample code	Core depth (m)	WC field[a] (%)	WC max[a] (%)	WC used[a] (%)	Radionuclide concentrations			DR_{cosmic} (Gy ka^{-1})	DR_{total} Q and fQ[b] (Gy ka^{-1})	DR_{total} F and PM[c] (Gy ka^{-1})
					U (ppm)	Th (ppm)	K (%)			
RIN1	4.12	16	39	20 ± 5	0.81 ± 0.17	3.52 ± 0.24	0.44 ± 0.03	0.135 ± 0.014	0.84 ± 0.05	1.50 ± 0.06
RIN2	6.12	17	46	20 ± 5	0.69 ± 0.15	3.31 ± 0.22	0.53 ± 0.04	0.108 ± 0.011	0.85 ± 0.05	1.67 ± 0.08
RIN3	6.34	19	34	20 ± 5	0.93 ± 0.18	3.20 ± 0.22	0.49 ± 0.04	0.105 ± 0.011	0.81 ± 0.05	1.63 ± 0.08
RIN4	9.04	18	40	20 ± 5	1.44 ± 0.26	4.90 ± 0.30	0.77 ± 0.05	0.081 ± 0.008	1.19 ± 0.07	1.86 ± 0.07
RIN5	10.25	24	48	25 ± 5	1.54 ± 0.27	6.00 ± 0.40	0.96 ± 0.07	0.073 ± 0.007	1.73 ± 0.14	1.82 ± 0.09
RIN6	16.55	23	49	25 ± 5	1.75 ± 0.29	6.70 ± 0.40	1.18 ± 0.08	0.044 ± 0.004	1.94 ± 0.15	2.03 ± 0.10
RIN8	29.63	19	42	20 ± 5	2.26 ± 0.35	6.80 ± 0.50	1.28 ± 0.09	0.020 ± 0.002	2.23 ± 0.18	2.34 ± 0.13
RIN13	35.37	15	45	20 ± 5	1.53 ± 0.24	5.50 ± 0.40	0.99 ± 0.06	0.015 ± 0.002	1.40 ± 0.06 (Q)	2.23 ± 0.11 (F)
									1.73 ± 0.14 (fQ)	1.91 ± 0.10 (PM)

[a] Water content (WC) as measured from the samples (field), and maximum absorption capacity as measured in laboratory tests (max) and as used for D_e determination. [b] Alpha efficiency of 0.04 ± 0.02 was assumed for fQ. [c] Alpha efficiency of 0.05 ± 0.01 and internal potassium content of $12.5\% \pm 0.5\%$ were assumed.

termined for present-day depths following Prescott and Hutton (1994). Water content relative to the dry weight of the sample and capacity of water absorption (DIN 18132:2012-04, 2016) were determined in the laboratory. Representative long-term water content estimates of 20 to $25\% \pm 5\%$ were used for total dose rate (DR_{total}) determination. Age calculations were conducted with ADELE 2017 software (https://www.add-ideas.com/, last access: 1 February 2020; Degering and Degering, 2020).

4 Performance tests

Performance tests were conducted on both the coarse- and fine-grained fractions of two representative samples (RIN2Q, RIN2F, RIN5fQ, RIN5PM). Preheat plateau tests were carried out on the natural dose while for thermal transfer and dose recovery tests, sample material was exposed to a daylight lamp for 16 h (Q, fQ) to 30 h (F, PM). All performance tests and measurements were conducted using preheating prior to the natural, regenerative and test doses for which the aliquots were heated with $5\,°C\,s^{-1}$ to the tested temperature and held for 10 s (Q, fQ) or 60 s (F, PM).

Both BSL and IRSL measurements were conducted following the single-aliquot regenerative-dose (SAR) protocol (Murray and Wintle, 2000) with test doses of ca. 46 and ca. 23 Gy administered, respectively. The initial signal was derived from the first 0.4 s of the BSL and the first 15 s of the IRSL signals. A late background subtraction using the last 40 s (BSL) or 50 s (IRSL) was applied. D_e values were calculated using the numOSL package for R (Peng et al., 2018). For Q and fQ, an IR depletion ratio step ($>20\%$) was implemented at the end of each sequence to check the adequacy of the sensitivity correction and for feldspar contamination. A maximum of four aliquots per sample failed this rejection criterion. None of the measured Q, fQ, F and PM aliquots presented dim ($<3\times$ background level) or imprecise ($>20\%$) test dose signals and were hence accepted. For RIN3 F, one aliquot was rejected as it failed the recycling ratio test ($>20\%$), and for RIN13 Q, three aliquots were rejected as their D_e values were in saturation.

4.1 Quartz OSL

For preheat plateau tests on the natural signal of Q (RIN2), statistically consistent (1σ) D_e values were obtained on the larger grain size fraction for preheats between 200 and 240 °C (Fig. 3). D_e values of fQ (RIN5) for this preheat temperature range are consistent at 2σ (Fig. 3). A given dose of ca. 130 Gy was fully recovered from both tested samples (RIN2 Q and RIN5 fQ; Fig. 3) at 240 °C with measured-to-given dose ratios (M / G ratios) of 1.01 ± 0.03 and 1.05 ± 0.04, respectively. Maximal thermal transfer was detected with <4 Gy, which is equal to less than 3.5 % of the natural D_e and is therefore considered negligible. Hence, a preheat temperature of 240 °C was chosen for both grain size fractions of quartz (Q, fQ) for all investigated samples.

4.2 Feldspar and polymineral IRSL

For F, poor recovery was obtained for preheats above 190 °C. Considering the poor performance at high temperatures and the early emergence of the 110 °C TL peak on the used Lexsyg Research reader (see Sect. 3), lower temperatures were tested and a full recovery of the given dose (ca. 130 Gy) was possible for F and PM with a preheat of 170 °C. No plateau is present, but increasing trends of D_e values from the natural signal were observed between 150 and 210 °C for F and between 170 and 210 °C for PM. Natural D_e values decrease rapidly for preheats above 210 °C, while thermal transfer behaves inversely. However, thermal transfer is within <2 Gy (ca. 1.5 % of the natural D_e) and is therefore negligible. To investigate whether thermal quenching induces an underestimation of D_e values at high preheat temperatures, preheat measurements were conducted on aliquots of RIN2 F, following Wallinga et al. (2000). Therefore, the natural signal was bleached with IR LEDs, a fixed dose of ca. 90 Gy was administered and each aliquot was preheated to

Appendix C
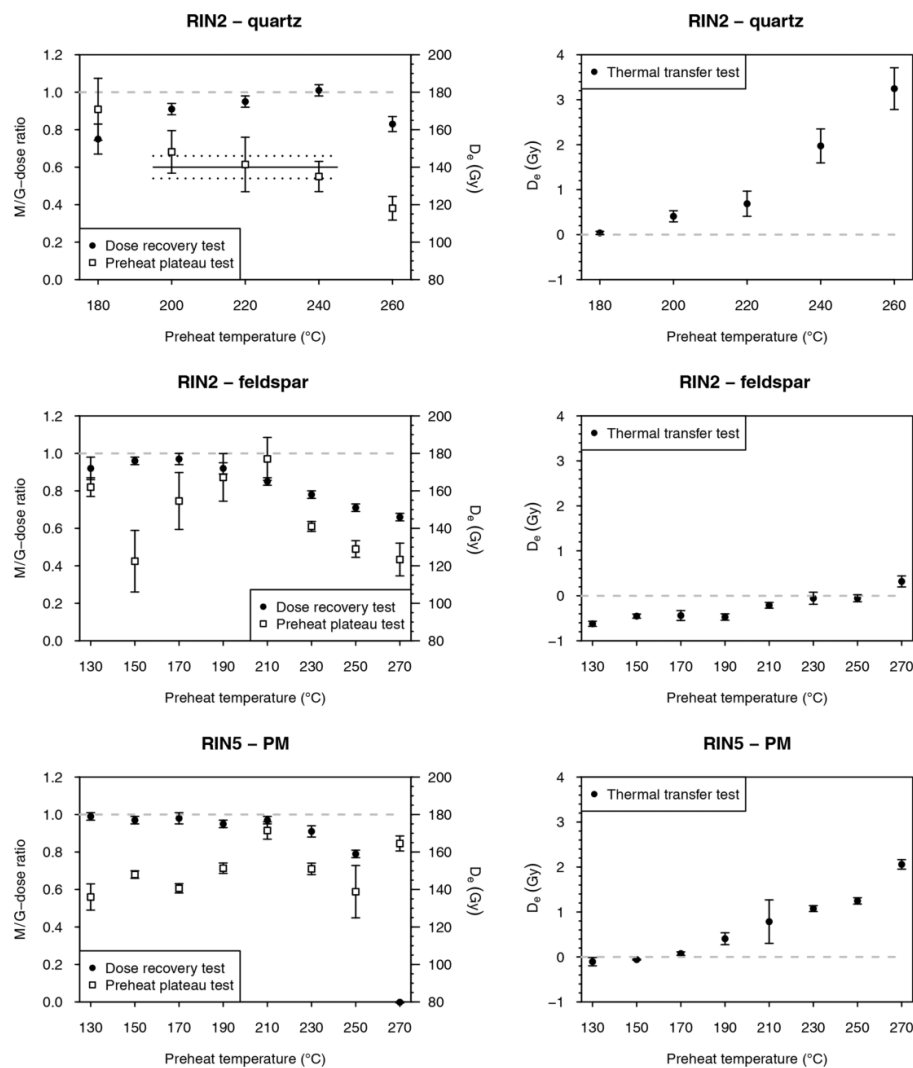
Figure 3. Preheat plateau, dose recovery and thermal transfer test results for Q and F of RIN2 and fQ and PM of RIN5. Presented are CAM D_e values with 1σ uncertainties for 3 (F, PM) or 5 (Q, fQ) aliquots per preheat temperature. Dose recovery results are presented as measured-to-given dose ratios (M / G ratio).

50 °C for 10 s, followed by IRSL at 50 °C for 0.1 s. This was repeated for preheat temperatures between 50 and 300 °C in 25 °C steps. After the highest preheat, the aliquots are expected to be sensitised and can be used for normalisation; therefore, the entire measurement sequence was repeated using the same fixed dose of ca. 90 Gy (Fig. 4). An increase in normalised IRSL sensitivity would be expected if the electron trapping probability changes with temperature (Wallinga et al., 2000). However, a decrease was observed for temperatures above 200 °C, suggesting that it is not a change

in trapping probability causing the lower natural D_e values and dose recovery ratios. Conversely, the high preheat temperature may cause a removal of signal commonly used for D_e determination. Therefore, a preheat temperature of below 200 °C is most advisable. The best performance of the SAR protocol was obtained at a preheat of 170 °C (Fig. 3), which suggests a much lower preheat than is conventionally used. Buylaert et al. (2011) advise against the use of preheats below 200 °C due to thermally unstable signals induced during laboratory irradiation. However, their study was con-

Appendix C
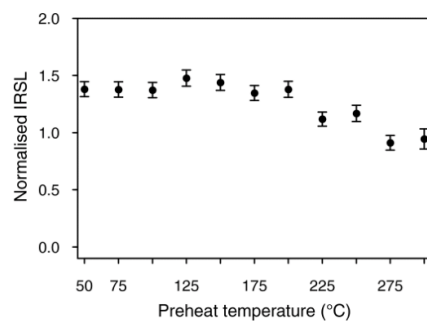
Figure 4. To determine thermal quenching, repeated short shine measurements of L_x/T_x for a given dose of 90 Gy after preheats at different temperatures were conducted on one aliquot of RIN2 F.
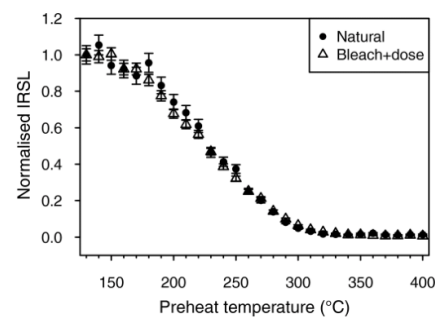
Figure 5. Short shine pulse annealing experiment on natural and laboratory-induced doses of two aliquots from RIN2 F. The IRSL signal is normalised to a test dose and renormalised to the first measurement.

ducted on a Risø reader with different reader-specific preheat conditions. It is stressed that temperature parameters of Risø and Lexsyg readers are not readily comparable. Nevertheless, to investigate a potential contribution from artificially filled unstable traps, short shine pulse annealing tests were conducted on aliquots of RIN2 F with naturally irradiated and laboratory-irradiated material following Wallinga et al. (2000). Each aliquot was preheated for 10 s and then stimulated with IR LEDs at 50 °C for 0.1 s. Preheats were conducted consecutively in 10 °C steps from 130 to 400 °C. The signal was normalised with a test dose measurement of the same aliquot and renormalised to the first measurement (Fig. 5). Signal distribution of both the natural and laboratory-induced irradiation are indistinguishable, and it is unlikely that a thermally unstable component from artificially filled traps contributes to the IRSL signal even at low preheat temperatures. Thermal stability of IRSL signals from the samples investigated here is given and thermal quenching was not detected; therefore, preheats of 170 °C are considered appropriate. In the absence of preheat plateaus in the natural signals, the dose recovery test results are indicative (RIN2 F 0.97 ± 0.03; RIN5 PM 0.98 ± 0.03), and hence preheats of 170 °C were used all for measurements.

However, the differences in temperature parameters make it necessary to test whether the configuration of the Lexsyg Research reader affects the temperature during stimulation as it does for preheating. Therefore, D_e values of the natural signal were obtained at stimulation temperatures of 30, 50 and 70 °C for one representative sample (RIN2 F) (Fig. 6). While the scatter in the natural D_e values decreases with stimulation temperature, mean D_e values of all stimulation temperatures are statistically consistent with each other, implying that differences between the reader systems may not be as pronounced in the low temperature range as they are at temperatures above 150 °C.
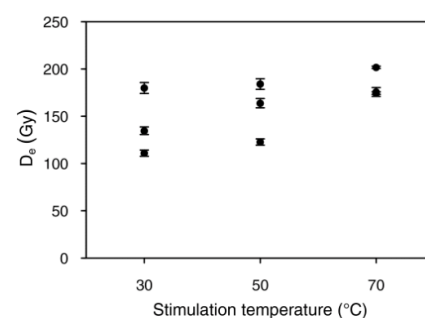
Figure 6. D_e determination of the natural signal using different stimulation temperatures for each three aliquots of RIN2 F.

5 Signal properties

5.1 Quartz OSL

Quartz grains from the investigated site are relatively dim and rarely present luminescent properties. Tests with an EMCCD camera showed that < 1 % of the coarse-grained grains emitted a natural luminescence signal when stimulated with blue light. This is common for quartz from Switzerland (Trauerstein et al., 2017) and to allow for bright enough signals during measurement, an aliquot size of 4 mm in diameter was chosen. While ca. 200 grains are measured at once using this approach, only a few grains are expected to significantly contribute to the emitted luminescence signal, and these are thereby considered small aliquots.

The signals emitted by Q and fQ are dominated by the fast component and reduce to background after about 2 to 4 s of stimulation (Fig. 7). To further investigate the BSL signals, signal decomposition was conducted (Fig. 8) using the numOSL package in R (Peng et al., 2018) that applies the "Levenberg–Marquardt algorithm" suggested by Bluszcz and Adamiec (2006). The initial signals consist of 95 % of

Appendix C
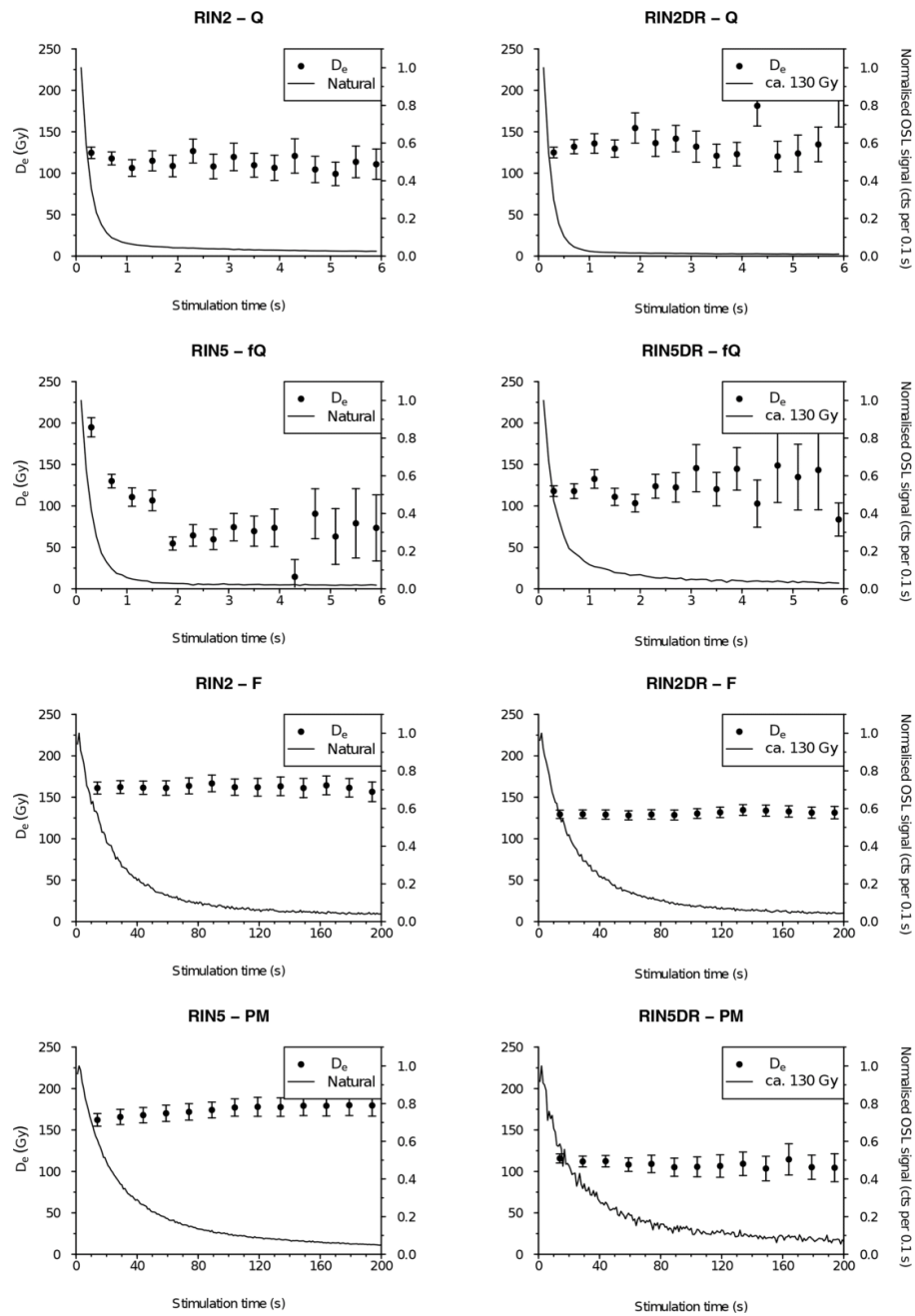
Figure 7. $D_e(t)$ plots of the natural dose determination and dose recovery (DR) tests for Q and F of RIN2 and fQ and PM of RIN5. $D_e(t)$ plots were calculated for 0.4 s intervals (Q, fQ) and 1.5 s (F, PM). The normalised luminescence signals of the natural or first given (DR) dose are presented.

Appendix C
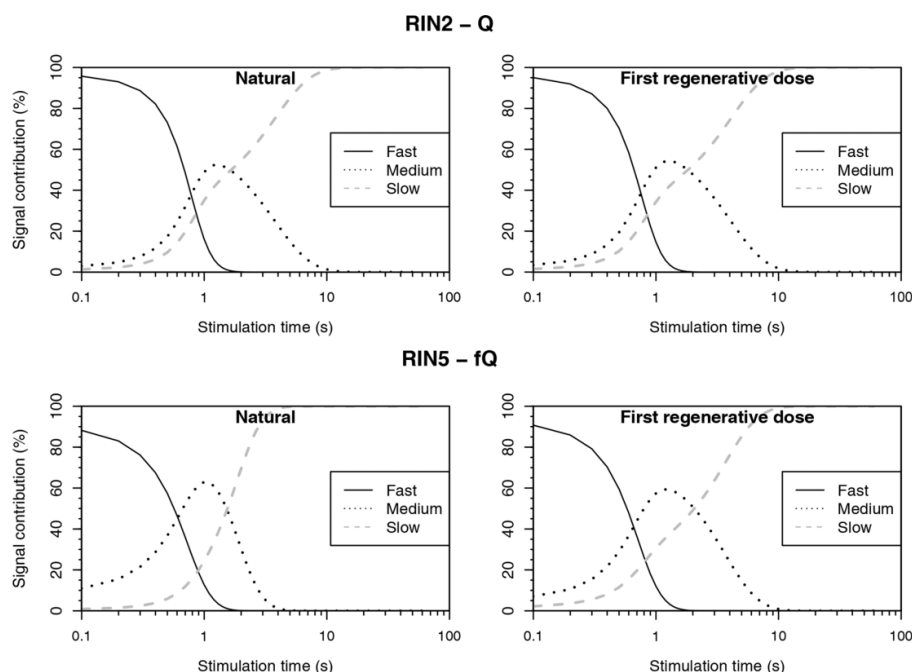
Figure 8. Component deconvolution of the natural and regenerative OSL response of RIN2 Q and RIN5 fQ.

the fast component for Q and 90 % of the fast component for fQ, while the relative contribution of the medium components to the natural and regenerative doses are almost identical. The latter is considered an indicator for a stable medium component (Steffen et al., 2009). Further, when assessing $D_e(t)$ plots with 0.4 s intervals of Q from RIN2 (Fig. 7), generally consistent D_e values are obtained for the measurement of the natural dose and the dose recovery experiment, which indicates uniformity of signal contribution. For RIN5 fQ, D_e values decrease with the shift of integration intervals between 0 and 2 s stimulation time. However, this phenomenon is only present in the natural signal but not in those of dose recovery tests. Li and Li (2006a) observed a similar decrease of D_e values within the first 3.6 s for their DGF-1 sample (Chinese coarse-grained aeolian deposit) and found an explanation in a thermally unstable medium component. They proposed the use of $D_e(t)$ plots to derive D_e values separately from the fast and medium component by fitting their Eq. (3). For RIN5 fQ, negligible differences were found for D_e values derived using either component by assuming photo-ionising cross sections, as proposed by Jain et al. (2003) and Li and Li (2006b). However, Steffen et al. (2009) found that the equation is highly dependent on the photo-ionising cross section of the individual components, the determination of which introduces an array of uncertainties and was therefore deemed unpractical.

D_e values derived using early background subtraction (0.4 to 1.0 s; cf. Cunningham and Wallinga, 2010) are statistically consistent with those obtained using late background subtraction (2σ). This indicates an unproblematic slow component. For D_e determination of Q and fQ, the first 0.4 s of the BSL signal was found appropriate as the initial signal, and a late background subtraction using the last 40 s was applied. Examples of extended dose response curves are shown for one aliquot Q from RIN2 and one aliquot fQ from RIN5 in Fig. 9. Laboratory saturation levels exceed 600 Gy (Q) and 800 Gy (fQ), and $2 \times D_0$ values are below 400 Gy (Q) and 580 Gy (fQ; Table 1). Dose response curves of both Q and fQ are well fitted with a double-saturating exponential and a single-saturating exponential function. The latter implies that a single type of trap is responsible for the signal (Aitken, 1998).

5.2 Feldspar and polymineral IRSL

In contrast to Q, the natural signal of 1 mm F aliquots (ca. 13 grains) is very bright and causes saturation of the photomultiplier tube, particularly at high doses. Noteworthy is that only few grains inherit an effective, natural luminescence signal with even less being particularly bright as shown by tests with an EMCCD camera (Fig. 10). A Schott NG-11 neutral density filter was tested together with the 410 nm-filter combination but failed in protecting the photomultiplier tube

Appendix C
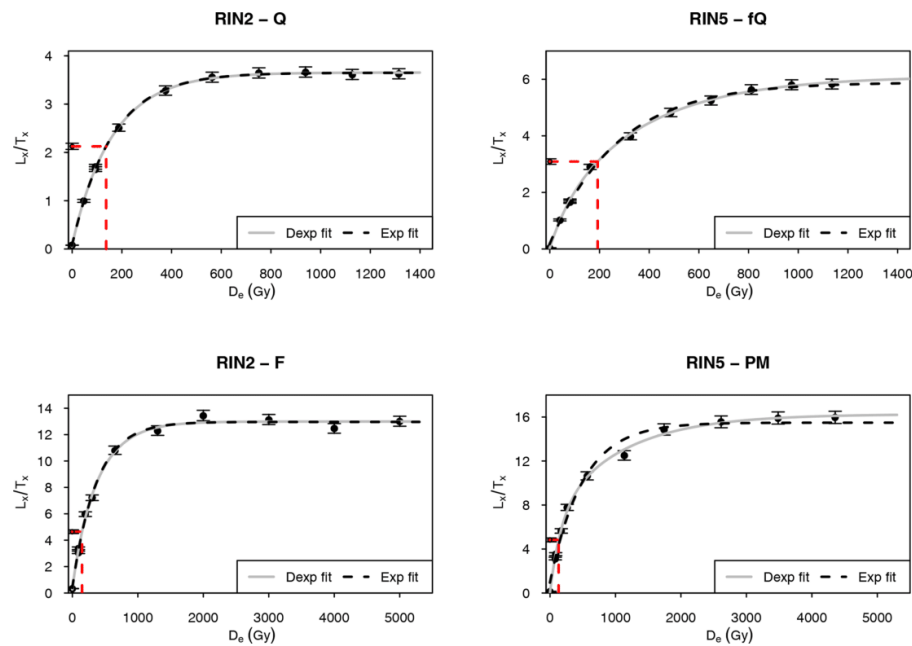
Figure 9. Extended dose response curves for RIN2 Q and F and RIN5 fQ and PM.

from saturation. A cardboard disc with a hole in its centre was mounted into the filter wheel, reducing the photon passage to 4 mm in diameter, which allowed for the retrieval of a detectable signal. A dose recovery test (given dose of ca. 130 Gy) was conducted with and without using the cardboard disc (Fig. 11). Results of both setups are statistically consistent with each other and suggest that the use of the cardboard is unlikely to impact the reliability of the D_e determination. Hence, the cardboard was used in all IRSL measurements within this study.

$D_e(t)$ plots with 1.5 s intervals show consistent results over the first 200 s of the IRSL signal as presented for both the natural signal and the artificial signal induced during dose recovery tests of RIN2 F and RIN5 PM (Fig. 7). For age determination, D_e values were derived using the first 1.5 s of the signal and a late background subtraction of the last 50 s. Examples of extended dose response curves are shown for one aliquot from RIN2 F and one aliquot from RIN5 PM in Fig. 9. Laboratory saturation levels exceed 1500 Gy (F) and 1800 Gy (PM), and $2 \times D_0$ values are about 600 Gy (F) and above 425 Gy (PM; Table 1). For both F and PM, dose response curves are well fitted with a double-saturating exponential and a single-saturating exponential function.

6 Fading attributes and correction

As the IRSL signal commonly is subject to a loss of signal over time, fading tests were conducted following Auclair et al. (2003) for a given dose of ca. 130 Gy. Three cycles with storage times of ca. 0 s, 1 h, 2.5 h, 5 h and 10 h were implemented per aliquot while the aliquot constantly remained on the sample arm. This reduces the possibility of sample material being lost during mechanical transfer of the aliquot between sample arm and storage carousel (Preusser et al., 2014). For all fading tests, aliquots previously used for D_e determination were utilised. Two fading correction procedures were conducted, following Lamothe et al. (2003) and Kars et al. (2008), respectively, using the R luminescence package (Kreutzer and Mercier, 2019; King and Burow, 2019). The first approach is based on the extrapolation of luminescence signal loss to a decadal percentage (g-value) that is used to correct the natural dose and the dose response points while the latter approach utilises the sample-specific density of recombination centres (ρ'-value) to correct the dose response curves. To apply both approaches, ρ'- and g-values were derived, whereby the latter was normalised to 2 d.

Fading properties (ρ'-value of 2.21×10^{-6}; g-value of $3.1\% \pm 0.6\%$ per decade) were obtained for RIN2 as a representative sample for the F fractions, and fading correction was applied to the F measurements, providing corrected D_e values and ages (Table 1). Following Kars et al. (2008), the

Appendix C
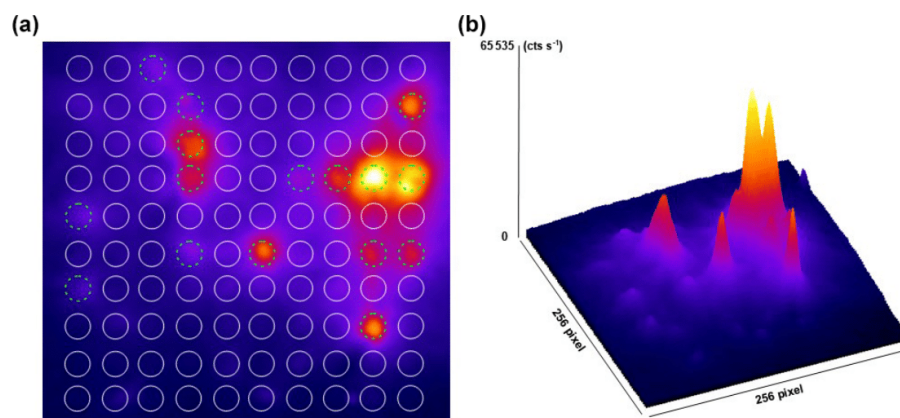
Figure 10. Coloured EMCCD image obtained from the natural IRSL signal of 100 F grains of RIN2. The grains were placed on a Risø single grain disc with a 10×10 grid of holes ($300 \, \mu m$ in diameter). **(a)** Holes containing F grains emitting luminescence are presented with dashed green circles, while those without emission are shown in white. **(b)** The 3D surface plot emphasises that some grains inherit very bright signals, while others are rather dim.
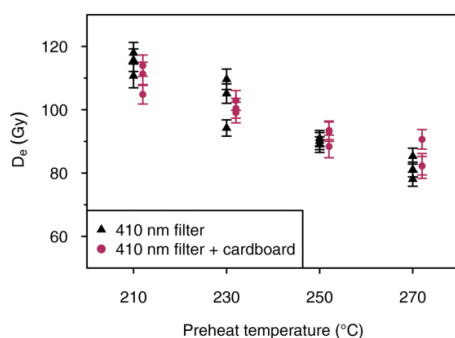

Figure 11. Dose recovery test (RIN2 F, 130 Gy given dose) at different preheat temperatures with and without a mounted cardboard barrier to reduce photon passage.

corrected F D_e values, except for RIN13 F, are about 16 % higher than those corrected using Lamothe et al. (2003). Kars-corrected D_e values are between 247 ± 7 Gy (RIN1) and 297 ± 6 Gy (RIN4) and well below $2 \times D_0$ (RIN1 measured 577 ± 20 Gy and simulated 560 ± 7 Gy; RIN2 measured 626 ± 22 Gy and simulated 602 ± 9 Gy; RIN3 measured 609 ± 18 Gy and simulated 590 ± 9 Gy; RIN4 measured 641 ± 26 Gy and simulated 612 ± 24 Gy). For RIN13 F, a significant number of aliquots 12 (Lamothe correction) and 19 (Kars correction) out of 30 measured aliquots are in saturation. Minimum CAM D_e values of > 695 and > 974 Gy are obtained, respectively, which are beyond the $2 \times D_0$ limit (measured 651 ± 32 Gy; Kars-simulated 666 ± 4 Gy). However, for all other samples the Kars-corrected F ages (for age determination, see Sect. 7) are in good agreement with those

of the Q fraction (statistically consistent at 1σ, Table 1). It cannot be excluded that this effect is due to an overestimation of both Kars-corrected F and Q ages. Due to the lack of evidence for the prior, the Kars et al. (2008) fading correction approach is considered most appropriate for samples of this study.

For PM, fading properties (ρ'-value of 1.89×10^{-6}; g-value of 2.4 ± 0.6 % per decade) were obtained from one representative polymineral sample (RIN5). Following Lamothe et al. (2003), the corrected ages are 20 % to 100 % lower than those corrected using Kars et al. (2008). As the latter have shown good agreement for F and Q ages, ages calculated using Kars-corrected PM D_e values are presented in the following. Corrected PM ages of RIN5 and RIN6 are, with 138 ± 7 ka and 169 ± 9 ka, 22 % and 44 % higher than the associated fQ ages. While RIN5 is younger than to be expected from the Q and fading corrected F ages of the overlaying samples (RIN1 to RIN4), the derived fading corrected age is still consistent at 2σ with the latter. The corrected PM age of RIN6 is statistically consistent (at 1σ) with the ages of the overlaying samples. For RIN8 PM and RIN13 PM, corrected ages of 471 ± 47 and 526 ± 53 ka were calculated, respectively. Fading corrected D_e values are, with 1101 ± 97 Gy (RIN8) and 955 ± 86 Gy (RIN13), far beyond the $2 \times D_0$ values (RIN8 measured 80 ± 40 Gy and simulated 536 ± 4 Gy; RIN13 measured 515 ± 39 Gy and simulated 534 ± 3 Gy).

Both g-values obtained in this study are similar to those previously found for northern Switzerland (see Sect. 1). However, while most studies have abstained from applying fading corrections, the here-presented Kars fading-corrected F and Q ages are in good agreement, thereby justifying the application of this fading correction.

Appendix C
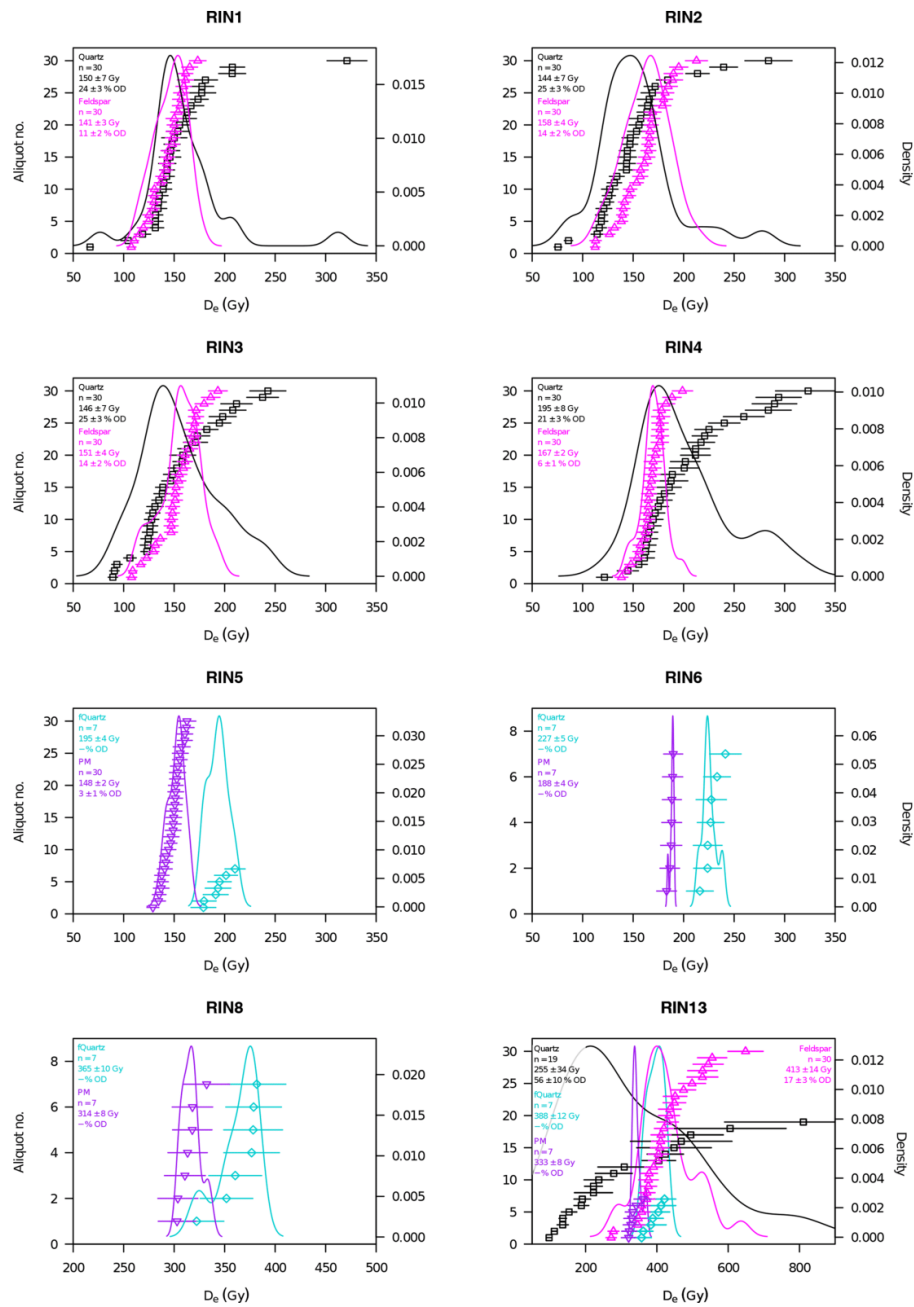
Figure 12. D_e distributions of all measured samples and minerals. CAM D_e values are given with 1σ uncertainty. F and PM D_e values are uncorrected.

Appendix C

7 D_e distributions and ages

7.1 Quartz OSL

The D_e distributions of the four top Q samples show the tendency towards being positively skewed and have overdispersion (OD) values between $21\% \pm 3\%$ and $25\% \pm 3\%$ (Fig. 12). Arnold et al. (2007) recommend the application of a three-parameter minimum age model (MAM3) (Galbraith et al., 1999) for D_e distributions of partially bleached samples that are significantly positively skewed and/or show OD values of $> 40\%$. Following this, skewness of RIN1, RIN2 and RIN4 require the use of an MAM3. However, the decision tree of Arnold et al. (2007) is based on fluvial samples with diverse bleaching histories that are comparably young (< 20 ka). For older samples, it is suggested that distributions may vary, as time-dependent factors are expected to contribute to the data spread (Galbraith and Roberts, 2012). For example, the impact of beta microdosimetry (Mayya et al., 2006) will increase with the age of the sample. Therefore, the application of an MAM3 was refrained from and derived CAM D_e values of between 144 ± 7 and 195 ± 8 Gy were used for the age determination of the top four samples (Table 1). Q ages for these samples range between 164 ± 9 ka (RIN4) and 180 ± 11 ka (RIN3) and are statistically consistent with each other (1σ).

The D_e distributions of RIN13 Q is also positively skewed but presents a much higher OD value, $56 \pm 10\%$, in comparison to the four top Q samples. Of the measured aliquots, 12% are in saturation, allowing only for the assessment of a truncated distribution. In this case, the application of the MAM3 is also recommended (Arnold et al., 2007). Besides an expected impact of beta microdosimetry, fitting uncertainties are likely accountable for the skewness and spread of the distribution. For RIN13 Q, the natural doses are projected on the high proportion of the dose response curves, emphasising any fitting uncertainty. Therefore, an MAM3 D_e value is unlikely to represent the distribution most appropriately and the CAM D_e value is considered to represent a more conclusive lower limit of the distribution. The CAM D_e value of 255 ± 34 Gy is consistent with the $2 \times D_0$ limit of 274 ± 16 Gy, and it is arguable whether an obtained age at this range is still reliable. However, the minimum CAM age of 183 ± 26 ka is consistent with ages of the top four samples, and from this and the stratigraphy it can be deduced that RIN13 is of similar age or older than RIN1 to RIN4.

The four fQ samples (RIN5, RIN6, RIN8, RIN13), representing depths of 10 to 36 m, show normally distributed D_e values (Figs. 2, 12, Table 1). This is to be expected for fine-grained samples, as the number of grains on each aliquot will have an averaging effect that will mask any skewness of the D_e distributions. CAM D_e values of 195 ± 4 to 388 ± 12 Gy were derived, which are all well below $2 \times D_0$ (Table 1). For the lowest samples (RIN13), the obtained age of 224 ± 18 ka is close to the upper limit of reliable quartz ages in the region

(Lowick et al., 2015). Obtained fQ ages for the two topmost lacustrine samples are 113 ± 9 ka (RIN5) and 117 ± 9 ka (RIN6). These ages are between 20% and almost 50% lower than ages derived for the Q fractions of RIN1 to RIN4. This, from a chrono-stratigraphy perspective, is unreasonable and can be ascribed to either issues with the D_e value or the dose rate determination and will be discussed in detail in Sect. 8.

7.2 Feldspar and polymineral IRSL

None of the F and PM D_e distributions show a trend towards being skewed and OD values are between 0% and 17% (Fig. 12). This is to be expected for the fine-grain PM aliquots that each represent an averaged D_e value derived from over a million grains. For F, each aliquot consists of only about 13 grains, whereof few give a luminescence signal (see Sect. 5.2), and the D_e distributions are not affected by skewness. Therefore, as no evidence for partial bleaching is observed, the CAM was applied for all F and PM samples (Table 1). For the upper four samples, Kars-corrected CAM D_e values of between 247 ± 7 Gy (RIN1 F) and 297 ± 6 Gy (RIN4 F) were derived, which equates to ages of 160 ± 7 ka (RIN4) to 167 ± 8 ka (RIN2). These ages are statistically consistent at 1σ with those of the Q fraction (Table 1). For RIN5 PM and RIN6 PM Kars-corrected CAM D_e values of 252 ± 3 and 343 ± 9 Gy or ages of 138 ± 7 and 169 ± 9 ka were obtained, respectively. RIN5 PM presents an age inversion (-22 ± 10 ka) in comparison with the overlying samples RIN1 to RIN4. A similar trend is found for both RIN5 and RIN6 fQ ages. This, from a chrono-stratigraphy perspective, is unreasonable and can be ascribed to either issues with the D_e value or the dose rate determination and will be discussed in detail in Sect. 8. However, the PM age of RIN6 is statistically consistent at 1σ with overlying F ages.

For RIN13 PM, the age is in agreement with the minimum age of > 437 ka obtained for the F fraction of the same sample. There are three possible explanations for the high D_e values of RIN8 and RIN13: (1) the sediment was deposited about half a million years ago, (2) the applied fading correction overestimates for doses derived from the higher dose range of the response curve or (3) these D_e values are the result of an averaged signal with a greater contribution of partially bleached, high residual signals. The latter is an effect that is to be expected for glacier-proximal deposits that are likely to have had limited light exposure during short transport times. From the sedimentological context, samples RIN8 and RIN13 are likely from such an environment. However, no drastic increase in D_e values was observed for the fQ fraction, but it has to be considered that the OSL signal of quartz bleaches faster than feldspar. Nevertheless, corrected D_e values are higher than the $2 \times D_0$ values. This measure has been introduced as a dating limit for quartz (Wintle and Murray, 2006) but was found to be an appropriate measure for adequately dating feldspars as well (Zhang and Li, 2020).

Appendix C
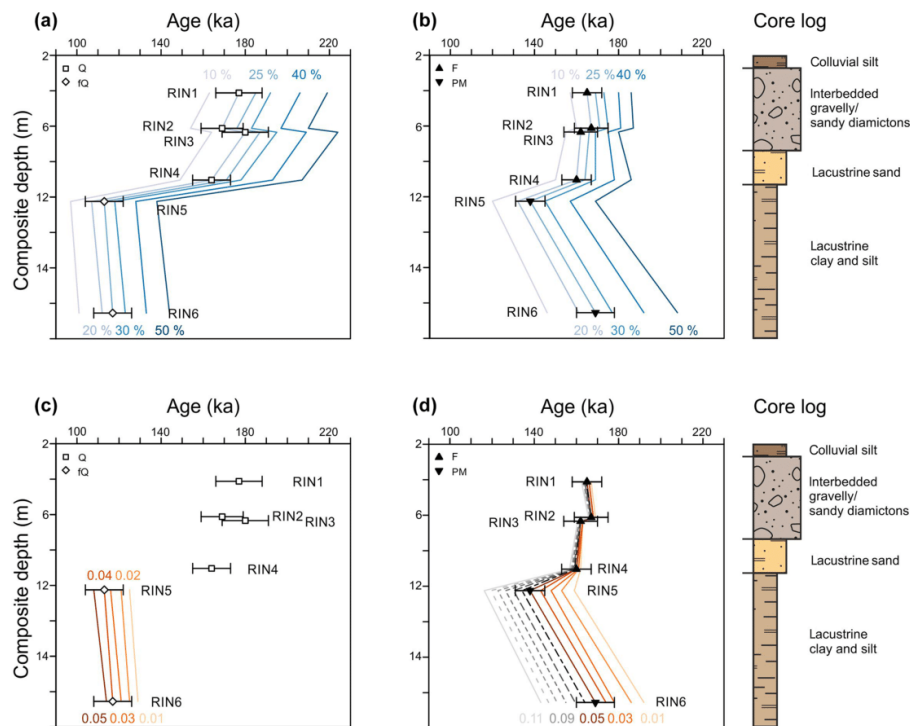
Figure 13. Ages of **(a)** Q and fQ and **(b)** F and PM (fading corrected following Kars et al., 2008) are shown for water contents between 10 % and 50 % and plotted against depth (line signature). **(c)** Ages of fQ are shown for alpha efficiency values between 0.01 and 0.05 and plotted against depth (line signature). No alpha component was considered for age determination of HF-etched Q, but accepted ages are presented for completeness. **(d)** F and PM (fading corrected following Kars et al., 2008) ages for alpha efficiency values between 0.01 and 0.11. Accepted ages are presented with 1σ uncertainties as point signatures. The upper part of the core log is given on the right for comparison (see Fig. 2 for the full log).

Therefore, D_e values of RIN8 PM, RIN13 PM and RIN13 F are unsuitable for the determination of finite ages.

8 Age comparison

For the top four samples, Q and fading-corrected F ages range between 160 ± 7 ka (RIN4 F) and 180 ± 11 ka (RIN3 Q) and are thereby statistically consistent with each other at 1σ. For the two samples (RIN5, RIN6) below, a discrepancy between fQ and PM ages (22 % to 44 %) is observed. In addition, fQ ages of these two samples are up to almost 50 % lower than those of the overlying samples RIN1 to RIN4. This leads to an age offset of ca. 50 ka between Q and fQ that is not accountable from a chrono-stratigraphic perspective. The observed age offset equals 20 % to 50 % difference and is likely to be emphasised through the actual age calculation, which in turn relies on derived D_e and DR_{total} values. The latter are all based on the assumptions that (1) the long-term average estimates of the water content are accurate and

(2) used alpha efficiency values are appropriate in this context.

8.1 Water content and age determination

A water content of $20\% \pm 5\%$ was assumed for all but two samples, which is within 5 % uncertainty of the measured field water content (Table 2). RIN5 and RIN6 have a slightly higher field water content (23 % to 24 %) due to their argillaceous character, and hence an average long-term water content of $25\% \pm 5\%$ was found to be more appropriate for these samples. For similar sedimentary facies, values between 20 % and 30 % have been used (Anselmetti et al., 2010; Dehnert et al., 2012; Lowick et al., 2015; Buechi et al., 2017). However, the assessment of an appropriate long-term water content is complex but important to avoid age over- or underestimations. It is well known that moisture has an attenuation effect of beta and gamma radiation (Zimmermann, 1971), which may lead to drastic changes in DR_{total} and thereby age determination (Nathan and Mauz, 2008). Be-

Appendix C

tween 34 % and 49 % of water, in relation to the samples dry weights, was absorbed over a 24 h period by unconsolidated sample material in this study. The highest amounts of water were absorbed by RIN5 and RIN6, which also presented the highest field water contents. For the purpose of comparison, the water content maximum can be set to 50 % to represent the highest observed absorption capacity for unconsolidated sample material (Table 2). The DR_{total} values are calculated for water contents between 10 % and 50 % in 10 % steps. In addition, a step with 25 % water content, as is assumed to be appropriate for age determination of RIN5 and RIN6, is included in the comparison. Recalculated ages (Fig. 13a and b) show that the difference in ages for the different water contents is up to 40 % for Q, 15 % to 25 % for F, and 40 % for PM and fQ. A water content of 10 % for Q and F (RIN1 to RIN4) results in statistically consistent ages at 2σ with fQ and PM (RIN5, RIN6) at 50 %. However, a 10 % moisture for the coarse-grained samples is unlikely, as under current conditions ground water penetrates these layers and oxidation features are present. Also, 50 % of moisture for fQ and PM are at the limit of maximum water absorption capacity for unconsolidated material of these samples. It is unlikely that for the consolidated deposits, as found in nature, the maximum absorption capacity will be equally high and that these samples were saturated to a maximum for over ca. 150 ka. Therefore, neither 50 % nor 10 % water content is considered representative as a long-term average. Consequently, assumptions about the water content may well have an effect on the age discrepancy between RIN5 and RIN6 and the coarse-grained samples from above (RIN1 to RIN4), but they are not the sole cause for this offset.

8.2 Alpha efficiency values and age determination

A further cause for the observed discrepancy may be found in the chosen alpha efficiency values (a-values), which account for the efficiency of alpha particles for producing luminescence and are grain size dependent (cf. Mauz et al., 2006). For the coarse Q fraction, the need to consider alpha radiation is circumvented by HF etching the outer rind of the grains and thereby removing the sphere penetrated by alpha particles. However, fQ grains cannot be etched due to the possibility of total dissolution, and therefore an appropriate a-value has to be chosen. In this study, an a-value of 0.04 ± 0.02 was used for fQ, following Buechi et al. (2017). In the literature, a-values between 0.02 ± 0.01 and 0.05 ± 0.01 have been presented for fine-grained quartz from several continents (e.g. Rees-Jones, 1995; Mauz et al., 2006; Lai et al., 2008), and a-values of 0.03 ± 0.02 to 0.05 ± 0.01 were used in studies of northern Switzerland (e.g. Gaar and Preusser, 2012; Lowick et al., 2015; Buechi et al., 2017). For the polymineral fractions, a-values of up to 0.10 ± 0.01 and 0.11 ± 0.01 (e.g. Rees-Jones, 1995; Lang et al., 2003; Schmidt et al., 2018a) are presented in the literature. However, for two study sites in northern Switzerland, a-values

with a mean of 0.05 ± 0.01 have been determined (Preusser, 1999a, b; Preusser et al., 2001). Considering that these two studies represent the nearest approximation of geographical position and provenance, their a-value was used here.

The impact of a-value estimates is investigated by recalculating ages for different a-values (0.01 to 0.05 for fQ and 0.01 to 0.11 for PM, Fig. 13c and d). For fQ and PM, a reduction of the a-value leads to a 11 % to 16 % age increase, while for corrected F the a-value has an insignificant impact onto the finite ages (ca. 2 ka). Recalculated ages are consistent with each other at 2σ over the a-value spectrum between 0.01 and 0.05. Between corrected F and PM samples, lower a-values (e.g. 0.01) will decrease the age differences. However, the chosen a-value of 0.05 is at the lower limit of values proposed in the literature. A sample-specific determination of a-values is needed to justify the use of a lower a-value. However, in the absence of sample-specific a-values and limited gain of age precision, the initially chosen a-value will be retained.

Also, with the lowest possible a-value of 0.01 for fQ, an offset to the Q ages of the top four samples and RIN5 and RIN6 is still apparent with ca. 20 ka. A further increase of the used a-values will amplify the age offset. Consequently, neither the chosen a-value nor water content is the sole cause for the observed age offset.

8.3 Implications

Neither the chosen water contents nor the a-values are the sole cause for the age offset between RIN5 and RIN6 fQ and RIN1 to RIN4 Q. Given the internal consistency of Q ages for RIN1 to RIN4 and the chrono-stratigraphic context, fQ ages of this study should be regarded as minimum age estimates. Unlike for other studies in the area (e.g. Gaar and Preusser, 2012), corrected F ages are in agreement with Q ages while uncorrected ages are suspect to significant age underestimation. However, obtained Q ages remain under the reliable quartz luminescence age limit of ca. 250 ka (Anselmetti et al., 2010; Dehnert et al., 2012; Lowick et al., 2015; Buechi et al., 2017).

With only minimum age estimates of the two lowest samples (RIN8 fQ > 163 ka, RIN13 Q > 183 ka, RIN13 fQ > 224 ka) it remains unclear whether the transition from glacial- to proglacial-influenced environments to a lacustrine environment was of a rapid nature or occurred much earlier than the deposition of the entire lacustrine sequence. For the lacustrine sequence, ages of 169 ka (RIN6 PM) and 138 ka (RIN5 PM) were obtained. The sandy top of the lacustrine unit is ca. 160 ka (RIN4 F, Q), which is statistically consistent with ages from the sandy diamicton (RIN1 to RIN3; 160 to 180 ka F and Q). This indicates a deposition of at least 16.6 m during Marine Isotope Stage 6 (MIS 6) with a rapid transition from lacustrine to colluvial-dominated periglacial environments.

Appendix C

9   Conclusions

Luminescence properties of coarse- and fine-grained quartz, feldspar and polymineral fractions of eight samples from a palaeovalley in northern Switzerland were assessed. Quartz components have been found to be stable, and the occurrence of a second exponential function in the dose response curves is missing. Noteworthy is the presence of positively skewed D_e distributions for coarse-grained quartz, but the lack of a comparable pattern for the slower-bleaching feldspar suggests that partial bleaching is unlikely to influence these distributions. However, an age discrepancy between fine- and coarse-grained quartz is present. Different scenarios for dose rate components (a-value, water content) are assessed but do not explain the age discrepancy. From the two applied fading corrections, the Kars-fading-corrected feldspar ages are in good agreement with each other, with the quartz ages and one fading-corrected polymineral age from the unit below. Noteworthy is the presence of positively skewed D_e distributions for coarse-grained quartz, while the slower-bleaching feldspar lacks a comparable pattern, suggesting that partial bleaching is unlikely to influence these distributions. Not all minerals, fractions or samples are suitable for dating using the here-presented luminescence techniques; nonetheless, this systematic investigation of different luminescence signals allows for a decisive chronology to be established. For the study site, Rinikerfeld, a deposition of at least 16.6 m during MIS 6 with a rapid transition from lacustrine to colluvial-dominated periglacial environments is reconstructed. For the two lowest samples, only minimum age estimates can be derived from the chrono-stratigraphic context, indicating that those glacial to proglacial diamictons are of similar age or older than the top units.

References

Aitken, M. J.: An Introduction to Optical Dating – The Dating of Quaternary Sediments by the Use of Photon-stimulated Luminescence, Oxford University Press, 267 pp., https://doi.org/10.5860/choice.36-6294, 1998.

Anselmetti, F. S., Drescher-Schneider, R., Furrer, H., Graf, H. R., Lowick, S. E., Preusser, F., and Riedi, M. A: A ~ 180,000 years sedimentation history of a perialpine overdeepened glacial trough (Wehntal, N-Switzerland), Swiss J. Geosci., 103, 345–361, https://doi.org/10.1007/s00015-010-0041-1, 2010.

Arnold, L. J., Bailey, R. M., and Tucker, G. E.: Statistical treatment of fluvial dose distributions from southern Colorado arroyo deposits, https://doi.org/10.1016/j.quageo.2006.05.003, Quat. Geochronol., 2, 162–167, 2007.

Auclair, M., Lamothe, M., and Huot, S: Measurement of anomalous fading for feldspar IRSL using SAR. Radiat. Meas., 37, 487–492, https://doi.org/10.1016/s1350-4487(03)00018-0, 2003.

Bini, A., Buoncristiani, J. F., Coutterand, S., Ellwanger, D., Felber, M., Florineth, D., Graf, H. R., Keller, O., Kelly, M., Schlüchter, C., and Schoeneich, P.: Die Schweiz während des letzteiszeitlichen Maximums (LGM) (Map 1 : 500 000), Swisstopo, Wabern, 2009.

Bitterli-Dreher, P., Graf, H. R., Naef, H., Diebold, P., Matousek, F., Burger, H., ND Pauli-Gabi, T.: Geologischer Atlas der Schweiz 1 : 25 000, Blatt 1070 Baden, Erläuterungen, Bundesamt für Landestopografie swisstopo, 152 pp., 2007.

Bluszcz, A. and Adamiec, G.: Application of differential evolution to fitting OSL decay curves, Radiat, Meas., 41, 886–891, https://doi.org/10.1016/j.radmeas.2006.05.016, 2006.

Buechi, M. W., Lowick, S. E., and Anselmetti, F. S.: Luminescence dating of glaciolacustrine silt in overdeepened basin fills beyond the last interglacial, Quat. Geochronol., 37, 55–67, https://doi.org/10.1016/j.quageo.2016.09.009, 2017.

Buylaert, J. P., Thiel, C., Murray, A. S., Vandenberghe, D. A., Yi, S., and Lu, H.: IRSL and post-IR residual dose recorded in modern dust samples from the Chinese Loess Plateau, Geochronometria, 38, 432–440, https://doi.org/10.2478/s13386-011-0047-0, 2011.

Cunningham, A. C. and Wallinga, J.: Selection of integration time intervals for quartz OSL decay curves, Quat. Geochronol., 5, 657–666, https://doi.org/10.1016/j.quageo.2010.08.004, 2010.

Degering, D. and Degering, A: Change is the only constant – time-dependent dose rates in luminescence dating, Quat. Geochronol., 58, 1–14, https://doi.org/10.1016/j.quageo.2020.101074, 2020.

Dehnert, A., Lowick, S. E., Preusser, F., Anselmetti, F. S., Drescher-Schneider, R., Graf, H. R., Heller, F., Horstmeyer, H., Kemna, H. A., Nowactzyk, N. R., Züger, A., and Furrer, H.: Evolution of an overdeepened trough in the northern Alpine Foreland

Appendix C

at Niederweningen, Switzerland, Quat. Sci. Rev., 34, 127–145, https://doi.org/10.1016/j.quascirev.2011.12.015, 2012.

DIN 18132:2012-04: Baugrund, Versuche und Versuchsgeräte – Bestimmung des Wasseraufnahmevermögens, https://doi.org/10.31030/1870018, 2016.

Duller, G. A.: A new method for the analysis of infrared stimulated luminescence data from potassium feldspar, Radiat. Meas., 23, 281–285, https://doi.org/10.1016/1350-4487(94)90053-1, 1994.

Duller, G. A.: Behavioural studies of stimulated luminescence from feldspars, Radiat. Meas., 27, 663–694, https://doi.org/10.1016/s1350-4487(97)00216-3, 1997.

Duller, G. A.: Single grain optical dating of glacigenic deposits, Quat. Geochronol, 1, 296–304, https://doi.org/10.1016/j.quageo.2006.05.018, 2006.

Gaar, D. and Preusser, F.: Luminescence dating of mommoth remains from northern Switzerland, Quat. Geochronol., 10, 257–263, https://doi.org/10.1016/j.quageo.2012.02.007, 2012.

Gaar, D., Lowick, S. E., and Preusser, F.: Performance of different luminescence approaches for the dating of known-age glaciofluvial deposits from northern Switzerland, Geochronometria, 41, 65–80, https://doi.org/10.2478/s13386-013-0139-0, 2013.

Galbraith, R. F. and Roberts, R. G.: Statistical aspects of equivalent dose and error calculation and display in OSL dating: An overview and some recommendations, Quat. Geochronol, 11, 1–27, https://doi.org/10.1016/j.quageo.2012.04.020, 2012.

Galbraith, R. F., Roberts, R. G., Laslett, G. M., Yoshida, H., and Olley, J. M.: Optical dating of single and multiple grains of quartz from Jinmium rock shelter, Northern Australia: Part I, experimental design and statistical models, Archaeometry, 41, 339–364, https://doi.org/10.1111/j.1475-4754.1999.tb00987.x, 1999.

Gegg, L., Kuster, A. M., Schmid, D., and Buechi, M. W.: Quaternary Boreholes QBO Riniken-1 & -2 (QRIN1 & QRIN2), Data Report, Nagra Arbeitsbericht NAB 18–40, 8 pp., available at: https://www.nagra.ch/de/cat/publikationen/arbeitsberichte-nabs/nabs-2018/downloadcenter.htm (last access: 4 February 2019), 2018.

Godfrey-Smith, D. I., Huntley, D. J., and Chen, W. H.: Optical dating studies of quartz and feldspar sediment extracts, Quat. Sci. Rev., 7, 373–380, https://doi.org/10.1016/0277-3791(88)90032-7, 1988.

Graf, A. A., Strasky, S., Ivy-Ochs, S., Akçar, N, Kubik, P. W., Burkhard, M., and Schlüchter, C.: First results of cosmogenic dated pre-Last Glaciation erratics from the Montoz area, Jura Mountains, Switzerland, Quatern. Int., 164–165, 43–52, https://doi.org/10.1016/j.quaint.2006.12.022, 2007.

Graf, H. R.: Stratigraphie von Mittel- und Spätpleistozän in der Nordschweiz, Textband, Federal Office of Topography swisstopo, 198 pp., 2009.

Huntley, D .J.: An explanation of the power-law decay of luminescence, J. Phys.-Condens. Mat., 18, 1359–1365, https://doi.org/10.1088/0953-8984/18/4/020, 2006.

Huntley, D. J. and Baril, M. R.: The K content of the K-feldspars being measured in optical dating or in thermoluminescence dating, Anc. TL, 15, 11–13, 1997.

Huntley, D. J. and Lamothe, M.: Ubiquity of anomalous fading in K-feldspars and measurement and correction for it in optical dating, Can. J. Earth Sci., 38, 1093–1106, https://doi.org/10.1139/e01-013, 2001.

Jain, M., Murray, A. S., and Bøtter-Jensen, L.: Characterisation of blue-light stimulated luminescence components in different quartz samples: implications for dose measurement, Radiat. Meas., 37, 441–449, https://doi.org/10.1016/s1350-4487(03)00052-0, 2003.

Kars, R. H., Wallinga, J., and Cohen, K. M.: A new approach towards anomalous fading correction for feldspar IRSL dating – tests on samples in field saturation, Radiat. Meas., 43, 786–790, https://doi.org/10.1016/j.radmeas.2008.01.021, 2008.

King, G. E. and Burow, C.: Calc_Huntley2006(): Apply the Huntley (2006) model, Function version 0.4.1, in: Luminescence: Comprehensive Luminescence Dating Data Analysis, edited by: Kreutzer, S., Burow, C., Dietz, M., Fuchs, M. C., Schmidt, C., Fischer, M., and Friedrich, J., R package version 0.9.0.109, available at: https://CRAN.R-project.org/package=Luminescence (last access: 7 November 2019), 2019.

Klasen, N., Fiebig, M., and Preusser, F.: Applying luminescence methodology to key sites of Alpine glaciations in Southern Germany, Quatern. Int., 420, 240–258, https://doi.org/10.1016/j.quaint.2015.11.023, 2016.

Kock, S., Kramers, J. D., Preusser, F., and Wetzel, A.: Dating of Late Pleistocene terrace deposits of the River Rhine using Uranium series and luminescence methods: Potential and limitations, Quat. Geochronol., 4, 363–373, https://doi.org/10.1016/j.quageo.2009.04.002, 2009.

Kreutzer, S. and Mercier, N.: Calc_Lamothe2003(): Apply fading correction after Lamothe et al., 2003. Function version 0.1.0, in: Luminescence: Comprehensive Luminescence Dating Data Analysis, edited by: Kreutzer, S., Burow, C., Dietz, M., Fuchs, M. C., Schmidt, C., Fischer, M., and Friedrich, J., R package version 0.9.0.109, available at: https://CRAN.R-project.org/package=Luminescence, last access: 12 November 2019.

Lai, Z. P.: Chronology and the upper dating limit for loess samples from Luochuan section in the Chinese Loess Plateau using quartz OSL SAR protocol, J. Asian Earth Sci., 37, 176–185, https://doi.org/10.1016/j.jseaes.2009.08.003, 2010.

Lai, Z. P., Zöller, L., Fuchs, M., and Brückner, H.: Alpha efficiency determination for OSL of quartz extracted from Chinese loess, Radiat. Meas., 43, 767–770, https://doi.org/10.1016/j.radmeas.2008.01.022, 2008.

Lamothe, M., Auclair, M., Hamzaoui, C., and Huot, S.: Towards a prediction of long-term anomalous fading of feldspar IRSL, Radiat. Meas., 37, 493–498, https://doi.org/10.1016/s1350-4487(03)00016-7, 2003.

Lang, A., Hatté, C., Rousseau, D. D., Antoine, P, Fontugne, M., and Zöller, L., Hambach, U.: High-resolution chronologies for loess: comparing AMS ^{14}C and optical dating results, Quat. Scie. Rev., 22, 953–959, https://doi.org/10.1016/s0277-3791(03)00035-0, 2003.

Li, B. and Li, S.-H.: Comparison of D_e estimates using the fast component and the medium component of quartz OSL, Radiat. Meas. 41, 125–136, https://doi.org/10.1016/j.radmeas.2005.06.037, 2006a.

Li, S.-H. and Li, B.: Dose measurement using fast component of LM-OSL signals from quartz, Radiat. Meas., 41, 534–541, https://doi.org/10.1016/j.radmeas.2005.04.029, 2006b.

Lowick, S. E., Preusser, F., Pini, R., and Ravazzi, C.: Underestimation of fine grain quartz OSL dating towards the Eemian: Comparison with palynostratigraphy from Az-

Appendix C

zano Decimo, northern Italy, Quat. Geochronol., 5, 583–590, https://doi.org/10.1016/j.quageo.2009.12.003, 2010.

Lowick, S. E., Trauerstein, M., and Preusser, F.: Testing the application of post IR-IRSL dating to fine grain waterlain sediments, Quat. Geochronol., 8, 33–40, https://doi.org/10.1016/j.quageo.2011.12.003, 2012.

Lowick, S. E., Buechi, M. W., Gaar, D., Graf, H. R., and Preusser, F.: Luminescence dating of Middle Pleistocene proglacial deposits from northern Switzerland: methodological aspects and stratigraphical conclusions, Boreas, 44, 459–482, https://doi.org/10.1111/bor.12114, 2015.

Mauz, B., Packmann, S., and Lang, A.: The alpha effectiveness in silt-sized quartz: New data obtained by single and multiple aliquot protocols, Anc. TL, 24, 47–52, 2006.

Mayya, Y. S., Morthekai, P., Murari, M. K., and Singhvi, A. K.: Towards quantifying beta microdosimetric effects in single-grain quartz dose distribution, Radiat. Meas., 41, 1032–1039, 2006.

Murray, A. S. and Wintle, A. G.: Luminescence dating of quartz using an improved single-aliquot regenerative-dose protocol, Radiat. Meas., 32, 57–73, https://doi.org/10.1016/s1350-4487(99)00253-x, 2000.

Murray, A. S., Buylaert, J. P., Henriksen, M., Svendsen, J. I., and Mangerud, J.: Testing the reliability of quartz OSL ages beyond the Eemian, Radiat. Meas., 43, 776–780, https://doi.org/10.1016/j.radmeas.2008.01.014, 2008.

Murray, A. S., Thomsen, K. J., Masuda, N., Buylaert, J. P., and Jain, M.: Identifying well-bleached quartz using the different bleaching rates of quartz and feldspar luminescence signals, Radiat. Meas., 47, 688–695, https://doi.org/10.1016/j.radmeas.2012.05.006, 2012.

Nathan, R. P. and Mauz, B.: On the dose-rate estimate of carbonate-rich sediments for trapped charge dating, Radiat. Meas., 43, 14–25, https://doi.org/10.1016/j.radmeas.2007.12.012, 2008.

Olley, J. M., Pietsch, T., and Roberts, R. G.: Optical dating of Holocene sediments from a variety of geomorphic settings using single grains of quartz, Geomorphology, 60, 337–358, https://doi.org/10.1016/j.geomorph.2003.09.020, 2004.

Pawley, S. M., Toms, P., Armitage, S. J., and Rose, J.: Quartz luminescence dating of Anglian Stage (MIS 12) fluvial sediments: Comparison of SAR age estimates to the terrace chronology of the Middle Thames valley, UK, Quat. Geochronol., 5, 569–582, https://doi.org/10.1016/j.quageo.2009.09.013, 2010.

Peng, J., Li, B., More, J., Garbow, B., Hillstrom, K., Burkhardt, J., Gilbert, P., and Varadhan, R.: numOSL: Numeric Routines for Optically Stimulated Luminescence Dating, R package version 2.6, https://CRAN.R-project.org/package=numOSL (last access: 12 November 2019), 2018.

Prescott, J. R. and Hutton, J. T.: Cosmic ray contribution to dose rates for luminescence and ESR dating: large depths and long-term time variations, Radiat. Meas., 23, 497–500, https://doi.org/10.1016/1350-4487(94)90086-8, 1994.

Preusser, F.: Luminescence dating of fluvial sediments and overbank deposits from Gossau, Switzerland: fine grain dating, Quat. Geochronol., 18, 217–222, https://doi.org/10.1016/s0277-3791(98)00054-7, 1999a.

Preusser, F.: Lumineszenzdatierung fluviatiler Sedimente: Fallbeispiele aus der Schweiz und Norddeutschland, Kölner Forum für Geologie und Paläontologie, 3/1999, edited by: Herbig, H. G., Geologisches Institut der Universität zu Köln, 62 pp., 1999b.

Preusser, F., Müller, B. U., and Schlüchter, C.: Luminescence dating of sediments from Luthern Valley, Central Switzerland, and implications for the chronology of the last glacial cycle, Quaternary Res., 55, 215–222, https://doi.org/10.1006/qres.2000.2208, 2001.

Preusser, F., Graf, H. R., Keller, O., Krayss, E., and Schlüchter, C.: Quaternary glaciation history of northern Switzerland, Quat. Sci. J., 60, 282–305, https://doi.org/10.3285/eg.60.2-3.06, 2011.

Preusser, F., Muru, M., and Rosentau, A.: Comparing different post-IR IRSL approaches for the dating of Holocene coastal foredunes from Ruhnu Island, Estonia, Geochronometria, 41, 342–351, https://doi.org/10.2478/s13386-013-0169-7, 2014.

Raab, T., Leopold, M., and Völkel, J.: Character, age, and ecological significance of Pleistocene periglacial slope deposits in Germany, Phys. Geogr., 28, 451–473, https://doi.org/10.2747/0272-3646.28.6.451, 2007.

Rees-Jones, J.: Optical dating of young sediments using fine-grain quartz, Anc. TL, 13, 9–14, 1995.

Schmidt, C., Bösken, J., and Kolb, T.: Is there a common alpha-efficiency in polymineral samples measured by various infrared stimulated luminescence protocols?, Geochronometria, 45, 160–172, https://doi.org/10.1515/geochr-2015-0095, 2018a.

Schmidt, C., Friedrich, J., Adamiec, G., Chruścińska, A., Fasoli, M., Kreutzer, S., Martini, M., Panzeri, L., Polymeris, G. S., Przegiętka, K., Valla, P. G., King, G. E., and Sanderson, D. C.: How reproducible are kinetic parameter constraints of quartz luminescence? An interlaboratory comparison for the 110 °C TL peak, Radiat. Meas., 110, 14–24, https://doi.org/10.1016/j.radmeas.2018.01.002, 2018b.

Spencer, J. Q. and Owen, L. A.: Optically stimulated luminescence dating of Late Quaternary glaciogenic sediments in the upper Hunza valley: validating the timing of glaciation and assessing dating methods, Quat. Scie. Rev., 23, 175–191, https://doi.org/10.1016/s0277-3791(03)00220-8, 2004.

Spooner, N. A.: On the optical dating signal of quartz, Radiat. Meas., 23, 593–600, https://doi.org/10.1016/1350-4487(94)90105-8, 1994.

Steffen, D., Preusser, F., and Schlunegger, F.: OSL quartz age underestimation due to unstable signal components, Quat. Geochronol., 4, 353–362, https://doi.org/10.1016/j.quageo.2009.05.015, 2009.

Swisstopo: swissALTI3D, Bundesamt für Landestopographie, swisstopo, available at: https://shop.swisstopo.admin.ch/en/products/height_models/alti3D (last access: 31 August 2018), 2013.

Thomsen, K. J., Murray, A. S., Jain, M., and Bøtter-Jensen, L.: Laboratory fading rates of various luminescence signals from feldspar-rich sediment extracts, Radiat. Meas., 43, 1474–1486, https://doi.org/10.1016/j.radmeas.2008.06.002, 2008.

Thiel, C., Buylaert, J-P., Murray, A. S., Terhost, B., Hofer, I., Tsukamoto, S., and Frechen, M.: Luminescence dating of the Stratzing loess profile (Austria) – Testing the potential of an elevated temperature post-IR IRSL protocol, Quatern. Int., 234, 23–31, https://https://doi.org/10.1016/j.quaint.2010.05.018, 2011.

Timar, A., Vandenberghe, D. A., Panaiotu, E. C., Panaiotu, C. G., Necula, C., Cosma, C., and van den Haute, P.: Optical dating of Romanian loess using fine-grained quartz, Quat. Geochronol., 5, 143–148, https://doi.org/10.1016/j.quageo.2009.03.003, 2010.

Timar-Gabor, A., Vandenberghe, D. A., Vasiliniuc, S., Panaoitu, E. E., Dimofte, D., and Cosma, C.: Optical

Appendix C

dating of Romanian loess: A comparison between silt-sized and sand-sized quartz, Quatern. Int., 240, 62–70, https://doi.org/10.1016/j.quaint.2010.10.007, 2011.

Trauerstein, M., Lowick, S. E., Preusser, F., and Veit, H.: Testing the suitability of dim sedimentary quartz from northern Switzerland for OSL burial dose estimation, Geochronomoetria, 44, 66–76, https://doi.org/10.1515/geochr-2015-0058, 2017.

Wallinga, J., Murray, A. S., and Duller, G. A.: Underestimation of equivalent dose in single-aliquot optical dating of feldspar caused by preheating, Radiat. Meas., 32, 691–695, https://doi.org/10.1016/s1350-4487(00)00127-x, 2000.

Wintle, A. G.: Anomalous Fading of Thermoluminescence in Mineral Samples, Nature, 245, 143–144, https://doi.org/10.1038/245143a0, 1973.

Wintle, A. G.: Luminescence dating: where it has been and where it is going, Boreas, 37, 471–482, https://doi.org/10.1111/j.1502-3885.2008.00059.x, 2008.

Wintle, A. G. and Murray, A. S.: A review of quartz optically stimulated luminescence characteristics and their relevance in single-aliquot regeneration dating protocols, Radiat. Meas. 41, 369–391, https://doi.org/10.1016/j.radmeas.2005.11.001, 2006.

Zhang, J. and Li., S.-H.: Review of the Post-IR IRSL Dating Protocols of K-Feldspar, Methods and Protocols, 3, 7, 1–20, https://doi.org/10.3390/mps3010007, 2020.

Zimmermann, D. W.: Thermoluminescent dating using fine grains from pottery, Archaeometry, 13, 29–52, https://doi.org/10.1111/j.1475-4754.1971.tb00028.x, 1971.

Appendix C

This page is intentionally left blank.

Declaration of consent

on the basis of Article 18 of the PromR Phil.-nat. 19

Name/First Name:	Gegg, Lukas
Registration Number:	17-128-240
Study program:	Doctoral Degree Program in Earth Sciences
	Bachelor ☐ Master ☐ Dissertation ☑
Title of the thesis:	The Mid-Pleistocene landscape history of the Lower Aare Valley with emphasis on subglacial overdeepening
Supervisors:	Prof. Dr. Flavio S. Anselmetti, Dr. Marius W. Buechi

I declare herewith that this thesis is my own work and that I have not used any sources other than those stated. I have indicated the adoption of quotations as well as thoughts taken from other authors as such in the thesis. I am aware that the Senate pursuant to Article 36 paragraph 1 litera r of the University Act of September 5th, 1996 and Article 69 of the University Statute of June 7th, 2011 is authorised to revoke the doctoral degree awarded on the basis of this thesis.

For the purposes of evaluation and verification of compliance with the declaration of originality and the regulations governing plagiarism, I hereby grant the University of Bern the right to process my personal data and to perform the acts of use this requires, in particular, to reproduce the written thesis and to store it permanently in a database, and to use said database, or to make said database available, to enable comparison with theses submitted by others.

Bern, September 27th 2021

Place, date   Signature